Multifunctional colloidal solutions for transient liquid assisted growth of superconducting nanocomposite films

Diana Garcia

Multifunctional colloidal solutions for transient liquid assisted growth of superconducting nanocomposite films

A dissertation submitted for the degree of

DOCTOR OF PHILOSOPHY IN MATERIALS SCIENCE

by

Diana Garcia

Supervisors:

Prof. Teresa Puig Molina

Dr. Susagna Ricart Miró

Dr. Ramón Yáñez

Superconducting Materials and Large Scale Nanostructures Department (SUMAN)

Facultat de Ciències

Universitat Autònoma de Barcelona

February 2024

The present doctoral thesis entitled "**Multifunctional colloidal solutions for transient liquid assisted growth of superconducting nanocomposite films**" is presented by Diana Garcia Franco to obtain the degree of Doctor of Philosophy in Materials Science.

The present thesis was carried out at the Superconducting Materials and Large Scale Nanostructures Department (SUMAN) at Institut de Ciència de Materials de Barcelona (ICMAB-CSIC) and the University Autonomous of Barcelona (UAB).

Bellaterra, 2024

Acknowledgements

I would like to thank the financial support of this thesis through the projects: Spanish Ministry of Science and Innovation through the “Severo Ochoa” Programme for Centres of Excellence in R&D (CEX2019-000917-S and FPI fellowship SEV-2015-0496-18-2), SUPERENERTECH and SUMATE projects (PID-2021-127297OB-C21 and RTI2018-095853-B-C21, co-fin-anced by the European Regional Development Fund, MCIN/AEI/FEDER, UE) and PTI+ TransEner CSIC programme for Spanish NGEU. We also thank the support from the European Union for ULTRASUPERTAPE project (ERC-2014-ADG-669504), IMPACT (ERC-2019-PoC-874964) and SMS-INKS (ERC-2022-PoC2-10108199), SUPERQUMAP project (Cost Action CA 21144), OPERA (Cost Action CA 20116), NANOCOHYBRI (cost Action CA 16218) and from the Catalan Government with 2021-SGR-00440, 2017-SGR-1519, and Catalan energy network XRE4S (2018 XARDI 00002).

Contents

List of Abbreviations and Symbols

ACN	Acetonitrile
B	External magnetic field applied
BF-HRTEM	Bright-field high-resolution transmission electron microscopy
BF-STEM	Bright-field Scanning Transmission Electron Microscopy
BHO	$BaHfO_3$
BSE	Backscattered Electrons
BZO	$BaZrO_3$
C	Actual concentration
CC	Coated Conductor
C_{eq}	Equilibrium concentration
CC	Coated Conductor
CSD	Chemical Solution Deposition
D_l	Diffusion Coefficient
DLS	Dynamic Light Scattering
DMF	N,N-Dimethylformamide
EDX	Energy Dispersive X-ray
EGA-MS	Evolved Gas Analysis by Mass spectrometry
EtOH	Ethanol
F_L	Lorentz-force
F_P	Pinning-force
FWHM	Full width at half maximum
FTIR	Fourier Transform Infrared Spectroscopy
GADDS	General Area Detector Diffraction System

GI	Grazing-Incidence
$H_{irr}(T)$	Irreversibility Line
Hc	Critical Magnetic Field
H2S2	Hybrid Hydrolitic-Solvothermal Synthesis
HLPE	Hybrid liquid-phase epitaxy process
HR XRD	High-resolution X-ray Diffraction
HRTEM	High-Resolution Transmission Electron Microscopy
HRTEM	High-Resolution Transmission Electron Microscopy
ICP-MS	Inductively Coupled Plasma Mass Spectrometry
I_c	Total Critical Current
I_{c-w}	Critical Current per Centimetre-Width
Jc	Critical current density
LMO	$LaMnO_3$
MEA	Monoethanolamine
MeOH	Methanol
MOCVD	Metal organic chemical vapour deposition
MW	Microwave
$\mu_o H^*$	Crossover Magnetic Field
NMR	Nuclear magnetic resonance
NC	Nanocrystal
NP	Nanoparticle
OM	Optical Microscope
PEG	Polyethylene Glycol
PLD	Pulser laser deposition
RCE-DR	Reactive evaporation and direct reaction method
$REBa_2Cu_3O_{7-\delta}$	REBCO
SAED	Selected Area Electron Diffraction
SC	Superconductor
SEM	Scanning Electron Microscopy
SEM	Scanning Electron Microscopy
SF	Stacking Faults
SMES	Superconducting Magnetic Energy Storage Devices
SQUID	Quantum Design Superconducting Quantum Interference Device
STO	$SrTiO_3$
Tc	Critical Temperature

t_{ind}	Induction Time
TLAG	Transient Liquid Assisted Growth
TEM	Transmission Electron Microscopy
TEM	Transmission Electron Microscopy
TFA	Trifluororo Acetate Route
TMAOH	Tetramethylammonium hydroxide
γ_{eff}	Effective Anisotropy Factor
ϵ	Nanostrain
η_0	Viscosity
λ	Penetration Depth
ρ	Resistivity
σ	Supersaturation
ξ	coherence length
ε	dielectric constant

Abstract

High-temperature superconducting (HTS) $REBa_2Cu_3O_{7-\delta}$ (RE = rare earth or yttrium) coated conductors (CCs) have emerged as a new class of materials with exceptional physical properties, such as high electrical currents without dissipation. These unique properties make them promising materials for energy production, efficient energy distribution and transportation, and energy consumption. However, the widespread implementation of HTS CCs requires a reduction in the high cost-performance ratio associated with the fabrication methods.

In this thesis, we have continued the investigation of the recently invented Transient Liquid Assisted Growth (TLAG) method, which uses chemical solution deposition (CSD) to fabricate high-performance epitaxial $YBa_2Cu_3O_{7-\delta}$ (YBCO) nanocomposite films at ultrafast growth rates. We have developed a novel methodology for preparing colloidal precursor solutions and demonstrated their suitability for fabricating low-cost and high-throughput films of high thickness. To overcome some of the limitations encountered in previous works, stable YBCO colloidal solution using metal-propionate salts and preformed-metal oxide nanoparticle (NP) solutions with 5-10 nm-sized NPs (6-24 % mol) have been synthesised.

We have demonstrated the outstanding performance of the developed multifunctional colloidal solutions in the TLAG process, preparing highly epitaxial films at the ultrafast growth rates of 1000-2000 nm/s, which was confirmed through *in-situ* X-Ray diffraction synchrotron experiments. These growth rates exceeded previous TLAG results by a factor of 10 and were 1.5-3 orders of magnitude higher than conventional growth methods. Furthermore, we achieved high performances with critical current densities of 1.5-2.6 MA/cm^2 at 77 K for a total film thickness of ~400–900 nm, with high NP amounts up to 24 %mol. Moreover, the developed YBCO colloidal solution characteristics, along with the effective optimisation of processing conditions allow an improved vortex pinning scenario in TLAG nanocomposite films. Therefore, the results obtained reveal the opportunities offered by the TLAG-CSD fabrication method and the impact it can have on industrial technology for the production of low-cost and high-performance superconducting layers, especially at high magnetic fields.

Motivation

Current developments in the energy field foresee the need to develop new functional materials compatible with the challenge of renewable and clean energy transition and to make them compatible with low-cost fabrication methods. In particular, the ability of high-temperature superconductors (HTS) to carry high electrical currents without losses at temperatures well above liquid helium, makes them materials with a very promising potential for this energy demand. The superior properties of HTS allow their use in low-consumption and innovative energy power electrical devices such as motors, generators, cables, and fusion, but also in other fields like accelerators, magnets and magnetic resonance, where low-temperature superconductors (LTS) have already demonstrated their imperative capacity.

Nevertheless, the utilisation of HTS is constrained by manufacturing costs, with copper wire emerging as the most economically competitive alternative in several applications. To overcome this bottleneck, research into fabrication strategies appeared with the aim of reducing the cost-performance ratio. The main relevant variables in this context are high performance, thickness, and fast growth rates.

Among the various approaches explored, the TLAG-CSD method, initiated in the SUMAN group shortly before this Thesis, proved to be a very interesting cost-effective and high-throughput process, which enables fast growth rates compatible with nanocomposites films, thereby achieving high performances at high magnetic fields. The present work aims for a better understanding of the TLAG process planning to go a few steps further. It develops an innovative strategy to fabricate superconducting nanocomposite films by TLAG-CSD using a novel colloidal precursor solution. This strategic implementation improves yield, thickness and growth rates compared to previously published findings on TLAG-CSD. It is also based on scalable processes in line with industrial fabrication requirements.

1

Introduction

1.1 Superconducting nanocomposite films

1.1.1 Superconductivity

Superconductivity is a quantum phenomenon that causes zero electrical resistance in various materials, including metals and metal oxides, when they are cooled below a certain critical temperature (Tc). In 1911, Kamerlingh Onnes discovered superconductivity while investigating the temperature dependence of electrical resistance in pure metals, such as mercury, thanks to the liquefaction of helium. This discovery led to a new field of research in materials [1–4]. In 1933 Meissner and Ochsenfeld discovered the expulsion of magnetic field in superconductors (SC) which explained the perfect diamagnetic behaviour observed in SCs when cooling down to Tc. Meissner effect explains that SCs levitate above a magnet below Tc [1, 4, 5] .

Fritz London and Heinz London presented the first theory to explain superconductivity in metallic superconductors in 1935. They described the behaviour of superconductors under an externally applied magnetic field [4]. In 1950, the Ginzburg-Landay theory explained the different behaviours observed in superconductors depending on the applied magnetic field. The theory describes superconductivity using the thermodynamic principles of phase transition. It explains the existence of two types of SC, type I and type II, depending on the different behaviour under the applied magnetic field. There are two key parameters: the penetration depth (λ) and the coherence length (ξ) [1, 4, 5]. Both parameters are characteristic of each material and are linked to the Ginzburg and Landau parameters ($\kappa = \lambda/\xi$) which differentiate between the two types of SC, as Figure 1.1 shows, depending on $\kappa <$ or $> 1/\sqrt{2}$.

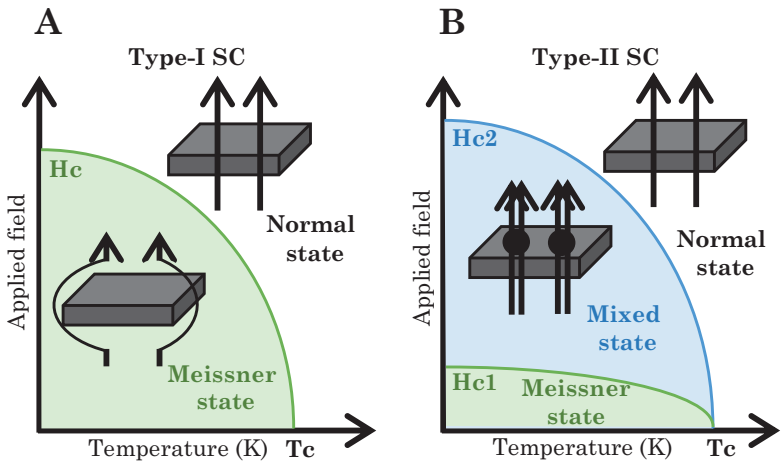

Figure 1.1 Scheme of the H-T dependent phase diagram for a (A) type-I and (B) type-II superconductor.

In type-I superconductors (SC), the coherence length surpasses the magnetic penetration depth ($\kappa < 1/\sqrt{2}$). In this case, we distinguish the superconducting state (Meisser state) below a certain critical field, Hc(T) from the normal state. Type-II SC ($\kappa > 1/\sqrt{2}$), on the other hand, distinguishes two SC states by two critical fields (Hc1 and Hc2). Below Hc1, the SC is in the Meisser state, and above Hc1, the magnetic field penetrates the material in quantised flux lines, called vortices. This region is called the Mixed state, where vortices are present in the superconducting material up to Hc2. Above Hc2, the superconducting state is destroyed to give rise to the normal state. The mixed state on type-II SC increased the critical magnetic field of these materials, making them capable of carrying large currents without losses at higher magnetic fields and temperatures [1, 4, 5].

Bardeen, Cooper, and Schrieffer's theory elucidated the microscopic theory (BSC) for conventional SC in 1957. Superconductivity was associated with the appearance of a weak interaction between two electrons possessing the same momentum and opposite spins, which results in the formation of bound pairs (boson-like particles), called Cooper pairs. The electrons are bound through a weak attractive interaction with the crystal lattice of the material (phonon), overcoming Coulomb repulsion and acting together as a single charged particle (electron-phonon-electron). The theory was able to explain the superconducting state as the condensation of all Cooper pairs in the low-energy state (superconducting state). Contrary to this, the normal state is reached when Cooper

pairs break into two excited electrons (fermion-like particles). This determines an energy gap (ΔG) between the SC and the normal state, as is schematically represented in Figure 1.2 [1, 4, 5].

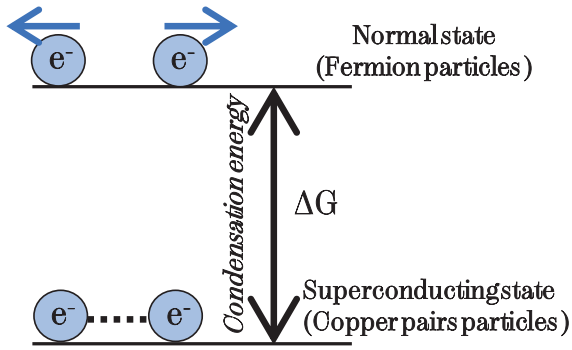

Figure 1.2 Scheme of thermodynamic phase transition of SC through BSC theory.

1.1.2 High-temperature superconducting materials

Low-temperature superconductors (LTS) have Tc values usually below 30 K, such as NbTi and Nb_3Sn, and are used in magnetic coils for applications like magnetic resonance imaging and particle accelerators. The superconducting properties of most LTS can be explained through BCS theory [3, 6]. Nevertheless, the low Tc exhibited by these superconductors poses a challenge to expanding their utilisation beyond medical instruments and fundamental research to encompass the energy sector. Research has focused on finding new superconducting materials that can operate at higher temperatures and magnetic fields to decrease their cost. In 1986, Bednorz and Muller discovered lanthanum-based cuprate perovskite ceramic material with Tc above 30 K, which was called high-temperature superconductor (HTS). HTS are type-II SC but cannot be explained by the BCS theory[3, 6].

One year later, $YBa_2Cu_3O7-\delta$ HTS was discovered with a Tc of 93 K, which is above the boiling point of nitrogen (77K). Various other cuprate-based HTS were identified, offering the opportunity for SC to operate under nitrogen cooling requirements (77 K), making it more cost-effective for power and magnet applications. Nowadays, the most potential HTS candidate for applications

is rare-earth-based cuprate, $REBa_2Cu_3O7-\delta$ (REBCO). The different applications include power cables and fault current limiters (FCL), which could work at low magnetic fields (<1 T) and around 77 K. In addition, HTS can be used for motors and generators, among others, which require higher magnetic fields in the range of 3-5 T and at 30-60 K of temperature. Then, ultra-high-magnetic field applications (>15T) such as fusion reactors, nuclear magnetic resonance (NMR) and superconducting magnetic energy storage devices (SMES) require cooling at lower temperatures (< 25 K) [3, 6–8].

HTS materials are type-II SC with superior magnetic properties where the superconducting state is kept up to higher magnetic fields. Their superconducting properties depend on the behaviour of vortices which are quantised magnetic flux lines generating quantum flux (Φ). These vortices are composed of circular superconducting currents (Js) of Cooper pairs flowing around the vortex core of normal electrons with a radius of $\sim 2\xi$. The surrounded superconducting currents circulate in dimensions of 2λ. A scheme of a vortex is shown in Figure 1.3A. When a current is applied through a superconductor, vortices feel a Lorentz-like force (F_L, comparable to a repulsive force in a charged particle. Consequently, the F_L results in the movement of vortices perpendicular to the magnetic field (B) and current density applied (J), following Equation 1.1 [4, 5, 9, 10].

$$\vec{F_L} = \vec{J} \times \vec{B} \tag{1.1}$$

The movement of vortices in a superconducting system results in energy dissipation and resistance, affecting current density transport. This is due to the motion of the normal electron from the core. However, the system avoids the condensation energy by placing vortices in non-superconducting sites (defects) of the material. This generates a pinning force (F_P) that tends to avoid current dissipation as long as $F_P > F_L$, preventing vortex motion by pinning them. Figure 1.3A shows a scheme of two forces acting on vortices under applied current and magnetic field.

In the mixed-state of superconducting systems, a critical current density (Jc) is defined when $F_P = F_L$. However, despite the vortex motion and current dissipation when $F_P < F_L$, the material remains in a superconducting state until

the upper critical field (Hc2) (Figure 1.1B). This results in an additional thermodynamic phase transition in the H-T phase diagram of superconducting systems, known as the irreversibility line, which depends on the magnetic field and temperature (Figure 1.3B).This line limits the region where vortices are pinned ($F_P > F_L$) and Jc≠0 from the region where vortices move ($F_P < F_L$), and Jc=0 (Figure 1.3B) [4, 5, 9–13].

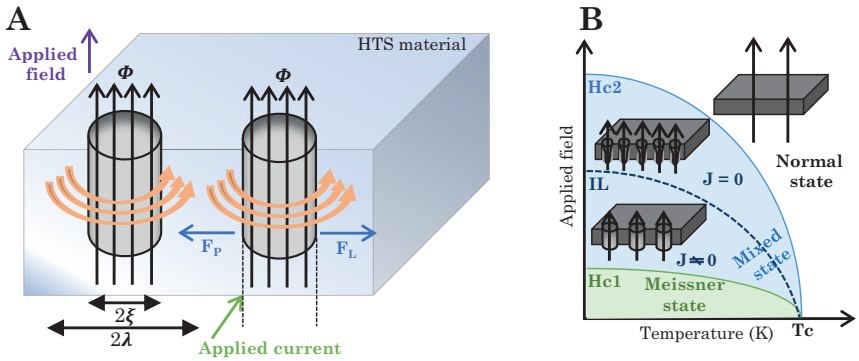

Figure 1.3 Scheme of (A) forces acting on vortices in mixed-state upon application of a driving current in applied field conditions and (B) H-T phase diagram of HTS materials.

The irreversibility line ($H_{irr}(T)$) is characteristic of each type of SC material but can be enhanced by increasing the pinning force, which in turn increases the maximum current without losses of the SC. This pinning force depends on the effective defect landscape that is able to pin vortices. To improve the superconducting properties of HTS, it is necessary to optimise the vortex-pinning landscape. This can be achieved by increasing defects with at least one dimension approximately equal to the vortex core diameter (~ 2ξ). A detailed discussion on vortex pinning will be done in section 1.1.4. In summary, the key parameters that characterise the phase diagram of SC materials and determine their performance, identifying their potential for further applications [6, 13] are:

⁕ **Tc**: The critical temperature is the transition temperature between the superconducting state and normal state. Above Tc, the superconductivity is destroyed.

⁕ **H_{irr}(T)**: The irreversibility line limits the H-T region beyond which vortices cannot be pinned and start moving, producing dissipation. Although the material remains superconducting.

⁕ **Hc2**(T): The upper critical field is the magnetic field that limits the superconducting state. Above it, superconductivity is suppressed.

⁕ **Jc(T,H)**: is the maximum current density that the material can carry without dissipation.

Considering this, YBCO, a cuprate-based HTS material, is the most potential candidate for power and high-field applications due to its high irreversibility lines, high Tc of 93K, and high upper critical field [4, 7, 13]. YBCO is a cuprate-based HTS that has been studied extensively and is used in this work.

1.1.2.1 REBCO Coated conductors

The main challenges for the applicability of REBCO include [6, 8, 13–16]:

1. **Ceramic character**: REBCO ceramic materials cannot be integrated as flexible wire.
2. **Anisotropy crystalline structure of REBCO**: it is needed to have epitaxial grain alignment of REBCO growth to keep high properties. Consequently, if we want to exploit the properties, the REBCO ceramic material needs to be grown with a high degree of texture, with grain boundaries below a critical angle threshold of θ_c ~4°. To fix the problem of misaligned grain boundaries, REBCO epitaxial films are grown on metal substrates that are buffered, flexible, and textured. This architecture is known as coated conductors (CCs) (see Figure 1.4). The superconducting layer (1-3 μm) is grown on a textured metallic tape with a complex buffer multilayer structure that contains a combination of different materials like MgO, YSZ, Y_2O_3, Al_2O_3, CeO_2, and $LaMnO_3$. On top of the superconducting layer (REBCO), there is a coating of Ag and Cu providing environment protection and thermal quench protection of the CC [6–8, 14, 17].

   Nowadays, there are industrially available REBCO CCs with two different architectures based on different fabrication methods: ion-beam-assisted deposition (IBAD) and deformation texturing using the rolling-assisted biaxially textured substrate (RABiTS). In addition, there are several companies worldwide producing CCs and the critical current per centimetre-width (Ic) values of industrialised CCs in the range of Ic = 1,000–1,600

A/cm-w at 4.2 K and 20 T, Ic = 350–700 A/cm-w at 20K and 20 T, and Ic = 350–750 A/cm-w at 77 K and 0 T [7, 8, 13, 14, 17].

REBCO has an oxygen-deficient triple-perovskite structure. An example of the unit cell of YBCO is shown in Figure 1.4. The Cu ion has two distinct crystallographic sites, one in the CuO-chain and the other in CuO_2 planes separate by the BaO-planes. The oxygen doping level of $YBa_2Cu_3O_{7-\delta}$ is primarily determined by the Cu-O chain, which defines key properties such as Tc, among others. Additionally, these chains serve as charged reservoirs, providing charge transfer to the CuO_2-plane. The maximum Tc is reached for a δ ~0.07, called the optimal oxygen doping. For $\delta < 0.07$, the system is in an underdoped state with a lower Tc value, while for $\delta >$ 0.07 the system could reach the overdoped state, which also has a lower Tc [4, 6, 18, 19].

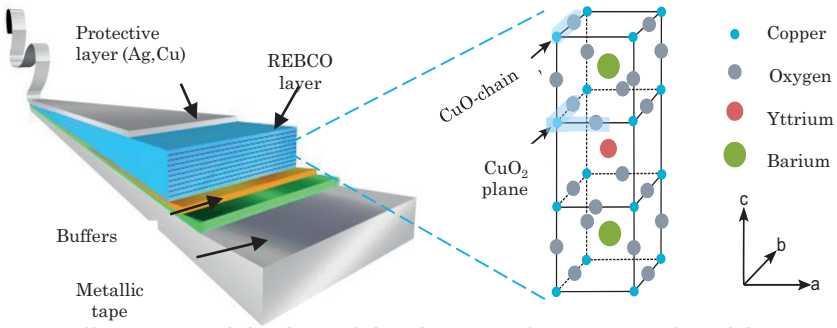

Figure 1.4 Illustration of the Coated Conductor architecture and YBCO unit cell structure with CuO-chains and CuO_2-planes indicate.Adapted from [4, 10]

3. **The Jc(H) vanishing above the irreversibility field**: The performance of HTS can be improved by increasing vortex pinning defect landscape design with the aim of increasing the irreversibility field.

Even though HTS's early problems have been fixed and their use in many integrated devices has been shown [14, 20, 21], it is still expensive to make CCs. The current typical REBCO CC prize ranges from 100-200 $/kAm. Therefore, the requirement of epitaxial REBCO films grown on lengthy and flexible tapes to facilitate application is a complex and costly process, which is the challenge of the HTS application. It also needs to consider the different requirements for the different applications of CCs, which are temperature and magnetic field-dependent. Consequentially, the present superconductivity research is focused

on the development of strategies to decrease the cost-performance ratio of CC technology [7, 13, 17, 22]. Some of these strategies involve:

❋ Increase manufacturing throughput by increasing fabrication process simplicity, efficiency, and yield, as well as decreasing architecture complexity.

❋ Increase the growth rate of REBCO CCs, which increases the overall production rate.

❋ Increase performance. There are different approaches to improving the performance of CCs, which include reducing the thickness of the substrate, increasing the thickness of the superconducting REBCO layer (increase Ic) of the CC architecture, and enhancing the vortex pinning landscape. The understanding of vortex pinning in SC materials allowed the design of an effective defect pinning landscape leading to very high performance by the use of nanocomposites [7, 13, 17, 22–24].

Nanocomposite CCs have been widely investigated and involve the introduction of non-superconducting nanostructured phases into the superconducting REBCO layer of CCs to pin vortices and increase the critical current density. Therefore, REBCO nanocomposite CC is a true opportunity for high-temperature applications but also for high-field and low-temperature applications. Nanocomposite and vortex pining will be discussed in more detail in section 1.1.4.

Therefore, a current and challenging topic is the reduction of the cost-to-performance ratio in CC fabrication through the development of fast epitaxial REBCO growth rate methods for high-performance superconducting REBCO nanocomposite film. Two key requirements for high performance are high biaxial texture to prevent high-angle grain boundaries and increasing the density of efficient pinning centres through nanoengineering of the defect pinning landscape.

1.1.3 REBCO nanocomposite film fabrication

The development of REBCO superconducting films (CCs) relies on their growth and optimisation to achieve high performance. Numerous different REBCO film fabrication methods can enable epitaxial REBCO nanocomposite growth

[6, 8, 13–16]. These methods can be categorised into simultaneous deposition and growth methods, where REBCO crystallisation steps occur simultaneously while REBCO precursor is deposited on the substrate, such as pulsed laser deposition (PLD), metal evaporation (ME), sputtering, and metalorganic chemical vapour deposition (MOCVD) methods. On the other hand, in sequential deposition and growth methods, precursor deposition occurs before REBCO growth in separate treatments, such as chemical solution deposition (CSD) methods. Although physical methods such as PLD are currently established for CC fabrication, their throughput and high cost due to the high vacuum requirements and capital investment limit them for cost reduction. For this reason, the development of low-cost methods such as chemical solution deposition (CSD) has become very interesting [7, 13, 17].

1.1.3.1 Chemical solution deposition method

The CSD method involves the preparation of a metalorganic REBCO precursor solution and the deposition through spin-coating, slot-die coating, or inkjet printing of the prepared solution under controlled conditions. This method enables the separation of the deposition step from the REBCO crystallisation, enabling the study, control, and optimisation of the quality of the precursor film microstructure deposited, which is relevant to the further REBCO growth step [7, 17, 25, 26]. Most importantly, for the high performance of REBCO films, the CSD method is compatible with the addition of preformed colloidal solutions with initially controlled characteristics such as size and homogeneity to increase the defect-pinning landscape through REBCO nanocomposite film formation [7, 13, 17, 22–24]. Therefore, the CSD method is a potential candidate for REBCO film fabrication process due to its high versatility at a low cost.

1.1.3.2 Growth processes for epitaxial REBCO layers

1.1.3.2.1 Nucleation and growth process principles of crystals and epitaxial films

The REBCO film crystallisation process follows the fundamental principles of the nucleation and growth of crystalline materials and epitaxial films.

The first step involves the formation of stable nuclei from a precursor phase, which must overcome an energy barrier. The driving force of crystallisation is the free-energy difference between the initial precursor phases and the new crystallised phase. The surface energy term depends on the interfacial free energy between the precursor and nuclei phases, while the volume energy term is proportional to the chemical potential difference between the phases (Equation 1.2) [25, 27–29].

$$\Delta G = \underbrace{A\gamma}_{\substack{Surface \\ term}} - \underbrace{B\Delta\mu}_{\substack{Volume \\ term}} \tag{1.2}$$

where Aγ is the surface energy term and B$\Delta\mu$ the volume energy term. The energy barrier for crystallisation decreases when the new solid-phase volume increases. The volume energy term is proportional to the $\Delta\mu$ parameter, which is the chemical potential difference between both phases (Equation 1.3). While the surface term goes against favourable nuclei formation due to the interfacial energy involved in the formation of a new surface, the energy barrier for crystallisation will decrease when the new solid phase volume increases ($B\Delta\mu > 0$). Both terms depend on the nuclei or cluster size (r) related to the A and B parameters, and only when nuclei reach a critical nuclei radius (r*) they become stable for continued growth (Equation 1.4). Above r*, the volume term dominates surface energy terms, and the energy barrier decreases. Substituting r for r* in ΔG results in Equation 1.5, where c is a factor number and v is the unit volume of one single molecule (the unit cell of REBCO).

$$\Delta\mu = \mu_{\text{precursor phase}} - \mu_{\text{new solid phase}} \tag{1.3}$$

$$r^* = \frac{2\gamma v}{\Delta\mu} \tag{1.4}$$

$$\Delta G_{hom}{}^{*} = c\frac{\gamma^3 v^2}{\Delta\mu^2} \tag{1.5}$$

$$\Delta\mu = k\mathrm{T}\ln(\sigma + 1) \tag{1.6}$$

The $\Delta\mu$ is related to the relative supersaturation (σ) and temperature of the substrate and precursor phases in a system through Equation 1.6. The σ is the relation between the actual concentration of a solute (C) and the equilibrium concentration (C_{eq}) of a solute (precursor phase) in a system. Supersaturation is the maximum solution concentration at specific thermal conditions, above the

solubility limit, where the system remains stable despite the saturated condition. Below C_{eq} (unsaturated system), the nucleation is not favourable. The time it takes to reach r* is directly related to the time when the concentration of solute is higher than the equilibrium concentration. This is known as the induction period of nucleation (τ) [25, 28].

Nucleation can be classified into two types: homogenous and heterogeneous. Homogenous nucleation does not require the presence of other particles or interfaces, while heterogeneous nucleation takes place at secondary sites such as defects, interfaces, and crystalline substrates [28]. As the REBCO layers need a high biaxial texture to carry a higher current density due to the anisotropy of the REBCO structure, their growth on top of the textured substrate (section 1.1.3) is mandatory, and the nucleation of REBCO films is heterogeneous.

The energy barriers for both types of nucleation are different (Figure 1.5A). This is because the surface term ($A\gamma$) is different for each type (Equation 1.2). In homogeneous nucleation, the entire spherical nuclei surface is in contact with the precursor phase, producing high interfacial free energy and increasing the surface term of the energy barrier (Figure 1.5B). In heterogeneous nucleation, the nuclei surface and volume are reduced by the formation of semi-sphere nuclei on the substrate surface, defined by a contact angle with the solid surface called the wetting angle (θ) (Figure 1.5C and Equation 1.7). This wetting angle also depends on the interfacial free energies between the substrate-precursor phase (λ_{sp}), precursor phase-nuclei (λ_{pn}) and substrate-nuclei (λ_{sn}) (Equation 1.8). Therefore, the energy barrier for heterogeneous nucleation (Equation 1.7) includes a shape factor, $f(\theta)$, which depends on wetting characteristics (Equation 1.8) related to surface energy, interface energy and strain energy (or lattice misfit between the different phases involved in the system (substrate, precursor phases, and nucleus)). Consequently, heterogeneous nucleation has a lower energy barrier (Figure 1.5A) and is thermodynamically more stable than homogeneous nucleation ($\Delta G_{het}^* < \Delta G_{hom}^*$) [28, 30–32].

$$\Delta G_{het}^* = \Delta G_{homo}^* \cdot f(\theta) \tag{1.7}$$

$$\gamma_{sp} = \gamma_{sn} + \gamma_{np} \cdot \cos(\theta) \tag{1.8}$$

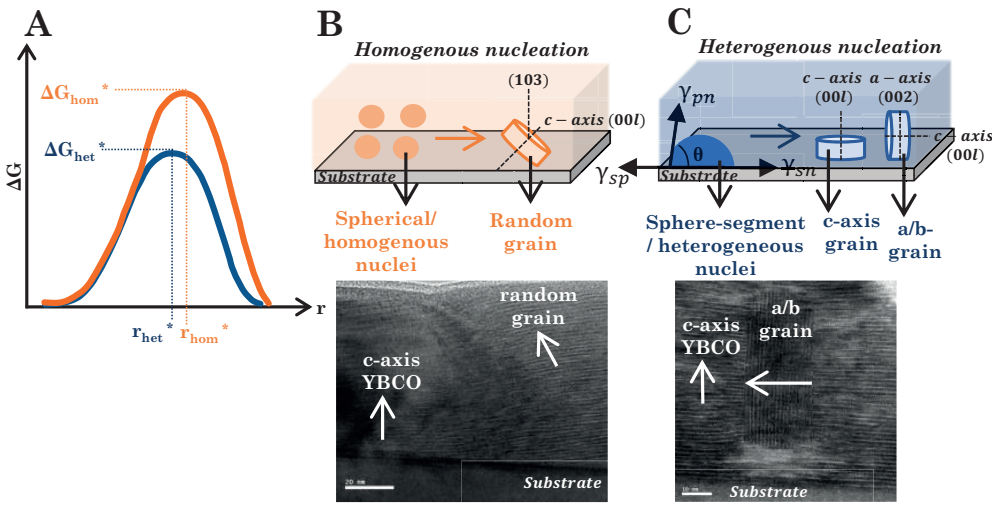

Figure 1.5 (A) Scheme of energy barrier dependence with nucleus radius of homogenous and heterogenous nucleation (B) Scheme of spherical nuclei that will result in randomly oriented grain in homogenous nucleation with an HRTEM image showing a YBCO film grown with a c-axis and randomly oriented grains and (B) Scheme of semi-sphere nuclei that will result in c-axis or a/b-oriented grains in heterogenous nucleation with an HRTEM image showing a YBCO film grown with a c-axis and a/b oriented grain.The white arrows indicate the direction of the c-axis for that grain.

For the nucleation and growth of epitaxial films, heterogeneous nucleation induces c-axis-oriented REBCO grains ((00l) orientations of REBCO) and a/b-nucleated grains ((h00) orientation) (Figure 1.5C). Moreover, as free energy depends on supersaturation, at very high supersaturation conditions, overall energy barriers decrease (Equation 1.2), and homogenous nucleation is also favourable, leading to misoriented or randomly oriented grains (Figure 1.5B). Therefore, at very high supersaturation conditions, the energy barriers of a/b and homogenous nucleation decrease, becoming in the same order as c-axis nucleation. For low supersaturation conditions, the difference between $\Delta G_{het(c)}^*$, $\Delta G_{het(a/b)}^*$, and ΔG_{hom}^* becomes significant, promoting c-axis nucleation [28, 30–32].Figure 1.6A shows the dependence of energy barriers from the c-axis, a/b, and random nucleation with supersaturation. The values are adapted from [10, 31, 33].

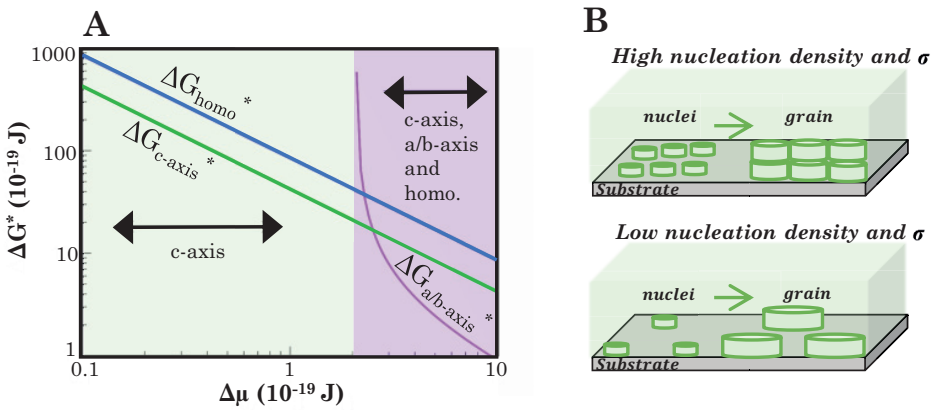

Figure 1.6 (A) Free energies of nucleation formation,ΔG, as a function of supersaturation for homogeneous and heterogeneous nuclei (c- and a/b-axis oriented grains).ΔG_{hom}* is exemplified using Equation 1.7 with f(θ)=0.5. The figure is modified from [10, 31]. (B) Schematic representation of nuclei ripening process under high nucleation density and supersaturation conditions and low high nucleation density and supersaturation conditions.

The nucleation rate (dN/dt) is the number of nuclei passing the critical size (r*) generated per unit volume per second, defined by Equation 1.9. Where No is the number of available sites for nucleation, k_b is the Boltzmann's constant and A* includes kinetic factors related to cluster movement to the substrate surface for heterogeneous nucleation. In addition, A* is related to the kinetics of atomic mobility, which is directly proportional to temperature and is referred to as atomic diffusivity, D(T). Considering this, the nucleation rate adopts the proportionality of Equation 1.10. The overall nucleation rate increases with higher site density and high atomic diffusivity, as well as with the exponential decrease of free energy with supersaturation (Equations 1.5 and 1.7) [29].

$$\frac{dN}{dt} = N_o \cdot A^* \cdot \exp\left(-\frac{\Delta G^*}{K_b T}\right) \tag{1.9}$$

$$\frac{dN}{dt} \propto N_o \cdot D(T) \cdot \exp\left(-\frac{\Delta G^*}{K_b T}\right) \tag{1.10}$$

The nucleation density, which increases exponentially with supersaturation, affects the growth of crystals (Equations 1.11). High supersaturation conditions lead to smaller grain sizes, forming a continuous film. Conversely, decreasing supersaturation results in dispersed nuclei and larger grains, making coalescence and merging difficult and resulting in long intergrain distances, leaving some film-free areas. Figure 1.6B illustrates the process of nuclei ripening into larger grains, depending on nucleation density.

Crystal growth is based on the diffusion of solute, surface diffusion, and grain growth, where supersaturation is also the thermodynamic driving force [13, 17, 27].

1.1.3.2.2 Growth methods for epitaxial REBCO layers at high rates

The cost-performance ratio of CCs is inversely proportional to the growth rate (G). This has led to the creation of high-speed growth methods for epitaxial REBCO layers. High supersaturation values are required for high growth rates, but they promote the nucleation of a/b grains and random nucleation. To achieve high-quality REBCO epitaxial layer growth methods at high rates, it is necessary to control a full c-axis nucleation window with maximum supersaturation conditions [7, 13, 17, 22, 34].

Over the past 35 years, different REBCO growth methods have enabled epitaxial REBCO layers to grow at high rates [7, 13, 17]. These methods can distinguish between the nature of the precursor phases (vapour, solid, or liquid) from where REBCO crystallises (solid phase). The nature of the REBCO precursor phases also significantly influences the growth rate. Interface diffusion and interfacial mobility in gas or liquid phases exhibit higher orders of magnitude compared to solids. However, atomic density at the growing interface is higher in the liquid phase than in the gas phase. Consequently, growth methods from the liquid phase exhibit the highest growth rates, as both atomic mobility and atomic density contributions are higher than for the gas phase [13]. Therefore, three types of growth methods can be distinguished:

❋ Growth from gas phase: in the vapour phase case, the supersaturation is controlled by the pressure of the adsorbed atoms at the growth surface, and the atomic density determines the growth rate. This is the case of methods such as PLD [17, 35, 36], and MOCVD [37, 38]. Although these methods are operating in the industry, they require ultra-high vacuum equipment and, in some cases, laser ablation, which increase the overall process cost and complexity. In addition, the typical growth rates of these methods are in the range of 0.5–25 nm/s. The supersaturation depends on the deposition rate, temperature, or oxygen pressure.

❋ Growth from liquid phase: Growth occurs from a Ba-Cu-O liquid phase in

which supersaturation is given by $\sigma = (C\text{-}C_{eq})/C_{eq}$, where C_{eq} is the RE equilibrium concentration in the liquid, and C is the actual RE concentration. Supersaturation can be modified by the RE solubility in the liquid phase, Ba-Cu-O liquid composition, temperature, and oxygen partial pressure (P_{O2}). The hybrid liquid-phase epitaxy (HLPE) process [39], the reactive evaporation and direct reaction (RCE-DR) method [40, 41] and the transient liquid-assisted growth (TLAG) process [42–46] are methods where the REBCO nucleation and growth occur from a liquid phase. High growth rates (10–2000 nm/s) can be reached due to the high atomic mobility and atomic density when a liquid phase is involved in nucleation and growth. In addition, these methods operate at intermediate pressures.

⁕ Growth from solid phase: When the nucleation and growth are from a solid precursor phase, the supersaturation for nucleation is controlled by the gas diffusion of volatile gases released in solid-solid reactions, which depend on water or oxygen pressure and temperature. This is the case of the trifluoroacetate based on chemical solution deposition method (TFA-CSD) [34, 47–52]. This growth method, based on a solid-solid reaction, yields small growth rates of 0.5–5 nm/s. This type of growth method works under atmospheric or slightly reduced pressures but requires complex furnaces to ensure proper gas flow.

REBCO film fabrication involves the deposition of precursor phases and REBCO growth steps. There are simultaneous and sequential methods, like PLD and MOCVD, occurring simultaneously in a vacuum chamber. Other methods, such as TLAG-CSD [42–46], TLAG-PLD [53], and TFA-CSD, deposit REBCO precursors at atmospheric pressure and pyrolyze them separately from REBCO crystallisation through a post-high-thermal treatment.

The REBCO film fabrication method affects the final REBCO microstructure, which is responsible for vortex pinning and the improvement of superconducting properties. Moreover, PLD, MOCVD, LPE, RCE-DR, TFA-CSD, and TLAG-CSD are methods compatible with REBCO nanocomposite film formation. However, growth methods based on the CSD technique such as TFA-CSD and TLAG-CSD [26, 54] are interesting due to the possibility of introducing preformed non-superconducting phases to increase vortex pinning before REBCO epitaxial growth. CSD methods allow for more control over the final characteristics of the non-superconducting phase [7, 13, 17, 22, 34].

1.1.3.3 TLAG-CSD approach for YBCO nanocomposite film fabrication

For the epitaxial formation of REBCO nanocomposite films, this thesis investigates the use of transient liquid-assisted growth based on chemical solution deposition (TLAG-CSD), a technique developed by the SUMAN group. This section will provide a comprehensive summary of the knowledge gained from the TLAG-CSD procedure and the findings derived from prior research, which served as the basis for the different advances explained in the subsequent chapters. Particularly, advancements have been made regarding the preparation of the REBCO colloidal precursor solution to increase the thickness and quality of precursor TLAG nanocomposite films. Furthermore, we demonstrate TLAG compatibility with thick epitaxial YBCO growth at high growth rates and high performance.

Prior investigations have revealed fast growth rates of up to 100 nm/s using acetate-based precursor solutions, resulting in a film thickness of 100 nm and achieving a critical current density (Jc) up to 5 MA/cm^2 at 77 K [10, 33, 55]. Drawing upon the advancements achieved in this thesis concerning thick TLAG nanocomposite films and the simultaneous investigation of pristine films performed in L. Saltarelli's thesis, recent demonstrations have shown growth rates of up to 2000 nm/s for film thicknesses ranging from 400 to 500 nm, utilising the propionate-based precursor solutions developed. This ultra-fast growth rate represents an advancement of 1.5-3 orders of magnitude compared to conventional methods. The described process emerges as a promising approach for high-throughput industrial production of coated conductors (CCs) due to its simple processing, ultra-fast growth rates, low cost, and high performance. The process involves four main steps: preparation and deposition of a metal-organic colloidal precursor solution, formation of a precursor REBCO precursor film, post-thermal high thermal treatment for YBCO growth, and final thermal treatment to induce a superconducting crystalline phase of YBCO [42–46].

1.1.3.3.1 Precursor solution preparation and deposition

The CSD-TLAG process is an environmentally friendly method for growing REBCO films, which do not use fluorine precursor solutions employed by

the trifluoroacetate route due to the low growth rates [56]. In previous studies, Yttrium, barium, and copper acetate salts were used as precursor salts in the fluorine-free YBCO solutions because they are easily dissolved, stable over time, and commercially available. The low-cost and facile solution preparation process involved dissolving acetate-based YBCO precursor salts in propionic acid (Hprop) excess, resulting in a high-degree conversion of acetate groups to propionates, resulting in the formation of corresponding propionate salts [56–59]. These solutions in Hprop were stable for up to 4 weeks.

Before deposition, the YBCO precursor solution was prepared by mixing solutions of acetates-salts in Hprop with methanol in a 50:50 %v/v ratio. The rheological properties of the solutions, such as viscosity and contact angle, have a strong influence on the final thickness and homogeneity of the films. A 50:50 %v/v ratio of MeOH:Hprop was found to be the optimal volume ratio to increase film thickness, ensuring film homogeneity. Furthermore, the film thickness could be improved by adding an additive, such as amines, which enhances the solubility of the precursor salts and increases the viscosity of the solution [33, 55].

Usually, the final total sum of metal concentration was ~ 1M, resulting in a final film thickness of 100–250 nm for a single layer, depending on additive addition. In addition, the compatibility of $BaZrO_3$ and $BaHfO_3$ NCs with these YBCO precursor solutions was demonstrated. However, the stabilisation of colloidal solutions involved adding the corresponding volume of colloidal solution (in ethanol) for the desired %mol (6-24%mol) to the solution of acetate-salts in Hprop (50%v/v) and then adding MeOH to reach a final %v/v ratio of 50:50 (alcohol:Hprop). Figure 1.7 shows a scheme of the procedure followed to prepare nanocomposite YBCO precursor solution [33, 55].

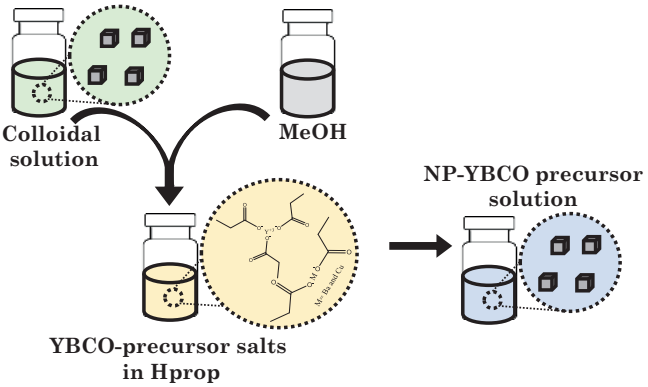

Figure 1.7 Scheme of nanocomposite YBCO precursor solution preparation.

The CSD method was capable of designing and tuning desired solution characteristics for accomplishing the requirements of the TLAG process for various Y/Ba/Cu compositions and NC amounts. The colloidal acetate-based precursor solutions were compatible with spin coating and industrially scalable deposition methods like inkjet printing.

The prepared precursor solutions were deposited on cubic, single-crystalline substrates (100) oriented such as $SrTiO_3$ (STO) or flexible metallic substrates such as IBAD tapes. A low lattice mismatch between YBCO and substrate (ϵ = ($a^{Substrate}$-a^{YBCO})/a^{YBCO}) is a requirement to promote epitaxial growth and reduce strained interface energy [60, 61]. STO substrates were chosen for their small lattice mismatch with YBCO (ϵ = 1.56%), high crystalline quality, very small roughness (<0.1 nm), and small thermal expansion. In addition, to ensure atomically flat-terraced surfaces, the substrates were previously subjected to high-thermal treatment [10, 33, 55].

The spin-coating methodology is an inexpensive and simple procedure for depositing uniform films, especially on small and flat substrates such as STO. The methodology involved depositing a volume of solution on top of the substrate, and through the centrifugal force generated by the rotation movement of the substrate, a uniform coating of substrates was obtained. After the spinning processes, the obtained film is dried on a hotplate to remove the remaining solvent [33, 55, 62].

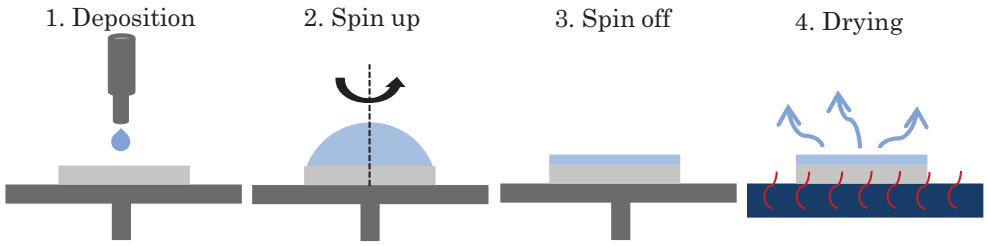

Figure 1.8 Scheme of nanocomposite YBCO precursor solution preparation.

The thickness and homogeneity of a spin-coating film are influenced by solution characteristics (concentration, viscosity), spin-coating parameters (rotation speed acceleration and time of spinning), solvent evaporation, and post-drying process steps. These parameters are dependent on film thickness, and their dependence was optimised for YBCO acetate-based precursor solutions [26, 33, 55].

Overall, the preparation of colloidal precursor solutions using acetate-salt was constrained to a total metal salt concentration of 1M, resulting in a final film thickness of 100 nm for a single layer. In the pursuit of advancing TLAG-CSD technology for coated conductor (CC) industrial production, it becomes imperative to surpass the 100 nm threshold for film nanocomposite thickness. Consequently, this Thesis was focused on designing a novel methodology to prepare colloidal precursor solutions, aiming to increase the concentration beyond 1 M and enhance rheological properties to demonstrate high-performance TLAG nanocomposite films of high thickness.

1.1.3.3.2 Pyrolysis step: 1st heating treatment

The TLAG process involves the thermal treatment of metalorganic precursor films to remove organic components and induce the formation of amorphous or nanocrystalline YBCO precursor phases. This process is known as the pyrolysis process, which converts YBCO precursor salts into $BaCO_3$, CuO, and Y_2O_3.

In CSD methods employing fluorine-free solutions, the presence of the $BaCO_3$ phase could involve the use of high temperatures (~ 1000 °C) to decompose it, which exceeds the YBCO processing growth conditions of interest [63, 64]. Additionally, the presence of $BaCO_3$ in the YBCO precursor films may result in carbon contamination of the final YBCO films, leading to a degradation

of superconducting properties [65, 66].

Despite the presence of $BaCO_3$ phase in thin YBCO precursor films, the TLAG process demonstrated the capabilities of eliminating this phase at rather low temperatures and without carbon residues in the final YBCO-grown films with strong epitaxial YBCO growth and high performance, at least for films up to 100 nm of total thickness[33, 42, 55, 59]. A mixer of orthorhombic and monoclinic $BaCO_3$ phases, with orthorhombic $BaCO_3$ being the majority phase, was obtained. It was also demonstrated that the presence of the monoclinic phase slows the kinetics of $BaCO_3$ elimination in the TLAG due to the conversion of the monoclinic phase to orthorhombic taking place before the formation of the transient liquid and subsequent YBCO growth [59].

The optimal thermal profile, atmosphere conditions, and decomposition paths during the pyrolysis of acetate-based precursor solutions were investigated using thermal analysis techniques such as thermal analysis coupled to in-situ infrared spectroscopic (TGA-IR) and microstructural studies. The thermal profile used in the pyrolysis process has to ensure complete organic decomposition to avoid carbon residues that may produce superconducting properties degradation [65, 66]. A temperature of 500 °C and slow heating ramps of 3-5 °C/min at 1 bar of oxygen pressure with a humid oxygen flow of 0.12L/min were found optimal to remove organic components and avoid crack formation during thermal decomposition [33, 59]. The pyrolysis process was performed under a humid oxygen atmosphere as the decomposition mechanisms of acetate-based salts involved hydrolysis and oxidation reactions and also to avoid sublimation of the copper propionate salt [44, 59].

Moreover, for thicker films, a high tendency to generate cracks was observed [67]. It was preliminary seen that the presence of an additive, such as an amine, produced smoother organic mass losses during pyrolysis, which consequently produced gradual gas release, expecting to limit the formation of cracks [44, 59].

The objective of fabricating thicker TLAG nanocomposite films, limited by the use of acetate precursor solutions, requires developing and tuning an appropriate colloidal precursor solution. This thesis demonstrates the significance of the NC stabilisation method, along with the chemical composition, properties, and rheological characteristics of the colloidal precursor solution, for producing

precursor films for nanocomposites. In addition, we show that the characteristics of the colloidal precursor solution developed have an important impact on the achievement of uniform nanocrystalline microstructures of the precursor nanocomposite films required for the subsequent YBCO growth by the TLAG process.

1.1.3.3.3 YBCO growth step through TLAG method: 2nd heating treatment

The growth of epitaxial YBCO through TLAG-CSD requires finding processing conditions to ensure complete $BaCO_3$ elimination and promote full c-axis nucleation. The TLAG process follows an ultrafast liquid-solid growth mechanism for YBCO, where REBCO crystallises from a non-equilibrium and kinetic-controlled liquid phase [10, 33, 42–44, 55]. The situ synchrotron X-ray diffraction (XRD) analysis revealed the key parameters in the process and was used to develop a kinetic diagram of YBCO films grown through TLAG [43].

The initial precursor system of $BaCO_3$- CuO-Y_2O_3 involves $BaCO_3$ elimination taking place at lower temperatures (~650-800°C) than expected from powders (~ 1000°C). Under temperature and oxygen partial pressure, in the $BaCO_3$- CuO-Y_2O_3 system, $BaCO_3$ reacts with CuO to form a (Ba-Cu-O) solid phase, which melts and forms a (Ba-Cu-O) liquid phase [10, 33, 42–44, 55, 68].

The $BaCO_3$ elimination can be explained through the $BaCuO_2$-CuO phase diagram, which is PO_2-T dependent and where the formation of an eutectic liquid is well-known under determined Ba:Cu composition (Figure 1.9) [10, 33, 69, 70]. The manner in which the liquid melts will depend on PO_2, T, and the amount of Ba/Cu, which is related to the Ba:Cu molar ratio of the precursor salts in solution. Although in the $BaCO_3$- CuO-Y_2O_3 solid system YBCO is the thermodynamic equilibrium product phase, the lower energy barrier for (Ba-Cu-O) liquid phase formation (kinetic transient product phase) favours the crystallisation of YBCO from the transient liquid instead of directly from the $BaCO_3$-CuO-Y_2O_3 solid phases. Consequently, TLAG is a non-equilibrium and kinetic-controlled growth process where YBCO crystallises from a transient Ba-Cu-O liquid phase where the $BaCO_3$ reaction is the limiting step [10, 33, 42–44, 55]. The initial in-situ XRD synchrotron experiments were crucial to concluding

this, as well as the fast growth rates achieved at that time (100 nm/s), which could not be obtained from a solid-solid reaction.

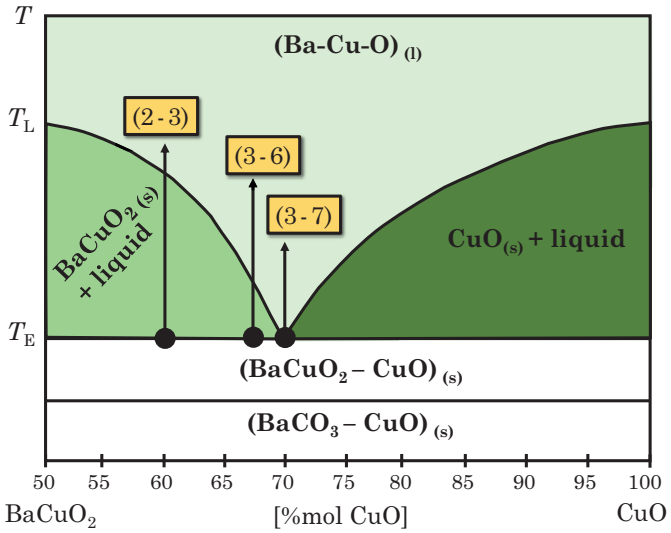

Figure 1.9 Schematic $BaCuO_2$-CuO phase diagram phase under atmospheric conditions adapted from [10, 69, 70]. The Ba:Cu molar ratio compositions studied in this work are included. The $BaCO_3$ and CuO initial precursor solid phases are also included.

In TLAG, the transient liquid phase can be reached from two main routes (Figure 1.10A): the temperature route (T-route) and the oxygen partial pressure route (PO_2-route). In the T-route, $BaCO_3$ elimination occurs simultaneously with YBCO crystallisation. Specifically, in this case, $BaCO_3$ reacts with CuO, forming the $BaCuO_2$-CuO transient liquid phase. As soon as the liquid phase is formed, YBCO crystallises from the liquid, and Yttrium diffuses to the substrate interface for YBCO nucleation and growth (Figure 1.10B) [10, 42]. On the contrary, the PO_2-route is a two-step process where $BaCO_3$ elimination is decoupled from YBCO growth. First, there is a heating step under a low oxygen partial pressure where YBCO is not thermodynamically stable ($\leq 10^{-}5$ bar), but $BaCO_3$ reaction with Cu_2O takes place and leads to a $BaCu_2O_2$ solid intermediate phase. Subsequently, by a fast PO_2 increase into a region where YBCO is stable, the $BaCu_2O_2$ solid phase forms the transient liquid, where again Y_2O_3 dissolves and diffuses and YBCO crystallises [10, 42]. The brown dashed area shows the area where liquid can form and YBCO is stable. It is limited by the $BaCO_3$ elimination, the peritectic (T_P), and the instabilities (T_{ins}) lines of YBCO. The key factor is the kinetically favoured formation of transient liquid from the

melting of $BaCuO_{2(s)}$+$CuO_{(}s)$ in T-route or $BaCu_2O_{2(s)}$ in PO_2-route [10, 33, 42, 43, 55]. Moreover, the furnaces required for these growth routes work at intermediate pressures, decreasing the complexity of the equipment required and the cost.

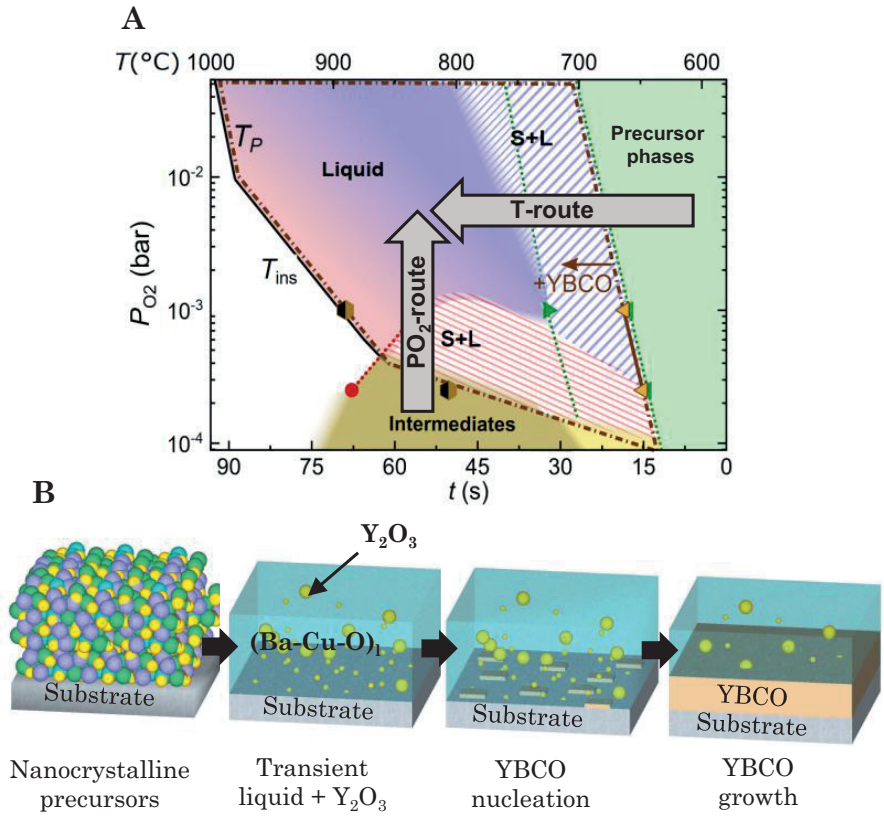

Figure 1.10 Two main TLAG routes. In the T-route, the heating is performed at constant PO_2 into the (Ba-Cu-O) liquid phase. The PO_2-route is based on two steps: first heating at low PO_2 ($\leq 10^{-}5$ bar) where YBCO is not stable, and then a PO_2-jump is performed at constant temperature in the stable region (brown dashed area). YBCO peritectic and instability lines (T_P and T_{ins}) are obtained from [68, 71] and the other lines are from previous experimental in-situ XRD analysis [10, 33, 43, 55].

The TLAG liquid-solid reaction mechanism is expected to have faster growth rates than solid-solid reactions. This is because atoms move around more freely and there is higher atomic density at the growing substrate interface in liquid-solid processes than in solid-solid reactions [13]. Earlier work demonstrates that Yttrium diffusivity in a (Ba-Cu-O) liquid phase can reach higher values of $4{\cdot}10^{-8}$ m^2/s compared to $8{\cdot}10^{-12}$ m^2/s in a solid phase [72, 73]. The growth rate (G) is also dependent on supersaturation (σ following $G \approx k\sigma$, where k is a

kinetic factor. In TLAG-CSD, the yttrium ion supersaturation in the (Ba-Cu-O) liquid phase is what drives the YBCO formation. This is because the nucleation barrier (ΔG) mainly depends on supersaturation, which in turn depends on surface energy, lattice misfit, or strain. Figure 1.10B shows a scheme of the different steps of TLAG. Therefore, when the actual Y concentration (C) exceeds the equilibrium concentration ($C>C_{eq}$), REBCO stable nuclei can be formed, reaching the critical size (r*), overcoming the energy barrier following $\sigma = (C\text{-}C_{eq})/C_{eq}$. The relation between supersaturation and YBCO nucleation can be understood through the thermodynamic phase diagram of $BaCuO_{2(s)}$-Y_2O_3 from [74] and considering the estimated values of 0.01-0.6% mol for C_{eq} and 10% mol for C in TLAG [33].

In conclusion, high supersaturation values are required to overcome the energy barrier for nucleation and achieve high growth rates. However, high supersaturation values favoured the formation of a/b nucleation and random nucleation (Figure 1.6A). Since c-axis nucleation is also controlled through supersaturation, we need to find the maximum supersaturation conditions to promote nucleation and growth at high growth rates while keeping in the region of full c-axis nucleation.

In the TLAG-CSD method, supersaturation and several key kinetic and thermodynamic parameters need to be controlled to promote full c-axis nucleation at high growth rates [10, 33, 42–44, 55]:

⁕ **Supersaturation: Y solubility and Ba:Cu molar ratio**: The equilibrium concentration C_{eq} depends on the solubility of Yttrium in the Ba-Cu-O liquid phase at each PO_2, which is primarily controlled by temperature and the Ba:Cu molar ratio of the liquid phase. Supersaturation decreases with the cooper content in the melt composition. The initial composition of the liquid phase is determined by the initial Ba:Cu molar ratio in the YBCO precursor solution. The stoichiometric YBCO composition of $Y_1Ba_2Cu_3$ is denoted as 2-3, while the cooper excess composition $Y_1Ba_2Cu_4.66$, which is the eutectic composition, is denoted as 3-7. The full liquid region is achieved at lower temperatures for 3-7 than for 2-3 due to the eutectic point (Figure 1.9). Therefore, $C_{eq}(T)$ is higher for 3-7 than for 2-3.

⁕ **Thermodynamoc parameters: T and PO_2**. The liquid formation and YBCO growth occur when we reach the PO_2-T region where YBCO is stable.

Supersaturation can also be modified through processing conditions due to the amount of liquid generated, depending on the temperature and PO_2. Furthermore, the full liquid region is achieved at lower temperatures for the 3–7 composition than for the 2–3, since 3-7 is the eutectic composition Figure 1.11 shows the quaternary Y-Ba-Cu-O kinetic phase diagram developed for PO_2-route using 3–7 composition [10, 43]. It is proposed the existence of two liquid phases with different copper oxidation states (+1 and +2), which vary depending on T-PO_2. This was proposed based on the results obtained in the ternary Ba-Cu-O kinetic phase diagram [10, 43]. The variation of the oxidation state of the (Ba-Cu-O) liquid might provide different liquid properties such as viscosity, capability for yttrium dissolution, and diffusivity. Therefore, T-PO_2 conditions as well as the type of liquid encountered will probably change supersaturation and nucleation density. Limited information is available in the existing literature regarding these melts, and there is an absence of data about the PO_2 of interest for the TLAG process. In fact, the corrosive nature of these melts makes the corresponding studies very difficult.

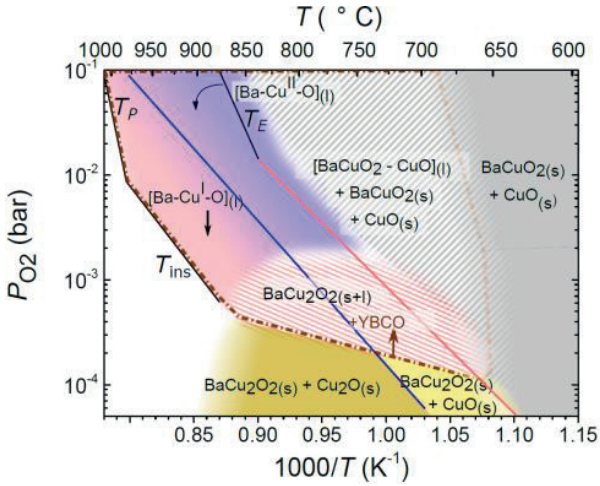

Figure 1.11 PO_2-route kinetic phase diagrams for the Y-Ba-Cu-O system with a 3-7 liquid composition. The different regions of the phase diagram are shown in different colours. The symbols indicate experimental data, and the colour meaning is specified in the legend. Solid lines are obtained from [68, 71, 75, 76]. Adapted from [43].

⁕ **Kinetic parameters**: In the case of the PO_2-route, which is the TLAG route used in this thesis, the heating rate is the main kinetic parameter controlling the first stage of the process. The increase in the heating ramp shifts the $BaCO_3$ reaction to higher temperatures, which may avoid its complete elimination before PO_2-jump. However, the slow heating ramp may influences the

coarsening of intermediate solid phases.

In conclusion, supersaturation is the driving force of the YBCO crystallisation through the TLAG-CSD method, which can be tuned and controlled through the initial solution composition and growth processing conditions. In the previous PO_2-route studies with the acetate-precursor solution, using 3–7 composition, heating at a low PO_2 in the range of 10^{-5} bar and at constant temperatures 800-860 °C and performing PO_2-jumps in the range of 10^{-3} bar, fast growth rates in the range of 100 nm/s of epitaxial YBCO thin films (100 nm thick) were achieved [10, 42]. Given the non-equilibrium characteristics of the TLAG-CSD method, this study investigates the kinetic and thermodynamic parameters influencing epitaxial growth at fast growth rates and the high performance of thicker nanocomposite films (>100 nm) derived from the colloidal precursor solution. These parameters include the heating ramp, initial low PO_2, final high PO_2, temperature, and solution composition.

1.1.3.3.4 Oxygenation step: 3rd heating treatment

The final $YBa_2Cu_3O_{7-\delta}$ (YBCO) crystallisation results in a crystalline structure very deficient of oxygen with low superconducting properties [77]. The oxygen content (7-δ) in $YBa_2Cu_3O_{7-\delta}$ influences its crystal structure and superconducting state. In low oxygen content, in the range of δ values from 1 to 0.65, YBCO adopts a tetragonal phase. The structure turns orthorhombic when δ is between 0.65 and 0. It then reaches a superconducting state with a high critical temperature and current densities [77–79]. To induce the incorporation of oxygen atoms into the CuO-chains of the crystal structure, a post-thermal treatment called the oxygenation step is necessary. The optimal thermal profile and oxygen flow value for reaching a high oxygen-doped state of YBCO after growth were established and investigated using electrical measurements in the thesis of A. Stangl [77]. The thermal treatment to obtain an optimally doped material consists of placing the sample in a tubular furnace and heating it to 450 °C at 10 °C/min, followed by a dwell of 120 min, and then cooling to room temperature at 10 °C/min using a flow of oxygen of 0.6 L/min and a total pressure of 1 bar. This previous established oxygenation treatment for thin TLAG films is also implemented during this thesis for thick nanocomposite films, and an exhaustive study is beyond the limits of this thesis.

1.1.4 Vortex pinning in REBCO nanocomposites films

REBCO, as a HTS material, exhibits dissipation above the irreversibility line. To increase critical current at high magnetic fields, vortices need to be pinned ($F_P > F_L$). To improve the performance of REBCO, it is necessary to control and optimise the defect landscape, which requires that the volume dimensions of the non-superconducting sites (defects or pinning centres) be in the range of REBCO superconducting coherence length ~2ξ (a few nanometers) to match the vortex core [4–6, 9–13]. Therefore, the efficiency of the defects will be dependent on the applied temperature, magnetic field strength, and orientation. Considering the anisotropy of the REBCO structure, the best superconducting properties are achieved by utilising the magnetic field oriented parallel to the CuO_2- planes (superconducting planes). This specific orientation significantly increases superconducting parameters such as Jc (H), Hc2, and Hirr. Nevertheless, operational flexibility is constrained, and nearly no practical devices can operate with the magnetic field aligned parallel to the ab-planes. Consequently, the challenge lies in controlling and optimising the vortex-pinning landscape of REBCO films in terms of specific dimensions, shape, orientation, distribution, and density of the defects. This is particularly crucial for the most challenging orientation of the magnetic field, which is parallel to the c-axis. The objective of this strategy is to reduce the anisotropy of the critical current density [10, 13, 24, 80, 81].

Defects can be distinguished based on their dimensionality, which mostly defines the pinning strength and allows us to differentiate between point, linear, planar, and spherical defects with isotropic or anisotropic behaviour. Isotropic pinning centres are equally efficient in all directions of the applied magnetic field, while in anisotropic defects, the pinning force is angularly dependent on the applied magnetic field. Point defects (OD) are atomic and cluster vacancies and are isotropic weak defects. Moving into the 1D category, mainly dislocations are identified as anisotropic strong defects. Twin boundaries and stacking faults (SFs) fall under the 2D category of anisotropic strong defects. Finally, mainly nanoparticles and locally tensile-strained regions (or nanostrain regions) are characterised as 3D isotropic strong defects [10, 23, 80–83]. Schematic overview of the defect landscape is shown in Figure 1.12.

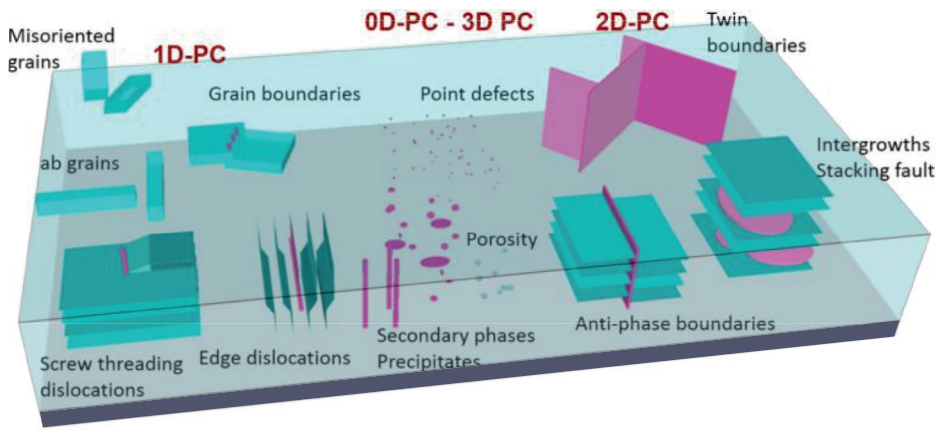

Figure 1.12 Schematic overview of possible defect landscape in YBCO films. 0D, 1D, 2D and 3D defect dimensions are shown, and defect regions that can act as pinning sites for vortex pinning are indicated in pink. Adapted from [83].

Defects can be naturally generated during growth, such as SFs, twin boundaries, and atomic vacancies, or introduced artificially, like nanoparticles, referred to as natural or artificial pinning centres (APCs). The nanoengineering of REBCO films through the introduction of secondary nanophases (APCs) has been proven to be the most effective strategy for improving the vortex-pinning REBCO landscape. Such films are referenced as nanocomposites, and films without APCs are referred to as pristine [7, 13, 17, 23, 41, 80, 81]. In CSD methods, the most common and successful APCs for the improvement of superconducting properties are nanoparticles, which are beneficial for a very wide range of temperatures and magnetic fields[13, 83, 84].

The introduction of nanoparticles in CSD films induces interfacial strain arising from the lattice mismatch between the nanophase and REBCO structures. This phenomenon results in an increased formation of SFs, which in turn generates partial dislocations surrounding them and nanostrain regions in order to mitigate the incoherent interface energy and increase the vortex pinning landscape. It is mandatory to guarantee the appropriate dimensions of APCs, as well as ensure that their composition does not react with REBCO, does not incorporate into the structure, and exhibits high thermal stability under the processing conditions [7, 13, 17, 23, 41, 80, 81]. The most commonly used secondary nanophases, especially in nanocomposites growth from physical methods, are $BaMO_3$ (M=Zr and Hf), Ba_2YMO_6 (M = Ta and Nb), and RE_2O_3 [13, 17, 85–92].

The main factor that determines the type and density of defects generated is the REBCO growth method. Simultaneous methods, such as vapour-solid methods, are successful in improving properties through strained, aligned NPs forming nanorods. On the contrary, sequential methods allow the formation of nanophases before REBCO growth or the use of already-performed nanophases with initially defined characteristics. In the case of solid-based growth methods, such as TFA-CSD, NPs appear randomly distributed, leading to the formation of a high density of SFs to minimise strain interface between the NP and the REBCO. Liquid methods exhibit differences depending on the nature of the liquid. Equilibrium liquids, such as HLPE, which is a simultaneous method, primarily generates nanorods as artificial pinning centres. In sequential liquid methods, like RCE-DR and TLAG, NPs emerge as the primary artificial pinning centres. In RCE-DR, they exhibit random orientation, while in TLAG, they tend to rotate in the liquid to get epitaxially oriented to minimise the interface energy [12, 13, 17, 23, 34].

In the context of CSD, most of the effort was focused on incorporating metalorganic salts into the precursor solution. This approach relies on the initial nucleation of nanoparticles (NPs) at low temperatures, followed by YBCO nucleation (spontaneous segregation approach), where small-sized and randomly oriented NPs are formed. However, this approach is more complicated when high growth rates are involved [13, 17, 48, 80, 87, 93, 94]. Instead, the addition of preformed NPs to the REBCO precursor solution is a potential strategy to better control the final nanocomposite characteristics.

The orientation of the NPs in the REBCO depends on the growth method. For TFA-CSD [85, 86, 95–99], with a solid-solid reaction mechanism, the NPs remain randomly oriented, generating incoherent interfaces, which are minimised by generating more defects such as SFs. For TLAG [10, 33, 55], the fast kinetics introduces novel vortex physics scenarios, resulting in a large defect microstructure with a high density of stacking faults, already in pristine films. Due to the liquid growth in TLAG, small-sized NPs can rotate to minimise the interfacial energy, tending to an epitaxial orientation with the REBCO matrix. Small NPs (about the diameter of the vortex core REBCO) might be able to directly pin vortices, which would also contribute to the enhancement of superconducting properties [10, 33, 55].

In summary, the introduction of non-reactive, high-thermal-stable, small-sized, non-aggregated colloidal solutions improved the superconducting properties of REBCO materials. Therefore, an effort is needed to optimise the synthesis of colloidal solutions with specific characteristics and understand their formation mechanism, which is crucial for their compatibility with the TLAG-CSD method. The state-of-the-art of synthetic strategies for $BaMO_3$ and BaM_2O_6 is discussed in the following section.

1.2 Metal oxide nanoparticles

The development of nanoscale materials is currently gaining interest due to their distinctive characteristics, including the surface-to-volume ratio and the quantum confinement effect [100–102]. The prospective applications of these materials in the disciplines of material science, chemistry, and medicine are numerous. Extensive research has been conducted on metal oxide nanoparticles (NPs), specifically those of the perovskites family, due to their diverse applications in different fields such as materials science, medicine, electrical devices, sensing, catalyst, among others [103–107]. The ability of these NPs to retain their stability despite undergoing high-temperature treatment is what makes them very interesting for different applications, such as the present work.

1.2.1 $BaMO_3$ and BaM_2O_6 NPs

YBCO layers have been improved by the addition of multiple compounds to improve vortex pinning such as perovskites of $BaZrO_3$ and $BaHfO_3$ by spontaneous segregation and performed approaches [42, 47, 48, 80, 85–87, 94] and including also the double-perovskite Ba_2YNbO_6 and Ba_2YTaO_6 NPs through spontaneous segregation approach [88–92, 108]. In CSD methods, the spontaneous segregation approach entails adding the respective precursor salts of the desired nanoparticle composition into the YBCO precursor solution for NP formation during film crystallisation. However, this method leads to a lack of control over the size, homogeneous distribution, and NP composition [47, 88, 89, 109].

The $BaZrO_3$ and $BaHfO_3$ are potential APCs candidates for REBCO nanocomposite films. In addition, both NC compositions show high melting points, in the range of ~ 2600-2700 °C ensuring high thermal stability under the high thermal processing conditions of REBCO growth methods [110, 111]. In addition, $Ba_2Y(Ta,Nb)O_6$ are stable compositions with melting points of 1512 °C for Nb_2O_6 [112] and ~ 1856 °C for Ba_2YTaO_6 [88]. Furthermore, $Ba_2Y(Ta,Nb)O_6$ compositions show inertness [88] with YBCO. Therefore, both types of NPs exhibit composition, structure, and high thermal stability to be compatible with the TLAG-CSD method using the preformed-NP addition approach. However, successful compatibility will be achieved by ensuring small sizes and homogeneous size distribution from the initial colloidal precursor solution to the TLAG nanocomposite films.

1.2.1.1 Synthetic strategies for $BaMO_3$ and BaM_2O_6 NPs

NPs are a hybrid system consisting of both core and surface stabilisers. The high surface-to-volume ratio of NPs gives them unique properties, as the exposed surface increases exponentially, making surface atoms more reactive than internal ones. However, this increase in surface energy produces a tendency for NPs to aggregate. To overcome this, stabilisers (organic or inorganic ligands), also known as surfactants or capping ligands, are needed in nanocrystal synthesis to stabilise NP surfaces during the synthesis, reducing the energy derived from their high surface-to-volume ratio and ensuring good colloidal stability of final metal oxide NPs in solution [103, 113–115].

The nucleation and growth mechanism of NPs in solution follows the basic principles explained in section 1.1.3.2.1 for crystals. The supersaturation of chemical precursors in solution is the driving force for homogenous nucleation to reach the critical radius, which corresponds to the minimum size at which a particle can survive in solution without being redissolved, overcoming the energy barrier. Homogenous and spherical nuclei are formed by overcoming a critical concentration of precursor, resulting in a supersaturated solution derived from chemical reactions of precursor monomers. The growth step involved nuclei diffusion in solution, followed by Ostwald ripening or coalescence mechanisms [113, 114].

The main parameters in the metal oxide nanoparticle synthesis that affect the characteristics of the final metal oxide colloidal solutions, such as size, shape, crystallinity, and aggregation, include reaction time, temperature, the concentration of precursors, and the nature and concentration of surfactants [113, 114]. [103, 113–118]. Various methodologies for synthesising $BaMO_3$ NPs have been reported, which can be divided into aqueous strategies such as the aqueous sol-gel route [103, 119] and hydrothermal method [120, 121] and non-aqueous strategies such as the non-aqueous sol-gel route [103, 122], polyol route [123–126] and solvothermal method [103, 120, 121, 127–130]. However, despite the high crystallinity and homogeneity achieved with a non-aqueous route compared to aqueous approaches, this results in long reaction times and high temperatures [122, 128, 129, 131]. Therefore, the successful synthesis of $BaMO_3$ NPs remains a complex challenge due to the difficulties in obtaining reduced-size, crystalline, and stable colloidal suspensions without agglomeration at reduced times and temperatures. The SUMAN group, in collaboration with the University Autonomous of Barcelona (UAB), developed a hybrid methodology for the synthesis of $BaMO_3$ nanocrystal (NC) solutions that combines the advantages of both the aqueous sol-gel route and the solvothermal method in a two-step process while mitigating their common drawbacks. Small-size NCs (~ 5 nm), highly crystalline, homogeneously distributed, and highly stable (several months) $BaMO_3$ colloidal solutions can be reached using the hybrid solvothermal process. Furthermore, it demonstrated the crucial role of water in the hydrolytic step, enabling the tuning and control of NC size from 4-20 nm by the water amount added to the precursor solution [132, 133].

In the mechanism proposed, the alcohol solvent interacts with the metal alkoxide precursor, making it stable in solution through the formation of an intermediate species (Equation 1.11). Subsequently, the hydrolysis of the metal alkoxide at room temperature takes place, which is extremely sensitive to hydrolysis (Equation 1.12). Then, polycondensation reactions of the resulting zirconium or hafnium hydroxide species from hydrolysis with barium hydroxide precursor take place (Equations 1.13 and 1.14). Polycondensation reactions result in a M-O-M framework or clusters, whose dimensions are strongly relevant in the NC formation. The amount of water added to the precursor solution determined the amount of M-OH species obtained from hydrolysis, which consequently defined the formation of large or short M-O-M chains ending on small

or bigger NCs. The system required a minimum amount of water added for NC formation, suggesting that water is the initiator of the nucleation process, and depending on the water amount, we do not reach a critical concentration and consequently critical size nuclei. Therefore, the hydrolytic step might be the limiting step of the mechanisms involved in NC nucleation. Then, this intermediate precursor solution is subjected to a thermal treatment (solvothermal step) through an autoclave system or MW thermal activation for the final crystallisation of NCs. In the solvothermal step, the stabiliser molecules also influence the final NC size by limiting the NC growth when attached to the surfaces [132, 133].

$$M(OBu)_4 + xEtOH \rightarrow M(OBu)_{4-x}(OEt)_x + xBuOH \quad (1.11)$$

$$M(OBu)_n + xH_2O \rightarrow M(OH)_x(OBu)_{n-x} + xBuOH \quad (1.12)$$

$$\text{-M-OH + H-O-M} \rightarrow \text{-M-O-M- + } H_2O \quad (1.13)$$

$$\text{-M-OH + Bu-O-M} \rightarrow \text{-M-O-M- + BuOH} \quad (1.14)$$

For tantalum and niobium oxide NPs, few references have been reported about their synthesis. The main compounds described were $(Ta,Nb)_2O_6$ and $(Ta,Nb)_2O_6$ NPs. These types of NPs were obtained through solvothermal [129, 134–136] and hydrothermal methods [137, 138] that mainly rely on aggregated NPs with ~ 20 nm of average size in form amorphous powders that require calcination steps to induce crystallization. In the case of $Ba(Ta,Nb)_2O_6$ NPs, it is observed the same behaviour as $(Ta,Nb)_2O_6$. Via citrate-gel and co-precipitation methods [139, 140] agglomerated of ~ 50-100 nm $BaNb_2O_6$ NPs were obtained in the form of powders, and post-thermal treatments were used to confirm the crystalline structure. It is also reported that the synthesis of $BaTa_2O_6$ nanorods in the form of powder by hydrothermal treatment with a length of 50-200 nm [141].

In this thesis, the precursor colloidal solution developed methodology for TLAG nanocomposite film formation required an improvement in the stability of preformed-NP solutions related to the type of ligand stabiliser. In addition, the growth of thicker TLAG nanocomposite films derived from the developed precursor colloidal solution required a fine-tuning of NP size (distinguished within sizes ranging from 5-10 nm), a narrow size distribution range, and high reproducibility. Therefore, in the case of $BaMO_3$ NCs, which have been previously studied, efforts are focused on a comprehensive investigation of the mechanism

and parameters, aiming to achieve fine control over size, distribution, reproducibility, and ligand functionalisation. On the other hand, effort is given to the initial synthesis of BaM_2O_6, which could potentially act as potential candidates as APCs for TLAG nanocomposite films. The main objective is to achieve small particle sizes and non-aggregation of these NPs in a solution.

1.2.2 Basic principles of surface functionalisation

As previously mentioned, NPs can be seen as a hybrid system consisting of both core and surface stabilisers. The surface of NPs plays a crucial role in determining their final properties. Hence, the examination of surface chemistry in the formulation of nanoparticles has garnered attention due to its possible modifications for further application [142–144]. The capping ligand provides kinetic stability for the NPs at the interface between the NP core and the solvent. The characteristics of these stabilisers and their interactions with the NP surface are important aspects that impact colloidal stability, non-aggregation, and subsequent usability [103, 113–115]. Moreover, acquiring a thorough comprehension of the stabiliser interacting with the NC surface and its mode of interaction with the NC interface allows for the modification of the NP surface, thus facilitating various applications and the emergence of novel characteristics [142–144].

Based on similarities in coordination chemistry, the covalent bond classification (CBC) is suggested as a good approximation of the different interactions that happen on NP surfaces. Surface ligands are categorised as L-type ligands, which are Lewis bases with two donor electrons (e.g., H_2O and NH_3) that interact with metal atoms. Z-type ligands are characterised as Lewis acids that lack donor electrons (e.g., BF_3) and interact with non-metallic atoms. It is now known that X-type ligands are radicals with a single electron donor, like H, Cl. These radicals can interact with both metal and non-metal atoms. Ultimately, ligands of the X^- type, which are anions, interact electrostatically with metal atoms, such as carboxylates. On the other hand, X^+ type ligands, which are cations, participate in electrostatic interactions with non-metal atoms, such as ammonium salts [115, 145–147]. Figure 1.13, shows a scheme of the different types of ligands and interactions.

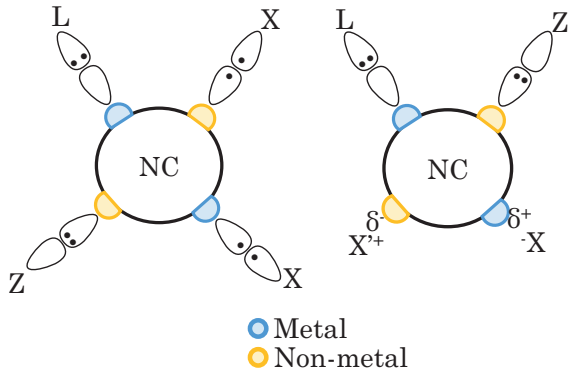

Figure 1.13 Scheme of CBC classification of surface ligands to describe the NC-surface interactions

The ligand exchange techniques are important because they can be used to find out about the surface features, stability in solution, and compatibility of NPs, depending on the purpose. NPs have a high surface energy, which makes ligand exchange difficult. A new ligand needs to be attached quickly and efficiently so that the old one can be released. This is done without exposing the thermodynamically unstable surface, which could lead to NP aggregation [148]. The proposed CBC theory can be utilised to prioritise ligand exchanges based on the contact strength of the existing surface ligand and the affinity of the new ligand towards the surface, which is dependent on the type of ligands involved. Generally, L- and Z-type ligands, which are two types of neutral interactions, can be exchanged depending on the affinity between the surface and the ligand. On metallic and non-metal surface sites, respectively, other ligands of the same type are likely to replace ligands of the L-type and Z-type. The desorption of X-type ligands, which results in the formation of charged species, is often thermodynamically unfavourable in non-polar solvents. However, it becomes more feasible and thermodynamically beneficial in aqueous systems due to solvation interactions. Thus, the substitution of X-type ligands with L-type ligands is not feasible. Finally, analogous ligands can replace ligands of the X^- and X^+, facilitating electrostatic exchange on the NP surface without significantly changing the interface [115, 142, 145].

Ligand exchange techniques are valuable for obtaining uniform colloidal solutions with a chosen stabiliser, even in situations where aggregated NPs are formed during the synthesis process [127, 149]. Various methods can be employed to facilitate ligand exchange. Some methods involve the precipitation of

NPs by introducing a solvent in which the stabiliser is not stable. Adding the new solvent and an excessive amount of ligand that is stable in this new solvent facilitates the ligand exchange. Therefore, it is typically employed for transitioning from water-based to non-water-based colloidal solutions [127, 149]. Additional methodologies included preserving the initial surface ligand by chemically reacting a new ligand with the existing ligand already attached [150]. Alternatively, some approaches employed a chemical process that resulted in the total removal of the ligand. Triethyloxonium tetrafluoroborate (Et_3OBF_4) [148] or nitrosonium tetrafluoroborate ($NOBF_4$) [151] are often used to strip original ligands from hydrophobic colloidal suspensions. This procedure entails the breaking of the NP-carboxylate bond, resulting in the stabilisation through BF_4^- anions and the presence of dimethylformamide (DMF) absorbed in polar solvent. Consequently, the NP surface that forms can bind a new capping ligand, depending on the chosen solvent.

Some of these ligand exchange approaches will be studied in the present work, especially for BaM_2O_6 (M=Nb and Ta) NP solutions.

1.3 Objectives

The main objective of this thesis is to study the superconducting YBCO films, fabricated through the TLAG-CSD process, by incorporating metal oxide nanoparticles to address the current challenges in superconducting coated conductor manufacturing. In this context, it is imperative to develop an innovative methodology for the formation of superconducting YBCO nanocomposite films via the TLAG-CSD process able to reach thicker films (>100 nm) at high growth rates (>100 nm/s) and higher performance (>1 MA/cm^2 at 77 K) than the previous study. The aim is, therefore, to design a stable colloidal precursor solution and fabricate nanocomposite film within a framework that prioritises cost-effectiveness, high throughput at high growth rates, high performance, and scalable fabrication procedures to meet market application demands. To achieve this goal, this work evolves through the following specific objectives:

- First, the synthesis of $BaMO_3$ (M=Zr and Hf) and BaM_2O_6 (M=Ta and Nb) nanoparticle solutions using an easy and reproducible synthetic approach. Applicability requirements include small sizes, homogeneous size

distribution, high stability, and reproducibility. The most complex concern involves fine-tuning nanoparticle size and surface functionalisation. Utilising the H2S2 process, previously developed for $BaMO_3$ (M=Zr and Hf) nanoparticles, the aim is to better understand the formation mechanism for precise control of size, size distribution, surface functionalisation, and reproducibility, which are crucial characteristics for further applicability in superconducting nanocomposite films. The other goal is to use preliminary knowledge about the H2S2 process to optimise a synthetic approach for BaM_2O_6 (M=Ta and Nb) nanoparticle solutions with the mentioned mandatory characteristics for the first time.

- Second, the development of a novel methodology to stabilise preformed metal oxide nanoparticle solutions in YBCO precursor solutions to obtain stable colloidal precursor solutions compatible with the TLAG-CSD process. This effort seeks to improve film quality, achieve thicknesses exceeding 100 nm, and reach high-performance TLAG nanocomposite films. Ensuring stability involves optimising the nanoparticle surface stabilisers and solvent compatibility of nanoparticle solutions with the YBCO precursor system and guaranteeing the stability of YBCO precursor salts in colloidal solutions.
- The final objective is to demonstrate the compatibility and improvements of the developed YBCO colloidal precursor solutions for the nanocomposite growth through the TLAG-CSD process, thereby decreasing the cost-performance ratio for further industrial fabrication. This includes achieving thicker nanocomposite films (>100 nm) than previous study, strong epitaxial YBCO growth, high growth rates (> 100 nm/s), and high-performance nanocomposite films with high critical current densities, especially at high magnetic fields.

2

Nanoparticle synthetic procedures

2.1 Introduction

The application of colloidal solution for YBCO nanocomposite film formation using the Chemical Solution Deposition (CSD) method requires small-sized NCs to act as pinning centres, NP composition non-reactive with YBCO with high thermal stability and purity. Furthermore, it is also necessary high concentrated, homogeneous and stable colloidal solutions without aggregation. The presence of aggregates can hinder the pinning enhancement blocking the electric percolation in the final nanocomposite film [24, 47, 85, 86, 95]. The optimisation of the NP synthesis of these metal oxide NPs was focused on the investigation and control of the synthetic parameters for the achievements mentioned above to ensure further compatibility and application in YBCO-nanocomposite films.

The hybrid solvothermal process employed for the synthesis of crystalline $BaMO_3$ nanoparticles called $BaMO_3$ nanocrystals (NCs) was developed by N. Chamorro thesis [133]. The mechanism proposed and initial relevant parameters in NC formation reported were summarised in the section 1.2.1.1. In the first part of this chapter, we continue investigating the previous work regarding these $BaMO_3$ NCs focusing on the desired characteristics for their further application in TLAG-CSD nanocomposite films. To achieve this, a comprehensive study of synthetic parameters was conducted, including the type of precursor solution, surface stabiliser and solvothermal temperature. These factors play a crucial role in controlling the final NC size, homogeneity, reproducibility and stability of $BaMO_3$ colloidal solutions. Finally, the versatility of the synthetic methodology was tested through microwave (MW) thermal activation a method previously reported for its ability to reduce reaction time compared to alternative thermal treatments.

In the second part of this chapter, we introduce the novel synthesis and characterisation of BaM_2O_6 nanoparticles (NPs) based on the hybrid synthetic process but without the presence of a stabiliser in the precursor solution. Our investigation delved into the synthetic parameters, specifically focusing on temperature, time, and surface functionalisation, to attain the desired characteristics for this particular type of NPs to ensure their further compatibility with TLAG-CSD nanocomposite films.

2.2 Experimental

2.2.1 Particle synthesis and characterisation

2.2.1.1 $BaMO_3$ nanocrystals

⁕ Autoclave system thermal activation

Zirconium or Hafnium (IV) n-butoxide (2.7 and 3.5 mmol respectively) and $Ba(OH)_2 \cdot 8H_2O$ (3.4 mmol) in 10 mL of absolute ethanol were mixed in a Teflon vessel, followed by the addition of Triethylene glycol (TREG) (44.5 mmol for $BaZrO_3$ and 51.9 mmol for $BaHfO_3$ NCs) under continuous stirring at room temperature. The solution was stirred until a homogeneous milky solution was obtained and then NH_3 25 %w/w was added (37-74 mmol as detailed later in section 2.3.1.3). After the addition, the reactor was sealed and heated up to 180 °C under stirring for 1 hour. The final mixture was cooled down to room temperature. $BaMO_3$ particles were separated from the reaction media by the addition of 80 mL of ethyl acetate, followed by centrifugation at 12,000 rpm for 10 min. Separated NCs (solid phase) were re-dispersed in 15 mL of absolute ethanol or desired solvent. In the final step, an extra centrifugation of 5,000 rpm for 10 min was performed and separated NCs (liquid phase) was isolated forming stable colloidal dispersions.

⁕ Microwave thermal activation

In a 25 mL round-bottom flask equipped magnetic stirrer, Zirconium or Hafnium n-butoxide (2.7 and 3.5 mmol respectively) and $Ba(OH)_2 \cdot 8H_2O$ (3.4 mmol) in 10 mL of TREG were added under continuous stirring at room temperature. The solution was stirred until we obtained a homogeneous milky solution and then Milli-Q H_2O (27.8 mmol as detailed later in section 2.3.1.3). After the addition, the resulting precursor solution was transferred to a Teflon vessel to be introduced in the Microwave (MW) system and heated with a ramp of 18 °C/min until 180 °C, held at 180 °C for 20 min, and cooled down to room temperature for 15 min. $BaMO_3$ particles were separated from the reaction media by the addition of 80 mL of ethyl acetate, followed by centrifugation at 12,000 rpm for 10 min. Separated NCs (solid phase) were re-dispersed in 15 mL of absolute ethanol or desired solvent. In the final step, an extra centrifugation of 5,000

rpm for 10 min was performed and separated NCs (liquid phase) were isolated forming stable colloidal dispersions.

2.2.1.2 BaM_2O_6 nanoparticles

* **Autoclave system thermal activation**

In a Teflon vessel, Niobium or Tantalum (V) ethoxide (0.88 mmol) and $Ba(OH)_2 \cdot 8H_2O$ (0.44 mmol) in 15 mL of absolute ethanol were added under continuous stirring at room temperature. After the addition, the reactor was sealed and heated up to 220 °C under stirring for 48h. The final mixture was cooled down to room temperature. BaM_2O_6 particles were separated from the reaction media by the addition of 15 mL of Milli-Q H_2O, followed by centrifugation at 12,000 rpm for 10 min. Separated NPs (solid phase) were washed twice via re-dispersed in 3 mL of absolute ethanol and then 15 mL of Milli-Q H_2O (15 mL) was added followed by centrifugation at 12,000 rpm for 10 min. Finally, separated aggregated NPs were re-dispersed in 15 mL ethanol.

* **Post-surface functionalisation by ligand stripping**

Ligand stripping reaction from the procedure of Evelyn. L [148] was used to obtain and homogeneous colloidal dispersion from the aggregated system, obtained after the solvothermal method, with some modifications on quantities and steps. The procedure consists of the previous precipitation of 1 mL of BaM_2O_6 (10-20 mg/mL) NPs by centrifugation at 3,500 rpm for 5 min followed by the re-dispersion of separated NPs on 4M N,N-Dimethylformamide (DMF) in acetonitrile (ACN) solution. Then, 0.9 mmol of Trimethyloxonium tetrafluoroborate was added to the milky solution and subjected to ultrasound treatment for 30-60 min to promote the surface ligand stripping.

Characterisation

Dynamic Light Scattering (DLS) was used to determine the hydrodynamic diameter, aggregation and homogeneity of particles in solution. Z-potential measurements by DLS technique was applied to know the surface charge (stability). Transmission Electron Microscopy (TEM) was employed to characterise the size, shape, and crystallinity by Selected Area Electron Diffraction (SAED) pattern. For crystallinity, powder X-ray Diffraction (XRD) has been used to determine the

crystalline structure and crystalline size of synthesised NPs. Stoichiometry confirmation of BaM_2O_6 NPs was determined by Inductively Coupled Plasma Mass Spectrometry (ICP-MS) analysis. Analysing the NP surface, Fourier Transform Infrared Spectroscopy (FTIR) provided information on the structure of the molecules (functional groups) capped onto the NP surface. Thermal stability studies and organic mass determination on the NP surface for the calculation of the final NP dispersion concentration were performed by Thermogravimetric analysis (TGA). Finally, Evolved Gas Analysis by Mass spectrometry (EGA-MS), has also been used to characterise the surface, by the mass of molecule fragments of volatile products attached to the NP surface during thermal degradation. TGA and EGA-MS experiments and data analysis were performed in collaboration with J.Farjas from the University of Girona.

2.3 Results and discussion

2.3.1 $BaMO_3$ nanocrystals

2.3.1.1 Nanocrystal synthesis and characterisation

The hybrid approach using autoclave thermal activation described in section 2.2.1.1 was used to synthesise $BaMO_3$ NCs where temperature and time reaction conditions were maintained (180 °C during 1 h) but using different precursor solutions. For $BaZrO_3$ NCs we used a non-stoichiometric Zr:Ba molar ratio of 1:3 and a molar ratio of metal:TREG of 1:16.5 to obtain a homogenous dispersion of small-sized NPs (<10 nm). $BaHfO_3$ NCs were synthesised by a stoichiometric reaction (Hf:Ba molar ratio of 1:1) and a molar ratio of metal:TREG of 1:15.3. The optimal values for both molar ratio metal:Ba and metal:TREG were optimised in [133]. Moreover, to ensure a homogeneous and reproducible synthesis, it is crucial to proceed with the reagent addition in the steps described in section 2.2.1.1 and ensure the preparation of homogeneous precursor solution before the solvothermal step.

Using the particle synthesis developed, we obtain a distribution of small NCs with a size average of 5 ± 1 nm with a square-like morphology for $BaZrO_3$ NCs and spherical for $BaHfO_3$ NCs by TEM (Figure 2.1A and B respectively).

DLS technique was employed complementary to TEM local analysis to evaluate the aggregation and homogeneity of particles in solution and in spite of being optimised for spherical particles, we considered that there are slight differences between spheres and cubes (case of $BaZrO_3$ NCs) and we can use it as an approximation. DLS measurements (insets from Figure 2.1A-B) show a high monodispersed colloidal solution as we obtain one single peak of ~ 6-7 nm. Particles show a pure cubic phase of perovskite structure (Figure 2.1C) with a crystalline coherent domain of ~5 nm estimated by Sherrer equation (section A.1.1) of their main diffraction peaks of (ll0) and (l00) that depends also on particle shape (K= 0.9 for spherical particles) [152–154]. During the thesis, the values of the average size of NCs provided were determined from TEM analysis in which the NC core size is observable, whereas by the Sherrer equation, only the crystalline core size can be obtained.

Calculated values of the sizes from the different techniques were summarised in Table 2.1.

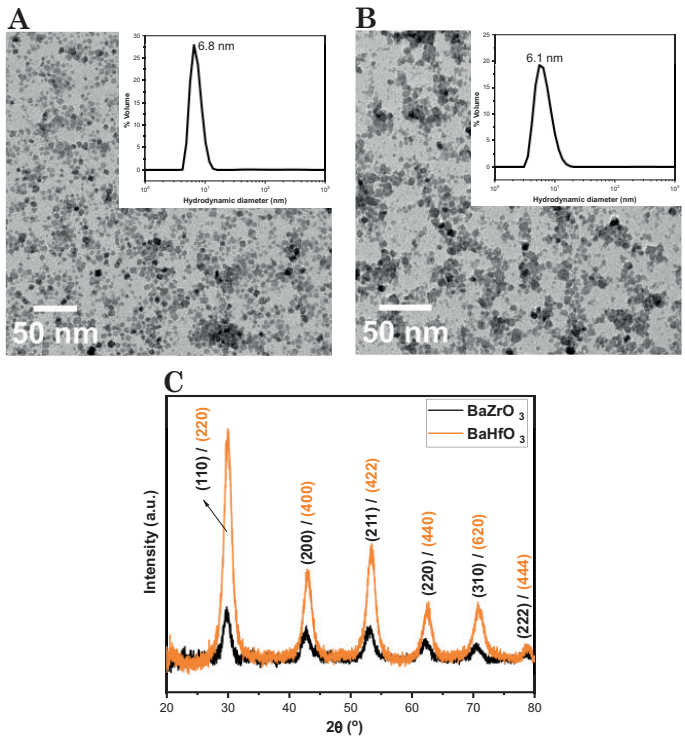

Figure 2.1 Particle size from DLS measurements (% in Volume) and the TEM images of the as-synthesised (A) $BaZrO_3$ NCs and (B) $BaHfO_3$ NCs and (C) the corresponding powder XRD patterns ($BaZrO_3$ in black and $BaHfO_3$ in orange). Planes of the cubic crystalline structure assigned with reference patterns (00-006-0399 and 00-024-0102) from the Internacional Centre of Diffraction Data.

Z-potential measurements were performed to know the surface charge of these NCs, the values indicate that both types of NCs are positively charged, and the values are above the stability limit established in colloid stability theory (≈ ±30 mV) [155, 156] ensuring colloidal stability in ethanol (Table 2.1). The Z-potential measurements shown correspond to the values obtained on the first day after NC synthesis as we observed that the stability evolved over time. Stability studies of both NCs in terms of aggregation by the presence of one or more DLS peaks above 10 nm by time and Z-potential vs time via DLS measurements are in section 2.3.1.4.

Table 2.1 Particle size from histograms of TEM images and crystalline size from Sherrer of XRD patterns. Hydrodynamic size and Z-potential values from DLS measurements of the as-synthesised NCs $BaZrO_3$ and $BaHfO_3$ NC solutions. Surface organic mass from TGA analysis.

	TEM size (nm)	Sherrer size (nm)	%Volume DLS (nm)	Z-potential (mV)	Surface Mass (%)
$BaZrO_3$	5 ± 1	5.4 ± 0.1	6.8	~ +60	13.4
$BaHfO_3$	5 ± 1	5.4 ± 0.1	6.1	~ +45	16.0

The final concentration of the NC suspensions was determined using the organic shell loss measured from TGA analysis (Figure A.1). We obtained high yields values of 66-94 % (120-170 mM) for $BaZrO_3$ and 44-70 % (100-160 mM) for $BaHfO_3$. The NCs synthesised through the H2S2 process via autoclave thermal activation exhibit homogeneous dispersion of small-sized NCs (<10 nm) with high crystallinity. Moreover, colloidal solutions show good dispersion/stability values at high concentrations. Details of the optimisation performed of the synthesis to achieve the features mentioned before are described in the following sections. In addition, the studies of the synthetic parameters with a relevant role in the reaction that allows the system to be controlled and reproducible are also explained.

2.3.1.2 Cleaning step optimization

Previous work done on the development of this synthetic methodology [133] described a washing procedure based on the addition of 10 mL of the ethyl acetate to the resulting solution after the solvothermal treatment, followed by centrifugation. Then, supernatant was discarded and 10 mL of ethyl acetate:ethanol (4:1) was added followed by sonication to ensure complete dispersion of the solid phase and finally centrifugation (this step is repeated twice). Later, the precipitate was dispersed into absolute ethanol. After this procedure, NCs solutions show a high polydispersity degree in DLS measurements and TEM analysis.

To enhance homogenous size distribution an extra-step centrifugation was optimized and implemented. This step consists of performing a final lower rpm

centrifugation discarding the solid and keeping the supernatant obtaining a stable and monodispersed NC solution at concentrations up to 80 mM.

In this thesis, the cleaning step was also optimised in order to increase the final NC concentration above 80 mM needed for their further application on the developed procedure to prepare YBCO-nanocomposite precursor solution (chapter 3). Considering the different %mol tested and final volume of the YBCO-nanocomposite precursor solution used during the thesis, it is required to reach NP concentrations ≥ 120 mM.

The resulting solution after solvothermal treatment was cleaned with an excess of ethyl acetate (80 mL) to decrease the polarity of the system since the NCs stabilised with TREG are more stable in polar solvents and precipitate while reagents excess after reaction are soluble in less polar solvents. Then, after centrifugation, separated NCs (solid phase) were dispersed in absolute ethanol.

By analysing the colloidal solutions before the implementation of an extra centrifugation step, we detected, in some cases, the formation of crystalline $BaCO_3$ particles. The SAED pattern shows several spots distributed in circles coming from random NC distribution observed in TEM image and also ordered single spots from crystalline $BaCO_3$ impurity (Figure 2.2A) . By powder XRD we identified the main peaks of $BaCO_3$ in the orthorhombic phase assigned with the reference pattern 00-005-0378 (Figure 2.2D). $BaCO_3$ impurity not always appeared and could be related to an incomplete reaction between reagents or could be a product of the secondary reaction of $Ba(OH)_2$ with CO_2 from the atmosphere as the reaction was not performed in an inert atmosphere [157, 158]. In the previous work, $BaCO_3$ impurity had also been detected in reactions without the use of aqueous ammonia which produces the poorly formation of NCs (no complete crystallisation) [133]. Moreover, apart from $BaCO_3$ impurity we detected the presence of aggregates of NCs in the TEM image (Figure 2.2B) and DLS measurements (Figure 2.3A).

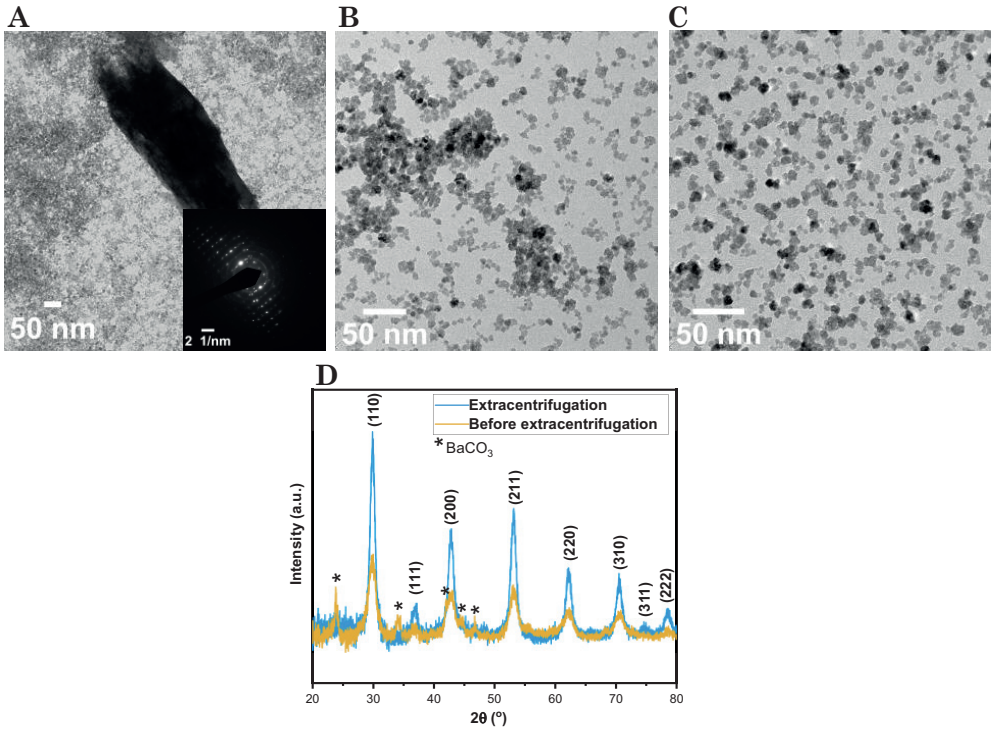

Figure 2.2 TEM images of $BaZrO_3$ NCs (A) before extra-centrifugation step showing $BaCO_3$ particle and the corresponding SAED image (B) before extra-centrifugation step showing the presence of aggregates (C) After extra-centrifugation step without aggregates (D) Powder XRD patterns before (orange) and after extra-centrifugation step (blue) with $BaCO_3$ peaks identified by stars.

We decided to incorporate the additional centrifugation step after the dispersion in absolute ethanol. In this case, we discarded the solid phase, keeping the liquid phase as the final stable colloidal solution. The results in this thesis demonstrated that this extra-centrifugation step enables the elimination of aggregates, while also removing $BaCO_3$ impurities. DLS measurements from before and after extra-centrifugation show the elimination of the aggregate peak of ~53 nm (Figure 2.3A)

Complementary, the histograms (Figure 2.3B) from TEM images of before and after the extra-centrifugation (Figure 2.2B and C) suggest that this centrifugation is not significantly affecting the NP size distribution. There were slight differences in FWHM values from the histogram distribution fitted curves from 4 to 3 nm after extra-centrifugation and also we obtained ±rsd values of ± 1 for both histograms.

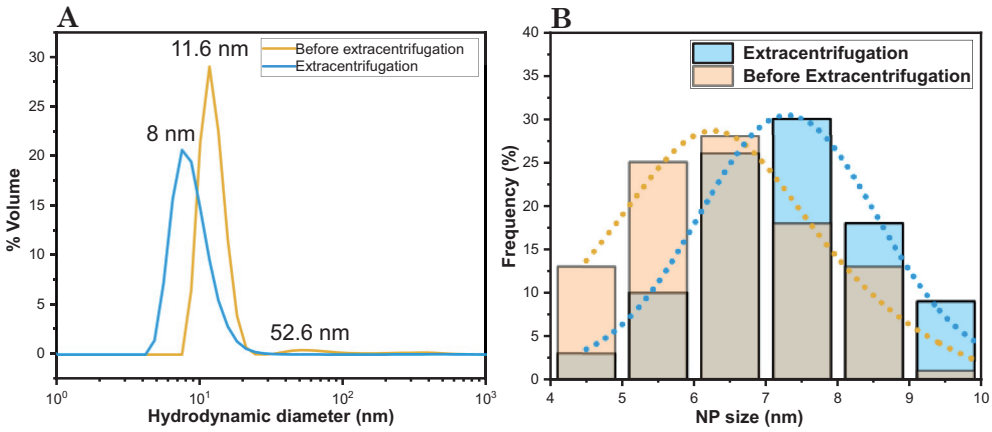

Figure 2.3 (A) DLS measurements and (B) Histograms from TEM images of nanosuspensions before (orange) and after extra-centrifugation step (blue).

Finally, we evaluated the influence of this extra-centrifugation step on the final NC concentration obtaining high yields values of 66-94 % for $BaZrO_3$ and 44-70 % for $BaHfO_3$. From these results, we can conclude that by optimising rpm and reducing the centrifugation steps from two (optimised in previous work) to one single step and with an extra centrifugation step at the end of the procedure, we were able to obtain stable and monodispersed solution at concentrations of ≥ 100 mM without impurities.

2.3.1.3 Tunning the synthetic parameters

2.3.1.3.1 Effect of the H_2O added in precursor solution

⁕ Role of ammonia

For the mechanism proposed for the hybrid solvothermal method (section 1.2.1.1) developed in the PhD thesis of N. Chamorro [132, 133], the hydrolysis reaction of metal alkoxides (Equation 1.12) was considered the limiting step of the synthesis (nucleation step). That previous work started to investigate the role of aqueous ammonia in the reaction concluding that this reagent did not play any additional role in the process such as base or as a cationic stabiliser ([132, 159, 160]) being just its water content that governs and controls the NC formation and final NC size. The amount of water in the precursor solution controls the concentration of intermediated hydroxide species (-M-OH) which were

the product of the hydrolysis of alkoxides (Equation 1.12) that then by polycondensations (Equation 1.13 and 1.14) generated short or large -M-O-M- chains (nucleation step) that finally produces smaller or bigger NCs after crystallization step (solvothermal treatment).

In this thesis, we carried on investigating the role of ammonia and/or water in detail because it was the main synthetic parameter found that has control over tuning NC sizes, which is very important for the further application of YBCO-nanocomposite films. H2S2 by autoclave system thermal activation was employed using 25 %w/w of aqueous ammonia or directly using its equivalent amount of MilliQ H_2O to study the effect of these reagents in the behavior of the final colloidal solution. Firstly, we performed three replicates using $NH_{3\,(aq)}$ and three replicates also with its equivalent in Milli-Q H_2O (Table 2.2 A-F) with the quantities previously optimized to obtain small-sized NCs (~ 5 nm). Finally, we checked also the effect of these reagents on NC size tuning using a higher amount of $NH_{3\,(aq)}$ and its equivalent in Milli-Q H_2O (Table 2.2 G-H).

Table 2.2 NC sizes from TEM histograms and Z-potential values from DLS measurements of reactions using Milli-Q H_2O or using the corresponding 25% w/w of aqueous ammonia.

Sample $BaZrO_3$	**$NH_{3(aq)}$ (mmol)**		**Milli-Q H_2O (mmol)**	**TEM size (nm)**	**Z-potential (mV)**
	NH_3	**H_2O**			
A	-	-	27.8	7 ± 2	40.2
B	-	-	27.8	7 ± 1	-
C	-	-	27.8	6 ± 1	-
D	9.3	26.3	-	5 ± 1	40.7
E	9.3	26.3	-	6 ± 1	-
F	9.3	26.3	-	5 ± 1	-
G	-	-	55.6	10 ± 3	47.2
H	18.5	52.5	-	10 ± 2	50

TEM sizes summarized in Table 2.2 for experiments A-F show that there were no significant differences in sizes if we considered average sizes from TEM histograms obtained by using $NH_{3\,(aq)}$ or Milli-Q H_2O. Then, we evaluated homogeneity by inset DLS measurements (Figure 2.4A-F). Reactions via Milli-Q H_2O in precursor solution (Figure 2.4 A-C) exhibit different degrees of aggregation from free aggregation (one single peak on DLS below 10 nm), partial aggregation (two peaks, one above 10 nm) and fully aggregation (two peaks above 10 nm).

In the case of tests performed using the same quantity of H_2O content in aqueous $NH_{3\,(aq)}$ (Figure 2.4 D-F), we obtained in the three cases homogeneous distribution without aggregation (one single peak below 10 nm). We cannot evaluate homogeneity based only on TEM images because we observed and analysed local regions of the TEM grid which contain "infinite" areas, and maybe the chosen region does not represent the overall sample. For example, could seem that there was NC aggregation, but it could be a drying effect of the concentrated colloidal solution during the preparation of TEM grid. For this reason, we always used DLS measurement as a complementary analysis to evaluate homogeneity and aggregation in the solution, while through TEM we determined the NC size and shape.

In addition, when we increased the amount of H_2O or $NH_{3\,(aq)}$ to increase NC size we observed the same behaviour as for small-sized NCs. TEM and DLS of Milli-Q H_2O sample (Figure 2.4G) show the presence of partial aggregation while the sample using $NH_{3\,(aq)}$ show monodisperse distribution (Figure 2.4H). If we compare the small and bigger NC TEM sizes (Table 2.2) we observed more differences in tuning the NC size when we used $NH_{3\,(aq)}$. Considering the standard deviations from $NH_{3\,(aq)}$ experiments we can distinguish between small-sized NCs of 4-7 nm and bigger NCs of 8-12 nm. In the case of NC size tuning by Milli-Q H_2O, the variations were from 5-9 nm to 7-13 nm. These results, show a clearer size difference in NC sizes with defined amounts of $NH_{3\,(aq)}$ than Milli-Q H_2O.

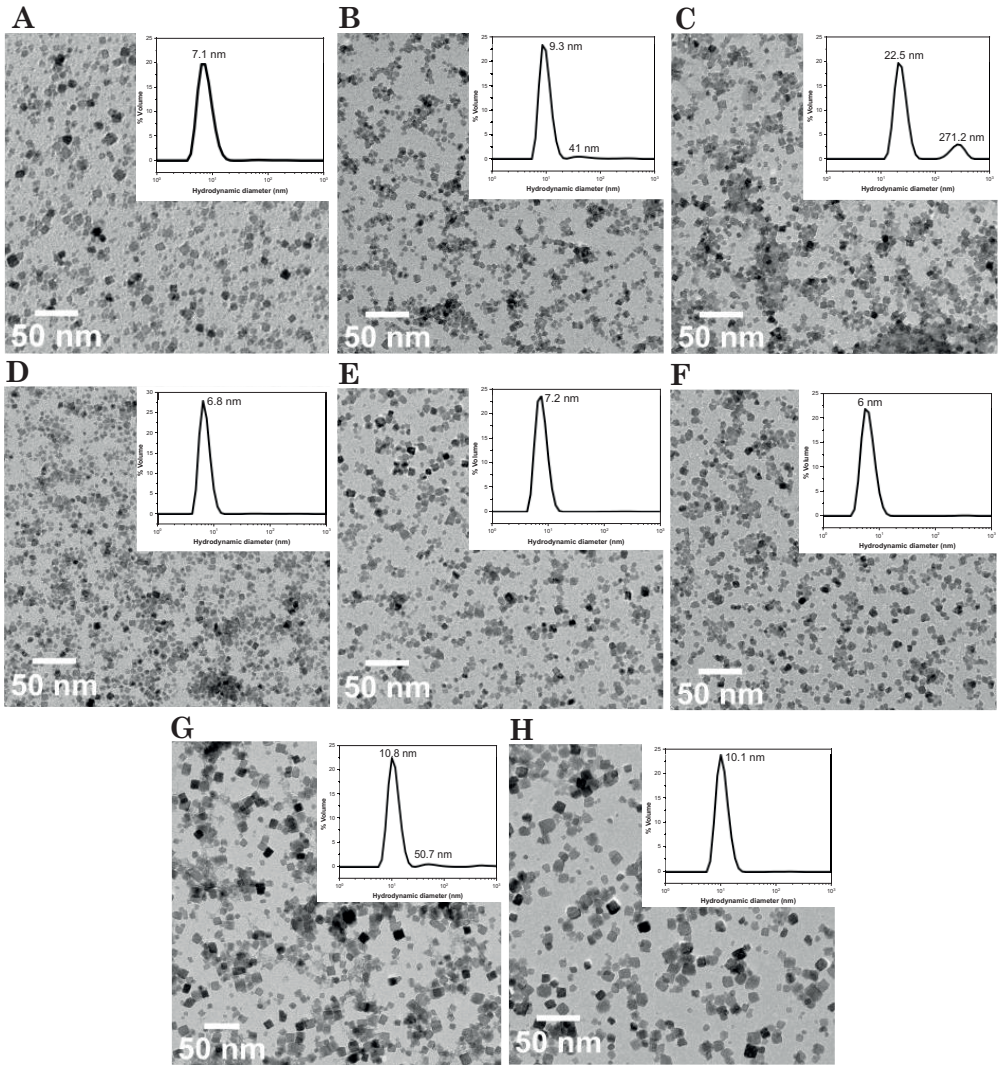

Figure 2.4 TEM and DLS of synthesised $BaZrO_3$ particles (A-C) using 27.8 mmol of Milli-Q H_2O (D-F) using 37.0 mmol of aqueous ammonia (G) using 55.6 mmol of Milli-Q H_2O and (H) 74 mmol of aqueous ammonia.

The different results obtained in the replicates indicate that we have an irreproducibility on the homogeneity of NC sizes, higher tendency to aggregation, and less control on tuning NC size using Milli-Q H_2O than using aqueous ammonia. We suggest an explanation of the role of aqueous ammonia in the reaction mechanism based on the basic principles of the sol-gel process discussed in the following subsection.

Sol-gel process

It is well known in the sol-gel process of silicon alkoxides and also for other metal alkoxides that hydrolysis ratio (h = mol H_2O/mol alkoxide), pH and nature of alkoxide group (R) are the most important parameters influencing the rates of hydrolysis and polycondensations reactions [161–163].

The hydrolysis ratio is determined by the amount of water in the system, which affects the kinetics of the hydrolysis reaction. It was reported that in the case of titanium alkoxides when h > 1.5, the reaction does not result in a stable solution of intermediate species resulting in the early precipitation of oxides [164]. Acid or basic catalysts were used to favour and increase rates of these sol-gel reactions, especially for silicon alkoxides, through the formation of charged intermediated species making the metal more reactive (electrophilic) towards nucleophilic attacks, which is the mechanism of these reactions. This influences the size and cross-linking of clusters or monomers from the nucleation step (resulting in a polymeric matrix of metal oxide bridges) that determine the final particle size and shape [161, 162, 165, 166]. Furthermore, the type of metal alkoxides is also a key parameter in sol-gel chemistry. Their chemical reactivity towards hydrolysis depends mainly on the electronegativity of the metal atom, its ability to increase the coordination number, the steric hindrance of the alkoxy group, and the structure of the metal alkoxides (monomeric $M(OR)_4$ or oligomeric $[M(OR)_4]_n$ structure). In the case of transition metal alkoxides which are strong Lewis acids (the preferred coordination number is higher than their valence), no catalyst is needed due to the fast reactivity towards hydrolysis increasing the hydrolysis rate. To moderate the reactivity of metal alkoxides, additives acting as ligands for OR group substitution such as carboxylic acids, β-diketones, among others, were used to avoid fast hydrolysis that produces uncontrolled aggregation or final precipitation of the final oxide [119, 161–163, 167].

$$NH_3 + H_2O \rightleftharpoons NH_4^+ + OH^- \quad (2.1)$$

$$M(OBu)_4 \xrightleftharpoons{H_2O} M(OH)(OBu)_3 + BuOH \quad (2.2)$$

$$M(OBu)_4 \xrightleftharpoons{OH^-} M(OH)(OBu)_3 + BuO^- \quad (2.3)$$

$$M(OBu)_4 \xrightleftharpoons{NH_3} M(NH_3)_2(OBu)_4 \xrightleftharpoons{H_2O \text{ or } OH^-} M(NH_3)(OH)(OBu)_3 + NH_3 + BuO^- \quad (2.4)$$

$$BuO^- \xrightleftharpoons{H_2O} BuOH + OH^- \quad (2.5)$$

Applying the principles of sol-gel in our system, which is a hybrid approach between aqueous sol-gel and solvothermal method, the kinetics of the hydrolysis and polycondensations reactions of the nucleation step could be affected by the following aspects:

◦ In our system, the water amount was always in excess either using Milli-Q H_2O or $NH_{3\,(aq)}$ and hydrolysis ratio (h) were ~ 10-20 (from smaller to bigger NCs) increasing also hydrolysis rate. In spite that we work with water excess, we adjusted the optimal water content range in our system to avoid the fast hydrolysis that results in the early precipitation of oxide. We reached a controlled equilibrium in the system where the amount of H_2O is the main parameter that governs NC formation and size.

◦ The hydrolysis of alkoxide took place **by nucleophilic substitution by H_2O (Equation 2.2)** [161–163]. Under strongly alkaline conditions, as our system (pH = 10-12), **OH^- species could also hydrolyse the alkoxide (Equation 2.3)**. At pH > 5, the condensation rate is faster than hydrolysis which decreases the probability that condensation begins before hydrolysis is complete. The high-hydrolysed species are immediately consumed, favouring small-sized particles [162]. Furthermore, we chose alkaline conditions as the resulting stabilised-NCs after solvothermal treatment were stable in these conditions.

◦ In the case of aqueous ammonia used as a hydrolysis initiator instead of Milli-Q H_2O other reaction equilibriums could be involved in the reaction mechanism of the system. In solution, **ammonia has the equilibrium Equation 2.1** but in strongly alkaline conditions (excess of OH^- species) the equilibrium is shifted to the left (to the formation of $NH_{3\,(aq)}$) following the Le Chatelier's

principle.

◦ Furthermore, Zirconium or Hafmium IV (d^0) show a high preference for high coordination numbers (above 4-coordination) forming a greater variety of complexes [157] and it is also reported the formation of alcohol, β-diketones, amines, carboxylic acids and other derivates alkoxides complexes of Ti, Zr and Hf alkoxides [168–172]. We suggested that **aqueous ammonia could coordinate as a neutral Lewis base to Zirconium or Hafnium (IV) n-butoxide (acid Lewis) by a nucleophilic attack (Equation 2.4)** increasing coordination number from 4 to 6 (octahedral complex). The ammonia is in excess respect to metal alkoxides in the system. The molar ratio mol pure NH_3 / mol metal alkoxide was ~ 3-7 (from smaller to bigger NCs). NH_3 could act as additive decreasing reactivity of alkoxide as -NH_3 is worst leaving group than -OR and/or blocking coordination sites at the metal decreasing hydrolysis rate.

◦ In addition, the equilibrium reactions of Equations 2.3 and 2.5 are shifted to the right due to the displacement of BuO^- species from hydrolysis reactions either by OH^- or through ammonia complex is also favoured by **the reaction of BuO^- species with water excess in the system forming BuOH which is a weak acid**.

We proposed that the hydrolysis through H_2O and OH^- and the formation of this octahedral complex by NH_3 that then could be hydrolysed are competitive reactions in the system. The different hydrolysis reactions (Equation 2.2-2.4) were schematically represented using the monomer form of the metal alkoxide for simplification, but equilibrium could be also used for their oligomer species. Hydrolysis from the octahedral complex by ammonia could slow down the rate of hydrolysis producing more homogeneous and short -M-O-M- chains that result in small-sized NCs. In the case of Milli-Q H_2O or OH^-, the hydrolysis is much faster, producing uncontrolled formation of -M-O-M chains that result in the presence of aggregation in some cases, irreproducibility and worst control on final NC size and homogeneity observed in Figure 2.4A-C and Table 2.2. Note that based on the findings presented in this thesis and the intricate mechanism proposed to explain the influence of ammonia on the synthetic method used, the process has been denoted as hybrid hydrolytic solvothermal synthetic (H2S2) process.

In spite of the suggestion of the interaction of ammonia in the hydrolysis through the formation of an intermediated octahedral complex in the precursor solution (nucleation step), it is discarded the final stabilisation of NC surface after solvothermal treatment (growth or crystallization step) by ammonia or ammonium cations. In previous work [132, 133], it was demonstrated the absence of nitrogen compounds on the NC surface by X-ray photoelectron spectroscopy (XPS). Further to this, we evaluated the surface charge of NCs by Z-potential measurements (Table 2.2) showing no significant differences in NC surface charge values between NC synthesised using $NH_{3\,(aq)}$ and Milli-Q H_2O. Complementary IR spectroscopy and powder XRD were performed with the aim of knowing the behaviour of ligands anchored onto NC surface and crystalline phase, respectively, using $NH_{3\,(aq)}$ and Milli-Q H_2O. IRs also show the same functional groups and relative intensities between peaks suggesting that we cannot differentiate between the molecules anchored to the NC surface from $NH_{3\,(aq)}$ and Milli-Q H_2O reactions (Figure 2.5A).

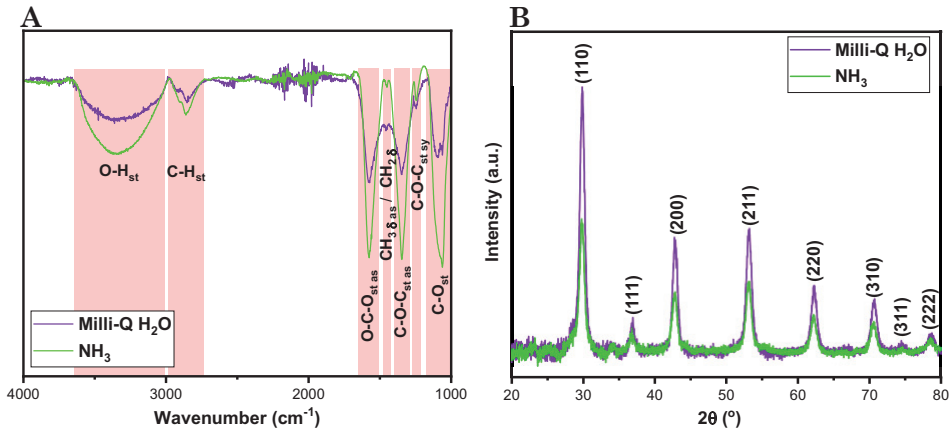

Figure 2.5 (A) FTIR-ATR spectra with the corresponding vibration band assignation and (B) powder XRD pattern of as-synthesised $BaZrO_3$NCs by Milli-Q H_2O (purple) and $NH_{3\,(aq)}$ (green).

XRD comparison shows that $NH_{3\,(aq)}$ or Milli-Q H_2O in precursor solution did not affect the final NC crystallinity, obtaining the same cubic phase assigned with reference patterns ICDD (00-006-0399) for both syntheses (Figure 2.5B).

⁕ Tunning NC size

Considering the results obtained in the previous section about reproducibility, homogeneity, and NC size control, we decided to perform all the reactions

during the thesis using $NH_{3\,(aq)}$.

The main objective of using preformed-NP solutions for YBCO nanocomposite films is to ensure predetermined characteristics of NPs such as size and homogeneity, that have a crucial effect on the final superconducting properties. For this reason, a controlled tuning of NC size is very important for the final nanoengineering of YBCO films, allowing better control of the final NCs coarsening, distribution, and aggregation during YBCO growth [24, 47, 85, 86, 95].

In this work, we tested different particle concentrations (%mol), NC composition ($BaZrO_3$ and $BaHfO_3$) and NC average sizes of 5, 7 and 10 nm in the optimisation of YBCO nanocomposite films via the use and control of preformed colloidal solutions with the desired features. During the nanocomposite YBCO film growth, in this thesis, the pushing effect and certain coarsening of NCs were observed with 5 and 10 nm NC-sizes (details in chapter 4). As these problems were related to the initial NC size, we followed the strategy of using NCs with a size between 5-10 nm. Fine-tuning of NC sizes was achieved by the H2S2 method using $NH_{3\,(aq)}$ which enables a high control of final NC size. The effect of increased aqueous ammonia quantity on the precursor solutions of $BaZrO_3$ and $BaHfO_3$ in the final sizes is summarised in Table 2.3.

Table 2.3 Information of NCs modifying the quantity of 25% w/w of aqueous ammonia in the precursor solution. Size and FWHM from histograms of TEM images, Sherrer size from powder XRD patterns and hydrodynamic size from DLS measurements.

NC type	TREG (mmol)	$NH_{3(aq)}$ (mmol)	TEM size (nm)	FWHM	Sherrer Size (nm)	%Volume DLS (nm)
$BaZrO_3$	44.5	37.0	5 ± 1	2.89	5.8 ± 0.1	6.8
$BaZrO_3$	44.5	52.9	7 ± 2	4.32	8.2 ± 0.1	7.5
$BaZrO_3$	44.5	74.0	10 ± 2	4.52	10.6 ± 0.5	8.1
$BaHfO_3$	51.9	37.0	5 ± 1	3.88	5.0 ± 0.3	6.1
$BaHfO_3$	51.9	52.9	6 ± 2	2.85	5.8 ± 0.1	7.1
$BaHfO_3$	51.9	74.0	11 ± 3	6.37	9.5 ± 0.4	9.2

The behaviour observed in both types of $BaMO_3$ NCs was similar. The

addition of more quantity of aqueous ammonia increases the NC size as more M-OH species are generated from hydrolysis that allows the formation of large -M-O-M- chains from polycondensations producing bigger NC sizes [132]. Optimisation of $NH_{3\,(aq)}$ quantities keeping the quantity of stabiliser (TREG) allows differentiating between 5, 6-7 and 10-11 average TEM sizes in a narrow range of size distribution (±rsd ≤ 3nm and FWHM ≤ 7nm).

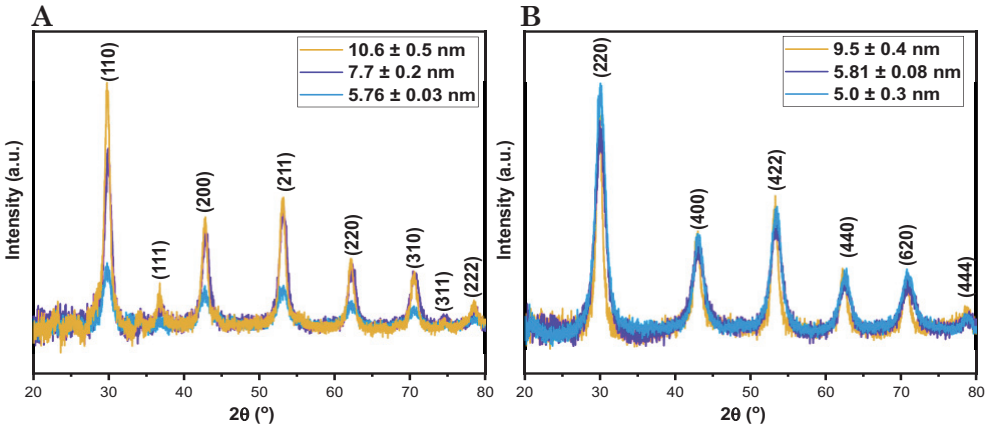

Figure 2.6 Powder XRD pattern of the as-synthesised NCs of small (blue), intermediate (purple) and big (orange) -sized of (A) $BaZrO_3$ NCs and (B) $BaHfO_3$ NCs. Planes of the cubic crystalline structure assigned with reference patterns (00-006-0399 and 00-024-0102) from the International Centre of Diffraction Data.

Additionally, despite the narrow range of size distribution obtained, the standard deviations and FHWM values from TEM histograms increase with the size of NCs (Table 2.3) meaning that the system becomes more polydisperse. NC size distribution in TEM histograms from both types of NCs (Figure 2.7) shows that we can differentiate between 5,6-7 and 10 nm (the centre of the fitted curve from the histogram) and that the fitted curve becomes broader by increasing NC size. This effect indicates the presence of more families of NC sizes (polydispersion). This effect may be attributed to the poor control of stabilisation when we increase the NC size by the amount of ammonia while maintaining a constant quantity of stabiliser [132]. Alternatively, it could be a consequence of the potentially faster and less controlled hydrolysis reaction when the amount of aqueous ammonia is increased. The quantity of TREG for both types of NCs was optimised to avoid aggregation for this range of NC size (5-10 nm) as shown by DLS measurements through the detection of one single peak of ~ <10 nm (Table 2.3).

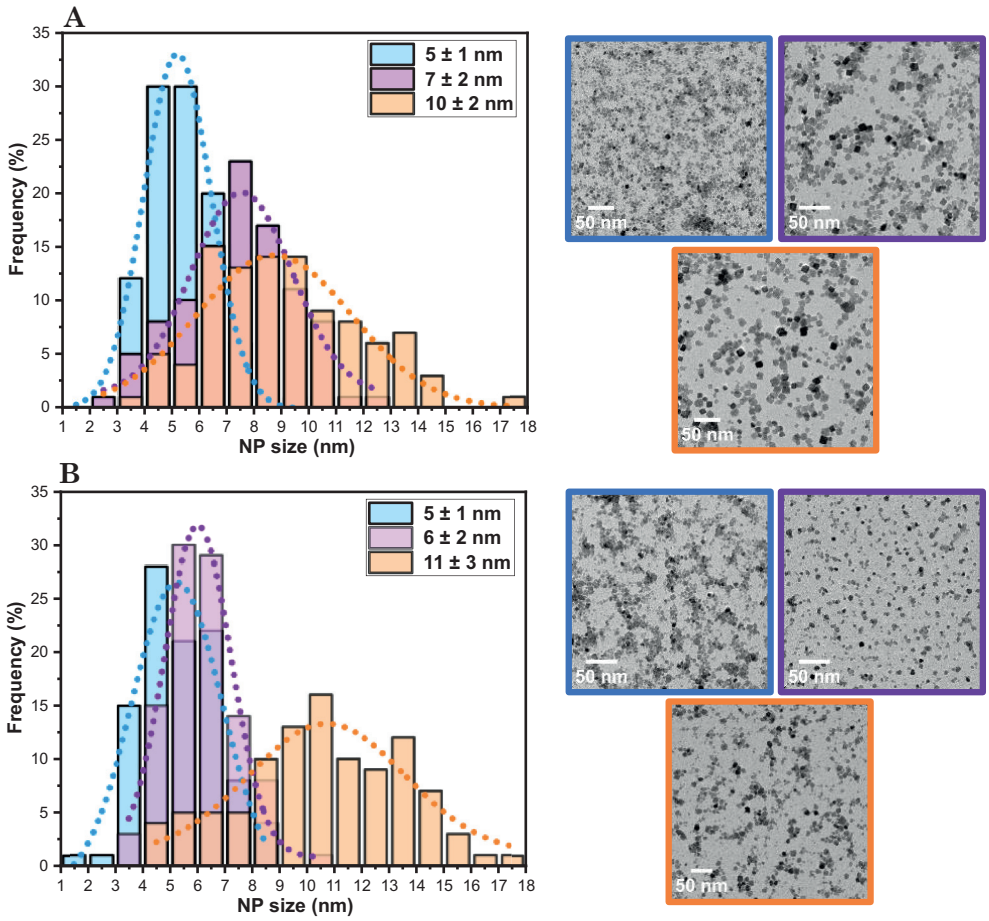

Figure 2.7 Histograms distribution from TEM and the corresponding TEM images from small (blue), intermediate (purple) and big (orange) as-synthesised NCs of (A) $BaZrO_3$ NCs and (B) $BaHfO_3$ NCs.

2.3.1.3.2 Polyol type effect

Considering the importance of ligand in NC surface stabilisation for good colloidal stability of final metal oxide NCs in solution and in the determination of final NC size and shape[103, 113–115, 118], the effect of polyol type was also investigated. The use of alcohols as stabilisers in the synthesis of NCs is commonly used including polyol-mediated synthesis with control of particle size, morphology and aggregation [122–126].

In previous work [133] the effect of the type and amount of polyol on $BaMO_3$ NCs synthesis had been preliminary studied. It was found that the

functionalisation with other types of polyol such as Diethylene glycol (DEG) and tetraethylene glycol (TEG) instead of triethylene glycol (TREG) of $BaMO_3$ NC surface was possible after optimisation of their quantities to ensure non-aggregation. Moreover, it was observed that using the same quantity of Milli-Q H_2O depending on the type of polyol used, we can modify also the size and shape of NCs.

Here, we also investigated the compatibility and stability of NCs stabilised with polyethylene glycol 200 (PEG) as a potential candidate to improve the stability of these NCs in their further application in high-ionic media as YBCO-precursor solutions. We chose PEG as the capping ligand as we expected that by increasing the ethylene oxide chain from TREG to PEG (solubilities in water are 1000 g/L and 70 g/L respectively), we could enhance stability in more apolar solvents such as propionic acid that we used for YBCO-precursor solutions. Furthermore, the use of PEG could enhance the NC stability in solution, decreasing NC aggregation tendency via steric hindrance from the larger ethylene oxide chain in the case of PEG than TREG.

Here, we optimised the NC synthesis and studied the effect of PEG in the final colloidal solutions. We followed the same synthetic procedure described in section 2.2.1.1 changing only the TREG for the desired quantity of PEG. Firstly, we studied the effect of PEG compared to TREG using the same amount of TREG optimized for $BaZrO_3$ and $BaHfO_3$ and keeping constant the quantity of $NH_{3\,(aq)}$. The quantities and results on shape and size with the two types of polyol for both types of NCs were summarised in Table 2.4.

Table 2.4 Comparision of $BaZrO_3$ and $BaHfO_3$ NCs stabilised with TREG and PEG with the corresponding optimized polyol quantities and results on the shape and NC sizes from histograms of TEM images.

Sample	NC type	Polyol type	Polyol (mmol)	$NH_{3(aq)}$ (mmol)	Shape	TEM size (nm)
A	$BaZrO_3$	TREG	44.5	74.0	Square-like	11 ± 3
B	$BaZrO_3$	PEG 200	44.5	74.0	Spherical	7 ± 2
C	$BaHfO_3$	TREG	51.9	74.0	Spherical	11 ± 3
D	$BaHfO_3$	PEG 200	51.9	74.0	Spherical	5 ± 1

Results in Table 2.4 show that using the same quantity for TREG and PEG and the optimized amount of $NH_{3\,(aq)}$ for bigger NCs (~ 10 nm), in the case of PEG, we obtained smaller NCs (~ 7 nm for $BaZrO_3$ and ~ 5 nm for $BaHfO_3$). Apart from the effect on NC size, we also detected in the case of $BaZrO_3$ an effect on morphology from square-like to spherical. The effect on the size and shape of these samples can be better observed in TEM images and DLS measurements (Figure 2.8). It is observed that using the same quantity for TREG and PEG, we also obtained non-aggregated and monodispersed NC solutions (one single peak in DLS).

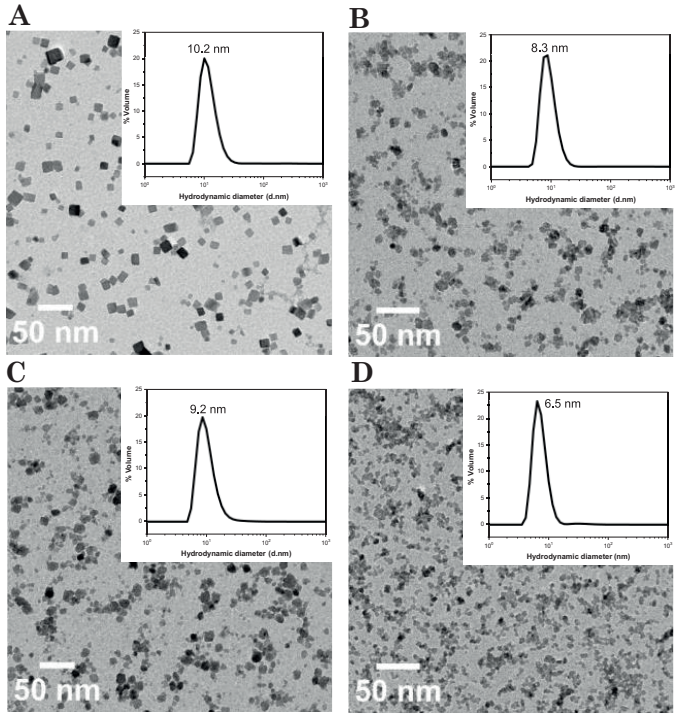

Figure 2.8 TEM images and the corresponding DLS measurement of as-synthesised $BaZrO_3$ NCs using the stabilisers (A) TREG (B) PEG and $BaHfO_3$ NCs (C) TREG (D) PEG.

A similar tendency was observed in the preliminary results reported in [133] using alternative polyols that contained a shorter ethylene oxide chain. Furthermore, similar to other types of NPs, we observed similar effect of polyol on the growth phase concerning the control of final NC size and morphology [125, 126, 173].

To further investigate the effect of polyol, we performed different experiments changing the molar ratio Metal:PEG in the case of $BaHfO_3$ NCs (Table 2.5) keeping constant the quantity of $NH_{3\,(aq)}$ to 74 mmol (optimised quantity for TREG-stabilised NCs of ~10 nm).

Table 2.5 TEM size of PEG-$BaHfO_3$ NCs synthesised using different concentrations of PEG and using 74 mmol of $NH_{3\,(aq)}$ in all the experiments.

$BaHfO_3$ Particles	PEG 200 (mmol)	Molar ratio Metal:PEG	TEM size (nm)
A	36.5	1:10.4	7 ± 2
B	51.9	1:14.8	5 ± 1
C	77.9	1:22.3	4 ± 1

TEM average sizes (Table 2.5) show that keeping constant the amount of $NH_{3\,(aq)}$, the NC size is also dependent on the ligand quantity. When the molar ratio Metal:PEG decreased from 1:22.9 to 1:10.7, the size of PEG-$BaHfO_3$ NCs increased from 4 to 7 nm (average TEM size). DLS measurements inset in the corresponding TEM images (Figure 2.9) show also differences in the behaviour of colloidal solutions. In the case of 1:10.4 molar ratio Metal:PEG we obtained peaks above 10 nm and together with TEM image (Figure 2.9A) confirmed the presence of partial aggregation that was avoided using 1:14.8 and 1:22.3 that show non-aggregated NCs (one single DLS peak). We conclude that a minimum amount of stabiliser is required to avoid aggregation, but an excess of stabiliser on the NC surface is attributed to a decrease in the final size of NCs, hindering their growth. [103, 174, 175].

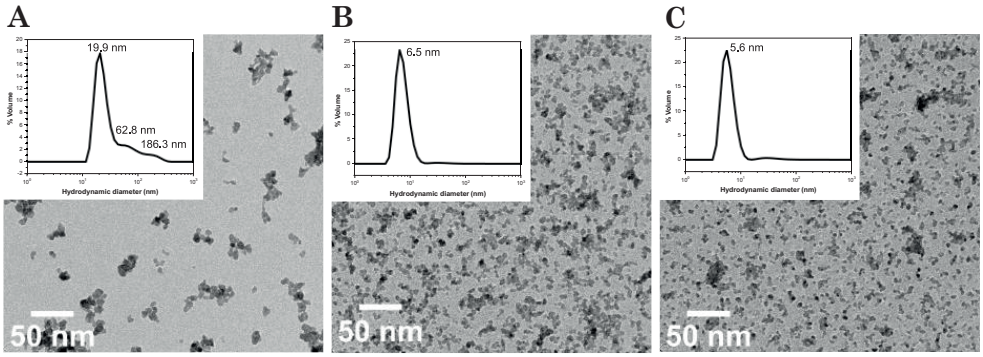

Figure 2.9 TEM images of synthesised PEG-stabilised $BaHfO_3$ NCs using the molar ratio Metal:PEG (A) 1:10.4 (B) 1:14.8 (C) 1:22.3.

Finally, we want to anticipate here that PEG-stabilised $BaMO_3$ NCs show good compatibility with YBCO precursor solution, and its relevance comes from the improvement in the YBCO precursor solution preparation using 7 nm size NCs (more details in Chapter 3). We performed a complete characterisation of PEG-$BaZrO_3$ NCs and we presented the comparison with TREG-$BaMO_3$ NCs, with the same size (~ 7 nm), which has been widely investigated (Table 2.6).

Table 2.6 Comparision of $BaZrO_3$ NCs stabilised with TREG and PEG with the corresponding optimised polyol and $NH_{3\,(aq)}$ quantities to obtain ~ 7 nm-sized NCs and results on the TEM and Sherrer sizes, Z-potential from DLS technique and surface mass loss from TGA.

	Polyol (mmol)	$NH_{3(aq)}$ (mmol)	TEM size (nm)	Scherrer size (nm)	Z-potential (mV)	Organic shell (%)
TEG	44.5	52.9	7 ± 2	7.7 ± 0.2	50.6	17.2
PEG	44.5	74.0	7 ± 2	7.3 ± 0.1	46.4	19.6

Results from Table 2.6 show that we were able to obtain 7 nm average size of NCs with TREG and PEG using the same polyol quantity by modifying the amount of $NH_{3\,(aq)}$. As it is mentioned in previous sections, both parameters polyol and $NH_{3\,(aq)}$ are involved in NC formation, controlling aggregation and the final NC size. Furthermore, we obtained square-like shapes for NCs synthesised using TREG and spherical by PEG but in both cases, we achieved monodispersed and non-aggregated colloidal solutions (Figure 2.10A). The higher hydrodynamic size of PEG-NCs than TEG-NCs could be related to the differences in dimensions of H-[O-CH_2-CH_2]$_n$-OH chain from the polymer (PEG) of n= 200 and the molecule of TREG n=3 increasing the NC surface shell size.

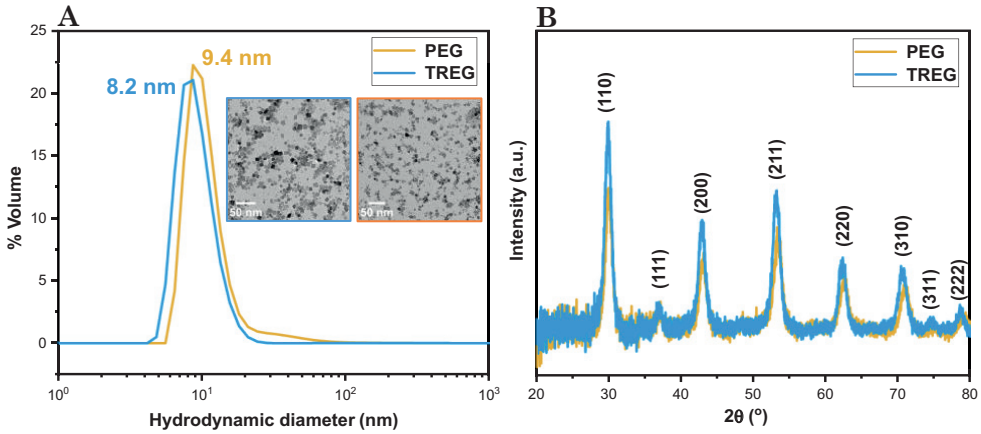

Figure 2.10 (A) DLS measurements of $BaZrO_3$ colloidal solution of 7 nm of average size synthesised using PEG (orange) and TREG (blue) with the corresponding TEM images inset and (B) Powder XRD patterns of PEG-NCs (orange) and TREG-NCs (blue) with cubic phase assigned with reference patterns (00-006-0399) from the Internacional Centre of Diffraction Data.

The PEG-$BaZrO_3$ NCs also crystallised in the same crystalline structure as TREG-$BaZrO_3$ (cubic phase) confirmed by XRD (Figure 2.10B). We also evaluated the surface charge of PEG-NCs that determine the colloidal solution stability and the value obtained was 46.4 mV which is above the stability limit (± 30 mV) and in the same range as NCs stabilised with TREG (positively charged). For their application in YBCO precursor solution the concentration of PEG-NC suspension was determined by the organic shell loss from TGA analysis (Figure B.2 in Appendix B) and we also obtained high yields of 76-79 % (137-143 mM).

2.3.1.3.3 Temperature effect

In previous sections, it is confirmed that the concentration of $NH_{3\,(aq)}$ and polyol stabiliser and its nature affect directly the aggregation, final NC size and shape. The temperature factor can also have an effect on the size, shape and crystallinity of final metal oxide NPs [103, 116, 117].

In Chamorro N. Thesis [133] temperature is another factor that was briefly investigated. It was found that 100 °C in the autoclave reactor was not enough to induce the complete NC crystallization obtaining an amorphous XRD pattern with $BaCO_3$ as an impurity. Increasing the temperature to 180 °C or even more (210 °C) NCs with the same size, shape and high crystallinity (cubic phase) were achieved. For this reason, 180 °C was the optimum reaction temperature chosen during this thesis.

The main reactions during this thesis were made using DAB-2 Berghof reactor where the thermal sensor is out of the reaction vessel, in the heating block. Considering this, the temperature chosen as a set point in the sensor is 15-30ºC less inside the reaction vessel and is not the real reaction temperature of NC formation. The incorporation of a new reactor, BR-100 Berghof, where the thermal sensor is inside the reaction vessel gave us the opportunity to study the real temperature needed for the NC formation and crystallisation. Apart from the control of temperature inside the vessel, this autoclave system has control of heating/cooling ramps and reaction pressure measured by a manometer.

We performed two experiments to study the reaction temperature effect on crystallinity and behaviour of NC solutions using the BR-100 Berghof reactor at 130 °C and 150 °C temperatures with the profile: 35 min to temperature

set point, keeping the temperature set point for 10 min and cooling until room temperature for 3h. We used the NC precursor preparation explained in section 2.2.1.1 and the $NH_{3\,(aq)}$ quantity optimised to obtain $BaZrO_3$ NCs of ~ 5nm of TEM average size.

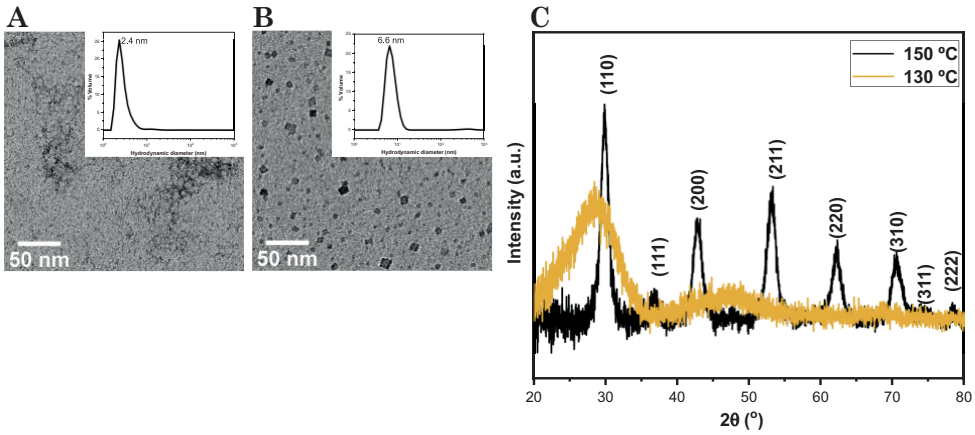

Figure 2.11 TEM image of $BaZrO_3$ NCs synthesised (A) at 130 °C (B) at 150 °C and (C) the corresponding powder XRD patterns using 130 °C (orange) and 150 °C (black) of temperature with a cubic phase assigned with reference patterns (00-006-0399) from the Internacional Centre of Diffraction Data.

These dispersions were characterised by TEM, DLS and XRD to know the size, shape, homogeneity and crystalline structure. At 130 °C we obtained an amorphous XRD pattern (Figure 2.11C) indicating no complete crystallisation. TEM image (Figure 2.11A) and DLS measurement inset show also the presence of very small particles without a defined faceting related to the no complete growth of NCs. At 150 °C we obtained a homogenous distribution without aggregation of small NCs with a size 6 ± 1 nm by TEM (Figure 2.11B). NCs show a cubic phase of perovskite crystalline structure with a crystalline coherent domain of 6.9 ± 0.5 nm calculated by Sherrer equation. The maximum pressure observed in the experiment at 150 °C was 10 bar. Considering these results, we conclude that a low reaction temperature of 150 °C is enough to achieve high crystallinity and good size distribution of $BaZrO_3$ NCs.

2.3.1.4 Stability of $BaMO_3$ colloidal solutions

For our application of colloidal solutions, it is important the control size, dispersion degree, shape and ligand functionalisation that avoid the aggregation of NCs and it is in charge of the compatibility and stability of the final NC dispersions in the system of the desired application. For the application of preformed $BaMO_3$ NCs in YBCO-nanocomposite films small-sizes, monodispersed and high stable colloidal solutions are important characteristics to ensure successful compatibility and enhancement of physical properties of the material. In previous sections, it was shown that we were able to tune the NC size in a narrow range of size distribution.

In this section stability studies during months were performed. Firstly, focusing on the final application of these NC on a YBCO-precursor solution which contains methanol and propionic acid (details in Chapter 3), we studied the stability of $BaMO_3$ NCs in methanol and tested the compatibility and stability with less polar alcohols (lower dielectric constant) and high viscosity values such as ethanol and n-butanol (see Table 2.7).

Table 2.7 Dielectric constant and viscosity values of solvents used for NC stability studies

Solvent	Dielectric constant (ε)	Viscosity (cP)
Methanol	32.7	0.54
Ethanol	24.5	1.07
n-Butanol	17.7	2.54

The colloidal solutions in the different solvents were prepared following the procedure explained in the experimental section (2.2.1.1) re-dispersing the solid phase after the first centrifugation in the desired solvent. The stability of $BaMO_3$ NCs with an average size of ~ 5 nm redispersed in the three different solvents was evaluated by the DLS technique to determine the hydrodynamic sizes and to perform electrokinetic measurements (Z-potential) during 90 days of the same NC solution (Figure 2.12).

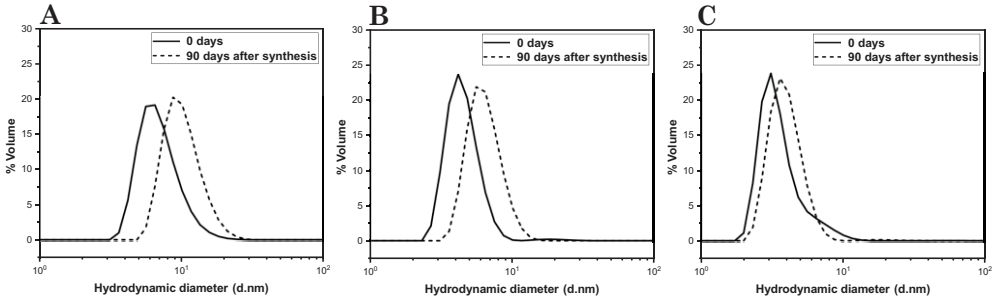

Figure 2.12 Hydrodynamic size at 0 days and 90 days after NC synthesis of $BaZrO_3$ nanosuspensions redispersed in (A) methanol, (B) ethanol and (C) n-butanol.

DLS measurements (Figure 2.12) show that $BaZrO_3$ NCs stabilised with TREG and redispersed in methanol, ethanol and n-butanol are monodispersed solutions by the presence of one single peak below 10 nm. After 90 days, the three colloidal solutions (> 100 mM) remained non-aggregated (one single peak) with a small shift in the size of ~ 1-3 nm.

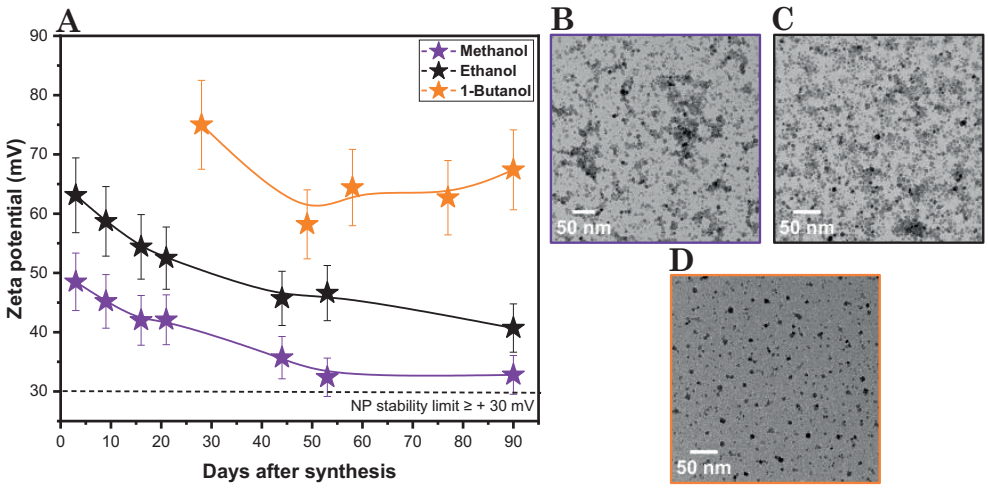

Figure 2.13 (A) Z-potential evolution from 0 day to 90 days of $BaZrO_3$ nanosuspensions redispersed in methanol (purple), ethanol (black) and n-butanol (orange) and the corresponding TEM images of (A) 6±1 nm size NCs in methanol, (B) 5±1 nm size NCs in ethanol and (C) 5±1 nm size NCs in n-butanol after 90 days.

The evolution of Z-potential over time (Figure 2.13A) shows that the stability of NCs increased in the direction of a decrease in the dielectric constant (ε) and an increase in viscosity from methanol < ethanol < n-butanol. The Z-potential analysis based on the electrophoresis movement through the Henry equation (Equation A.9 in Appendix A.3) which is directly proportional to the viscosity and inversely proportional to the dielectric constant of the dispersant

[176, 177]. This relation between the parameters explained the high values obtained for n-butanol with the highest viscosity and lowest dielectric constant and on the contrary for methanol. Furthermore, the Hückel approximation used for Z-potential analysis for small-sized particles and non-aqueous media came from the thicker expected slip-plane layer of particle surface when the dispersant polarity decreased. This could also explain the highest and most stable Z-potential values for n-butanol with an expected thicker slip-plane layer that enhances the electrostatic repulsion and stability of particles [178–180].

In the three solvents, the surface charge was positively charged, and the values were above the colloid stability limit ± 30 mV [155, 156] ensuring a high stability of NCs in solutions over 90 days. The Z-potential values from the different solvents increased in the same order mentioned before. Methanol shows lower stability as after 90 days, Z-potential values decreased from ~ 50 mV to ~ 33 mV.

These results show that TREG-stabilised $BaMO_3$ NCs were compatible and stable in a certain range of polarity allowing their application in different types of systems. In our case, we chose to work with $BaMO_3$ NCs redispersed in ethanol to ensure high stability of NCs in solution and keep the solubility and stability of YBCO precursor salts which also depends on the solvent mixture used (discussed in Chapter 3).

Moreover, we observed differences in stabilisation when we used these NCs on the YBCO-precursor solution depending on NC core size (TEM size) we decided to perform the same stability studies using DLS measurements over 2 years of $BaZrO_3$ and $BaHfO_3$ NCs of 5 ± 1 nm and 11 ± 3 nm of size (Figure 2.14) redispersed in ethanol. Hydrodinamic size results show that after 2 years the colloidal solutions of both types of NCs with 5 ± 1 nm and 11 ± 3 nm of size remain non-aggregate in solution (one single peak) with a small shift of 1-2 nm in size.

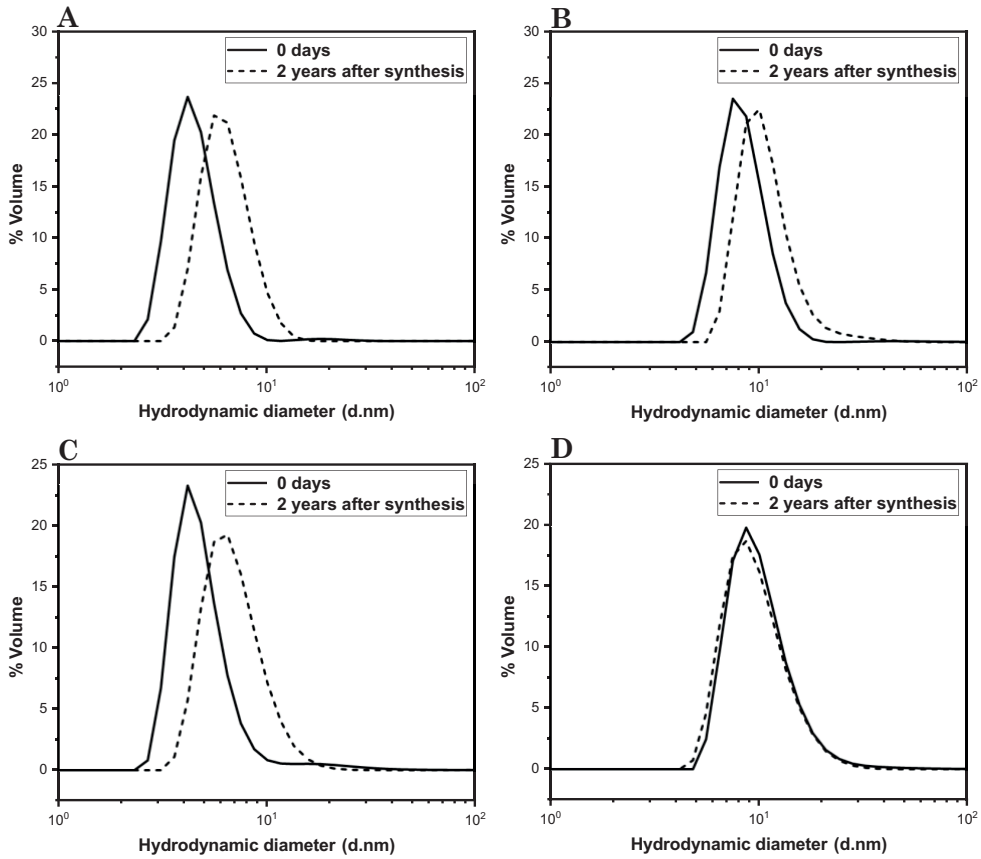

Figure 2.14 Hydrodynamic size of colloidal solutions at 0 days and 2 years after of NC synthesis of (A) 5± 1 nm $BaZrO_3$ NCs, (B) 11± 3 nm $BaZrO_3$ NCs and (C) 5± 1 nm $BaHfO_3$ NCs and (D) 11± 3 nm $BaHfO_3$ NCs.

Complementary, we checked the stability in solution by Z-potential measurements (Table 2.8), depending on size for both types of NCs, showing that after 2 years the surface charge values were also above the NP stability limit in solution (± 30mV) for small and bigger-sized NCs.

The stabiliser TREG was always in excess in the precursor solution (molar ratio metal:TREG was 1:16.5 for $BaZrO_3$ NCs and 1:14.8 for $BaHfO_3$ NCs and we kept these quantities for the synthesis of 5 to 10 nm NCs. The organic mass present on the NC surface of both $BaMO_3$ NCs of 5 ± 1 nm and 11 ± 3 nm of size was analysed by TGA (Figure B.3) and the values are in Table 2.7. There is a slight difference in the organic shell on the NCs of 5 ± 1 nm and 11 ± 3 nm. The organic shell (%) increased 3.1% in the case of $BaZrO_3$ and 2.1% in the case of $BaHfO_3$ NC when the NC size increased. The synthetic routes of polyols

from the polymerisation of ethylene oxide used water or alcohols as initiators and alkaline catalysts such as hydroxides, alkoxides, amides and amines at low temperatures ~100 °C [181, 182]. Furthermore, it is also reported the oxidation of polyols in alkaline conditions by a catalyst [183, 184]. These conditions were similar to our precursor solution in solvothermal treatment with TREG. In the case of bigger-NCs, we added more aqueous ammonia than smaller-NCs where polymerisation or/and oxidation of TREG could be more promoted by acting as a catalyst. These possible reactions could end on different molecular weight polyol that could interact with NC surface explaining the slight differences in % of organic shell depending on NC size.

Table 2.8 TEM size from histograms of TEM images, Z-potential values after 2 years from DLS measurement and surface mass from TGA technique of $BaZrO_3$ and $BaHfO_3$ NCs solutions of 5 ± 1 nm and 11 ±3 nm size.

NC composition	TEM size (nm)	Z-potential after 2 years (mV)	Organic shell (%)
$BaZrO_3$	5 ± 1	40.2	13.4
$BaZrO_3$	11 ± 3	38.8	16.5
$BaHfO_3$	5 ± 1	45.8	16.0
$BaHfO_3$	11 ± 3	38.6	18.1

In the case of PEG-stabilised NCs, the colloidal solutions also show high stability, with a small shift in hydrodinamic size after 180 days and Z-potential values were above ± 30 mV (Figure 2.15).

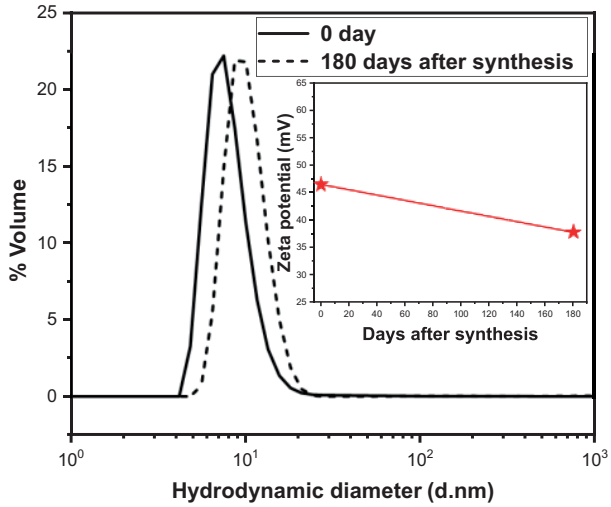

Figure 2.15 Hydrodynamic size of colloidal solution at 0 days and 180 days after NC synthesis of $BaZrO_3$ NCs stabilised with PEG with the corresponding Z-potential values inset from DLS measurements.

We conclude that stability studies demonstrated that TREG and PEG-stabilised colloidal solutions with high concentrations (>100 mM) of both types of $BaMO_3$ NCs redispersed in polar solvents have long-time stability in solution applications.

2.3.1.5 NC synthesis through MW thermal activation

The NC synthesis by MW method is suggested to be a more efficient and faster process (reducing considerably the reaction time) with a more homogeneous heating process compared with convection heating (solvothermal by autoclave thermal activation) [127, 185, 186].

We checked out the compatibility of H2S2 process with the MW thermal activation for $BaMO_3$ NC synthesis using MW oven of Milestone FlexiWAVE model which offers interesting characteristics such as a temperature control system by optic fiber, pressure control (inside the reaction vessel) and also the carousel option to perform several reactions at the same time. These features open up the possibility of easing the scalability of the method. Moreover, MW equipment allows good control of the heating/cooling ramps.

The first experiments with MW were made using the same precursor solution as the solvothermal method (section 2.2.1.1) that contains ethanol and

TREG as a liquid phase in excess. Using this solvent mixture with MW irradiation we found uncontrolled reactions at low temperatures that produce high (~ 15 bar) and irreproducible pressures before heating up at 180 °C. This irreproducibility in pressure could be explained due to the homogenous and faster heating with MW irradiation compared with conventional ones (solvothermal) that produce early and faster ethanol evaporation (b.p 78 °C). In addition, as the precursor solution for MW was prepared outside the Teflon reaction vessel and then was transferred depending on the time of precursor solution preparation we were generating more or less butanol as subproduct from hydrolysis reaction (Equation 1.12) before MW heating which also has a low boiling point of 117 °C.

For these reasons, we decided to perform the MW NC synthesis optimisation eliminating ethanol as solvent and working with TREG (p.b 285 °C) as solvent and stabiliser using the precursor solution preparation described in section 2.2.1.1. Using this precursor solution for MW thermal activation we achieved low and reproducible pressures of 3-4 bar heating with a ramp of 18°C/min until 180°C, holding the corresponding final temperature for 20 min and cooling in 15 min. In the case of solvothermal treatment, the heating ramp was 4.5°C/min for 180°C, holding for 1h at 180°C and cooling in 2.5h.

The MW optimization was started in parallel with other studies discussed above and before the good results were obtained with $NH_{3\,(aq)}$ as NC size control agent. For this reason, the MW synthesis was performed using 27.8 mmol of Milli-Q H_2O corresponding to obtain small-sized NCs (~ 5 nm).

The final NC size of the resulting colloidal solution using MW method from the histogram of TEM image (Figure 2.15B) was 4.2 ± 0.9 nm which matches well with NC size calculated from XRD pattern (Figure 2.15A) of 3.0 ± 0.1 nm. Concerning the crystallinity of NCs obtained via MW method, XRD measurements show the typical cubic phase structure as those obtained by the autoclave method.

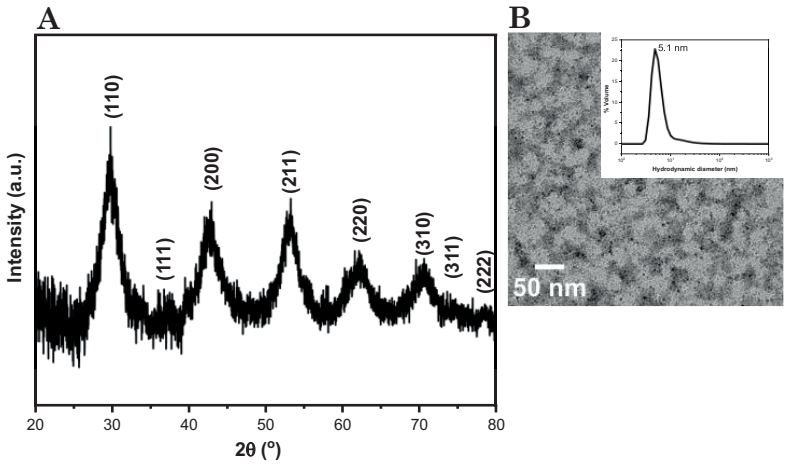

Figure 2.16 (A) XRD pattern of NCs obtained via MW thermal activation assigned with reference patterns (00-006-0399) from the Internacional Centre of Diffraction Data and (B) the corresponding TEM image with DLS measurement inset.

DLS measurements (inset of Figure 2.15B) show that we are able to obtain small-sized NCs with homogenous distribution (one single peak in DLS) using TREG as solvent and stabiliser in precursor solutions and MW radiation.

Analysing the surface by Z-potential measurement we observed that NCs obtained by MW radiation were also stable dispersions with positive surface charged (Z-potential obtained was 56.9 mV). The stability of as-synthesised MW-NCs was also evaluated showing high stability after one year (39.2 mV) ensuring good colloidal stability in solution. The surface of NCs synthesised by MW method was also analysed by TGA (Figure B.4) resulting in the detection of a 21.9 % of organic mass shell used to calculate a final concentration of NC suspension of ~ 100 mM.

After these results, the two methods (Autoclave and MW) show us compatible results concerning NC size, crystallinity, homogeneity and solution stability. The main differences are the solvents used in the precursor solution and reaction time. Complete characterisation of NC surfaces synthesised with only TREG in precursor solution and MW radiation and ethanol/TREG for autoclave should be performed to determine if there are significant or no differences in molecules attached to the surfaces. A shorter reaction time was achieved via MW treatment with a total reaction time of 45 min respect solvothermal method (total reaction time ~ 4h).

2.3.2 BaM_2O_6 nanoparticles

We started synthesising $Ba_2Y(Ta,Nb)O_6$ NPs but the optimisation of different reaction parameters ended in aggregation, lack of crystallinity and organic nature in samples indicating that we might not reach the needed solvothermal conditions in our autoclave system for the complete formation of these double-perovskite NPs. For this reason, we decided to synthesise $Ba(Ta,Nb)_2O_6$ NPs in solution for the first time as we expect that these compositions will be also stable and non-reactive with YBCO composition with a large lattice mismatch. We optimised the reaction in the direction of ensuring the requirements for successful compatibility with YBCO precursor solutions, such as small-sized NPs (< 10 nm) with homogeneous distribution high stability in solution and high concentrations.

2.3.2.1 Nanocrystal synthesis and characterisation

⁕ TREG-assisted H2S2 process

The optimization was started using H2S2 procedure with the optimised solvothermal conditions for $BaMO_3$ NCs (1 h, 180 °C). In the precursor solution, stoichiometric M:Ba molar ratio of 2:1, ethanol as solvent, TREG as a stabiliser and $NH_{3\,(aq)}$ as hydrolysis initiator were used.

In the first experiment performed, we used the same molar ratio Ba:TREG (1:14.8) as the stoichiometric reaction for the synthesis of ~ 10 nm $BaHfO_3$ NCs using 74.0 mmol of $NH_{3\,(aq)}$ (see Table 2.3).

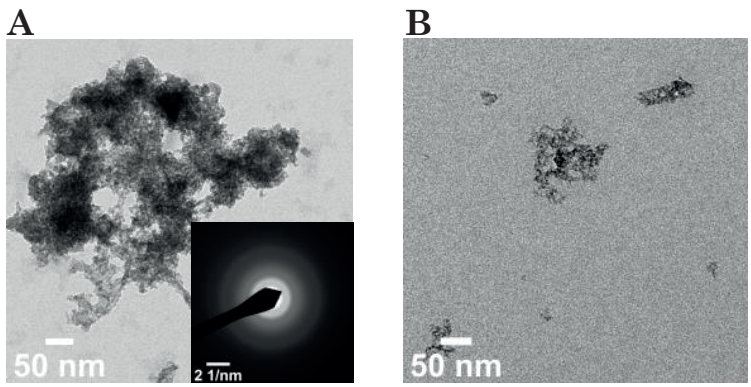

Figure 2.17 TEM images of as-synthesised $BaTa_2O_6$ NPs using the molar ratio Ba:TREG of (A) 1:15.3 with the corresponding SAED image inset (B) 1:68.5

TEM image (Figure 2.17A) shows an aggregation of small-sized NPs (~ 3-4 nm). The corresponding SAED pattern shows blurred circles instead of spots distribution in circles around the middle where the radius corresponds to the d-spacing of each plane which is attributed to the random distribution of crystalline NPs. This indicates that the low temperature of 180 °C used in solvothermal treatment was insufficient to induce crystallisation in the case of BaM_2O_6 NPs. If NPs are amorphous, the blurred circles of SAED pattern could be explained by the carbon diffraction of the TEM grid.

Firstly, we tried to solve the problem of aggregation by increasing the molar ratio Ba:TREG to 1:68.5 and TEM also showed the formation of aggregates of small-sized NPs (~ 3-4 nm) (Figure 2.17B).

These results show that these BaM_2O_6 NPs had a different behaviour than $BaMO_3$ NCs. The hydrolysis of Tantalum and Niobium (V) ethoxide could be different than for Zirconium and Hafnium (IV) butoxide. As we discuss in section 2.3.1.3 is known that the reactivity of alkoxides towards hydrolysis depends mainly on the electronegativity of the metal atom, its ability to increase the coordination number, the steric hindrance of the alkoxy group, and the structure of the metal alkoxides [119, 162, 167].

⁕ Surfactant-free H2S2 process

Concerning the results obtained in TREG-assisted H2S2 and the few references for BaM_2O_6 NPs regarding the non-aqueous and surfactant-free synthesis of $(Ta,Nb)_2O_6$ [129, 135], polyol route [123] and hydrothermal synthesis of Ta_2O_6 and $BaTa_2O_6$ NPs [137, 138, 141] we decided to eliminate the use of capping ligand and increase the solvothermal temperature of the H2S2 process. We know from $BaMO_3$ NCs that stabiliser and reaction temperature have an influence on the behaviour of final colloidal solutions.

Using the experimental procedure described in section 2.2.1.2 we obtained aggregates of small-sized NPs of 4-5 nm for $BaNb_2O_6$ and 3-4 nm for $BaTa_2O_6$ with spherical shape observed by TEM (Figure 2.18A and B). XRD patterns showed poorly crystalline NPs after solvothermal treatment at 220 °C for 48 h (Figure 2.18C). Despite the lack of crystallinity, our efforts on optimisation were centred on reducing the high reaction temperature and long reaction times reported for the synthesis of these types of NPs [129, 135–138] and considering that the maximum temperature of the reactor used is 250 °C.

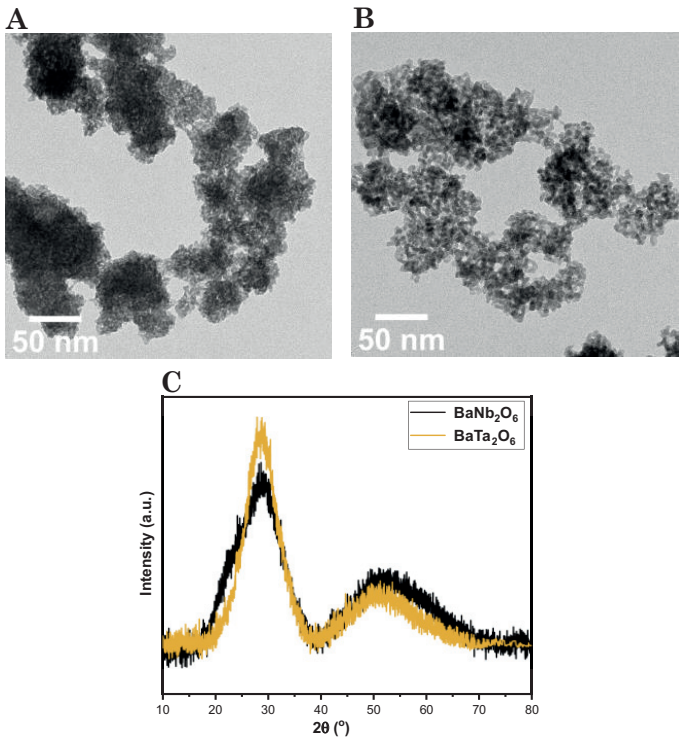

Figure 2.18 TEM images of the as-synthesised (A) $BaNb_2O_6$ and (B) $BaTa_2O_6$ NPs and (C) the corresponding powder XRD patterns ($BaNb_2O_6$ in black and $BaTa_2O_6$ in orange).

Crystallinity was evaluated through High-Resolution TEM (HRTEM) of $BaNb_2O_6$ NPs in order to confirm if these NPs were crystalline (by observing crystalline planes) and their small size explains the broad XRD pattern or if NPs were amorphous. HRTEM images show an aggregate of ~ 135 nm (Figure 2.19A). Analysing a high magnification image from a concrete area of the aggregate (Figure 2.19B) suggests that the spherical shape and size observed in low magnification TEM maybe it is an overlap contrast of multiple NPs aggregated. Considering this, we opted to provide the TEM size as a size range instead of calculating TEM average size from histogram of a TEM image until we can accurately measure it by disaggregating the NPs. Furthermore, going to high magnification in HRTEM we observed that in the dark region of the image (Figure 2.19C), that corresponds to NPs, we cannot identify lattice fingers and faceting of NPs. The comparison with the same high magnification in HRTEM image of amorphous carbon-coated TEM copper grid without NPs (Figure 2.19D) confirmed that $BaNb_2O_6$ NPs were amorphous.

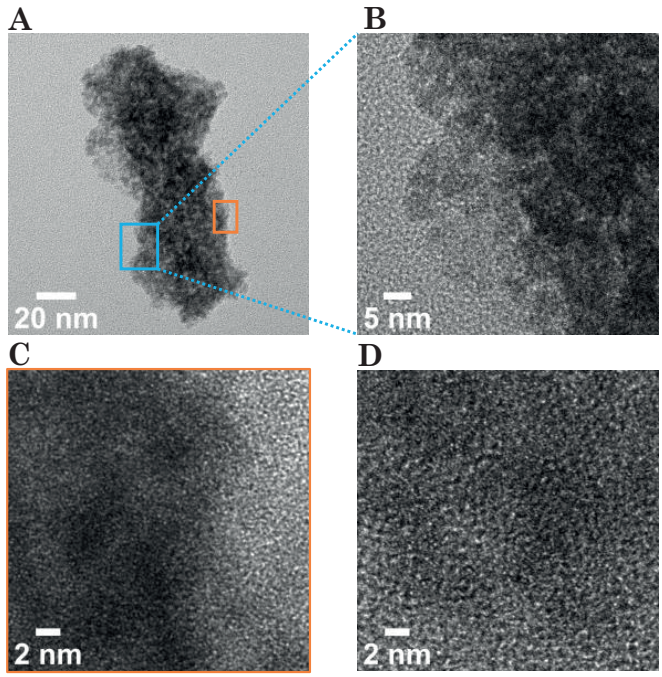

Figure 2.19 HRTEM images of (A) Aggregated of $BaNb_2O_6$ NPs (B) zoom at high magnification of the blue region of aggregate (C) zoom at high magnification of the orange region of aggregate (D) image of carbon-coated TEM copper grid zone without NPs at the same magnification of image C. .

Annealing treatments at different temperatures ranging from 500 to 900 °C of dried powder of $BaNb_2O_6$ and $BaTa_2O_6$ respectively were performed to induce crystallisation after a high-thermal treatment in a solid state. The as-synthesized NPs were dried and subsequently heated to the desired annealing temperature in an oven with a heating rate of 15 °C/min for 6 h in air.

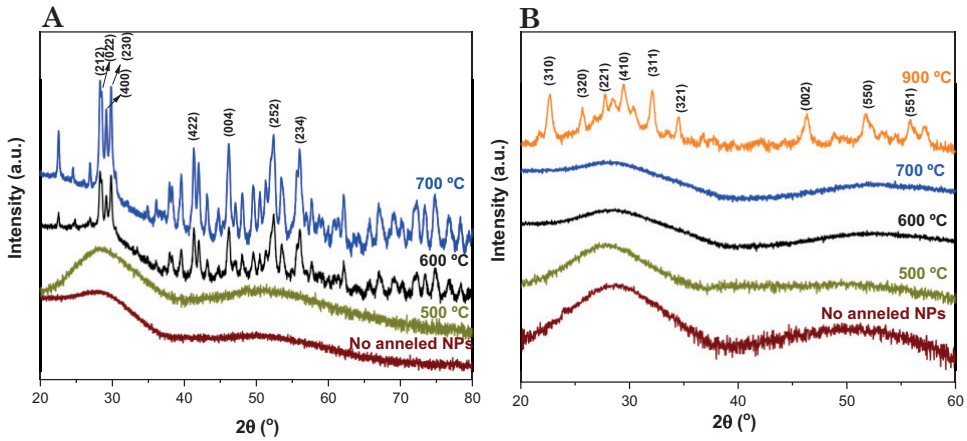

Figure 2.20 XRD patterns of (A) $BaNb_2O_6$ powder NPs after solvothermal treatment (dark red) and annealing treatments at 500 °C (green), 600 °C (black) and 700 °C (blue) (B) $BaTa_2O_6$ powder NPs after solvothermal treatment (dark red) and annealing treatments at 500 °C (green), 600 °C (black), 700 °C (blue) and 900 °C (orange).

If we analyse the crystalline structure we observe that $BaNb_2O_6$ NPs crystallise at 600 °C in an orthorhombic phase of $CaTa_2O_6$-type structure and $BaTa_2O_6$ NPs at 900 °C in hexagonal phase of tungsten-bronze type structure. Planes of crystalline structures were assigned with reference patterns (00-014-0027 and 04-009-2823) from the Internacional Centre of Diffraction Data for $BaNb_2O_6$ and $BaTa_2O_6$ respectively. As was previously reported, $BaNb_2O_6$ crystallise in two polymorphs where the orthorhombic phase was obtained at low temperatures and the hexagonal phase at high temperatures [139, 140, 187, 188]. In the case of $BaTa_2O_6$ three polymorphs of orthorhombic, tetragonal and hexagonal phase from low to high-temperature [188–190] were found in the literature. Still, it was also reported the obtention of hexagonal phase prepared by low-temperature hydrothermal method [141]. The particle size and morphology of the calcined powders of $BaNb_2O_6$ at 700 °C and $BaTa_2O_6$ at 900 °C were examined by TEM (Figure B.5A and B). After the exposition of NPs to high temperatures, we promote the sintering process by obtaining irregular shapes and agglomeration until the NP fusion [191]. The inset SAED pattern of calcined powder of $BaTa_2O_6$ NPs (Figure B.5B) shows circles with bright spots corresponding to interplanar distances for the respective particles and how the crystallinity has been improved.

In addition, stoichiometry confirmation was employed by Inductively Coupled Plasma Mass Spectrometry (ICP-MS) analysis. The determined quantities

of metals of $BaNb_2O_6$ and $BaTa_2O_6$ from ICP-MS and molar ratio Ba:M calculated were summarised in Table 2.9.

Table 2.9 Quantities of %Ba,%Ta and %Nb analysed by ICP-MS and calculated values of Molar ratio Ba:M of $BaNb_2O_6$ and $BaTa_2O_6$ powder NPs samples.

	%Ba (%w/w)	%Ta (%w/w)	%Nb (%w/w)	Molar ratio Ba:M
$BaNb_2O_6$	24 ± 1.4	-	37 ± 1.1	1:2.4
$BaTa_2O_6$	16 ± 1.7	51 ± 5	-	1:2.3

The molar ratio of Ba:M results obtained from ICP-MS were ~ 1:2 confirming stoichiometric BaM_2O_6 composition for both types of NPs.

The final concentration of the NP solutions was determined using the organic shell loss measured from TGA analysis (Figure B.6 in Appendix B). We obtained yields values of 78 % (34 mM) for $BaNb_2O_6$ and 75 % (22 mM) for $BaTa_2O_6$ NPs.

The optimisation of the synthetic parameters to achieve these small-sized BaM_2O_6 NPs without surfactant during solvothermal treatment and the strategies to avoid their aggregation is discussed in the following sections.

2.3.2.2 Tuning of the synthetic parameters

2.3.2.2.1 Temperature effect

It is known that the reaction temperature has an effect on the final behaviour of metal oxide NPs (size, shape, crystallinity,...) [103, 116, 117]. For $BaMO_3$ NCs it was found that it required a minimum solvothermal temperature to induce the crystallisation of NCs (section 2.3.1.3.3). The references reported regarding M_2O_6 and BaM_2O_6 particles synthesis have in common the use of high-temperature treatment 200-300 °C and long reaction times (1 day to 4 days) and in some cases, a post-annealing treatment was performed to achieve crystalline NPs [129, 135–138].

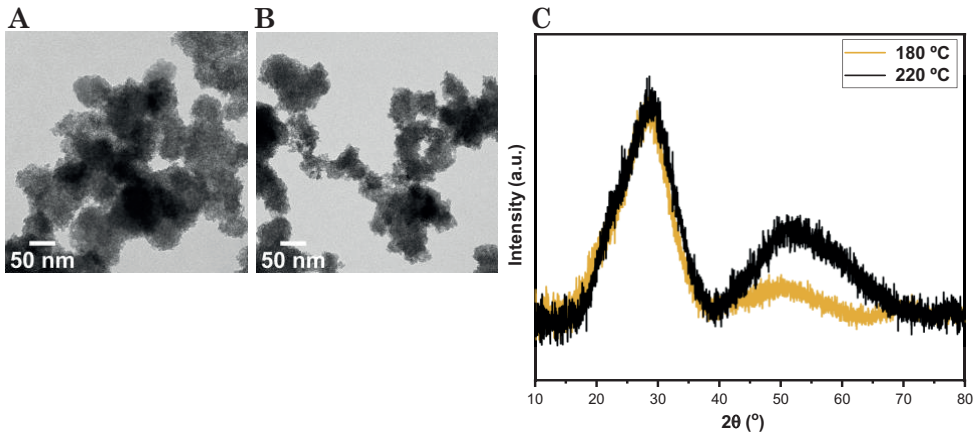

Figure 2.21 TEM image of $BaNb_2O_6$ NPs synthesised (A) at 180 °C (B) at 220 °C and (C) the corresponding powder XRD patterns using 180 °C (orange) and 220 °C (black) of temperature.

We performed several reactions at different solvothermal temperatures from 180 to 250 °C following the experimental procedure of the solvothermal method described in section 2.2.1.2. Firstly, we started using 180 and 220 °C for $BaNb_2O_6$ NPs. After solvothermal treatment at 180 °C, we obtained some gel in the resulting solution suggesting that this temperature is not enough for the complete transformation of the resulting polymeric matrix of metal oxide bridges from hydrolysis and polycondensation reactions [161]. In spite of this observation, we proceed with the cleaning and characterisation of the colloidal solutions. We obtained large aggregates of 4-5 nm of NPs at both temperatures as TEM images shown (Figure 2.21A and B) due to the absence of a stabiliser in the reaction. In addition, crystallinity was analysed by obtaining broad XRD patterns (Figure 2.21C) for both temperatures indicating no significant influence of temperature on crystallinity enhancement.

After these results, we have also decided to try to synthesise $BaTa_2O_6$ NPs at 250 °C in order to induce crystallinity by raising the temperature which is the maximum work temperature of DAB-2 Berghof reactor. TEM image (Figure 2.22A) of $BaTa_2O_6$ NPs show the same behaviour as $BaNb_2O_6$ NP solutions. We also obtained large aggregates of small-sized NPs (3-4 nm) and amorphous XRD pattern (Figure 2.22 A and C). Therefore, by increasing the reaction temperature to 250 °C did not result in a difference in NP size and improvement of crystallinity.

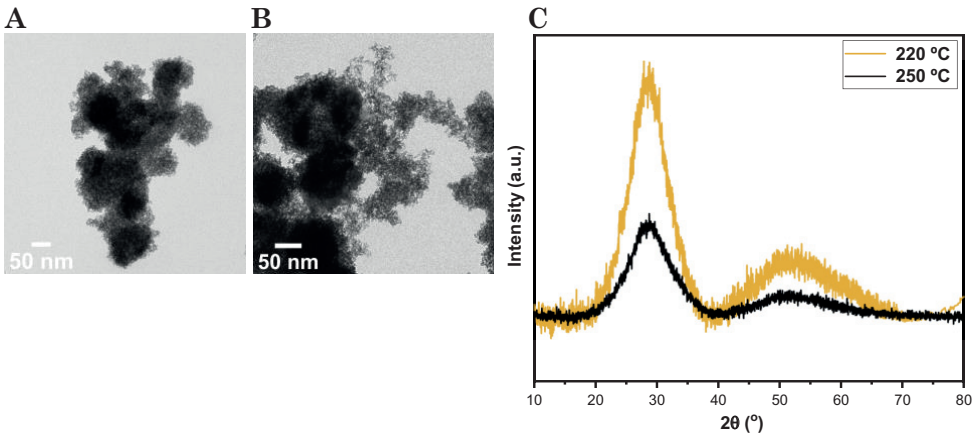

Figure 2.22 TEM image of $BaTa_2O_6$ NPs synthesised (A) at 220 °C (B) at 250 °C and (C) the corresponding powder XRD patterns using 220 °C (orange) and 250 °C (black) of temperature.

Concerning crystallinity, as we cannot improve it by increasing the reaction temperature from 220 to 250 °C (maximum temperature of the reactor) and as we observed the same NP behaviour by TEM analysis at both temperatures we chose 220 °C as the optimal reaction temperature for the formation of BaM_2O_6 NPs. Finally, as we discussed in the previous section (2.3.2.1), the crystallinity was also evaluated by HRTEM which confirmed that NPs synthesised at 220 °C are amorphous.

2.3.2.2.2 Time effect

The reaction time is another key parameter influencing the behaviour of the final colloidal solutions [103, 116, 117] and as the reported synthesis of $BaTa_2O_6$ nanorods, through hydrothermal method [141], the complete reaction and well-crystallisation was achieved at 270 °C during 48h we decided to perform different experiments at 220 °C during various reaction time (24, 48 and 70 h).

TEM images of $BaNb_2O_6$ (Figure 2.23A-C) and $BaTa_2O_6$ (Figure 2.23D-F) NPs synthesised during various time reaction shown the formation of small-sized NPs aggregated with no variation in NP size by increasing the time of solvothermal treatment. At the different reaction times, we obtained 4-5 nm of $BaNb_2O_6$ NPs and 3-4 nm of $BaTa_2O_6$ NPs.

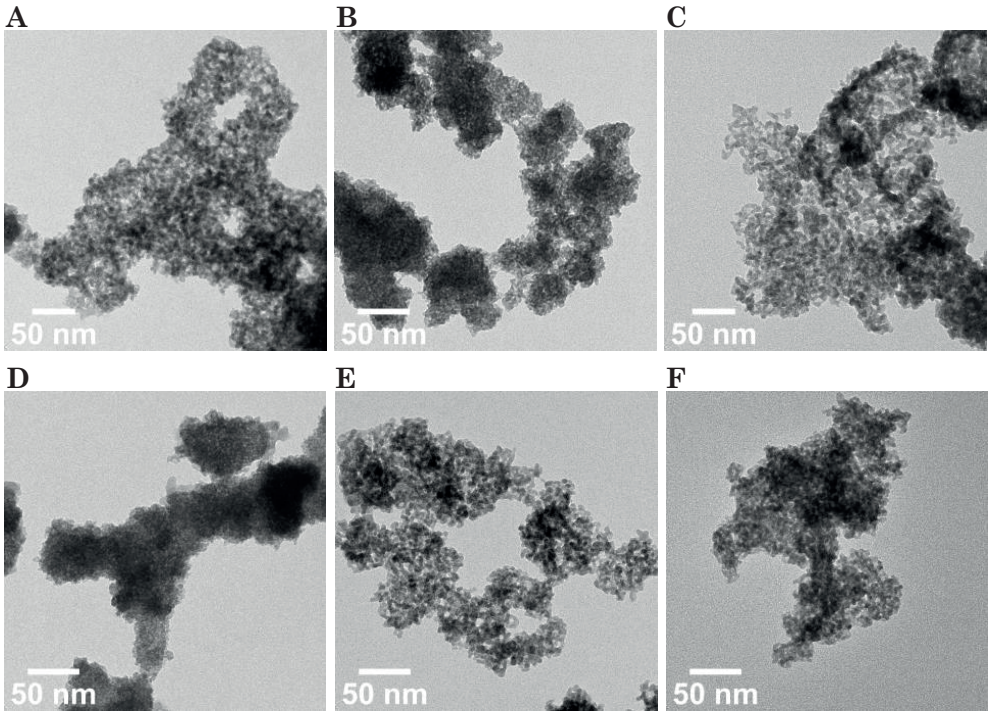

Figure 2.23 TEM images of $BaNb_2O_6$ NPs synthesised at 220 °C during (A) 24h (B) 48 h (C) 70 h and $BaTa_2O_6$ NPs synthesised at 220 °C during (D) 24 h (E) 48 h (F) 70 h.

Furthermore, in the case of the experiments using 24 h of reaction time, it was observed gel after the heating treatment in the autoclave system suggesting that the solvothermal reaction was not completed. Finally, we chose 48h as the optimal reaction time due to no gel being observed and the time increase did not result in crystallinity improvement (Figure B.7).

2.3.2.2.3 Ligand functionalisation during solvothermal process

We discussed in section 2.3.2.1 that using TREG as a stabiliser in ethanol, aggregation is not avoided after solvothermal treatment. We performed several experiments using different capping ligands acting as solvents and stabilisers following the procedure described in section 2.2.1.2 changing ethanol by the desired stabiliser. Reaction in Benzyl alcohol was employed since it was previously used and reported for Tantalum and Niobium (V) oxide NPs [129, 134, 135] and TREG was also tried due to ethylene glycol functionalisation was also reported for these types of NPs [136]. In addition, we performed a reaction in

Propionic acid which contains a carboxylic group instead of hydroxides of benzyl alcohol and TREG which is also able to be attached to the surface. Furthermore, through these experiments, we tested if pH modifications in the synthesis could allow differences in the final colloidal solution behaviour. We mentioned in section 2.3.1.3.1 that pH could have an influence on sol-gel reactions [161–163] and also electrostatic stabilisation, more predominant in polar protic solvents, is also easily tuned by ionic strength and pH [160, 192, 193].

Analysing the final colloidal solutions in Benzyl alcohol, TREG and Propionic acid by TEM (Figure 2.24) we observed NP aggregation and organic matter appearance suggesting that the possible repulsive forces and steric hindrance from Benzyl alcohol, TREG and Propionic acid solutions surface functionalisation were not strong to avoid NP aggregation and ensure stability.

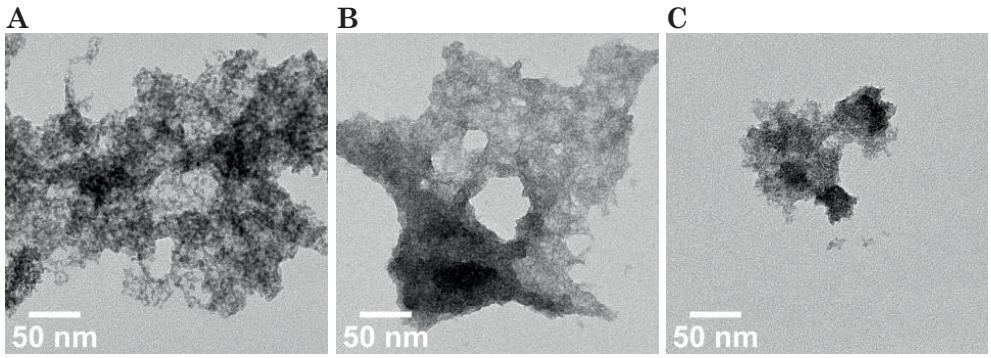

Figure 2.24 TEM images of $BaNb_2O_6$ NPs synthesised at 220 °C during 48 h in (A) Benzyl alcohol (B) TREG and (C) Propionic acid.

.

The reported hydrothermal synthesis of tantalum oxide and alkali tantalates shows a strong dependence of shape, aggregation degree, as well as, composition on the pH value. They obtained non-defined shape and aggregation in acidic conditions attributed to fast hydrolysis at low pH values [137]. In the case of $BaNb_2O_6$ synthesised in Propionic acid (pka ~ 5) we also observe aggregation and non-NP faceting and it seems that going to less acidic conditions from TREG (pka ~ 14) to Benzyl alcohol (pka ~ 15), despite we observe aggregation, the shape of NPs is more defined. We decided to perform the optimisation of BaM_2O_6 NPs in ethanol (pka ~ 16) which is slightly more basic than Benzyl alcohol and due to the compatibility of ethanol with developed YBCO precursor solutions have been demonstrated for $BaMO_3$ NCs (Chapter 3).

After these results where the surface functionalisation by adding stabilisers in the precursor solution mixture was not successful in avoiding NP aggregation, we decided to focus on post-solvothermal surface functionalisation strategies.

2.3.2.3 Post-surface functionalisation

2.3.2.3.1 Analysing of surface chemistry

The complete characterisation of the surface chemistry of NPs allows the control and prediction of the compatibility and stability of the colloidal solutions in different systems. Furthermore, the knowledge of the stabiliser capped onto the NP surface allows the surface chemistry design. There are several approximations to modify the surface of as-synthesised NPs by post-ligand exchange methodologies giving the possibility to attach a new ligand on request depending on the final NP properties desired and the final application [142, 144, 145].

To this aim, we decided to employ two surface techniques: IR and EGA-MS with powders of $BaNb_2O_6$ and $BaTa_2O_6$ to identify the molecules attached to the surface. First of all, IR spectroscopy was employed with the aim of knowing information on the structure of the molecules capped onto the surface of $BaNb_2O_6$ and $BaTa_2O_6$ NPs. The IR spectra (Figure 2.25A) show the same band position and relative intensities indicating the same composition of the surfaces from $BaNb_2O_6$ and $BaTa_2O_6$ NPs. From the precursor solution used, we suggested that the surface could be stabilised by a carbonate (CO_3^{-2}), carboxylated (RCO_2^-), ethoxide ($CH_3CH_2O^-$) or hydroxide (OH^-).

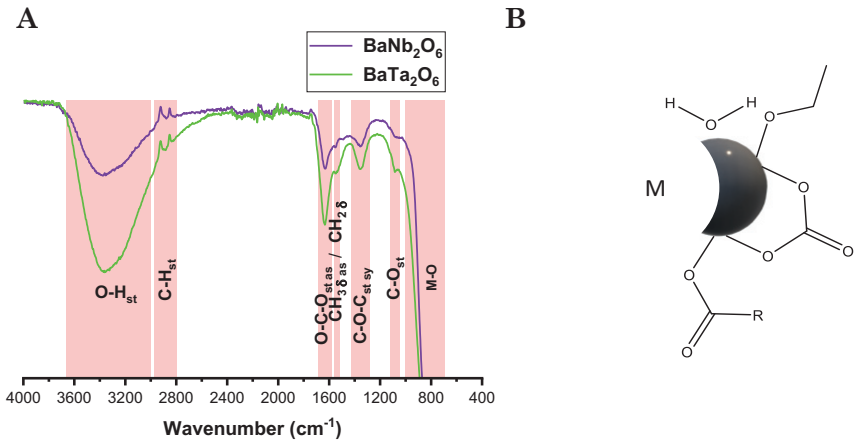

Figure 2.25 (A) FTIR-ATR spectra of $BaNb_2O_6$ (purple) and $BaTa_2O_6$ (green) powder NPs and (B) Schematic representation of the molecules attached to the surface of BaM_2O_6 NPs.

We observed a broad band at ~ 3365 cm^{-1} corresponding to stretching of hydrogen-bonded OH group that could be attributed to the presence of some residues of ethanol coming to the no complete dried treatment to obtain powders, or water adsorbed onto NC surface or solvated alkoxide [194–196]. OH^- anion was discarded as we expected a sharp peak for the free OH group. The peaks in the range of ~2880-2890 cm^{-1} and ~ 1550cm^{-1} were due to C-H stretching and bending vibrations of alkanes that could come from the alkane chain of ethanol or ethoxide [197]. The band around ~ 1080 cm^{-1} was from CO bonded stretching vibration that could be promoted by ethanol or it is reported the shift of CO peak to higher wavenumber in the case of alkoxides compared to the respective alcohol [196, 197]. Finally, we observed bands at 1630 and 1355 cm^{-1} corresponding to symmetric and asymmetric stretching of (OCO) group. In Table 2.10 is reported the common bands of the different coordination modes of carbonate and carboxylate-based compounds [115, 194, 198].

Table 2.10 Comparison of the asymmetric and symmetric stretching bands of (OCO) group presented by carbonate and carboxylate moieties from literature references.

	$\nu_{st\ as\ (OCO)}$ (cm^{-1})	$\nu_{st\ as\ (OCO)}$ (cm^{-1})
Carbonate monodentate	1446-1590	1368-1395
Carbonate bidentate	1553-1644	1243-1355
Carboxylate monodentate	1600-1725	1267-1380
Carboxylate bidentate	1580	1410-1440

The experimental peak positions of (OCO) groups observed of as-synthesised NPs were compatible with the range of reported vibration modes of carbonate bidentate and carboxylate monodentate. Considering the IR spectra obtained (Figure 2.25A), we suggest that the surface could be capped with water, ethoxide anion or solvated from the metallic precursor, carbonate anion from the no-inert atmosphere during the NP synthesis or acetate anion as carboxylate from the possible oxidation of ethanol or ethoxide precursor or a mixture of these possible stabilisers (Figure 2.25B).

Complementary, we decided to perform EGA-MS analysis of $BaNb_2O_6$ NPs, a high-sensibility technique to detect all the volatiles released from the NP surface during the heating process. From the molecules that we proposed that could be surface stabilisers, we expected to see the main fragmentation patterns by the detection of fragments shown in Scheme 2.1. In the case of ethoxide, the decomposition was observed at ~ 300 °C and the main gaseous products observed were ethylene (M/Z = 28 27 and 26), methane (M/Z = 16, 15, 14 and 13) and in minor quantities, propane (M/Z = 29,28,27,44,43 and 39), ethanol (M/Z = 31 and 45) and water (M/Z = 17 and 18) [199]. We expected to observe acetate fragmentation in acetone form (M/Z = 43 and 58) due to the conditions of the experiments following the Scheme 2.1 [200, 201]. In addition, we expected the loss of CO_2 from the carbonate decomposition [202].

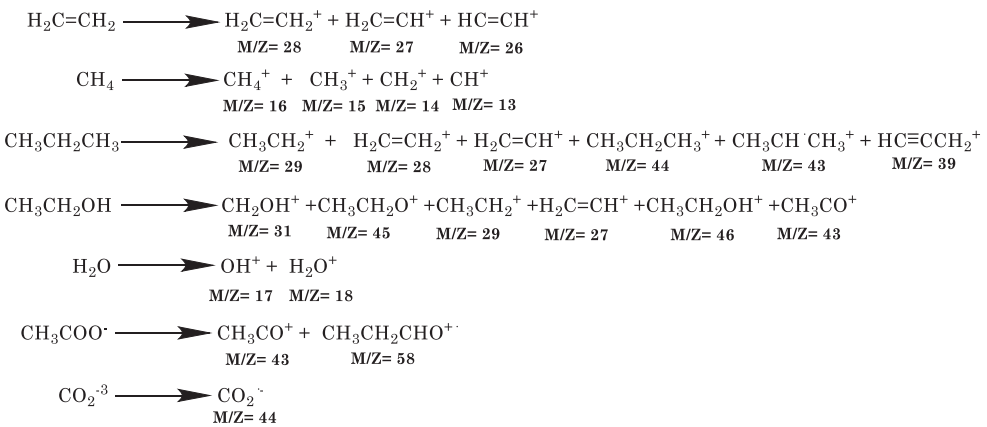

Scheme 2.1 Expected mass of theoretical fragmentation produced by ethylene, methane, propane, ethanol, water and acetate and carbonate anion.

The EGA-MS curves evolution of the main peaks is shown in Figure 2.26A. Peaks of M/Z= 31,45,17 and 18 at ~160 °C can be attributed arising from ethanol

and H_2O respectively (Figure 2.26B and C). The peak curves from ethanol and H_2O showed a different evolution indicating that they did not come from the release of the same process and had different origins. As we used chamber vacuum pressure of 10^{-6} mbar for EGA-MS, the boiling point of free water is around -70 °C suggesting that water could be absorbed on NP surface [200]. When the temperature increases around 320-340 °C the peaks of M/Z= 29, 27 and 43 were detected and could be assigned as secondary fragments of ethanol. Still, these peaks increased when the main peaks of ethanol M/Z= 31 and 45 were decreasing suggesting that these peaks correspond to the fragmentation of other molecules. The peaks M/Z = 28,27 and 26 were the main fragments of ethylene, M/Z= 16,15,14 and 13 of methane and M/Z= 29,28,27,44,43 and 39 of propane detected at 320-340 °C, altogether coming from the decomposition of ethoxide (Figure 2.26D). Moreover, in spite of the M/Z= 43 peak being a secondary fragment of propane, acetate specie assignation cannot be discarded due to the M/Z= 58 fragment was also observed at 330-340 °C. Therefore, the M/Z= 43 and 58 fragments were assigned to come from acetate species (Figure 2.26E) despite the intensity of peaks being lower than for fragments coming from ethoxide anion species. Finally, CO_2 can be also detected by the presence of M/Z = 44 peak around 340 °C coming from carbonate or also could be a subproduct of the decomposition of acetate anion or ethoxide as followed the same temperature evolution as their corresponding main peaks of M/Z= 43 and M/Z= 28 fragments respectively (Figure 2.26E).

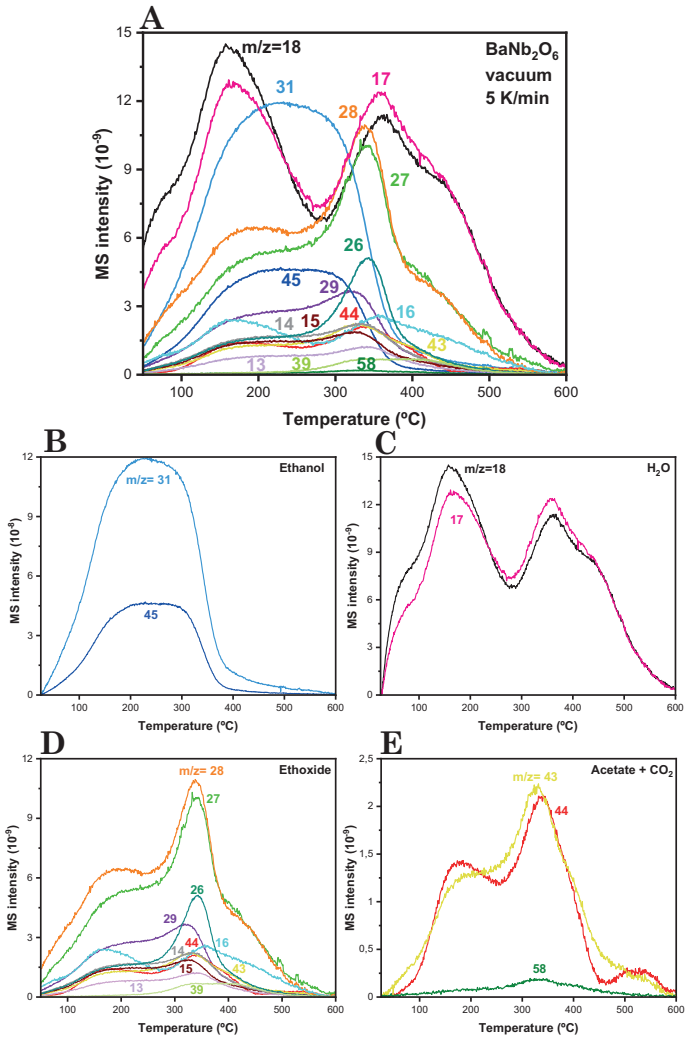

Figure 2.26 EGA-MS analysis of $BaNb_2O_6$ NPs with detected M/Z peaks for ethylene, methane, propane, ethanol, water and acetate and carbonate anion release.

In summary, we postulated that the presence of adsorbed water detected at 100 °C, acetate at 330 °C and ethoxide at 360 °C as molecules or ions capped onto the NP surface. The carbonate anion presence cannot be discarded but requires confirmation by other techniques as IR and EGA-MS were not decisive in a clear differentiation with acetate species.

2.3.2.3.2 Post-surface functionalisation by carboxylic-based ligand exchanges

From surfactant-free H2S2 process, we obtained NP aggregates with a lack of redispersitibility as it was also reported in other cases [130, 135]. Ligand exchange methodologies are employed to promote stable colloidal solutions with a desired stabiliser even if aggregated NPs are obtained after the synthetic process [127, 149].

As we described in the introduction, the covalent-bond classification model has been postulated as a good approximation to explain NC-ligand binding [145–147]. In addition, can be used to describe the different possible ligand exchanges on NP surfaces. In our case, we have suggested in the previous section the presence of adsorbed water (L-type ligand) and ethoxide, acetate and carbonate anions (X and L-type ligands) (Figure 2.27A). It is reported that the exchange of X-type ligands, which were the main postulated stabilisers in our system, became easier and thermodynamically favourable in polar solvents which can solvate released charged species allowing the exchange by electrostatic interactions. This implies, that X-type ligands would be favoured by the exchange using analogous ligands [115, 145]. For these reasons, we decided to perform different ligand exchanges using carboxylic-based ligands well-reported and successfully post-surface modification [127, 143, 145, 149] for metal oxide NCs. Specifically, we employed Dopamine hydrochloride and 3,4-dihydroxyhydrocinn-amic acid and L-lysine hydrochloride previously used in the research group for metal fluoride NCs ligand exchanges [115] with the corresponding equivalents of tetramethylammonium hydroxide (TMAOH) to obtain the carboxylated conjugated base by deprotonation. Finally, we tried also to post-functionalise the surface by 2-[2-(2-Methoxyethoxy)ethoxy]acetic acid (MEEAA) as compatibility and good colloidal stability of MEEAA-stabilised-$BaMO_3$ NCs in low-fluorine YBCO precursor solution has been demonstrated [86].The possible binding moieties of these molecules to the metal NP surface atom were schematically shown in Figure 2.27B-E.

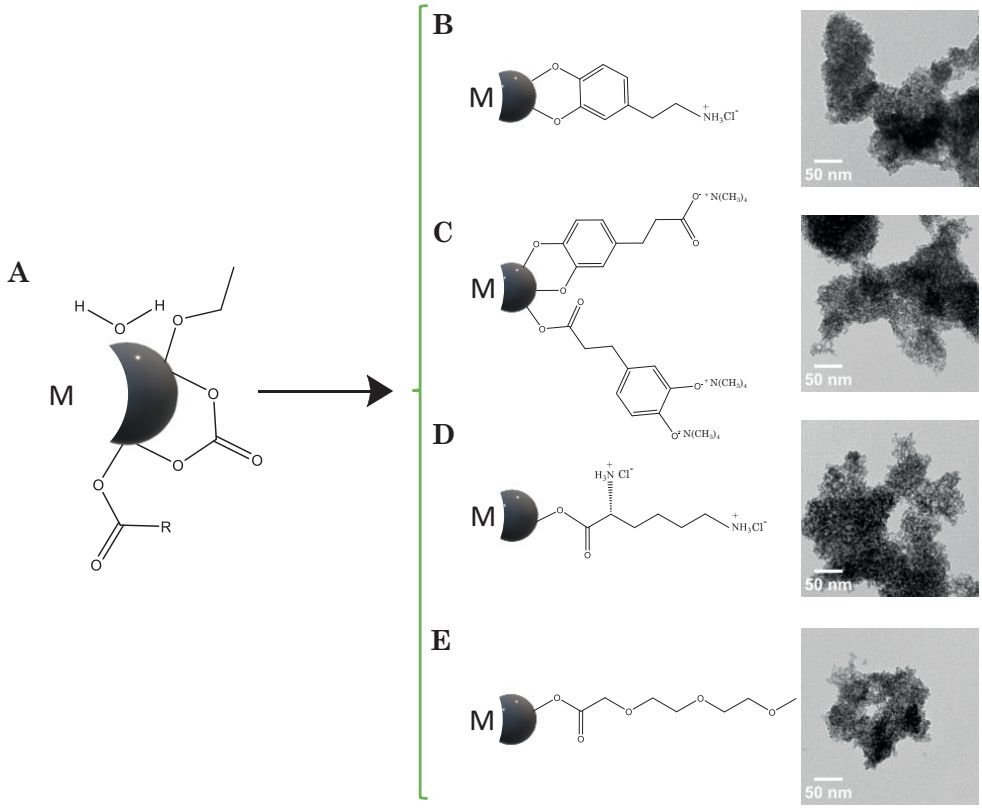

Figure 2.27 (A) Schematic representation of the surface chemistry of BaM_2O_6 NPs and surface with the corresponding TEM obtained after ligand exchanges by (B) Dopamine hydrochloride (C) 3,4-Dihydroxyhydrocinnamic acid (D) L-lysine hydrochloride and (E) MEEAA.

The general procedure to perform the ligand exchange of Dopamine hydrochloride and 3,4-Dihydroxyhydrocinnamic acid and L-lysine hydrochloride in water was based on [115] reference. The procedure consists of the previous precipitation by centrifugation of 1 mL of washed $BaNb_2O_6$ NPs (~ 34mM) in ethanol. Then, the solid phase was redispersed in 1 mL of Milli-Q water followed by the additon of 20 mg of the desired ligand and the corresponding equivalent of TMAOH for (2,3 and 1 equivalents respectively). Finally, the solution was sonicated for 20 min to promote exchange. In the case of the MEEAA ligand, we followed the procedures according to the references [203–205]. The ligand exchange was based on the addition of 320 μL of MEEAA ligand onto 3 mL of washed $BaNb_2O_6$ NPs (~ 23mM) and after that, the solution was subjected to ultrasound treatment for 30 min.

After the treatment of ligand exchange solutions in the ultrasonic bath we expected clear NP dispersion from the initial milky solutions [115, 149] (aggregated-$BaNb_2O_6$ NPs) if the resulting exchange performed was successfully in surface functionalisation and NP disaggregation. In the resulting solutions treated with L-lysine and MEEAA no colour visual changes have been observed. Still, in the case of Dopamine and 3,4-Dihydroxyhydrocinnamic acid, the solutions became coloured yellow-brown and red-brown respectively. The red-brown colour was associated with the deprotonated form of 3,4-Dihydroxyhydrocinnamic acid attached to the surface of LaF_3 NCs [115].

We characterised the different ligand exchange solutions by TEM before the cleaning step to eliminate ligand excess. The corresponding TEM images were shown in Figure 2.27 where we observe aggregates of NPs which means that the ligand exchange procedures were not complete to avoid aggregation or that directly we can not functionalised the surface by these new ligands. In our case, we performed ligand exchanges from agglomerates of NPs, which is already a thermodynamically stable system and the exchange promoting a homogenous and non-aggregated system, where surface energy is higher, will be less favourable and difficult than in the case of starting from a homogeneous colloidal dispersion. In a non-aggregated system, with exposed and thermodynamically unstable surfaces which are highly reactive surfaces, the exchanges are expected to be more favourably and easier.

2.3.2.3.3 Post-surface functionalisation by ligand stripping

After the results of the previous section, we decided to use a ligand exchange strategy which implies a chemical reaction during the exchange process. As we postulated water, ethoxide, acetate and/or carbonate could be attached to the surface of $BaNb_2O_6$ NPs (section 2.3.2.3.1) we decided to use an alkylating agent as triethyloxonium tetrafluoroborate (Et_3BF_4) [148] or nitrosonium tetrafluoroborate ($NOBF_4$) [151] commonly applied to strip surface native ligands with an NC-carboxylate interaction by electrophilic alkylation from cation attack that produces the ligand cleavaged. The resulting positive surface from stripping is electrostatically stabilised by BF_4^- anions and adsorbed DMF in polar solvents. The suggested stripping reaction effect in our system is represented in Scheme 2.2.

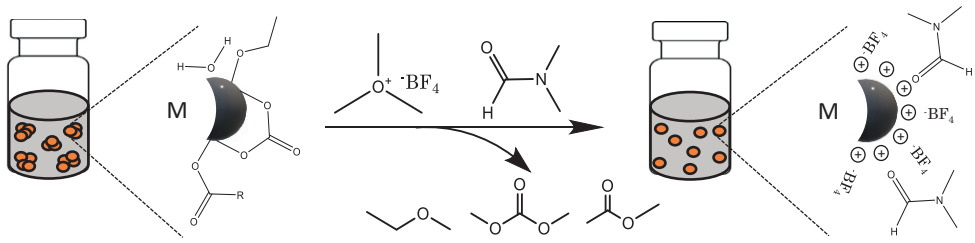

Scheme 2.2 Ligand stripping of aggregated-BaM_2O_6 NPs with trimethyloxonium tetrafluoroborate (Me_3BF_4).

The ligand stripping procedure followed and applied in our system (section 2.2.1.2) was based on L.Rosen [148] method using in this case the widely employed trimethyloxonium tetrafluoroborate (Me_3OBF_4) as alkylating agent.

The resulting solution after ligand stripping of aggregated-$BaNb_2O_6$ and $BaTa_2O_6$ colloidal solutions were characterised by TEM. The TEM images (Figure 2.28A and B) show the final disaggregation of the synthesised BaM_2O_6 NPs. We achieved the formation of non-aggregated, small-sized NPs (3.8 ± 0.8 nm for $BaNb_2O_6$ and 3.2 ± 0.8 nm $BaTa_2O_6$ respectively) with spherical shape and narrow-size distribution.

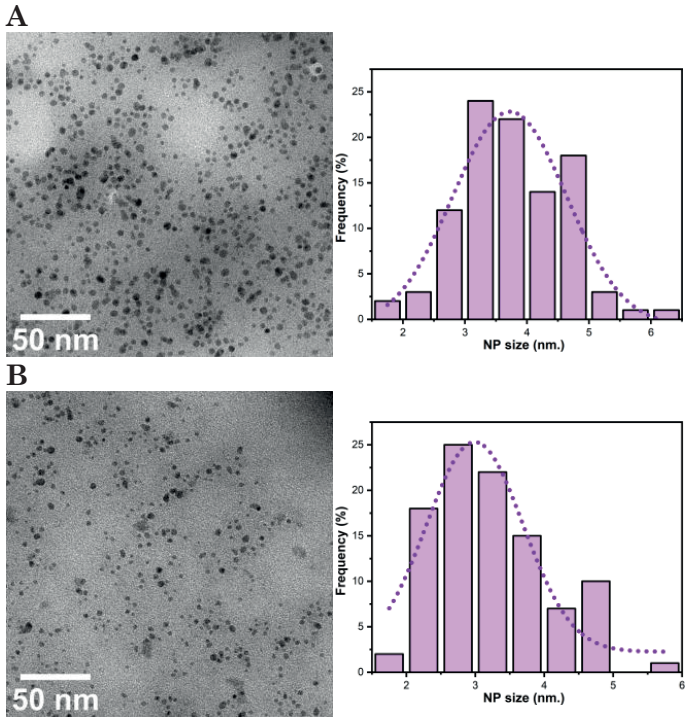

Figure 2.28 TEM images and the corresponding histogram from ligand stripping of (A) $BaNb_2O_6$ and (B) $BaTa_2O_6$ NPs.

Concerning these results, by ligand stripping methodology, we were able finally to disaggregate NPs from the surfactant-free solvothermal treatment and functionalised the surface to achieve homogeneous BaM_2O_6 NP dispersions.

Finally, the crystallinity of BaM_2O_6-stripped NPs was evaluated through powder XRD as depicted in Figure 2.29. A comparison was made between the XRD patterns of the BaM_2O_6 synthesized via the solvothermal method and those obtained after ligand stripping. It was observed that the NP disaggregation resulting from the stripping reaction led also to broad XRD patterns, which resembled the effect observed after thermal treatment (solvothermal process). The broad XRD patterns observed can be attributed to either the presence of amorphous NPs (no improvement of crystallinity after stripping treatment), as confirmed by HRTEM analysis in the case of the as-synthesized NPs after solvothermal treatment, or the effect of small-sized NPs (approximately 3-4 nm), which produces broader peak widths. These parameters are interconnected in the Sherrer equation [153, 154].

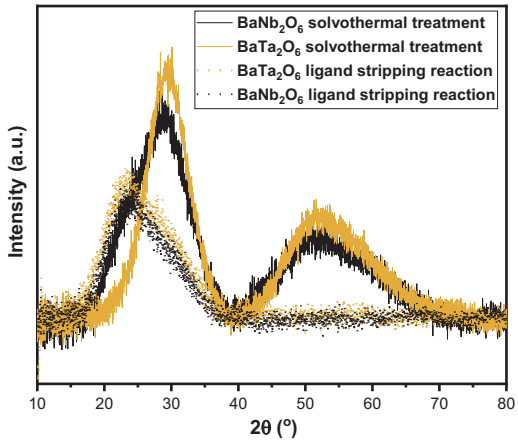

Figure 2.29 Powder XRDs of $BaNb_2O_6$ NPs after solvothermal treatment (black line) and after ligand stripping reaction (black dashed line) and powder XRDs of $BaTa_2O_6$ NPs after solvothermal treatment (orange line) ligand stripping reaction (black dashed line).

⁕ Application of stripped-$BaNb_2O_6$ NPs in YBCO nanocomposite films

The small-sized, homogenous distribution and crystallisation temperatures of 700-900 °C demonstrated in the previous sections provide stripped-BaM_2O_6 NPs suitable to be compatible with YBCO nanocomposite films. Preliminary results of the application of stripped-$BaNb_2O_6$ NP solutions for YBCO nanocomposite film formation, through the low-flour TFA method, are shown in section B.1 in Appendix B.

The results obtained demonstrated that these types of NPs are compatible with the growth of YBCO nanocomposite films, exhibiting NP composition stability and epitaxial YBCO growth at a growth temperature of 820 °C. By optimising processing conditions to reach strong epitaxial YBCO growth, we anticipate an improvement in the texture quality of the films. Furthermore, further efforts on alternative post-surface functionalisation strategies excluding the presence of flour will enable BaM_2O_6 NPs also be suitable for the TLAG process via fluorine-free YBCO colloidal precursor solutions.

2.4 Conclusions

In this chapter, we investigated the two-step synthetic process that combines the advantages of the aqueous sol-gel route and the solvothermal method,

which we have denoted as hybrid hydrolytic solvothermal synthetic (H2S2) process, for $BaMO_3$ (M=Zr and Hf) and BaM_2O_6 (M=Nb and Ta) NPs. The behaviour of the two types of binary metal oxide NPs ($BaMO_3$ and BaM_2O_6 were investigated postulating the main parameters that govern the size, homogeneity and stability of colloidal solutions.

In the case of $BaMO_3$ NCs, the optimisation of the cleaning step together with the extra-centrifugation step at the end of the process was helpful in obtaining monodisperse solutions at high NP concentrations of ≥ 100 mM without impurities such as the observed $BaCO_3$ solid phase.

Despite water is the key factor that governs the NCs formation controlling the final NC size, we established that the use of ammonia in the precursor solution has a significant role in the hydrolysis reaction controlling the homogeneity and reproducibility. We proposed that ammonia has an influence on the mechanism slowing down the rate of the reaction through the formation of an uncharacterised intermediate complex that ends in better control of the final behaviour of NC solutions than using water. In addition, it was discarded the presence of ammonia between the ligands anchored onto the NC surface and its influences on crystallinity. We obtained undistinguished results between ammonia and water in terms of the IR and XRD patterns respectively. Finally, the use of controlled amounts of ammonia in the precursor solution produces crystalline and homogeneous $BaMO_3$ NC dispersions of 5, 6-7 and 10 nm with high concentrations (≥ 100 mM).

In the line of investigation and control of the final behaviour of colloidal solutions, it was observed that the type of polyol used in the precursor has an effect on the final size and shape of NCs as the stabiliser is also involved in the NC formation mechanism. The compatibility of PEG stabiliser with $BaMO_3$ NCs was demonstrated achieving small-sized, homogenously distributed and highly crystalline spherical NCs. The NC size could be tuned also by the PEG quantity in the precursor solution. These studies reveal that we can control the NC formation either by tunning ammonia or polyol quantity which is important to obtain final colloidal solutions with desired features to be compatible with different systems

The temperature of solvothermal treatment is another critical synthetic

parameter influencing in this case crystallinity. 150 °C was found to be the minimum solvothermal temperature to induce complete crystallisation of $BaMO_3$ NCs.

The stability of the final $BaMO_3$ NC dispersions is critical for their further application in solution and we also evaluated through DLS measurements of hydrodynamic size and Z-potential values. Long-time stability of 2 years of TEG-stabilised $BaMO_3$ NC solutions redispersed in ethanol with either 5 or 10 nm NC size was demonstrated. In addition, the compatibility and stability of other solvents with different polarities such as Methanol and n-Butanol also displayed opening the versatility and compatibility with other types of systems. Moreover, PEG-stabilised $BaMO_3$ NC solutions also show a high stability of at least 180 days.

Finally, we proved the compatibility of H2S2 method with MW thermal activation obtaining consistent results concerning NC size, crystallinity, homogeneity and solution stability with those obtained from the autoclave thermal activation. Via MW method, we reduced the solvothermal treatment time from 4h to 45 min with respect to the autoclave system.

In the second part of the chapter, BaM_2O_6 NP solutions were synthesised and characterised, for the first time, using the H2S2 method without surfactant stabilisation and a post-surface functionalisation based on ligand stripping. We achieved small-sized (< 5 nm) and non-aggregated NPs in the solution and despite the lack of crystallinity we observed an improvement of the resulting material state from the previously reported gels, of these types of NPs, to a colloidal solution.

We found that these types of NPs require higher temperatures and longer reaction times than $BaMO_3$ NC to observe the complete reaction of metal precursors after solvothermal treatment. We chose 220 °C during 24h, as the optimal conditions of the process to ensure a complete reaction and as increasing temperature and time did not release an effect on the size, aggregation, or enhancement of crystallinity of NPs. These solvothermal conditions optimised are much softer than found conditions in literature. Annealing treatments were performed to induce crystallisation in the solid form where we identified that $BaNb_2O_6$ NPs crystallise at 600 °C in an orthorhombic phase and $BaTa_2O_6$ NPs at 900 °C in hexagonal phase.

Although we are not able to stabilize and avoid aggregation during solvothermal treatment, we observe a better definition of the NPs morphology using less acidic conditions in the precursor solution such as Ethanol and Benzyl alcohol as solvents that might be related to the hydrolysis kinetics which is is pH dependent. For this reason, we chose ethanol as the optimal solvent for the precursor solution.

By using IR and EGA-MS techniques, we unravelled the NP surface composition focusing on understanding the better ligand exchange for the specific surface ions/molecules of the aggregated system. From the results obtained, we postulated that the surface chemistry could be composed of a mixture of absorbed water, acetate, carbonate and ethoxide ions. Despite the ligand exchange of X-type being postulated to be favourable by analogous ligands, the post-surface functionalisation by different carboxylic-based ligands (Dopamine, 3,4-Dihydroxyhydrocinnamic acid, L-lysine and MEEA) was not successful. In a thermodynamically stable system as an aggregated-NP solution, the ligand exchange is expected to be less favourable and difficult than in the case of starting from a non-aggregated and homogeneous colloidal dispersion. For this reason, we decided to use a harder desegregation strategy as ligand stripping with Me_3OBF_4 which finally produced the disaggregation of these NPs by removing surface ligands through alkylation and stabilizing the resulting surface by BF_4^- anions and DMF.

Preliminary results of the application of stripped-$BaNb_2O_6$ NPs for YBCO nanocomposite film formation show that these types of NPs are compatible with YBCO growth. We reached epitaxial YBCO nucleation where NPs crystallise and are also stable at the growth temperature of 820 °C.

3

YBCO nanocomposite precursor solution and films

3.1 Introduction

Previous studies in the research group have demonstrated that employing environmentally friendly non-fluorinated precursor solutions using acetate-based precursor salts in a kinetically driven TLAG-CSD method facilitates the formation of YBCO layers at growth rates surpassing 100 nm/s.The driving force of this innovative process is the Yttrium supersaturation in the transient liquid, which strongly depends on the liquid properties and characteristics. These can be controlled and easily modified by designing the characteristics of the precursor solution to yield the desired and uniform nanocrystalline precursor films, from which the liquid phase originates. Therefore, for the liquid-solid mechanism of the TLAG-CSD process, YBCO precursor solution and the characteristics of the YBCO precursor solution and the resulting nanocrystalline precursor films are fundamental for the final high-performance epitaxial films [42, 44, 46]. Although the preceding acetate-based fluorine-free solutions have been fundamental in advancing our comprehension of the TLAG-CSD process, their applicability is limited to the thick film prerequisites of CC manufacturing [10, 33, 55].

In this chapter, we describe the optimisation performed to design a novel YBCO nanocomposite precursor solution. This new solution is based on the utilisation of YBCO pure propionate-precursor salts and amine additive, to prepare thick YBCO nanocomposite films. The investigation involved the stabilisation of $BaZrO_3$ (BZO) and $BaHfO_3$ (BHO) NC solutions to ensure compatibility with YBCO precursor solutions. Our primary focus was on achieving enduring solution stabilities and physicochemical solution characteristics that yield homogenous, nanocrystalline, thick precursor films with the desired composition and microstructure. The potential capabilities of the developed YBCO nanocomposite precursor solutions for homogeneous YBCO nucleation and the ultrafast epitaxial growth of high-performance nanocomposite films were revealed through solution characterisation and analysis of structural composition and microstructure characteristics.

3.2 Experimental

3.2.1 YBCO nanocomposite precursor solution preparation

The preparation of YBCO nanocomposite precursor solutions was consistent regardless of the desired Y/Ba/Cu stoichiometry and NC amount (6-24 % mol) in the solution. The different YBCO stoichiometries of the solutions were denoted by considering the Ba:Cu molar ratio of the transient liquid formed during the TLAG process, as shown in Table 3.1. The corresponding optimal monoethanolamine (MEA) content for each composition and a total solution volume of 5 mL are also presented in Table 3.1.

Table 3.1 Summary of YBCO stoichiometries used in solutions and the corresponding Cu:MEA molar ratio and %v/v of MEA optimised for each composition.

YBCO stoichiometry	Composition	Cu:MEA molar ratio	$\%_{v/v}$ MEA (for 1.5M, volume 5 mL)
$Y_1Ba_2Cu_3$	2-3	1:0.8	3.9
$Y_1Ba_2Cu_4$	3-6	1:0.66	3.4
$Y_1Ba_2Cu_{4.66}$	3-7	1:0.61	3.4

The total concentration of metal salts in YBCO nanocomposite precursor solutions for spin-coating deposition was 1.5 M, regardless of the solution composition and NC amount. The volume of NC solution (mL) corresponding to the various %mol tested was calculated by applying the desired %mol to the total moles of Yttrium, which is the limiting reagent and is specific for each composition, the total sum of metal concentration, and total solution volume. Additionally, Table 3.2 presents the optimised %v/v ratios of MeOH:EtOH:Hprop used for each NC amount. The stability of these solutions, dependent on the %v/v ratio of the solvent mixture used, will be discussed in the following section 3.3.1.1.

Table 3.2 Summary of the MeOH:EtOH:HPprop %v/v ratio optimised for each NC amount (6-24 %mol) and the corresponding solution stability.

NC amount (% mol)	MeOH:EtOH:Hprop $\%_{v/v}$ ratio	Solution stability
6	25:25:50	> 3 months
12	25:25:50	> 3 months
18	25:25:50, 20:30:50	> 3 months
24	15:35:50, 20:30:50	1 to 3 months

The general procedure is described for the preparation of 5 mL of precursor solution with 1.5 M, 3-7 composition, and 12% mol BZO or BHO NCs with a %v/v ratio of 25:25:50 MeOH:EtOH:Hprop but it can be followed for the different compositions and NC amounts explained above (Table 3.1 and 3.2).

1. In a round bottom flask, 0.1720 g of MEA corresponding to 3.4% v/v for 3-7 composition was added.

2. Followed by the addition of 0.8mL (12 %mol) of NC solution with 142 mM of NC concentration to the flask at room temperature under an inert atmosphere (Ar) and stirred for 5 min. Then, the 0.2 mL of EtOH to reach 25 %v/v of the total final volume (5 mL).

3. Then, 1 mL (25 %v/v) of methanol (MeOH) and 2 mL (50 %v/v) of propionic acid (Hprop) were added to the mixture under Ar atmosphere and stirred. After the addition of the Hprop, the solution exhibited a milky appearance (Figure 3.1A). The solution was stirred overnight until a clear solution was obtained (Figure 3.1B).

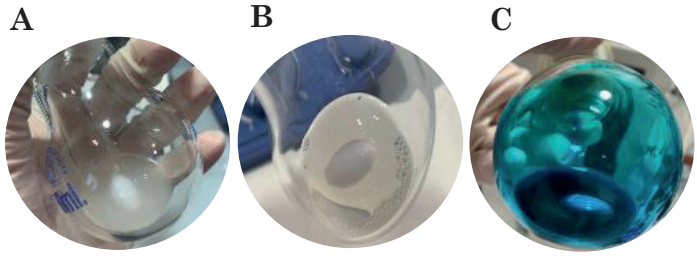

Figure 3.1 Images of YBCO nanocomposite precursor solution at various steps of preparation: (A) After Hprop addition to the MEA, NC solution, EtOH and MeOH mixture, resulting in a milky appearance (B) Clear solution obtained after leaving the mixture (A) overnight stirring and (C) resulting blue-coloured solution after the addition and dissolution of the metal propionate-based precursor salts.

4. After overnight stirring, $Ba(CH_3CH_2COO)_2$ and $Cu(CH_3CH_2COO)_2$ were added to the clear solution under Ar flow and stirring. Then, the Ar was turned off, and the mixture was heated at 35-40 °C under vigorous stirring until complete dissolution of the salts (1-2h) was observed, depending on the %v/v EtOH in the solution. Subsequently, $Y(CH_3CH_2COO)_3$ was added under Ar flow. Then the argon was turned off, and complete dissolution of all the precursors was achieved under stirring at 35–40 °C for approximately 30 minutes, resulting in an intense blue-coloured solution (Figure 3.1C).

5. After completely dissolving the salts, the solution was cooled to room temperature while stirring and then transferred to a volumetric flask. The volume was adjusted with the same solvent ratio (expressed as %v/v) used initially.

6. Finally, the final solution is filtered with a specific filter designed for viscous solutions and transferred to a vial, sealed under an Ar atmosphere, and stored in a desiccator.

Characterisation

The behaviour of NCs in YBCO precursor solution was evaluated using XRD and TEM techniques. The crystallinity of NCs in the solution was analysed through XRD measurements in a capillary tube. The size and distribution of NCs were examined by TEM. Moreover, rheological properties such as viscosity and contact angle of YBCO nanocomposite precursor solutions were measured. The water content in the solutions was determined using the Karl-Fischer titration method [206, 207]. Finally, the decomposition process of the nanocomposite precursor solution was investigated through TGA.

3.2.2 YBCO nanocomposite precursor films formation: deposition and pyrolysis procedures

Prepared YBCO nanocomposite precursor solutions were deposited via the spin-coating method (section 1.1.3.3.1) in an ISO7 grade clean room (<30% humidity). The spin-coating process was conducted under controlled conditions (<10% humidity) using a nitrogen atmosphere, employing a spinning rate of

6000 rpm for 2 minutes on single crystals of 5x5x0.5 mm in size of (001) $SrTiO_3$ (STO) or $LaMnO_3$ (LMO) substrates [33, 55].

Before deposition, the substrates were subjected to an annealing process (Figure 3.2) at 900 °C for 5 h in dried oxygen flow of 0.5 L/min to achieve atomically flat-terraced surfaces [10, 33, 55]. Subsequently, substrates were cleaned using acetone and methanol to eliminate possible impurities.

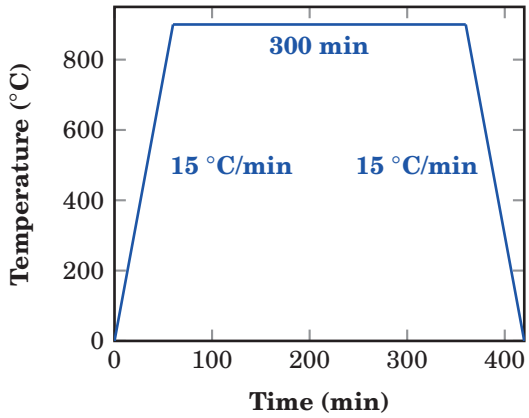

Figure 3.2 Substrate heat treatment profile used in TLAG films.

The YBCO nanocomposite precursor films were obtained by spin-coating 15 μL of the YBCO nanocomposite precursor solution using a microsyringe onto the polished substrates, under the spinning conditions mentioned above. After deposition, the sample was placed on a hot plate for 5 minutes at 60 °C to facilitate solvent evaporation.

Immediately after 5 minutes of drying, the sample was transferred to a tubular furnace to undergo pyrolysis heat treatment before the final YBCO crystallisation to obtain nanocrystalline nanocomposite precursor films. The pyrolysis ovens were also located inside the ISO7 grade clean room under controlled ambient conditions. The pyrolysis process was performed by heating at a rate of 3 °C/min to 240 °C, then the heating ramp was increased to 5 °C/min until reaching 500 °C, followed by a 5-minute dwell. Finally, the sample was cooled to room temperature at a rate of 15 °C/min. The thermal profile is shown in Figure 3.3. Additionally, the entire process was performed with an oxygen flow rate of 0.12 L/min. At approximately 110 °C, the flow was changed to humid oxygen with a water vapour partial pressure of 23 mbar. The pyrolysis profile and conditions were optimised in previous studies [33, 55], and more details about the

procedure are explained in section 1.1.3.3.2.

Additionally, to increase the thickness of the nanocomposite precursor films, a multi-deposition process was employed. This entails successive deposition and pyrolysis steps for each layer until the desired thickness is achieved. Throughout this thesis, we found it necessary to modify the thickness of the pristine layers used in multilayered nanocomposite precursor films derived from 1.5 M YBCO pristine precursor solutions [46]. To reduce the thickness of the pristine precursor layer, we diluted a 1.5 M YBCO pristine precursor solution to a lower concentration, achieving the desired thickness.

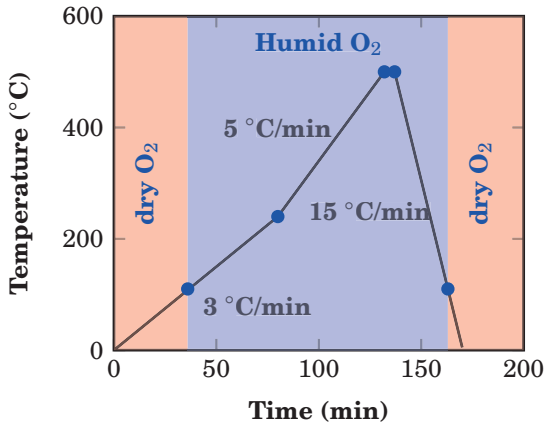

Figure 3.3 Pyrolysis heat treatment profile used for TLAG films.

Characterisation

The homogeneity of the nanocomposite precursor films was analysed using optical microscopy (OM). The structure and phase composition of the films were characterised through 2D X-ray diffraction measurements with a General Area Detector Diffraction System (GADDS). For a high signal of randomly oriented phases such as YBCO precursor phases and NCs, high-resolution (HR) XRD measurements in grazing-incidence (GI) geometry were performed. Additionally, to enhance the detection of NCs, GI measurements focusing on the region (29-32° $\theta - 2\theta$) of the most intense peak (110) of BZO and BHO phases were conducted for 1 hour.

Finally, the microstructure of nanocomposite precursor films was also analysed by the TEM technique to evaluate the thickness, distribution, and sizes of

NCs and the resulting nanocrystalline YBCO precursor phases. The TEM characterisation was performed by Dr. K. Gupta.

3.3 Results and discussion

3.3.1 YBCO nanocomposite precursor solutions

3.3.1.1 Stabilisation of NC solutions in YBCO precursor solutions

The insights gained from prior studies on acetate-based fluorine-free solutions have been crucial for understanding the TLAG-CSD process. Additionally, the TLAG-CSD process has demonstrated its potential by achieving an ultrafast growth rate of 100 nm/s, compatibility with nanocomposites, and high critical current densities ranging from 3-5 MA/cm^2 for a film thickness of 100 nm [10, 33, 42, 55]. Further advancements of the TLAG process to adapt it for coated conductor technology require thicker films while maintaining the process's robustness. However, limitations in the solubility of YBCO precursor salts in acetate-based fluorine-free solutions have been observed, restricting the total metal salt concentrations to 1 M and resulting in a maximum thickness of 100 nm [33, 55].

The thickness of the film is primarily influenced by the rheological properties of the YBCO precursor solutions and the deposition method [33, 42, 55]. Subsequent efforts initially focused on designing a YBCO fluorine-free precursor solution capable of reaching final total salt concentrations above 1 M while being compatible with the TLAG-CSD process for forming thick, epitaxial, and high-performance YBCO superconducting films. To this end, a novel class of metal-organic precursor solution based on fluorine-free pure metal-propionate salts was proposed. The development of the propionate-based YBCO precursor solution aimed at low cost-effectiveness, robustness, reproducibility, scalability, and compatibility with the TLAG-CSD process. The demonstrated and reported results for the pristine YBCO precursor solution case [46] served as a starting point for the optimization process of nanocomposite YBCO precursor solutions.

The propionate-based precursor solution was developed using yttrium, barium, and copper propionates, all synthesised in-house. This strategy was chosen to avoid obtaining mixtures of acetate-propionate salts [59], a common issue with acetate-based solutions. The careful selection of pure propionate salts aims to ensure reproducibility in the decomposition paths of precursor salts, thereby promoting the formation of the desired YBCO precursor phases in the films. Although homogeneous films were successfully obtained using a mixture of Hprop and MeOH (50:50) with metal-propionate salts, the limited solubility of $Cu(CH_3CH_2COO)_2$ imposed a constraint, permitting a maximum concentration of 1 M and resulting in a precursor film thickness of 100 nm. To overcome this limitation, Monoethanolamine (MEA) was introduced as an additive to the solutions. MEA has shown potential due to its chemical affinity for copper, facilitated by its amine group, which enhances copper-propionate salt solubility by coordination (Cu-N complex). Additionally, MEA's short carbon chain enables effective CO_2 diffusion during the pyrolysis process, a critical aspect in the formation of orthorhombic $BaCO_3$. The presence of monoclinic $BaCO_3$ phase was found to delay the $BaCO_3$ elimination reaction, the limiting step in YBCO crystallisation, as reported in previous studies [33, 59, 67]. MEA ultimately decomposes during the pyrolysis treatment under the specified conditions.

Furthermore, MEA was demonstrated to play a significant role in the characteristics of both YBCO precursor solutions and films. Firstly, MEA improved the solubility of copper propionate salt, enabling higher total salt concentrations of up to 1.5 M. Additionally, it contributed to an increase in solution viscosity, which directly correlates with an increase in final film thickness. The coordination of amine to the copper-centre also ensured the long-term stability of the solutions. Importantly, MEA's contribution to the metal-organic framework resulted in smoother organic decomposition during the pyrolysis step, which helped avoid crack formation, especially in thicker films. This enhancement in precursor film quality was demonstrated through the achievement of chemical and microstructural nanoscale homogeneity in YBCO precursor films, with thicknesses reaching up to 400 nm for a single layer. The precursor films exhibited smooth surfaces and low porosity, promoting the formation of primarily the orthorhombic $BaCO_3$ phase, which decomposes more rapidly than its monoclinic counterpart [64]. Additionally, the homogeneous distribution and nanometric sizes of $BaCO_3$, Y_2O_3, and CuO contributed to the ultrafast epitaxial growth of

YBCO and the high performance of TLAG films.

A further advancement in the developed YBCO precursor solutions was demonstrating their compatibility with NC solutions for forming thick YBCO nanocomposite films. For this purpose, we optimised the propionate-based precursor solution to ensure compatibility with colloidal solutions and meet the aforementioned requirements, enhancing the TLAG-CSD process for coated conductors (CCs).

The preparation of YBCO colloidal precursor solutions with acetate salts involved a step where the initial total salt concentration was diluted to 1 M. This occurred during the mixing of the NC solution with the previously prepared YBCO pristine precursor solution (as detailed in section 1.1.3.3.1) before deposition. Unfortunately, this dilution step limited the concentration to lower values, resulting in thinner films. To overcome this limitation and avoid dilution, we introduced a new strategy to stabilise the NC solutions within the YBCO precursor solutions. This strategy involved using the NC solution as one of the solvents used for dissolving the propionate salts. A schematic representation of this approach is depicted in Figure 3.4.

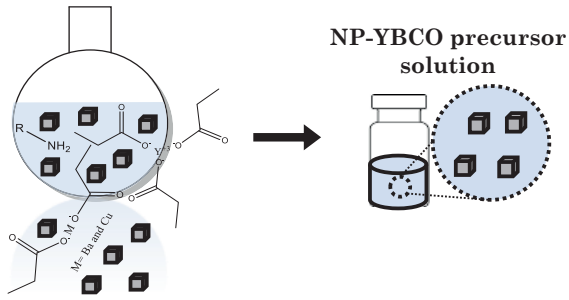

Figure 3.4 Scheme of propionate-based nanocomposite YBCO precursor solution.

In this section, we will focus on solutions with a 1.5M total salt concentration, a 3-7 composition, and 12% mol of 5 nm-sized BZO NCs, unless otherwise specified. Previous investigations have demonstrated that this specific YBCO stoichiometry promotes the epitaxial growth of YBCO in the TLAG process [10, 42, 55].

The developed pristine propionate-based solutions were prepared using a 50:50 mixture of Hprop and MeOH. This solvent ratio was selected based on prior studies with acetate-based precursor solutions, which indicated that the inclusion of MeOH increases the final film precursor thickness. However, a

higher %v/v of MeOH led to inhomogeneity and reproducibility issues in pyrolysed films [33, 55]. Consequently, we initiated the optimisation with NC solutions that were redispersed in MeOH following their synthesis (section 2.2.1.1). This method was initially adopted to preserve the optimised 50:50 MeOH:Hprop %v/v ratio as outlined in the procedure described in section 3.2.1.

The MeOH:Hprop 50:50 %v/v ratio (Solution 1 in Table 3.3) in the nanocomposite precursor solution exhibited stability for one day. After this period, a white solid was observed, likely due to NC precipitation. Moreover, the resulting pyrolysed film from this solution demonstrated inhomogeneities when examined using the MO technique (Figure C.1A). This phenomenon could be attributed to the lower stability of BZO NCs in MeOH, as previously demonstrated in section 2.3.1.4. This instability led to the detection of defects on the same day of solution preparation and ultimately to the precipitation of NCs. Furthermore, an attempt to increase the MEA concentration to 4%v/v to enhance solution stability resulted in inhomogeneous pyrolysis (Figure C.1B). This outcome aligns with previous observations of excessive MEA in the pristine case [46].

In light of these results, we shifted our focus to alternative strategies for enhancing the stability of nanocomposite precursor solutions. Recognizing the necessity of alcohol in the solvent mixture for achieving thicker precursor films [33, 55], we opted to use NC solutions redispersed in EtOH, where NCs exhibit better stability (section 2.3.1.4). Consequently, we conducted studies on the stability of nanocomposite precursor solutions by varying the %v/v ratio of MeOH:EtOH:Hprop. The outcomes of these studies are presented in Table 3.3.

Table 3.3 Solution stability of nanocomposite precursor solutions (3-7 composition, 1.5M, 12% mol BZO and 3.4%v/v MEA) varying the %v/v ratio MeOH:EtOH:Hprop.

Solution	MeOH ($\%_{v/v}$)	EtOH ($\%_{v/v}$)	Hprop ($\%_{v/v}$)	Solution stability
1	50	-	50	1 day
2	35	15	50	< 1 week
3	30	20	50	< 1 week
4	25	25	50	> 1 week
6	20	30	50	> 1 week
7	15	35	50	> 1 week
6	-	50	50	< 1 day

The results obtained from varying the %v/v ratio of MeOH:EtOH:Hprop

revealed that a %v/v of MeOH above 30% led to low stability, ranging from less than one week to only one day as the MeOH volume percentage increased (Solutions 1-3). In these cases, NC precipitation (white solid) was observed after the time mentioned. However, stability significantly improved over one week by increasing the EtOH content to 25-35 %v/v (Solutions 4-7). In these solvent mixtures, $Cu(CH_3CH_2COO)_2$ salt (blue solid) precipitation occurred after approximately one week. Additionally, $Cu(CH_3CH_2COO)_2$ showed slight solubility difficulties when using 25-35%v/v of EtOH under the optimised conditions of temperature and time for the %v/v MeOH:Hprop of 50:50 (30 °C and 30 min). It was necessary to increase the temperature to 35-40 °C and the time to 1-2 hours for proper dissolution of $Cu(CH_3CH_2COO)_2$ in these cases. Furthermore, the limited solubility of $Cu(CH_3CH_2COO)_2$ salt worsened when using 50%v/v of EtOH, leading to copper precipitation on the final day of solution preparation.

We chose 25:25:50 %v/v ratio as the optimal solvent mixture for nanocomposite precursor solutions to ensure long-time solution stability while using softer conditions during solution preparation (35 °C for 1h). This solvent mixture was a compromise for $Cu(CH_3CH_2COO)_2$ salt solubility and stability as well as NC stability. Consequently, this solvent mixture has been predominantly utilised for the preparation of nanocomposite precursor films, except for specific cases involving 18% and 24% mol, which will be explained later.

Furthermore, we observed that the behaviour of NCs in the YBCO precursor solution appears to depend on the size of the NCs. This could be attributed to the slight differences in Z-potential and the percentage of the organic shell that vary with the NC size. Specifically, as the NC size increased from approximately 5 nm to 7 nm and then to 10 nm, the stability of the solution decreased from over one week to just 2-3 days.

To address the issue of NC precipitation, we opted to replace the TREG stabiliser with polyethene glycol (PEG), anticipating an improvement in NC stability within YBCO precursor solutions. The larger ethylene oxide chain of PEG, compared to that of TREG, was expected to enhance stability in more apolar solvents like Hprop. Additionally, ether and hydroxide functional groups in PEG were considered to maintain a certain affinity for polar solvents such as MeOH and EtOH. Furthermore, the extended ethylene oxide chain in PEG was anticipated to promote stabilisation through steric hindrance. The optimisation and

characterization of BZO and BHO NCs stabilised with PEG were detailed in section 2.3.1.3.2, where prolonged stability in EtOH was confirmed. PEG was also found to undergo complete thermal decomposition below 500 °C, suggesting its suitability for compatibility with YBCO precursor solutions (section 2.3.1.3.2).

For stabilizing PEG-stabilised BZO and BHO NCs with sizes of approximately 7 nm and 5 nm, a solvent mixture with a MeOH:EtOH:Hprop %v/v ratio of 25:25:50 was used. The results showed a significant improvement in solution stability, which increased from 2-3 days to over 3 months when using PEG as the stabiliser for approximately 7 nm-sized BZO NCs. A summary of the stability study, considering both the NC size and the type of stabiliser, is provided in Table 3.4.

Table 3.4 Solution stability of nanocomposite precursor solutions (3-7 composition, 1.5M, 12% mol BZO and 3.4%v/v MEA) and %v/v ratio MeOH:EtOH:Hprop of 25:25:50 varying NC size, composition and type of stabiliser.

NC type	NC size (nm)	Polyol type	Solution stability
BZO	5 ± 1	TREG	> 1 week
BZO	7 ± 2	TREG	2-3 days
BZO	10 ± 2	TREG	2-3 days
BZO	7 ± 2	PEG	> 3 months
BHO	5 ± 1	TREG	> 1 week
BHO	5 ± 1	PEG	> 3 months

Finally, with 7 nm-sized BZO NCs stabilised with PEG, we evaluated their stability while varying the NC amount (6-24%mol) in YBCO nanocomposite precursor solutions. Although we obtained BZO and BHO NC solutions with high concentrations in the range of 100-160 mM (refer to section 2.3.1.1), these concentrations were sometimes insufficient to achieve 18% and 24% mol in YBCO nanocomposite solutions while maintaining the 25:25:50 (MeOH:EtOH:Hprop) %v/v mixing solvent ratio. Consequently, the stability of the resulting solutions was investigated using alternative %v/v ratios of solvents, including those with more than 25% v/v of EtOH, enabling an increase in NC amounts to 18% and 24% mol. The results indicate that for MeOH:EtOH:Hprop %v/v ratios of 25:25:50 and 20:30:50, stability was maintained for 6-18% mol beyond 3 months. However, the 15:35:50 ratio, needed in some cases for 24% mol, exhibited a decrease in stability from 3 to 1 month. The comprehensive findings of this study

are summarised in Table 3.2.

Considering these results, the solvent mixture of MeOH:EtOH:Hprop represents a balance between maintaining BZO and BHO NC stability and ensuring copper-propio-nate salt solubility and stability. The studies conducted on stabilising NC solutions in YBCO precursor solutions, wherein NC solutions were employed as part of the solvent mixture for dissolving YBCO precursor salts, demonstrated the feasibility of maintaining a high total salt concentration at 1.5 M. Overall, not only is the developed methodology applicable to the BZO and BHO NCs, but it is also expected to be compatible with other types of nanoparticle solutions by optimising the solvent mixture. This optimisation will ensure the stability of both the nanoparticles (NPs) and YBCO precursor salts for the specific preformed-NP solution used. In the particular case of BZO and BHO NCs, the YBCO nanocomposite precursor solutions exhibited long-term stability, even with increased NC amounts up to 24% mol. In the subsequent section, we will carry out the characterisation of the developed YBCO nanocomposite precursor solutions to confirm their compatibility with the deposition and pyrolysis processes.

3.3.1.2 Characterisation of YBCO nanocomposite precursor solution

The characterization of the YBCO nanocomposite precursor solution described in this section will focus on solutions with a 1.5M total metal salt concentration, a 3-7 composition, and 12% mol of NCs (BZO and BHO). In certain instances, comparisons were made with YBCO pristine precursor solutions having the same concentration and composition.

The behaviour of NCs in the highly ionic media of YBCO precursor solutions was initially evaluated through XRD and TEM analysis. Firstly, the diffraction pattern obtained from a nanocomposite precursor solution with ~5 nm-sized BZO NCs prepared using a capillary tube, exhibited no signal of the most intense peaks (110) and (200) of the cubic phase of BZO. Subsequently, we measured a nanocomposite precursor solution with ~10 nm-sized BZO NCs instead of ~5 nm-sized, and the BZO peaks were detected in the XRD pattern. Figure 3.5 shows the comparison of both patterns. This result suggests that the

~10 nm-sized BZO NCs remain crystalline in the YBCO precursor solution and that the 10 nm-sized BZO NCs did not dissolve during the preparation of the precursor solution. However, further analysis using other techniques is necessary to confirm the behaviour of 5 nm-sized BZO NCs.

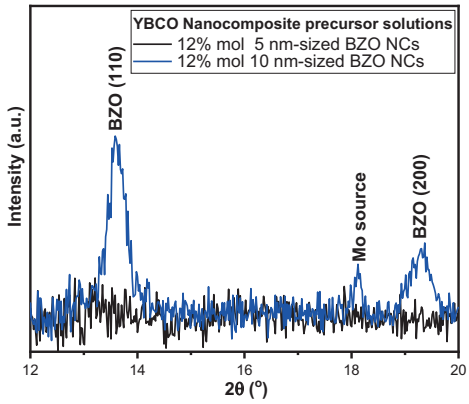

Figure 3.5 XRD patterns of YBCO nanocomposite solutions with 5 and 10 nm-sized BZO NCs.

To confirm if ~ 5 nm sized-BZO NCs did not dissolve during solution preparation, TEM analysis of nanocomposite precursor solution was performed. The TEM image (Figure 3.6B) shows the presence of BZO NCs not-aggregated in YBCO nanocomposite precursor solution, confirming that 5 nm-sized BZO NCs did not dissolve. However, it is confirmed that this NC size did not yield a sufficient signal in capillary XRD. Furthermore, during the thesis, we performed different studies of the influence of tunning NC size and composition. For this reason, NC distribution and TEM size were evaluated from different YBCO nanocomposite precursor solutions containing ~ 5 nm sized-BZO TREG-stabilised NCs (Figure 3.6B), ~ 5 nm sized-BHO TREG-stabilised NCs (Figure 3.6D) and ~ 7 nm sized-BZO PEG-stabilised NCs (Figure 3.6F). These TEM images were compared with the respective TEM images of the same samples dispersed in EtOH (Figure 3.6A, C and E, respectively) to discern any differences before and after their introduction to YBCO precursor solutions.

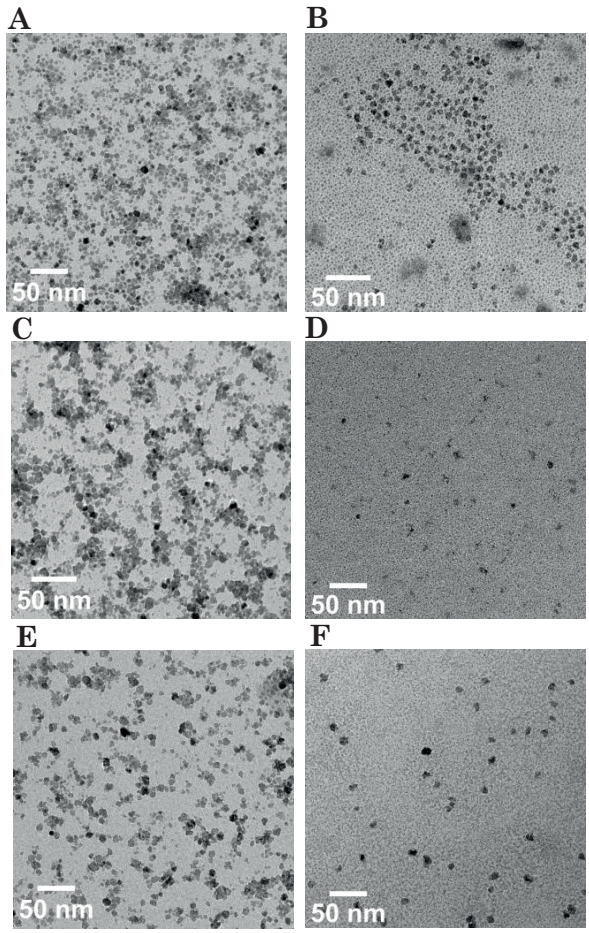

Figure 3.6 TEM images of the as-synthesised colloidal solution in EtOH of (A) ~ 5 nm sized-BZO TREG-stabilised NCs, (C) ~ 5 nm sized-BHO TREG-stabilised NCs and (E) ~ 7 nm sized-BZO PEG-stabilised NCs and their corresponding TEM images when these colloidal solutions were used in YBCO nanocomposite precursor solutions (B),(D) and (F).

The TEM images provide evidence that both 5 nm-sized BZO and BHO NCs stabilised by TREG or 7 nm-sized BZO NCs stabilised by PEG, remain undissolved in YBCO nanocomposite precursor solutions. In addition, these three types of NCs appear to maintain a homogeneous distribution within the YBCO nanocomposite precursor solutions. The TEM is a local technique that should not be used alone to confirm aggregation, homogeneity and stability of NCs in YBCO nanocomposite precursor solutions. In addition, DLS measurements cannot be performed complementary to TEM due to potential interference

between the wavenumber of the blue colour from solutions and the wavenumber of the DLS equipment. Such interference may lead to errors in detection. To obtain complementary information regarding NC aggregation and distribution, further analysis will be carried out through TEM imaging of the nanocomposite precursor films after deposition and pyrolysis treatment using these solutions 3.3.2.2. Finally, Table 3.5 shows the TEM sizes obtained from histograms of TEM images (Figure 3.6B, D and F) of the different YBCO nanocomposite precursor compared to the initial NC solutions used in ethanol (Figure 3.6A, C and E). The values obtained indicated that the NCs retain their initial TEM size in YBCO nanocomposite precursor solutions.

Table 3.5 Particle sizes from histograms of TEM images from Figure 3.8A-F.

NC type	TEM size of NCs in EtOH (nm)	TEM size of NCs in YBCO nanocomposite precursor solution (nm)
TREG-stabilised BZO	5 ± 1 nm	5 ± 1 nm
TREG-stabilised BHO	5 ± 1 nm	5 ± 2 nm
PEG-stabilised BZO	7 ± 2 nm	8 ± 2 nm

The final characteristics of the YBCO precursor films are dependent on the YBCO precursor solution composition and its rheological properties. Especially, rheological properties and the total sum of the metal concentration of solutions exhibit a direct correlation with the resulting thickness and homogeneity of the final precursor films [33, 42, 55]. The rheological properties, such as viscosity and contact angle, of YBCO nanocomposite precursor solutions were measured. Table 3.6 shows the corresponding values obtained compared to pristine precursor solutions as different mixtures of solvents were used which could influence solution rheology properties. Pristine precursor solutions were prepared using a 50:50 %v/v ratio of MeOH:Hprop, while the standard nanocomposite precursor solution employed a 25:25:50 %v/v ratio of MeOH:EtOH:Hprop. The viscosity and contact angle of nanocomposite YBCO precursor solutions slightly exceeded pristine YBCO precursor solution values, possibly related to the higher viscosity of ethanol than methanol (0.983 and 0.507 mPa·s at 30 °C, respectively) and the increased solid phase fraction due to the presence of NCs which also influence viscosity [208–210]. The effect of solution concentration, viscosity, and contact

angle on the final nanocomposite precursor film thickness using the developed YBCO nanocomposite precursor solution will be analysed in section 3.3.2.2.

We also performed measurements of water content in solutions through the Karl-Fischer titration method [206, 207] as previous studies of CSD suggested that may influence in crack formation of pyrolysed films [33] and the final properties of the REBCO layers[96, 211]. In particular, for acetate-based precursor solutions, it has been established that YBCO film quality is significantly compromised beyond a water content threshold of 2 wt% in solutions [33, 55]. A detailed study of water content in propionate-based precursor solutions was carried out in L. Saltarelli thesis for the pristine case, which was performed in parallel with this one. This study demonstrated that the previously imposed threshold could be increased up to 4 %wt while maintaining strong YBCO epitaxial nucleation and good superconducting properties. However, it is still pending to demonstrate if we can operate beyond the 4 %wt. On the day of preparation, the nanocomposite precursor solutions showed 0.8 %wt of water and increased to 2.7 % upon remeasurement after 2 months.

Table 3.6 Summary of viscosity, contact angle and water content of nanocomposite precursor solution compared to pristine precursor solution.

Solution type	Viscosity (mPa·s)	Contact angle (º)	Water content (%wt)
Pristine	8.50 ± 0.05	17 ± 0.1	0.61 ± 0.06
Nanocomposite	11.78 ± 0.08	23.4 ± 0.9	0.80 ± 0.06

Moreover, the thermal decomposition of metal-organic precursors in nanocomposite precursor solution was analysed through TGA. The TGA registers the organic mass loss from the solutions subjected to a heat treatment up to 500 °C under a humid oxygen atmosphere, similar to the conditions employed in the pyrolysis step. Previous studies have used thermogravimetric analysis to understand the decomposition of acetate-based YBCO precursor solutions [44]. Figure 3.7 shows the TG decomposition profiles obtained from nanocomposite precursor solution compared to pristine precursor solution. The results suggest that both types of solutions undergo similar organic thermal decomposition, indicating that the presence of NCs in the solution does not significantly influence the decomposition of YBCO propionate-based precursor salts. Moreover, in both nanocomposite and pristine cases, the mass loss observed is 45.3% and 44.7%

respectively, in agreement with the expected theoretical ones (42.8% and 42%). Given the small quantity of NCs (12% mol, approximately 1.6% wt concerning the total weight of YBCO precursor salts), the obtained mass loss values are quite similar. The slightly higher mass loss for the nanocomposite precursor solution could be attributed to the decomposition of the organic shell stabilizing BZO NCs. It was demonstrated that the decomposition of YBCO propionate-based precursor salts follows the same mechanisms as for acetate-based precursor salts, obtaining the same desired YBCO precursor phases (section 1.1.3.3.2). The main differences between both cases are the smoother decomposition profile of propionate-based precursor solutions due to the presence of MEA additive in solutions [46].

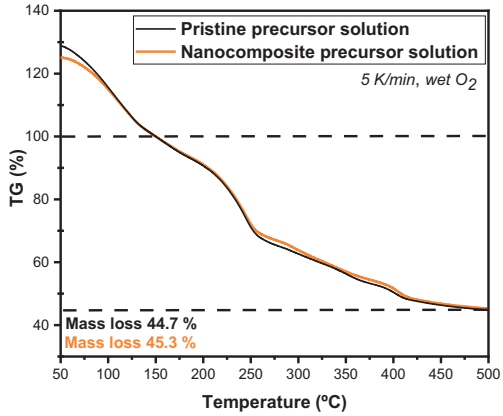

Figure 3.7 TGA analysis of YBCO nanocomposite solution compared to YBCO pristine solution.

To conclude, the characterization performed in this section on YBCO nanocomposite precursor solutions allows an understanding of the physicochemical properties influencing the deposition and pyrolysis processes, as previously demonstrated [33, 55]. In addition, the results could be used as a tool to ensure the stability and reproducibility of the CSD process. In addition, the highly concentrated precursor solutions and high viscosities are linked to the formation of thicker precursor films, an aspect that will be further demonstrated in the subsequent section. Furthermore, the following section will provide detailed insights into homogeneity, precursor phases, and microstructural analyses, all achieved using the developed YBCO nanocomposite precursor solution.

3.3.2 YBCO nanocomposite precursor films

3.3.2.1 Surface homogeneity and structural characterisation

The subsequent steps in the TLAG-CSD process, after YBCO precursor solution preparation, are the deposition and pyrolysis treatment (section 3.2.2). Following the deposition of the precursor solution using the spin-coating technique, the organic components of the samples are removed through a low-temperature pyrolysis treatment at 500 °C. This process involves the conversion of propionate-based YBCO precursor salts into the corresponding YBCO precursor oxide phases for the TLAG process [44, 46, 59]. The reaction of each propionate-based YBCO precursor salt to the corresponding oxide involves multiple steps, as illustrated in Scheme 3.1.

$$Cu(CH_3CH_2COO)_2 \longrightarrow CuO$$

$$Ba(CH_3CH_2COO)_2 \longrightarrow BaCO_3$$

$$Y(CH_3CH_2COO)_3 \longrightarrow Y_2O_3$$

Scheme 3.1 Multiple steps reactions of the conversion of YBCO propionate-based salts into the corresponding YBCO precursor oxide phases.

In this section, we will demonstrate the compatibility of developed YBCO nanocomposite precursor solutions with deposition and pyrolysis treatments used in the TLAG-CSD process. To achieve thicker films through the CSD method, we use a multideposition approach, which involves successive deposition and pyrolysis processes to reach the desired thickness (section 3.2.2). The multideposition strategy in nanocomposite precursor films was mainly based on the multilayered architecture composed of an initial pristine layer on top of the STO substrate, denoted as SEED layer, followed by one or two nanocomposite (NP) layers. Previous studies in the TFA-CSD route demonstrated that the use of a pristine SEED layer before the nanocomposite layer avoided interface problems, such as NC accumulation at the substrate interface, during YBCO growth [47, 85, 95]. The role of the seed layer will be discussed in detail in section 4.3.2.4 and its influence in grown TLAG nanocomposite films. During the thesis, it was necessary to modify the standard multilayered architecture. In some

cases, this modification implied the addition of a pristine layer at the end of the multideposition process, placed on top of the NP layer, denoted as the pristine CAP layer. Schemes illustrating both described architectures are presented in Figure 3.8A-B.

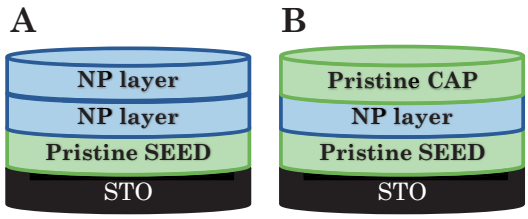

Figure 3.8 Scheme of multilayered architecture nanocomposite films with (A) pristine SEED and 2 NP layers and (B) pristine SEED, 1 NP layer and pristine CAP layer.

Firstly, the surface quality of the resulting nanocomposite precursor films was analysed through the MO technique. It was observed that homogenous and crack-free precursor nanocomposite films with 12%mol NCs can be reached for the different three compositions (Figure 3.9A-C), that are, 2-3, 3-6 and 3-7, using their corresponding optimal quantity of MEA (Table 3.1).In this section, our focus will be on pyrolyzed films consisting of two layers, specifically a pristine SEED layer and a NP layer, with all layers having a 3-7 composition unless specified differently.

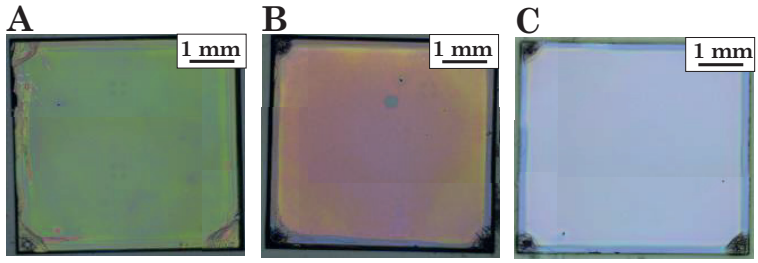

Figure 3.9 MO images precursor nanocomposite films with seed layer and 1 NP layer of (A) 2-3 composition using 1.5 M + 3.4%v/v MEA solution + 12% mol NCs,(B) 3-6 composition using 1.5 M + 3.4%v/v MEA solution + 12% mol NCs and 3-7 composition using 1.5 M + 3.4%v/v MEA solution + 12% mol NCs.

Moreover, the developed nanocomposite precursor solution demonstrated the capability to produce smooth and crack-free precursor films for all the NC amounts tested, from 6 to 24% mol (Figure C.2A-D), for BZO (Figure C.2A-D) and BHO NC compositions (Figure C.2E-F) and the different NC sizes tested

(Figure C.3A-C). Additionally, the MO images show that homogenous precursor films can be obtained with solutions containing 7 nm-sized BZO NCs stabilised with PEG (Figure C.3B). Moreover, despite the solution stability of 2-3 days observed for 10 nm-sized BZO NCs stabilised with TREG, smoother precursor film surfaces can be achieved (Figure C.3C). Finally, high-quality surfaces were obtained by increasing the number of layers from two to four (Figure C.3D).

The crystalline phases present in nanocomposite precursor films of pristine SEED and one NP layer with 12% mol 5 nm-sized BZO or BHO NCs, prepared using this solution, were analysed through XRD. In the 2D GADDS XRD patterns (Figure 3.11A), we identified the desired YBCO precursor phases for TLAG, including mainly orthorhombic $BaCO_3$, CuO, and Y_2O_3. This confirms the favourable and potentially compatible nature of the developed nanocomposite precursor solutions for the TLAG-driven growth of YBCO. Additionally, no significant differences were observed compared to the YBCO precursor phases obtained in the pristine case, suggesting that the introduction of NCs may not disturb the decomposition paths of propionate-based precursor salts.

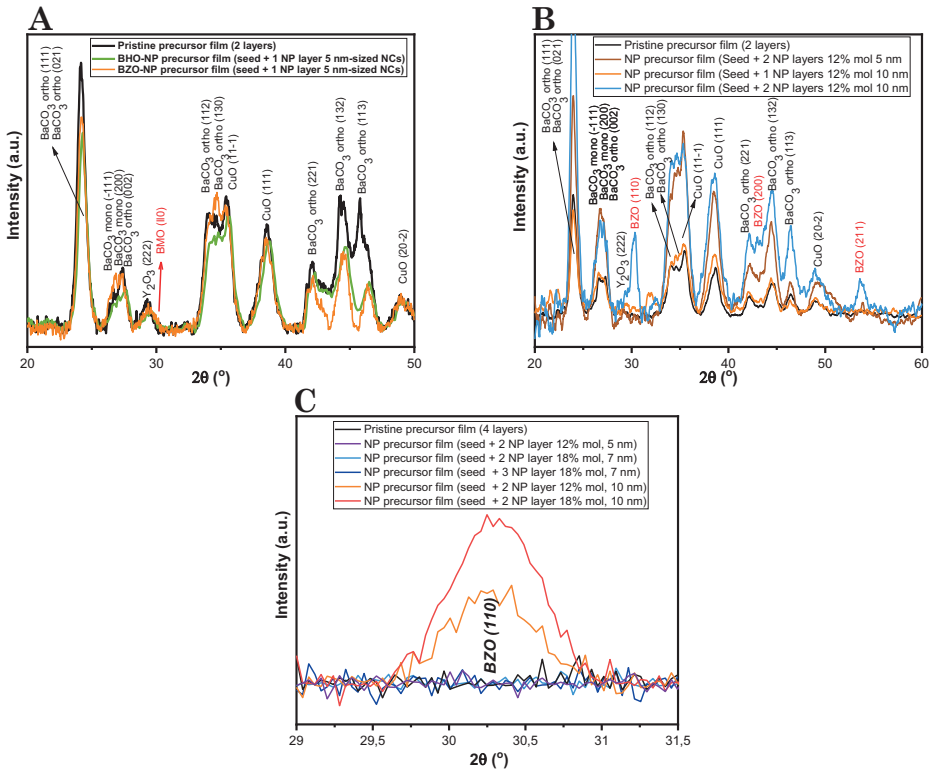

Figure 3.10 (A) GADDS XRD patterns of precursor nanocomposite films with seed layer and 1 NP layer of 12 %mol 5 nm-sized BZO (green) and BHO NCs (orange) compared to two layers pristine sample (black), (B) GI XRD patterns of different precursor nanocomposite films varying NC size and NP layer thickness and (C) GI XRD patterns centring 2θ in the most intense peak of BZO (110).

Concerning the identification of NCs, the main peak (110) corresponding to BZO and BHO NCs was not detected in GADD XRD patterns (Figure 3.11A). To enhance the intensities of the crystalline phases, especially for the NC phase, HR-XRD measurements in GI geometry were performed. Additionally, since small-sized NCs of 5 nm produce broader diffraction peaks than larger NCs, according to Scherrer's equation [152–154], leading to lower intensity, the NC size in nanocomposite precursor films was increased from 5 to 10 nm. In some cases, an additional NP layer was introduced. The GI XRD patterns obtained from nanocomposite samples with 12 %mol BZO, varying NP thickness layer, and NC size, are shown in Figure 3.11B. In these GI measurements, the most intense peaks of BZO NCs were finally identified in the nanocomposite precursor film composed of a pristine seed and two NP layers of 12% mol BZO NCs with a size of 10 nm. This suggests that 5 nm-sized NCs produce broader peaks with

lower intensity, making them undetectable in XRD. Another possibility is that the YBCO nanocomposite precursor solution or the precursor film preparation treatment affected the crystallinity of the NCs.

To maximise the diffraction signal from the NC phase, we subjected different pyrolyzed nanocomposite films to GI measurements over 1 hour, centred in the 2-2θ range of the most intense peak of BZO phase (110), 29-32°. These measurements were performed on nanocomposite precursor films with NC amounts of 12 and 18 %mol, different NC sizes (5, 7, and 10 nm), and varying NP layer thicknesses (from seed and 2 NP layers to seed and 3 NP layers). The results are shown in Figure 3.11C. The signal of (110) BZO peak appears in nanocomposite precursor films composed of a pristine seed and two NP layers with 12 %mol or 18 %mol BZO NCs with a size of 10 nm. Therefore, the detection of diffraction from the NC phase in XRD analysis requires a minimum of 2 NP layers with 10 nm-sized NCs in the multilayered architecture of nanocomposite films.

To further investigate the distribution and size of crystalline phases and confirm NC crystallinity, especially for samples with 5-nm sized NCs, the microstructure of the nanocomposite precursor films will be analysed through TEM in the following section.

3.3.2.2 Microstructural analysis

The TLAG process is a liquid-assisted growth process that follows a liquid-solid reaction mechanism. In this process, YBCO precursor phases react to form a barium cuprate liquid phase, from which YBCO finally crystallises. Therefore, homogeneity and nanocrystalline sizes of YBCO precursor phases are essential for favouring homogenous and speeding up the transient liquid formation which promotes ultrafast epitaxial YBCO growth and high-performance thick films [10, 42, 43, 46].

The microstructural nanoscale homogeneity for nanocomposite precursor films was investigated by the TEM technique by Dr. K. Gupta. The cross-sectional HAADF-STEM images of two-layer (Figure 3.12A) and three-layer (Figure 3.12B) pyrolyzed nanocomposite films show dense, homogeneous, and high thicknesses of the multi-deposition layers. The estimated thicknesses were 500 nm for two-layer films and 1100 nm for three-layer films.

Additionally, despite the presence of pores in the pyrolyzed matrix (dark contrast areas in HAADF-STEM images), which possibly originate from the CO_2/CO_2 gas diffusion resulting from the decomposition reactions of YBCO precursor salts during the pyrolysis treatment, the nanocomposite films exhibit a high degree of thickness uniformity and compactness. The nanocomposite precursor films displayed a porosity of $0.6 \pm 0.1\%$ and an average pore size of 3-4 nm. Therefore, the nanocomposite precursor films showed similar microstructure homogeneity and pore density $1 \pm 0.2\%$ as pristine precursor films [46], suggesting no influence of NCs on the precursor microstructure formation. Porosity was evaluated by processing the cross-sectional HAADF-STEM images with image analysis software ImageJ [212] and the average pore sizes were calculated from the histograms of measured pore areas [46]. The achieved smooth surfaces, homogeneity, low porosity, and high thicknesses of both pristine and nanocomposite YBCO precursor films are attributed to the presence of MEA in the matrix during the pyrolysis processes [46].

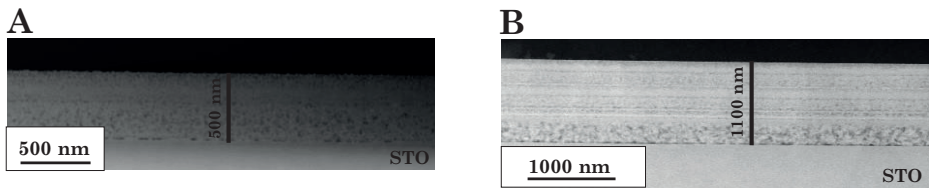

Figure 3.11 Cross-sectional HAADF-STEM images of nanocomposite precursor films composed of (A) seed layer + 1 NP layer and (B) seed layer + 2 NP layers.

The homogeneity, crystallinity state and sizes of YBCO precursor phases were analysed using HRTEM. The HRTEM images (Figure 3.13A-B) show an amorphous matrix with a uniform distribution of the desired YBCO nanocrystalline precursor phases ($BaCO_3$, CuO and Y_2O_3), which were previously identified in XRD measurements (Figure 3.11A). The typical crystalline sizes observed were 10-30 nm for orthorhombic $BaCO_3$, 5-10 nm for the minor proportion of monoclinic $BaCO_3$, 15-40 nm for the CuO phase, and 5-7 nm for Y_2O3 nanoparticles.The obtained lower porosity and dense microstructures, where YBCO precursor phases were identified close to each other with homogeneous distribution and small sizes in the nanometric scale, promote the fast reaction of $BaCO_3$ with CuO to form the Ba-Cu-O transient liquid phase in the TLAG process. In addition, the small sizes of Y_2O_3 nanoparticles could contribute to the homogeneous epitaxial YBCO growth with ultrafast growth rates. The driving force of

this process is the Yttrium supersaturation in the liquid phase [42, 43], which depends on the atomic diffusivity, and such diffusivity increases with decreasing particle size [213] (details in section 1.1.3.3.3).The observed behaviour of YBCO precursor phases in the nanocomposite films was also identified in pristine pyrolyzed films, suggesting that NCs did not influence the proper formation of YBCO precursor phases [46].

Finally, the distribution, size, and crystallinity of NCs after the pyrolysis treatment were also investigated through HRTEM. Nanocomposite precursor films were analysed, prepared with initial colloidal solutions containing 12% mol of 5 nm-sized BZO and BHO NCs, as well as 12% mol of 10 nm-sized BZO NCs. The HRTEM images show that 5 nm-sized BHO (Figure 3.13A-B) and BZO NCs (Figure 3.13C) were homogeneously distributed and non-aggregated within the YBCO precursor matrix, without a significant increase in NC size compared to their initial average diameter in the NC solutions. The NC coarsening is a phenomenon that can occur due to high-temperature treatments during film formation [55, 214]. In the case of nanocomposite precursor films with BZO with an initial size of 5 nm, we measured BZO NCs of 5-7 nm, for 5 nm-initial-sized BHO NCs, we identified 4-6 nm, and for 10 nm-initial-sized BZO NCs, we obtained BZO NCs of 10-12 nm. Moreover, these results confirmed that 5 nm-sized NCs retained their crystallinity after solution preparation and pyrolysis processes, even though they could not be detected by XRD measurements of nanocomposite precursor films (Figure 3.11A-C).

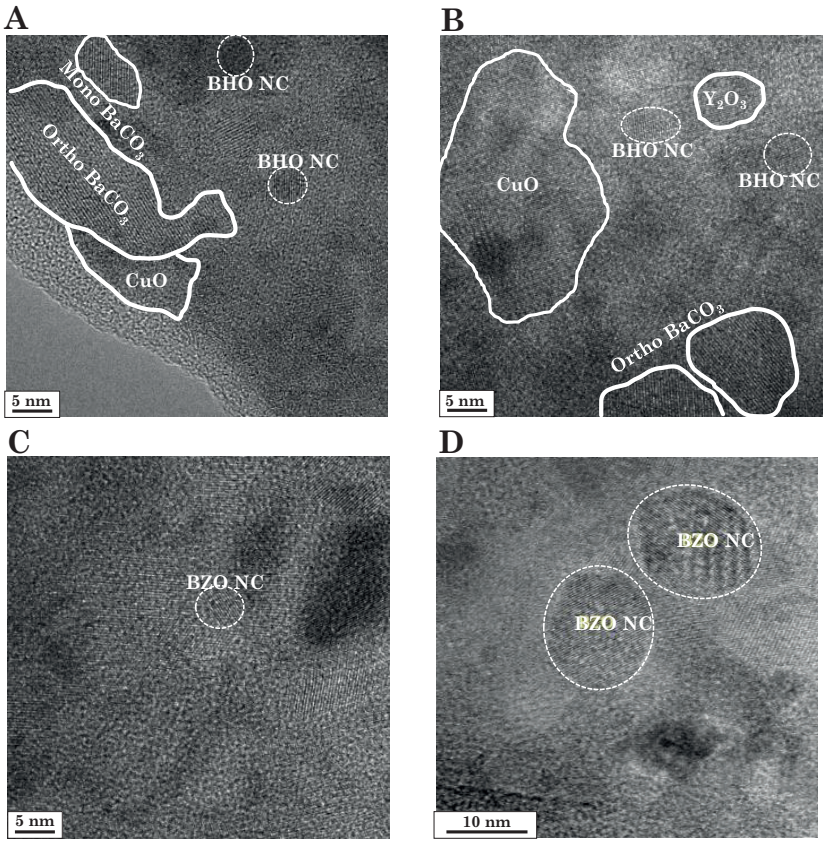

Figure 3.12 HRTEM images of (A),(B) different regions of the nanocomposite precursor film with 5 nm-sized BHO NCs displaying YBCO precursor phases and embedded BHO NCs, (C) Nanocomposite precursor film with 5 nm-sized BZO NCs showing an area with an embedded BZO NC and (D) Nanocomposite precursor film with 10 nm-sized BZO NCs showing embedded BZO NCs.

In conclusion, we have successfully demonstrated the compatibility of the developed propionate-based nanocomposite precursor solution with the pyrolysis treatment in the TLAG-CSD process. The resulting nanocomposite precursor film exhibits microstructural characteristics essential for the subsequent YBCO growth step. These characteristics include a homogeneous and thick nanocrystalline matrix containing the desired YBCO precursor phases, with NCs uniformly distributed across the film and no significant NC coarsening. Further analysis of the reproducibility and long-term stability of these solutions will be performed in the subsequent section.

3.3.3 Stability of YBCO nanocomposite precursor solutions and films

The stability of the different optimised nanocomposite precursor solutions depending on NC size, type of stabiliser, and NC amount was investigated in section 3.3.1.1. In this section, we will demonstrate, through TEM and MO techniques, the reproducibility of the deposition processes when using optimal and long-stable YBCO nanocomposite precursor solutions.

The nanocomposite precursor solutions (6-18 % mol) with PEG-stabilised NCs showed high stability (> 3 months). In this section, we will present the stability studies performed with a nanocomposite precursor solution consisting of 1.5M, 3.4% MEA, 20:30:50 %v/v ratio of MeOH, EtOH:Hprop with 18% mol 7 nm-sized BZO NCs stabilised with PEG. Firstly, the simple deposition of several mL of this YBCO precursor solution in a watch glass did not reveal the presence of solid precipitates, suggesting that NC and YBCO propionate-precursor salts remained dispersed in the solution. Then, the behaviour of NCs in the YBCO precursor solution after 4 months of solution preparation was evaluated through TEM. The TEM image shows the presence of non-aggregated BZO NCs, confirming that NCs did not dissolve in high-ionic solutions, such as YBCO precursor solutions, after 4 months of being stabilised and dispersed.

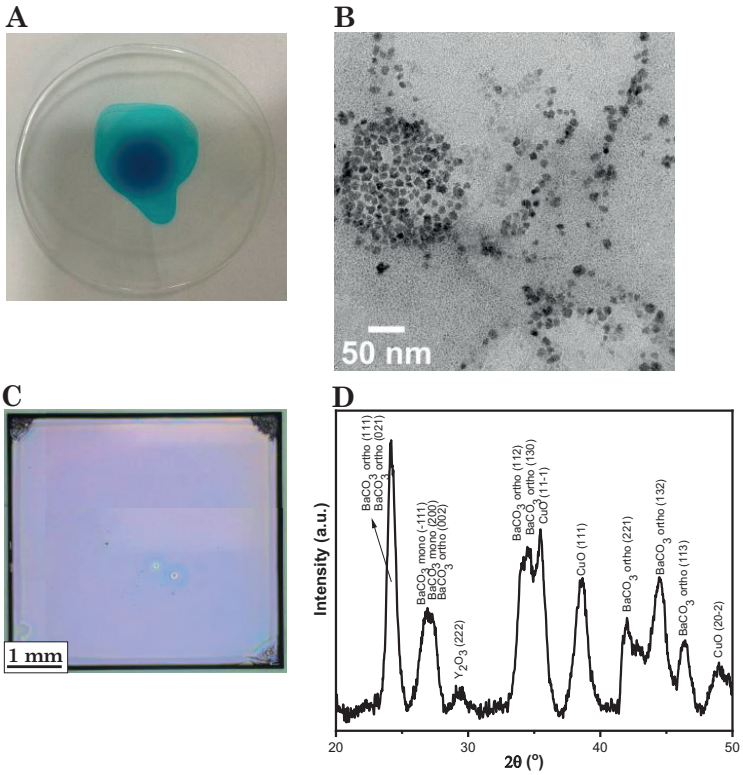

Figure 3.13 (A) Image of deposition of some mL of nanocomposite precursor solution (1.5M, 3.4% MEA, 20:30:50 %v/v ratio of MeOH,EtOH:Hprop with 18% mol 7 nm-sized BZO NCs stabilised with PEG) in a glass watch, (B) TEM image of the nanocomposite precursor solution (A), (C) MO image of the nanocomposite precursor film from solution (A) and (D) 2D GADDS XRD pattern of the nanocomposite precursor film from solution (A).

Considering that the stability of solutions significantly influences the spin-coating deposition and pyrolysis processes where morphological irregularities were observed on the film surface, YBCO nanocomposite precursor films were prepared using the solutions mentioned above, which remained stable for 4 months. The sample was characterised by MO and XRD. The MO image shows smooth, crack-free surface films without inhomogeneities, with the same high surface quality demonstrated in section 3.3.2.1. Moreover, we analysed if the crystalline phase composition was maintained when using an older solution through XRD analysis. The resulting XRD pattern displays the same YBCO precursor phases ($BaCO_3$ mainly in its orthorhombic phase, CuO, and Y_2O_3) obtained using a solution prepared on the same day as the deposition and pyrolysis processes (Figure 3.10A). These results confirm the long-time stability

of YBCO nanocomposite precursor solutions, ensuring that nanocomposite precursor films will exhibit the desired characteristics for the TLAG process, even when using a solution that was prepared several months earlier.

3.4 Conclusions

In the study performed in this chapter, we have successfully developed a YBCO nanocomposite solution preparation, demonstrating its capabilities and compatibility with the TLAG-CSD process to obtain high-performance epitaxial YBCO nanocomposite films. This achievement is based on the use of metal propionates precursor salts of yttrium, barium, and copper, MEA additive and NC solutions as part of the solvent mixture for the dissolution of salts.

Some of the solution's characteristics were initially optimised and demonstrated for pristine solutions, which were then adapted and optimised to be compatible with NC solutions. In addition, we successfully achieved the same desired characteristics for nanocomposite precursor solutions, such as solution concentration, high-quality precursor films, high thicknesses, and optimal nanocrystalline precursor YBCO phases for the TLAG process.

The use of in-house-prepared metal-propionate precursors, as opposed to commercially available acetate precursors, eliminates the risk of product mixtures arising from the incomplete conversion of acetate precursors. This approach ensures high-purity, high-yield, and cost-effective results. The addition of MEA additive enhances the solubility of copper-propionate salt, leading to increased solution concentration and viscosity. Consequently, this results in the formation of high-thickness nanocomposite precursor layers.

The BZO and BHO NC solutions show poor stability in the optimised system designed for pristine solutions, utilising a solvent mixture with a 50:50 (MeOH:EtOH) %v/v ratio, resulting in inhomogeneous pyrolyzed nanocomposite films. We decided to use NC solutions in ethanol, where these NCs demonstrate better stability compared to methanol. The introduction of ethanol in the solvent mixture used in the system produced a decrease in the solubility and stability of cooper-propionate salt compared to 50:50 (MeOH:EtOH) %v/v ratio.

Therefore, we optimised the YBCO precursor solutions with specific solvent mixtures of MeOH:EtOH:Hprop to ensure BZO and BHO NC stability and copper-propionate salt solubility and stability. We successfully stabilised increased NC amounts up to 24% mol and utilised different NC sizes (5, 7, and 10 nm). Additionally, we improved the stability of these nanocomposite solutions for several months by using PEG-stabilised NCs instead of TREG-stabilised NCs. The demonstrated enduring stability of nanocomposite precursor solutions enables the scalability of the process with low cost and robustness. Furthermore, beyond the successful compatibility with various Ba:Cu molar ratios, NC amounts, and NC sizes that were demonstrated using the developed methodology to prepare YBCO colloidal solution with BZO and BHO NCs, it is expected that this methodology will also be compatible with other types of preformed-NP solutions. Once optimising the solvent mixture for each particular type of preformed-NP solution.

Firstly, it was confirmed that NC did not dissolve and retained their crystallinity in YBCO nanocomposite precursor solution, as demonstrated through solution-XRD and TEM techniques. Additionally, thermal and solution rheology studies have revealed some characteristics of the solutions. The thermal results obtained suggest that the NCs did not significantly influence the organic thermal decomposition pathways when compared to pristine solutions. The viscosity and contact angle of nanocomposite YBCO precursor solutions were slightly higher than those of pristine YBCO precursor solutions, possibly related to the higher viscosity of ethanol than methanol and due to the presence of solid NC phase, explaining the observed high thickness (450-500 nm for one layer).

The compatibility of nanocomposite precursor solution with deposition and pyrolysis treatment was evaluated in terms of surface quality, structural composition and microstructural characteristics. Smooth and crack-free precursor nanocomposite films were successfully obtained for various compositions (2-3, 3-6, and 3-7), as well as different NC concentrations (6-24% mol), NC sizes (5, 7, and 10 nm), NC compositions (BZO and BHO), and increased film thickness from 2 to 4 layers. XRD analysis confirmed the presence of the desired YBCO precursor phases for TLAG processes.

In conclusion, these solutions successfully produced homogeneous, high-thickness, and low-porous nanocrystalline microstructures with the desired nanocrystalline precursor phases homogeneously distributed, including embedded NCs. The capability to achieve even thicker and more homogeneous films (approximately 1 μm) was demonstrated through the deposition of multilayered samples using spin coating. Moreover, microstructural characterisation through TEM analysis has been crucial in understanding the behaviour of NCs in pyrolyzed nanocomposite films. Homogeneous, non-aggregated, and crystalline NCs were identified, retaining their initial size in solution. These results evidence the importance of optimising reproducible, fully dissolved, and stable nanocomposite precursor solutions for the successful development of high-performance nanocomposite precursor layers with the desired characteristics essential for homogeneous epitaxial growth and ultrafast rates in the TLAG process. Furthermore, the developed fast, facile, and tunable nanocomposite precursor solution preparation method enhances cost-effectiveness while increasing the reproducibility, robustness, and quality of the CSD method.

4

Nanocomposite films through TLAG-CSD PO_2-route

4.1 Introduction

The final section of the thesis focuses on demonstrating the compatibility of the developed nanocomposite precursor solution with the Transient Liquid Assisted Growth (TLAG) process, specifically in terms of epitaxial growth of YBCO and enhancement of superconducting properties. The chapter describes the challenges encountered during the optimisation of nanocomposite film growth through the TLAG-CSD PO_2-route, a two-step process. The first part discusses the optimisation of growth conditions using a slow heating ramp of ~0.2 °C/s. Initially, bad wetting issues limit critical current density, leading to the exploration of different strategies, including substrate changes and variations in supersaturation conditions. Later, it is observed that the slow heating ramp induces precursor phase coarsening and the formation of large secondary phases, also limiting superconducting properties. To overcome this, the setup is improved with higher heating ramps.

The second part focuses on optimising nanocomposite films using a fast heating ramp of ~1 °C/s, resulting in a reduction of secondary phases and an improvement in critical current density. New challenges, such as NC pushing and interface porosity, appear. Strategies like using 7 nm-sized NCs, employing a pristine layer on top of the nanocomposite layer, and modifying the multideposition architectures of the films are studied. Despite encountering challenges, the implemented approaches lead to strong epitaxial nucleation, high critical current densities, and smoother Jc decay in nanocomposite films compared to pristine films. Interestingly, this improvement is demonstrated across different NC amounts (6-24%) and different film thicknesses (400-900 nm).

In addition, the last part of the chapter describes some relevant results from *in-situ* synchrotron XRD diffraction analysis of the developed TLAG nanocomposite film using propionate-based precursor colloidal solutions to comprehend the kinetic mechanism of the TLAG approach. A total of five beamtimes were carried out during the PhD thesis, in collaboration with two synchrotron facilities. Three beamtimes were performed at the DiffAbs Beamline at SOLEIL Synchrotron in Saint-Aubin, France, under the supervision of Beamline Scientist Dr. Cristian Mocuta. Two additional beamtimes were conducted at the NCD-Sweet Beamline at the ALBA Synchrotron in Cerdanyola del Vallès, Spain,

with the assistance of Beamline Scientist Dr. Eduardo Solano. A custom-designed setup was developed to replicate the experimental conditions of the standard tests conducted at ICMAB, which were characterised using *ex-situ* techniques.

4.2 Experimental

Procedure and conditions details

The final step in the formation of TLAG nanocomposite films from pyrolysed precursors films (Chapter 3) is the YBCO crystallisation. In this chapter, we investigated the growth of nanocomposite films through the PO_2-route. The P-route is based on a two-step process where initially the sample is heated to high temperature (830-860 °C) under a low oxygen partial pressure, below the YBCO stability line (10^{-5}-10^{-6} bar) [68]. Subsequently, upon the set temperature is achieved, a fast pressure jumps to high oxygen partial pressure, where YBCO nucleation is reached ($\geq 10^{-3}$ bar), is carried out. Finally, the film is maintained under the specified conditions for 2 or 5 min before being cooled down to room temperature.

The PO_2-route experiments were performed with an in-house tubular furnace belonging to the SUMAN group. The oven consists of a furnace quartz tube connected to two different and independent pressure systems, one with a turbomolecular pump and another with a rotary pump to reach the desired oxygen partial pressures. The regulation of oxygen pressure is achieved by needle valves in each pumping system and we have in-situ readings by two pressure meters. The fast pressure switching between the two circuits is provided by two electro-valves. The other end of the tube is where the sample is placed in a crucible connected to a thermocouple to read and record temperature during the process.

The first part of this chapter was done with the furnace in a static mode where the maximum heating ramp possible was ~0.2 °C/s. Then, the investigation, using the slow-heating ramp, provided limitations in high current densities even after tuning growth conditions including temperature, pressure, liquid composition and other parameters. Going one step further the heating ramp parameter was investigated by improving the furnace set-up. This enhancement

involved placing the furnace on top of rails, enabling fast heating ramps of ~1 °C/s. A picture of the furnace with the last set-up is shown in Figure 4.1A. Furthermore, with the new set-up, we not only achieved the fast heating ramp requirement but also decreased the total duration of the heating treatment from ~6 h to 30 min. The slow and heating ramp profiles are shown in Figure 4.1B and C respectively.

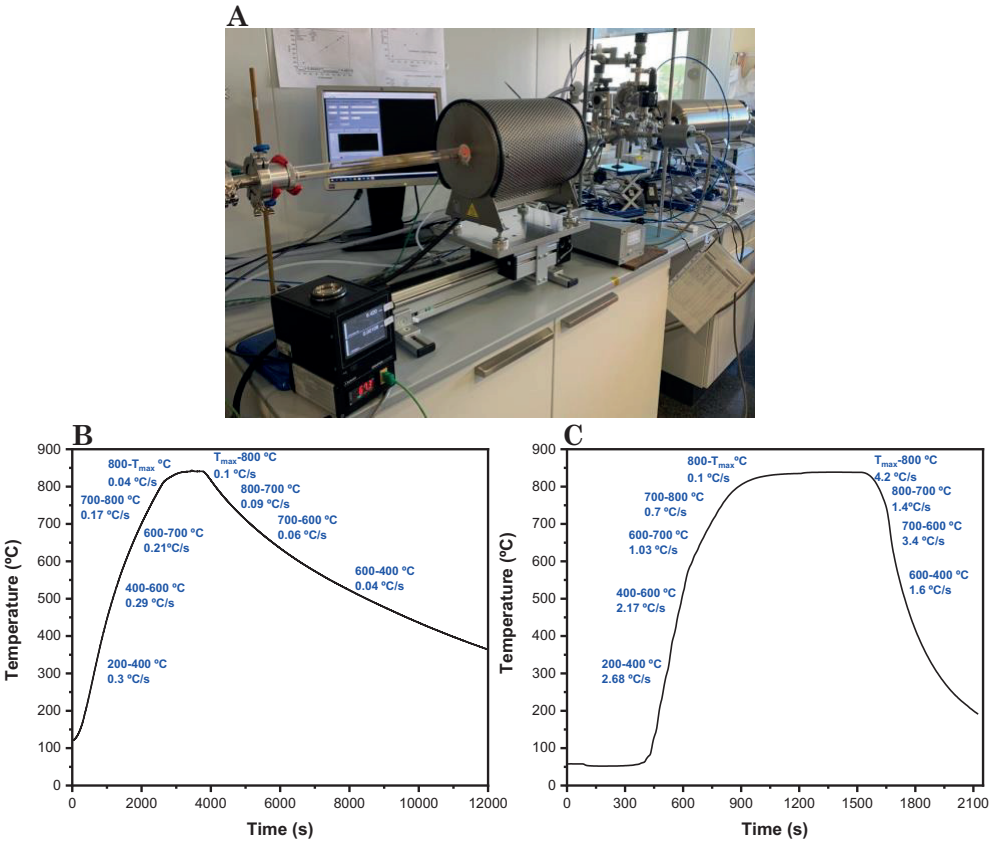

Figure 4.1 (A) Image of furnace used for PO_2-route experiments and temperature profile as a function of time using (B) slow heating ramps and (C) fast heating ramps.

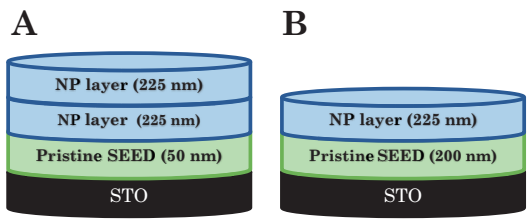

Figure 4.2 Scheme of multilayered architecture nanocomposite films with (A) pristine SEED (50 nm) and 2 NP layers (450 nm) and (B) pristine SEED (200 nm) and 1 NP layer (225 nm) used in slow and fast heating ramps, respectively.

The utilisation of this furnace for TLAG nanocomposite film growth will be discussed in the following sections. The chapter was divided into two parts: one regarding the investigations with the slow-heating ramp and the other regarding fast heating ramp. This division was necessary due to the non-equilibrium and kinetic behaviour of the TLAG process, which required different conditions and optimisation for each heating ramp.Table 4.1 summarises the different types of substrates, liquid compositions, and architecture of the samples with the corresponding thickness used during each optimisation. Specifically, a scheme of the two architectures used with the corresponding thickness of each layer is shown in Figure 4.2A-B.

In the first sections of the chapter, $BaZrO_3$ (BZO) and $BaHfO_3$ (BHO) have been considered equivalent, expecting the same behaviour. Both compositions are chemically compatible with YBCO growth through the Ba-Cu-O liquid phase, which is a corrosive and reactive liquid [215] and previous investigations have not revealed discernible differences in YBCO nucleation and superconducting self-field properties between these two compositions [10, 55].

Table 4.1 Comparision of type of substrate, liquid composition, sample architecture and NP size and composition used for slow and fast heating ramps during each optimisation.

Heating ramp	Substrate	Liquid composition	Sample architecture	NP characteristics
Slow (~ 0.2 °C/s)	STO, $LaMnO_3$ (LMO) buffer on STO	2-3, 3-7	Pristine seed (50 nm) + 2 NP layers (450 nm)	12 %mol (5 nm BZO)
Fast (~ 1 °C/s)	STO	3-6, 3-7	Pristine seed (200 nm) + 1 NP layers (225 nm)	6-24 % mol (5,7 and 10 nm BZO and BHO)

In the last step, before physical characterisation, the grown samples are exposed to a post-heating oxygenation treatment with the thermal profile shown in Figure 4.3 to reach the superconducting orthorhombic phase of YBCO (section 1.1.3.3.4).

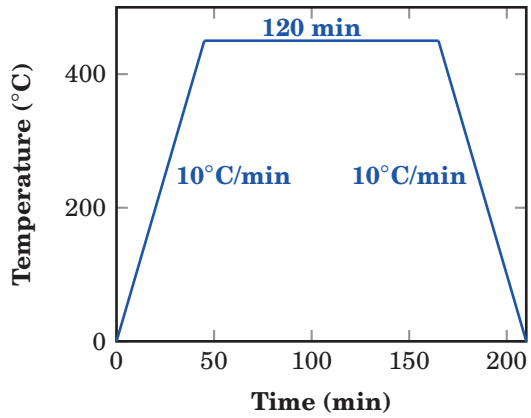

Figure 4.3 Oxygenation profile under 0.6 L/min of dry oxygen for TLAG films

Characterisation

The texture quality, identification of phases and their orientations were evaluated by 2D X-ray diffraction measurements with a General Area Detector Diffraction System (GADDS). High-resolution X-ray Diffraction (HR XRD) measurements in θ-2θ geometry over a 2θ range of 20-120° were performed to analyse the texture quality from the resulting high-intensity of (00l) planes of YBCO. From θ-2θ HR XRD pattern, the c-axis and nanostrain (ϵ) values were calculated. For a high signal of randomly oriented phases, such as secondary phases, HR XRD in grazing-incidence (GI) geometry measurements were carried out. The texture quality was also evaluated through the rocking curve of YBCO (005) and ϕ-scan of (102) reflections. Quick and non-destructive electromagnetic characterisation of critical temperature (Tc) and critical current density (Jc) were measured by a Quantum Design Superconducting Quantum Interference Device (SQUID) magnetometer. In addition, electrical transport measurements of Tc by the Van der Pauw method and Jc (H,T,θ) were carried out, and pinning properties were evaluated in collaboration with Aiswarya Kethamkuzhi carrying her Ph.D. thesis in the SUMAN group. Electron microscopy techniques were also used to characterise the samples. Scanning Electron Microscopy (SEM) characterisation was performed to obtain images of film surfaces to check the

surface homogeneity and identify regions of different compositions. Finally, the microstructure of nanocomposite TLAG films was also analysed by TEM to correlate the results of the YBCO texture and physical properties with the defect landscape, NP distribution, and sizes after the growth process and identify secondary phases. The TEM characterisation was undertaken by Dr. K. Gupta from SUMAN group.

4.3 Results and discussion

4.3.1 Growth of TLAG nanocomposite films with slow heating ramp

4.3.1.1 Nanocomposite films crystallisation via optimal growth conditions for pristine films

The starting conditions of the first part of PO_2-route investigation using slow heating ramp (~0.2 °C/s) and other optimisations for nanocomposites film studies were the ones provided by pristine samples where fully epitaxial nucleation and good superconducting properties conditions were achieved. The growth of pristine YBCO films was carried out by the PhD Thesis of L. Saltarelli which has been running in parallel with this one. The in-house PO_2-route furnace described in section 4.2 was used for the growth of YBCO nanocomposite films with a pristine seed layer of (50 nm) and two nanocomposite layers (450 nm of total thickness) with 12 %mol of BZO NPs.

The optimised condition found for the pristine sample on STO was heating to 840 °C with a heating ramp of ~0.2 °C/s under $PO_2 = 10^{-5}$ bar to allow the elimination of $BaCO_3$. Then, at the final temperature, a PO_2 jump was performed to a $PO_2 = 1.8{\cdot}10^{-3}$ bar holding during 5 min at this conditions. After the dwell for 5 minutes, the sample is cooled to room temperature. Nanocomposite film was grown under these conditions.

The YBCO texture of pristine and nanocomposite-grown films was evaluated by 2D XRD GADDS and the surface microstructure of the films was observed by SEM as shown in Figure 4.4A and B respectively. We can observe in

2D XRD GADDS images for both samples that highly epitaxial nucleation was achieved with some minor contribution of random YBCO. From the resulting integrated XRD pattern of 2D XRD GADDS images, we evaluate the epitaxial growth by analysing the area of (005) and (103) reflections and determine a value that allows comparing random contribution between different samples following the equation:

$$R = \frac{\text{Area YBCO (103)}}{\text{Area YBCO (103)} + \text{Area YBCO (005)}} \tag{4.1}$$

Following equation 4.1 we calculated a random contribution of R = 0.05 and R = 0.04 for pristine and nanocomposite films. Previous studies considered that a random contribution of $R \leq 0.05$ is not adverse in terms of the final properties of the sample [55]. The surface microstructure of both samples was analysed by SEM as shown in Figure 4.4. In the case of pristine (Figure 4.4A), the surface is homogeneous and flat, and small particles homogeneously distributed with the same morphology are observed on the surface. We identified these particles as CuO phase coming from the use of an excess of copper in the 3-7 composition that was expelled to the surface. This phenomenon in 3-7 composition of TLAG films was previously observed in L. Soler [33] and J.Jareño [55] thesis using acetate-based YBCO precursor solutions and also using propionate-based precursor solutions developed and used in this thesis, which were firstly identified in pristine samples [46]. SEM image of nanocomposite film (Figure 4.4B) shows a different surface from pristine film. A blurry surface and a non-homogeneous and continuous layer are observed. Moreover, we detect large holes where white particles are placed. SEM image in backscattered electrons (BSE) imaging mode (Figure 4.5A) shows different contrasts between the different areas, indicating different compositions of these mentioned areas.

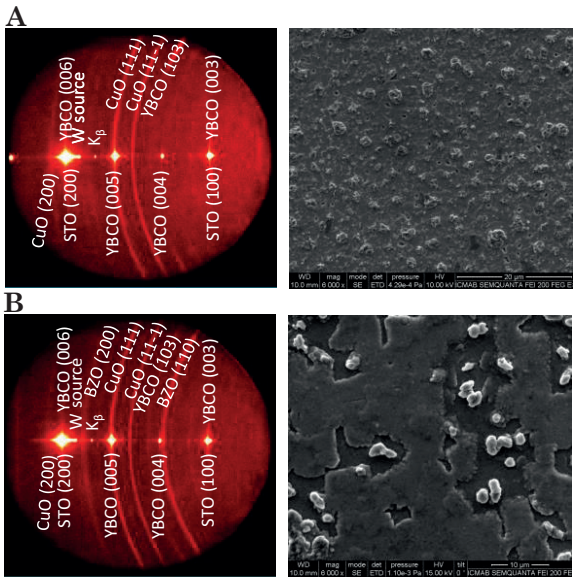

Figure 4.4 2D GADDS XRD and SEM images of (A) pristine film (B) nanocomposite film with 12%mol BZO grown at 840 °C with a PO_2 jump from 10^{-5} bar to $1.8{\cdot}10^{-3}$ bar.

In order to analyse the effect of the minor contribution of YBCO random nucleation and the surface observed on the superconducting properties, SQUID measurements were performed. We obtained a T_c and J_c self-field at 77 K of 90 K and 1.6 MA/cm^2 and 88 K and 0.2 MA/cm^2 for pristine and nanocomposite film, respectively. It seems that the small random contribution encountered (R = 0.04-0.05) is not detrimental to the final superconducting properties. Therefore, the causes of the lower properties obtained from nanocomposite films in comparison to pristine samples should come from different factors than YBCO texture. These differences may be attributed to the different behaviour observed on the surfaces of both films. Different factors can hinder current percolation, such as the presence of non-superconducting secondary phases and poor grain connectivity resulting from bad wetting or pores [10, 33, 55].In order to identify the possible reasons for bad percolation in this particular case, the microstructure inside the nanocomposite film was analysed by TEM.

Through high-angular dark field-scanning TEM (STEM-HAADF) analysis of a large area of nanocomposite film (Figure 4.5B) we confirm that the dark areas previously seen in the SEM image (green square of Figure 4.5A) were not uncovered STO substrate regions. Some regions are just steps on film thickness (thinner epitaxial YBCO areas of ~ 75 nm) and others areas are accumulations

of other phases of ~ 70-90 nm of thickness. These voids on the film might result from transient liquid wetting problems with the substrate or due to a low nucleation density derived from the too-high interface strain energy between YBCO grains and substrate. The different sources of poor wetting will be discussed in detail later.

We expected a total thickness of ~ 500 nm from the pyrolyzed precursor film, and we observed a maximum thickness of 600 nm in some regions, including secondary phases inside the film, which were identified by Bright-field high-resolution transmission electron microscopy (BF-HRTEM) and we will discuss later. In addition, Ba-Cu-O phases were also identified by energy dispersive X-ray (EDX) of STEM-HAADF image on top of the YBCO layer. Then, we analysed in detail, with high-magnification STEM-HAADF images, two regions of the nanocomposite film. First, we identify by EDX of STEM-HAADF image (Figure 4.5D) that the dark area with blurry morphology in the SEM image (green square in Figure 4.5A) contains 30-50 nm sized BZO NCs and Ba-Cu-O phases forming a thin layer of ~ 70-90 nm of thickness. Then, the transition region between dark (thin) to grey (thick) area (orange square in Figure 4.5A) was also analysed by STEM-HAADF (Figure 4.5C). Agglomeration of BZO NCs is detected in the transition from a thin to a thick layer, indicating that some NCs were expelled during the YBCO growth process and accumulated in the not-wetted regions. In addition, white particles identified as CuO phase are also placed in bad wetting areas, which comes from the copper excess used in the 3-7 composition.

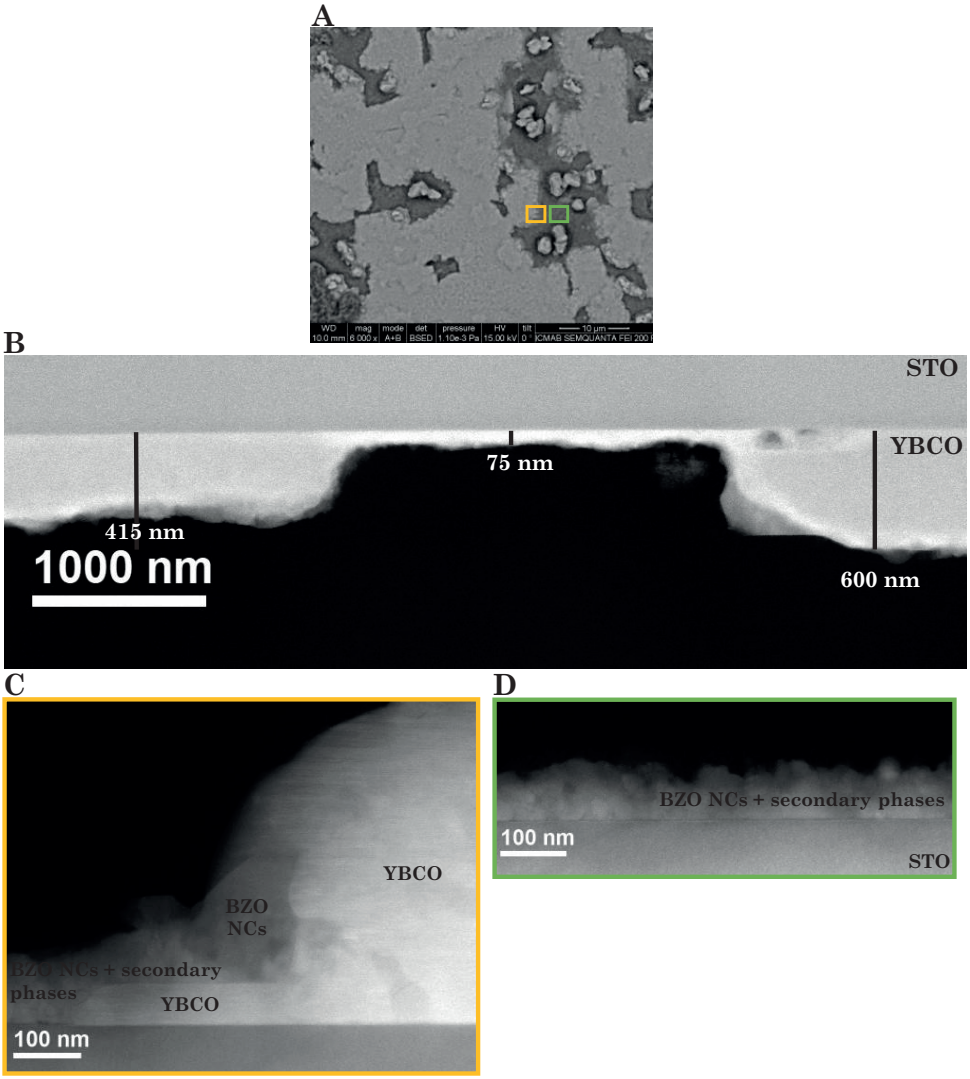

Figure 4.5 (A) SEM image in BSE imaging mode (B) low-magnification STEM-HAADF image of full cross-section area of the film and high-magnification STEM-HAADF images of (C) transition area between the dark region and grey region from BSE SEM image (yellow square) and (D) dark region from BSE SEM image (green square) from nanocomposite film with 12% mol BZO grown at 840 °C with a PO_2 jump from 10^{-5} bar to 10^{-3} bar.

Finally, we used the bright-field high-resolution imaging mode of HRTEM (BF-HRTEM) in order to identify phases inside the film through diffraction planes. The phases Y_2BaCuO_5 and $BaCu_3O_4$ of 20 nm are identified inside the film and in the interface of STO and YBCO (4.6A and B). These phases inside the film could be detrimental to the superconducting properties. Furthermore,

despite we observe some BZO NCs agglomerated in the bad wetting regions we also detect a few BZO NCs inside the film. NCs with a size of ≤ 15-20 nm are epitaxially oriented with the c-axis growth of YBCO while > 20 nm of NCs size are randomly oriented. Epitaxial embedded NCs in TLAG nanocomposite films are possible using the TLAG process as the YBCO growth is assisted through the formation of a liquid Ba-Cu-O phase allowing NP rotation during the YBCO growth [10, 55].

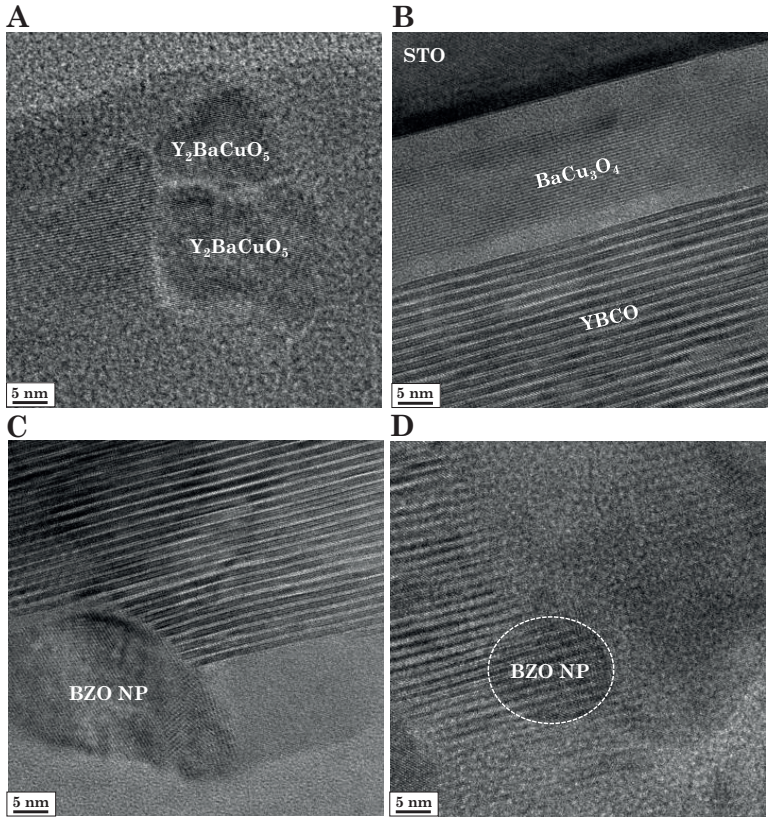

Figure 4.6 BF-HRTEM images of (A) Area with Y_2BaCuO_5 particles, (B) Area with a $BaCu_3O_4$ particle, (C) Area with a BZO Nc randomly oriented and (D) Area with epitaxial BZO NC from nanocomposite film with 12% mol BZO grown at 840 °C with a PO_2 jump from 10^{-5} bar to 10^{-3} bar.

Considering these results, the discontinuities in the epitaxial YBCO film-like holes might be from a poor wetting problem which could hinder the good percolation of current [216–219] and cause accumulation of other phases (agglomeration of BZO NCs and Ba-Cu-O phases) in these regions and also the observation of non-stoichiometric Y_2BaCuO_5 phase inside the film. Wetting

phenomena could be attributed to the high interfacial energies between (Ba-Cu-O) liquid phase with the substrate (bad wetting) or between the YBCO solid phase with the substrate (dewetting). As we mentioned in the introduction (section 1.1.3.2.1) the surface energy of heterogeneous nucleation depends on the interface-free energies of all the involved phases in nucleation (precursor phases, nucleus, and substrate), defining the wetting characteristics of nuclei (Figure 1.5C). Consequently, high surface energy will increase nucleation energy (according to Equation 1.2), favouring poor wetting. Concerning this, we can define two types of poor wetting, depending on the sources and involved nucleation phases:

⁕ **Dewetting (YBCO solid phase-substrate strain)**: The high interfacial energy between YBCO solid nuclei and substrate due to the higher lattice mismatch increases the energy for nucleation, which consequently reduces the nucleation density. The lower nucleation density results in well-faceted and separated YBCO grains (Figure 1.6B) arising to minimise the interface energy favouring dewetting. Porosity derived from low nucleation density which produces large grain sizes, ending in the observation of large holes, is also another source of superconducting cross-section decreased [216] being the main limitation in TFA-CSD process [217–219]. The dewetting effect (poor grain connectivity) is enhanced by exposing a grown solid to a post-thermal treatment, especially at high temperatures and long times and with thinner films [219]. Consequently, to avoid dewetting, nucleation density needs to increase by decreasing the lattice mismatch between YBCO and substrate, which will decrease the nucleation energy barrier (ΔG^*) or by increasing supersaturation to overcome the increase in the energy barrier of the strain according to Equation 1.10. The supersaturation can be increased by decreasing the copper content in the liquid phase, determined by the initial solution composition, or by tuning the processing condition (T-PO_2).

⁕ **Bad wetting (Ba-Cu-O liquid phase-substrate strain)**: Large interruption areas of the epitaxial film could also come from the high interfacial energy between the substrate and a liquid phase as Ba-Cu-O melt [215]. In our case, the pores observed can also arise from bad wetting of the liquid phase, as YBCO crystallisation takes place in the Ba-Cu-O transient liquid phase. Therefore, the wettability of the Ba-Cu-O liquid phase with the substrate is dependent on the interfacial energy between both phases, which derives from bad-wetting

areas to minimise the interfacial surface energy. In previous TLAG studies [10, 33, 55] bad wetting effect was postulated to increase due to the high diffusivity in Ba-Cu-O liquid phase, as high Yttrium diffusivity in BaO-CuO melt phase from other liquid-based techniques was also reported [27, 72, 73].

Furthermore, the melt derived from 3-7 composition might have a higher diffusion coefficient (D_l) than stoichiometric composition (2-3) as the viscosity of 3-7 liquid is expected to be lower and D_l is related to the viscosity (η) according to the Stokes-Einstein equation (Equation 4.2).

$$D_l = \frac{kT}{6\pi r \eta} \tag{4.2}$$

$$\eta = Ae^{\frac{E}{RT}} \tag{4.3}$$

$$\eta = \eta_0 (1 + af) \tag{4.4}$$

D_l is also associated with the radius (r) of the moving particles and is proportional to the temperature [213]. The viscosity of a melt follows the Arrhenius form (Equation 4.3) showing an exponential temperature dependence [220–222]. Furthermore, as our system consists of a liquid phase with solid phases of Y_2O_3 particles and BZO NCs their behaviour could also be related to the simple model that describes the viscosity of suspensions (two-phase mixtures) by Equation 4.4. The viscosity of a two-phase mixture depends on the viscosity of the pure liquid (η_0), a constant that depends on particle shape (α) and the solid phase fraction in the suspension (f) [208–210]. Following Equation 4.4 we expect a higher viscosity for 2-3 than 3.7 liquids, as the 2-3 liquid is always closer to the liquid-solid region of the $BaCuO_2$-CuO phase diagram (Figure 1.9) than the 3–7 composition (eutectic composition). Consequently, the higher possible presence of a solid fraction in the liquid phase derived from 2-3 compared to the 3–7 composition results in a higher viscosity, according to Equation 4.4.

In conclusion, bad wetting might arise from the low viscosity of 3-7 composition, which would promote an increase of Ba-Cu-O liquid diffusivity. This phenomenon is enhanced at high temperatures since viscosity decreases with the temperature, and consequently increasing D_l. In addition, supersaturation also decreases to small values with temperature, where at these conditions the induction time (τ) for YBCO nucleation is longer, which could also contribute to giving enough time for cation diffusion and formation of secondary phases

[33] as the ones observed in our nanocomposite sample (Figure 4.6A and B). In addition, under these conditions, BZO NCs have more time to diffuse and agglomerate on the surface (Figure 4.5C and D).

Considering the different sources previously identified as potential impediments to achieving high critical currents in the TFA-CSD route [34] and in the TLAG-CSD process [10, 33, 55], which include bad wetting issues, we proposed that this problem in the nanocomposite sample mainly contributed to the low Tc and Jc self-field observed. The following section is focused on strategies to solve poor wetting problems and improve superconducting properties.

4.3.1.2 Strategies towards avoiding poor wetting

In the previous section, we postulated that lower Jc values in the case of nanocomposites are linked to bad wetting of the transient Ba-Cu-O liquid with the substrate promoted by interface strain or by a dewetting effect from the strain between YBCO solid phase with the substrate, or a combination of both effects. These effects are dependent on liquid properties and composition, growth conditions and lattice mismatch, among others. We followed different strategies to limit the liquid movement and/or reduce the high YBCO/subtrate strain in the direction of decreasing the energy of the system by minimising the interface energies:

1. **Film thickness**. The first and easy approach applied was based on covering the holes that did not reach the STO substrate by increasing the total thickness from 500 nm (50 nm SEED layer + 2 NP layers of 450 nm) to 700 nm (50 nm SEED layer + 3 NP layers of 650 nm). We expected that the increase in the amount of liquid phase could be enough to homogeneously cover the STO surface. The SEM characterisation of thick nanocomposite film (Figure 4.7A) shows that the poor wetting effect persists even with increased thickness, observing the same surface morphology as with 500 nm of film thickness (Figure4.4B). It was previously reported in TLAG films grown using acetate-based precursor solution [33] that liquid wetting problems were even worse with film thickness increased (from 90 nm to 400 nm) suggesting that this effect might be from another source in the case of the TLAG process.

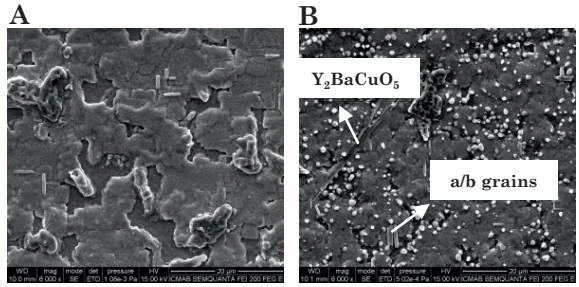

Figure 4.7 SEM images of (A) Nanocomposite film of 725 nm (50 nm SEED + 3 NP layers of 675 nm) with 12%mol BZO grown at 840 °C with a PO_2 jump from 10^{-5} bar to 10^{-3} bar with and (B) Nanocomposite film of 500 nm (50 nm SEED + 2 NP layers of 450 nm) with 12%mol BZO grown at 840 °C with a PO_2 jump from 10^{-5} bar to $2.8{\cdot}10^{-3}$ bar.

2. **Type of substrate** The wettability of liquid over the surface changes with surface properties where solid surface chemistry has a major influence for modifying surface energy [223]. Furthermore, it was reported in the literature that the affinity of liquid to wet depends on the type of substrate used [215]. Especially in TFA-CSD films, poor wetting phenomena was observed by the formation of large and faceted separated grains arising to minimise the interface energy generated by the higher lattice mismatch of YBCO with substrate [219]. When the energy for nucleation increases, the nucleation density is reduced, resulting in large and separated YBCO grains favouring dewetting. Consequently, to avoid this effect, we need to decrease nucleation energy while increasing nucleation density. For that, it is required to reduce strain between YBCO and substrate or, as we used a liquid-assisted growth process, increase supersaturation in the Ba-Cu-O liquid phase. In pristine TLAG films using 3-7 composition, it was found that growing YBCO on top of Sr_2AlTaO_6 (LSAT) substrate bad dewetting was reduced. Thickness discontinuities were observed that did not reach the LSAT substrate instead of completely uncovered areas in the case of STO [33].

   The first strategy tried was the use of an LMO buffer on STO substrate grown through Pulser Laser Deposition (PLD) instead of STO with a closed lattice parameter to YBCO (ϵ = ($a^{Substrate}$-a^{YBCO})/a^{YBCO}). We expected that the decreasing lattice mismatch from +1.9 % (ϵ^{STO}) to +1.56 % (ϵ^{LMO}) would induce higher nucleation density avoiding bad wetting.

   The growth of a nanocomposite film with 3-7 composition on LMO (50 nm

SEED layer + 2 NP layers of 450 nm with 12% mol BZO) was performed at 840 °C with a PO_2 jump from 10^{-5} bar to 10^{-3} bar. The 2D GADDS XRD image (Figure 4.8A) shows that no fully epitaxial nucleation is achieved on LMO observing misoriented reflections such as random YBCO (103) and (102)/(200) from a/b grains. The surface morphology was characterised by the SEM technique observing a full surface of misoriented grains but forming a continuous layer where some small-sized voids were detected which could be attributed to the random distribution of YBCO grains and not to a liquid wetting problem.

Despite the random and a/b YBCO nucleation obtained at the growth conditions used, it seems that by decreasing the interfacial energy using LMO substrate, high nucleation density was promoted avoiding bad wetting. As the YBCO nucleation density changes depending on the substrate used, the growth conditions for epitaxial nucleation should also change evidenced by the obtention of fully epitaxial film in the case of STO (Figure 4.4B) grown in the same processing conditions as LMO. Going in the direction of favouring epitaxial nucleation we decreased supersaturation by increasing temperature up to 860 °C with a PO_2 jump from 10^{-5} bar to $2.8{\cdot}10^{-3}$ bar. The characterisation of the YBCO texture by 2D GADDS XRD (Figure 4.8B) shows that at these conditions we enhance heterogeneous nucleation as we can observe that the ring of YBCO (103) is almost eliminated but fully epitaxial nucleation is not achieved as we cannot eliminate completely a/b grains. Inside the heterogeneous nucleation, c-axis orientation has lower surface energy than a/b and under low supersaturation conditions, c-axis is favoured. Perhaps, we have grown this sample above supersaturation conditions where the energy barrier for both orientations became of the same order [10, 33]. The SEM image (Figure 4.8B) confirms the presence of a/b grains (perpendicular elongated grains) but we observe a totally holes-free continuous layer.

In conclusion, the supersaturation conditions employed for the growth of YBCO on LMO substrate, for the eutectic liquid composition (3-7), were sufficiently higher to increase the nucleation density to avoid dewetting. However, these conditions were not optimal for achieving full c-axis nucleation.

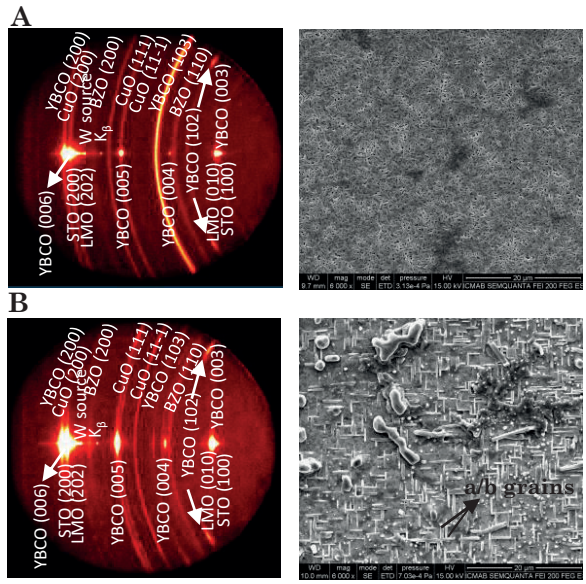

Figure 4.8 2D GADDS XRD and SEM images of nanocomposites films on LMO with 12%mol BZO and 3-7 composition grown at (A) 840 °C with a PO_2 jump from 10^{-5} bar to 10^{-3} bar and (B) 860 °C with a PO_2 jump from 10^{-5} bar to $2.8{\cdot}10^{-3}$ bar.

3. **Supersaturation: PO_2-temperature and liquid composition dependence**

   In a third strategy for solving the wetting issue, we tested the increase in nucleation density by increasing supersaturation while at the same time, limiting the mobility of Ba-Cu-O liquid phase (diffusivity). However, the increase in supersaturation goes against favouring heterogeneous nucleation. Consequently, we needed to find compromise conditions to avoid dewetting while maintaining epitaxial nucleation.

   Firstly, we grew a nanocomposite sample on STO with 3-7 composition performing a PO_2 jump from 10^{-5} bar to $2.8{\cdot}10^{-3}$ bar instead of 10^{-3} at 840 °C. By increasing final PO_2 we increased supersaturation, and also at $2.8{\cdot}10^{-3}$ bar we jumped in a different area of the kinetic phase diagram (Ba-Cu^{+2}-O full liquid phase region instead of Ba-Cu^{+1}-O full liquid phase region in Figure 1.11) [10, 43]. The cooper oxidation state in the Ba-Cu-O liquid phase, depending on PO_2 could modify the liquid properties such as viscosity related to diffusivity and consequently the wettability of the liquid. The SEM image of the nanocomposite film grown to $2.8{\cdot}10^{-3}$ bar of final PO_2 (Figure 4.7B) shows that the bad wetting seems

to be reduced as the discontinuities in thickness are shorter than the observed in Figure 4.4B. In addition, elongated grains with a needle-like shape are observed, which in previous studies was identified as the segregated Y_2BaCuO_5 phase derived from bad wetting problems [33]. Despite reducing bad wetting by increasing supersaturation through PO_2 we are still observing its effect.

Going in the direction of increasing supersaturation to reach higher values of nucleation density, we performed experiments using the stoichiometric composition Y:2Ba:3Cu (2-3) on STO under $2.8{\cdot}10^{-3}$ bar of final PO_2. Supersaturation (σ) is given by $\sigma = (C\text{-}C_{eq})/C_{eq}$ and since C_{eq} decreases with Cu content in the liquid, σ will be higher for liquid phase derived from 2-3 than 3-7 composition [33, 224]. Furthermore, as we expected a higher viscosity for 2-3 composition compared to 3–7 composition, 2-3 composition might have a lower diffusion coefficient (Equations 4.4 and 4.2).

The first experiment with 2-3 composition was carried out at 850 °C with a PO_2 jump from 10^{-5} bar to $2.8{\cdot}10^{-3}$ bar. The SEM image in standard and BSE imaging mode (Figure 4.9A) shows the final reach of totally pore-free film formation with some a/b grains. CuO particles (white spheres) and additional phases (dark elongated particles), possibly originating from the solidification of the melt, are also observed. These particles are placed on top of the surface, which should not block current percolation.

As the presence of misoriented grains could be a limiting superconducting cross-section factor [10, 34, 55], the XRD texture was evaluated through 2D GADDS XRD. The 2D GADDS XRD image (Figure 4.9A) confirms the presence of some random YBCO and a/b grains. Increasing supersaturation with 2-3 composition, homogenous and a/b nucleation is favoured but as C_{eq} depends also on temperature [33], supersaturation in 2-3 composition could be decreased by increasing temperature promoting c-axis nucleation. We performed a second experiment increasing the temperature from 850 °C to 860 °C with the same PO_2 jump. The random and a/b nucleation contributions seem to be decreased by increasing temperature as YBCO (103) reflection intensity is almost eliminated and YBCO (102) intensity is reduced (Figure 4.9B). The surface morphology of the film analysed by SEM (Figure 4.9B) displays the typical dewetting problem also

found in TFA-CSD films which end in faceted grains [219] hindering current percolation. The self-field Jc at 77 K and 5 K of both nanocomposite films with 2-3 composition were measured by SQUID measurements. The nanocomposite grown at 850 °C reached a Jc of 1.0 MA/cm^2 at 77 K and 15.2 MA/cm^2 at 5 K whereas nanocomposite grown at 860 °C showed a Jc of 0.1 MA/cm^2 at 77 K and 0.9 MA/cm^2 at 5 K. Therefore, despite the decrease in random and a/b nucleation increasing the temperature to 860 °C, the poor grain connectivity observed resulted in a reduction of Jc.

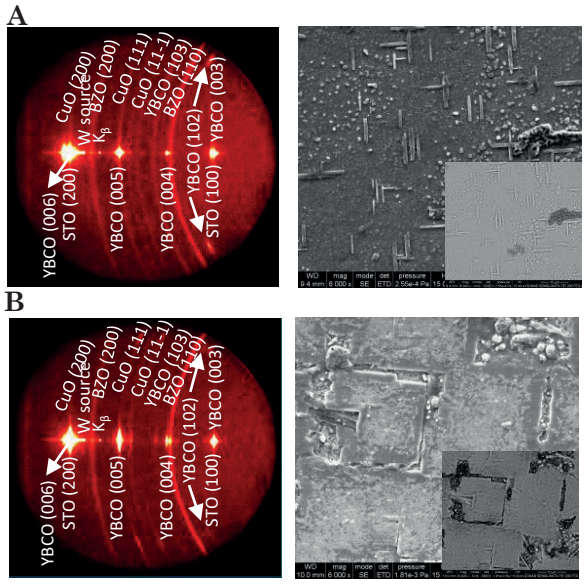

Figure 4.9 2D GADDS XRD and SEM images (BSE images inset) of nanocomposites films on STO with 12%mol BZO and 2-3 composition grown at (A) 850 °C with a PO_2 jump from 10^{-5} bar to $2.8{\cdot}10^{-3}$ bar and (B) 860 °C with a PO_2 jump from 10^{-5} bar to $2.8{\cdot}10^{-3}$ bar.

Considering these results, it was demonstrated that increasing nucleation density either by using LMO substrate with 3-7 composition or increasing supersaturation through higher final PO_2 with 3-7 composition or lower Cu-content composition (2-3), which also reduces liquid diffusivity, are effective tools to limit poor wetting. These effective strategies that go in the direction of minimising interfacial energy between YBCO/subtrate and decreasing the nucleation energy barrier seem to indicate that the initial large holes mainly came from a dewetting issue and not from a bad wetting of the intermediate liquid phase.

Despite these strategies going against favouring c-axis nucleation as we increase supersaturation, the most straightforward strategy for preventing dewetting and obtaining high epitaxial nucleation was achieved by optimising growth conditions (temperature and PO_2). The higher supersaturation associated with the 2-3 composition limits the temperature and PO_2 window of full c-axis nucleation, being smaller than for 3-7 composition. Consequently, we had to grow at higher temperatures for 2-3 than 3-7 composition, where dewetting due to temperature appeared, hindering current percolation. For this reason, initially, we fully characterised the nanocomposite of 2-3 composition grown at 850 °C with a PO_2 jump from 10^{-5} bar to $2.8{\cdot}10^{-3}$ bar before continuous optimisation.

4.3.1.3 YBCO texture quality and physical characterisation of the best nanocomposite film at slow heating ramp

The nanocomposite film of 2-3 composition with 12% mol BZO (50 nm SEED layer + 2 NP layers 450 nm) grown at 850 °C with a PO_2 jump from 10^{-5} bar to $2.8{\cdot}10^{-3}$ was the sample that reached the highest Jc value of slow heating ramp (1.0 MA/cm^2 at 77 K). A Tc of 89 K was determined by resistivity measurement.

HR XRD scan in a wide range of θ-2θ was measured to determine the c-axis lattice parameter. The value obtained is 11.69 Å which is inside the range of previously determined values in TLAG nanocomposites films with 100 nm of thickness [10, 55]. The high supersaturation of 2-3 composition promoted some random contribution, quantified as R = 0.1, calculated from the integration of XRD GADD image and Equation 4.1, and also a/b-nucleation observed in the 2D XRD image (Figure4.9A). Despite this, the width of the rocking curve of (005) YBCO Bragg peak and ϕ scan obtained are 0.21° and 0.69° respectively (Figure 4.10A and B). The values achieved are in the range of the strong epitaxial TLAG thin films ($\Delta\omega_{(005)}$ = 0.1-0.9° and $\Delta\phi_{(102)}$ = 0.6-1.6°) [10, 33, 55] and are competitive with the lowest values reported in the literature for other liquid-based growth process. Therefore, despite some grain misalignment being present in the nanocomposite film we might consider that the following strategies went in the good direction.

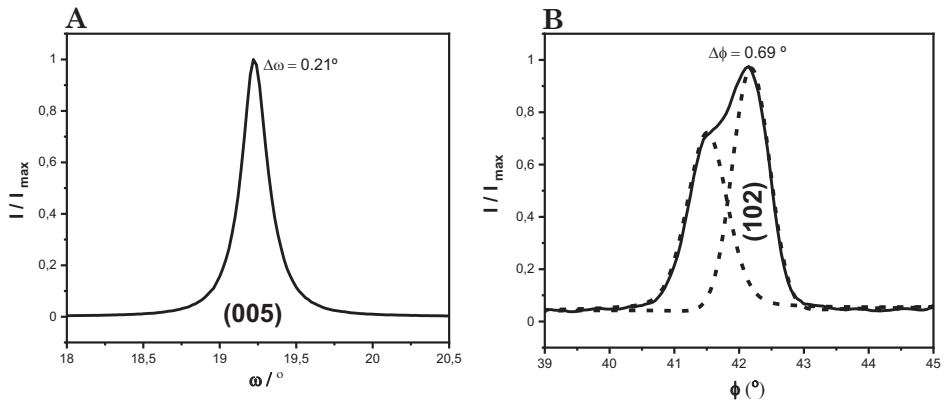

Figure 4.10 (A) Rocking curve and (B) ϕ scan of nanocomposite sample of 2-3 composite with 12%mol grown at 850 °C, heating with slow ramp, with a PO_2 jump from 10^{-5} bar to $2.8{\cdot}10^{-3}$.$\Delta\phi_{(102)}$ was obtained from FWHM of peak fitting of (102) reflection after deconvoluting from an overlapping peak from a STO reflection tail.

4.3.1.4 Limitations to high critical current densities with slow heating ramp

This section aims to compare pristine films with nanocomposite films grown using the slow heating ramp and to identify the causes of the current limitations. In the case of pristine films grown using slow heating ramp of ~0.2 °C/s it was found the best performance with 3-7 composition heating up to 840 °C with a PO_2 jump from 10^{-5} bar to $1.8{\cdot}10^{-3}$ bar. On the other hand, the best performance of nanocomposite films was achieved with 2-3 composting heating up to 850 °C with a PO_2 jump from 10^{-5} bar to $2.8{\cdot}10^{-3}$ bar. Therefore, the best texture and performance for nanocomposite and pristine films were achieved using different compositions and growth conditions reaching a maximum Jc at 77 K of 1.0 MA/cm^2 and 1.6 MA/cm^2, respectively. The corresponding SEM images (Figures 4.4A and 4.9A) show that homogenous films are finally obtained but a smoother surface was achieved in the case of the pristine sample. In addition, high epitaxial nucleation was reached but some random contribution remains in both cases, especially for nanocomposite film grown from a higher supersaturated liquid (2-3 composition). Moreover, growth conditions optimisation was also done to improve YBCO texture and superconducting properties where bad wetting and reactivity problems were also encountered.

The differences mentioned between pristine and nanocomposite films evidence that there should be slight differences in the YBCO growth mechanism when NCs are introduced. At the same time, there should be a common source in both cases employing the slow heating ramp which limited the improvement of performance to 1.0-1.6 MA/cm^2. There are several sources which could hinder current percolation in HTS [27] and in TLAG films [10, 33, 55] and we investigated the ones involved in these cases. Despite the a/b-grains and random nucleation contribution present in the films, the texture quality evaluated 4.3.1.1 was in the range of strong epitaxial films discarding it as the main cause of critical current reduction.

The carbon contamination of YBCO structure and its retention at grain boundaries [225] is another source of Tc and Jc density at self-field decreased [66, 225]. Consequently, we carried out GI XRD measurements where the signal of polycrystalline phases, as precursor phases from pyrolysis ($BaCO_3$ phase) and secondary phases are enhanced. The GI XRD patterns obtained from the best pristine and nanocomposite film are shown in Figure 4.11A. The most intense peaks of crystalline $BaCO_3$ phase (red arrow) are not detected meaning that complete $BaCO_3$ elimination is achieved in both compositions and growth conditions used for pristine and nanocomposites, respectively. This is in agreement also with the high Tc values reached of 89.2 K for nanocomposite and 90.2 K for pristine film, from transport measurements, which suggests that the YBCO phase is not carbon contaminated.

Furthermore, the formation of secondary phases during YBCO growth could also limit the superconducting cross-section or contaminate the grain boundaries [216]. In the GI XRD pattern (Figure 4.11A) we detect peaks from $Ba_2Cu_3O_6$ and Y_2BaCuO_5 phases. The reduction of the superconducting cross-section by the non-superconducting phase depends on its final size and the total film thickness. To better identify secondary phases embedded inside the film and determine their size, TEM characterisation of a pristine film was performed. The high-magnification STEM-HAADF image (Figure 4.11C) and HRTEM image (Figure 4.11D) shows the presence of $Y_2Cu_2O_5$, CuO, Cu_2O and BaY_2CuO_5 phases inside the film with a sizes above 50 nm. Some of these particles are detected placed in the discontinuities between YBCO grains.

The developed kinetic phase diagrams from in-situ XRD measurements of

TLAG films [43] show that at the first stage of the PO_2-route the main reactions of precursor solid phases are the reduction of CuO to Cu_2O and the reaction of the CuO/Cu_2O with $BaCO_3$ to mainly formed $BaCu_2O_2$ phase as the intermediated specie at 10^{-5} bar. These solid phases are different from the expected equilibrium phases (Y_2BaCuO_5 + $YBa_3Cu_2O_y$) from the previously reported YBCO phase diagram [68] and was attributed to the fast heating of the initial precursors in TLAG process. Concerning this, we evaluated the solid phases resulting from the first step of PO_2 in our system. We performed an experiment using a pristine sample (3-7 composition) which consists of heating with the fast heating ramp to a high temperature (840 °C in this case) under low PO_2 (10^{-5} bar, below the YBCO instability line), and then cooling without performing the PO_2 jump. These types of experiments are called quench processes. The resulting crystalline phases from the quench experiment are shown in Figure 4.11B. We found the formation of mainly Ba-Cu-O phases where $Ba_2Cu_3O_6$, Y_2BaCuO_5 and $Y_2Cu_2O_5$ are also the previous ones identified after the complete growth process through GI XRD and TEM characterisation. Therefore, the secondary phases observed after the YBCO growth (after the PO_2 jump) might be formed as a consequence of the slow heating used in the first step. The other Ba-Cu-O phases obtained cannot be confirmed if are formed before the PO_2 jump due to the $BaCu_2O_2$ phase being the main specie observed by in-situ XRD measurements but could come also from the fast solidification of the liquid phase from the faster cooling ramp used for quench experiments.

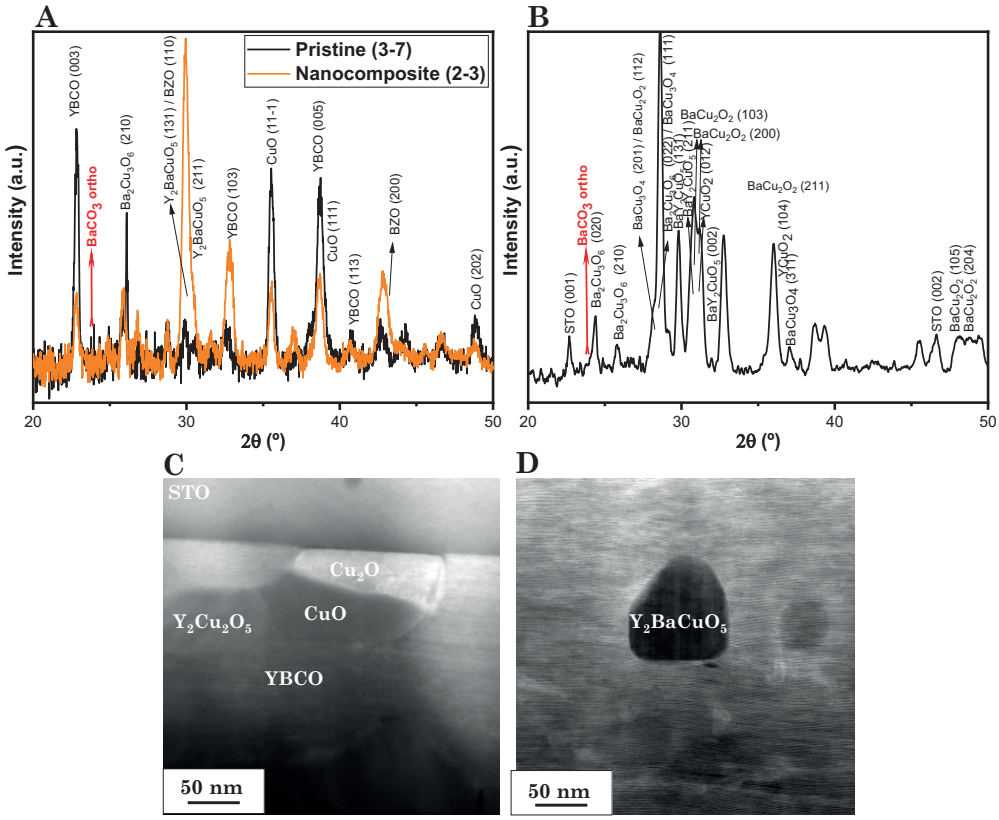

Figure 4.11 (A) GI XRD pattern of nanocomposite of 2-3 composition and pristine of 3-7 composition films with the best performance of slow heating and (B) GI XRD pristine film (3-7 composition) after a quench process at 840 °C and 10^{-5} bar with slow heating ramp of ~0.2 °C/s. Planes were assigned with the reference patterns: 04-006-6962 (YBCO), 00-005-0378 (BZO), 04-016-5583 ($Ba_2Cu_3O_6$), 00-038-1434 (Y_2BaCuO_5), 04-009-6869 ($BaCu_3O_4$), 00-039-0245 ($BaCu_2O_2$), 00-039-0244 ($YCuO_2$), 00-048-1548 (CuO) and 00-035-0734 (STO). (C) high-magnification STEM-HAADF images and (D) Bright-field HRTEM images of pristine film with 3-7 composition.

We postulate that the limited critical current densities obtained were derived from the use of a slow heating ramp (~0.2 °C/s) which could induces coarsening of precursor phases and the formation of large secondary phases. To overcome this problem and improve superconducting properties we carried out modifications in the set-up of the PO_2-route oven to achieve higher heating ramps of ~1 °C/s (details in section 4.2). The optimisation of TLAG nanocomposite films using the fast heating ramp is explained in the following section.

4.3.2 Growth of TLAG nanocomposite films with fast heating ramp

4.3.2.1 Heating ramp influence on the $BaCO_3$ elimination and secondary phases

Since the PO_2-route consist of two steps where YBCO crystallization is decoupled from $BaCO_3$ elimination, different kinetic parameters could affect each stage. Via in-situ XRD synchrotron experiments TLAG PO_2-route kinetic phase diagram was developed and it was demonstrated that the heating ramp is the main kinetic parameter governing the first stage of the process [43]. CuO reduction to Cu_2O and $BaCO_3$ elimination reactions are shifted to higher temperatures by increasing the heating ramp. In addition, it was observed that the YBCO growth rate depends significantly on $BaCO_3$ elimination and the heating ramp. Using fast heating ramps, coarsening of precursor and intermediate phases might be avoided favouring fast reactions of phases [10, 43].

The microstructure of the pristine film analysed in the previous section (Figure 4.11C-D) shows the coarsening of CuO, Cu_2O and also secondary phases such as BaY_2CuO_5. These phases were placed inside the film which could be related to the slow speed used for heating. Placing the furnace on top of the rails allows the heating ramp to be improved up to ~1 °C/s.

Firstly, we checked $BaCO_3$ elimination and secondary phases at the first step PO_2-route before YBCO nucleation with the modified set-up. We performed quench experiments with pristine and nanocomposite films. We heated with the fast heating ramp to 835 °C under low PO_2 of 10^{-5} bar and then cooling without performing the PO_2 jump. A detailed study of $BaCO_3$ elimination with the fast heating ramp was carried out in L.Saltarelli thesis for pristine samples. The GI patterns (Figure 4.12) show that we are also able to completely eliminate $BaCO_3$ phase (red arrow) heating at ~1 °C/s. Furthermore, the comparison of GI XRD patterns of pristine films quenched using slow (Figure 4.11B) and fast heating ramp (Figure 4.12) show an improvement in minimising secondary phases of Ba-Cu-O phases and BaY_2CuO_5 phase by the use of the fast heating ramp. The intensities of the corresponding Ba-Cu-O phases and BaY_2CuO_5 phase are reduced and some completely disappear whereas $BaCu_2O_2$ phase is

the main precursor phase detected after heating up to 835 ° and 10^{-5} bar. We also expected to mainly form $BaCu_2O_2$ solid phase when we performed the complete growth profile (Figure 4.1C), including the PO_2 jump to a high PO_2 where the YBCO phase is stable (≥ 10^{-4} bar), which is also correlated with the in-situ synchrotron XRD results [43].

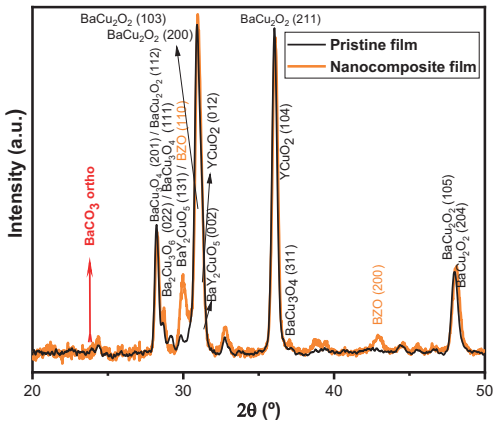

Figure 4.12 GI XRD patterns comparison of pristine (black) and nanocomposite (orange) films after a quench process at 835 ° and 10^{-5} bar with fast heating ramp of ~1 °C/s. Planes were assigned with the reference patterns: 00-005-0378 (BZO), 04-016-5583 ($Ba_2Cu_3O_6$), 00-038-1434 (Y_2BaCuO_5), 04-009-6869 ($BaCu_3O_4$), 00-039-0245 ($BaCu_2O_2$) and 00-039-0244 ($YCuO_2$).

Finally, the $BaCO_3$ elimination and secondary phases using the fast heating ramp were also evaluated for nanocomposite films. In the GI XRD measurement (Figure 4.12) we observe that after the quench at 835 ° and 10^{-5} bar, no peaks of $BaCO_3$ are detected, indicating also complete $BaCO_3$ elimination with a fast heating ramp of ~1 °C/s for nanocomposite films. Regarding secondary phases, we identify the same peaks as the pristine film, where the $BaCu_2O_2$ phase is also the main compound detected in both cases. Some secondary phases are more relevant in the case of nanocomposite film than pristine, although we also expected the same improvement in minimising secondary phases with a fast heating ramp for nanocomposite film, as can also be seen comparing the GI XRD pattern of the quench experiment with fast heating (Figure 4.12) and GI XRD of already grown nanocomposite film with slow heating (Figure 4.11A).

In summary, the heating ramp parameter has an influence on the precursor and intermediated phases obtained in the first stage of the PO_2-route (heating step under low PO_2). An enhancement in reducing secondary phases

was observed with a fast heating ramp for pristine and nanocomposite films. Concerning this, we expected differences in the final YBCO crystallisation (after PO_2 jump) depending on the heating ramp used. The intermediate precursor phases formed were different, and we suggested that utilising the fast heating ramp would result in less coarsening of any phase involved in the growth process.

4.3.2.2 Optimising nanocomposite growth conditions at fast heating ramps with 5 nm NCs

In this section, we will concentrate our efforts on optimising the growth of epitaxial nanocomposite films using the fast heating ramp (~1 °C/s). We considered as good starting conditions to promote high critical current densities due to the coarsening of precursor, intermediate phases and nanocrystals are expected to be further diminished [10] and secondary phases were demonstrated to be reduced and complete $BaCO_3$ elimination was ensured in the previous section 4.3.2.1.

The initial growth condition of nanocomposite films with fast heating ramp was the ones with strong epitaxial nucleation and good Tc and self-field Jc from the optimisation of pristine films with 3-7 composition. The multilayer architecture of the nanocomposite samples was changed (Table 4.1) to a pristine seed of 200 nm and one NP layer of 225 nm on STO to be in agreement with pristine film thickness. The nanocomposite films used contain 12% mol of ~5 nm-sized BHO NCs to promote that NCs themselves can act as pinning sites since an effective dimension for an artificial pinning centre should be in the range of the YBCO coherence length ξ (a few nanometres). [10, 55].

The nanocomposite film (3-7 composition) was grown heating to 835 °C with a heating ramp of ~1 °C/s under $PO_2 = 10^{-5}$ bar. Then, we performed a PO_2 jump to 10^{-3} bar with a dwell time of 5 min at these conditions. The temperature profile is shown in Figure 4.1C. The 2D GADDS XRD images and SEM images of pristine and nanocomposite films grown under this condition are displayed in Figure 4.13A-B.

From the texture point of view, highly epitaxial nucleation is reached for both samples as no reflections of misoriented YBCO orientations (random and

a/b-grains) are detected and (00l) YBCO reflections are shown in 2D GADDS XRD images (Figures 4.13A and B). The corresponding SEM images show that more flat surfaces are obtained in the case of pristine than for nanocomposite films as we previously observed for slow heating (Figures 4.4A and 4.9A). SQUID measurements were also performed for both films observing in the case of pristine film and improvement of Jc self-field at 77 K from 1.6 MA/cm^2 to 2.5 MA/cm^2 by increasing the heating ramp. In the case of nanocomposite film, self-field Jc is almost kept from 1.0 MA/cm^2 to 0.7 MA/cm^2 increasing heating ramp.

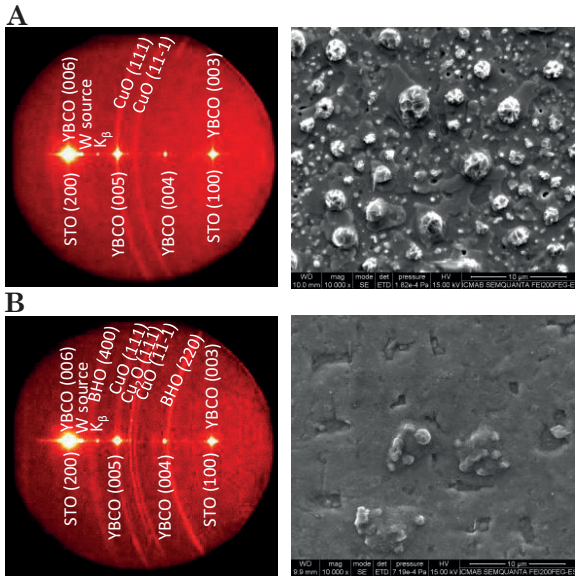

Figure 4.13 2D GADDS XRD and SEM images of (A) pristine film with 3-7 composition (B) nanocomposite film with 12%mol BZO and 3-7 composition grown at 835 °C with a PO_2 jump from 10^{-5} bar to 10^{-3} bar.

The different surface morphologies and critical current densities obtained for nanocomposite and pristine films with fast heating and slow heating suggest that NCs could sightly affect the kinetics of the TLAG process. We decided to tune liquid composition and the PO_2 jump for nanocomposite films to improve critical current densities. We carried out two experiments growing with 3-6 composition (Y:2Ba:4Cu) at different final PO_2, which is an intermediate liquid composition between 2-3 and 3-7 compositions and shows a sightly higher supersaturation than 3-7. The first sample was grown by performing a PO_2 jump from 10^{-5} bar to $1.8{\cdot}10^{-3}$ bar (Figure 4.14A) and the second one from 10^{-5} bar to

10^{-3} bar (Figure 4.14B). The XRD texture of both samples shows that by raising the final PO_2 we increase supersaturation conditions promoting the formation of random YBCO and a/b-grains. We detect (103), (102) and (200) plane reflections at $1.8{\cdot}10^{-3}$ bar. The SEM image of the sample grown at $1.8{\cdot}10^{-3}$ bar also confirms the formation of a/b grains by the presence of perpendicular grains under the growth conditions mentioned. By reducing the final PO_2 to 10^{-3} bar with 3-6 composition, we achieve highly epitaxial nucleation and smoother surface (Figure 4.14B) than with 3-7 composition grown at the same T-PO_2 conditions (Figure 4.13B). Despite the increase of supersaturation with 3-6 respect to 3-7 composition decreasing the final PO_2 from 1.8 10^{-3} bar to 10^{-3} bar we also tuned supersaturation diminishing and achieving strong YBCO epitaxial growth with 3-6 composition.

The good texture and morphology obtained for this nanocomposite were reflected in an improvement of critical current density, achieving a self-field Jc of 2.1 MA/cm^2 at 77 K and 20.2 MA/cm^2 at 5 K. This result confirms an enhancement of superconducting properties by increasing the heating ramp and using 3-6 composition with better wettability. Therefore, ensuring the optimal precursor and intermediate phases, and limiting phase coarsening in the first step of the PO_2-route dependent on heating ramps along with the optimal YBCO growth conditions for epitaxial nucleation are crucial aspects for promoting c-axis nucleation and good properties.

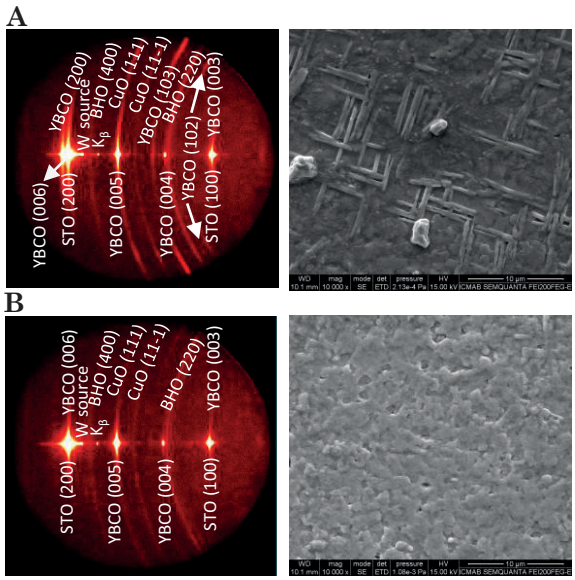

Figure 4.14 2D GADDS XRD and SEM images of nanocomposite films with 3-6 composition grown with fast heating ramp at (A) at 835 °C with a PO_2 jump from 10^{-5} bar to $1.8{\cdot}10^{-3}$ bar and (B) at 835 °C with a PO_2 jump from 10^{-5} bar to 10^{-3} bar.

The microstructure of the nanocomposite film of 2.1 MA/cm^2 at 77 K was analysed by TEM and the results are presented in Figure 4.15. The cross-section STEM-HAADF images (Figure 4.15A and B) show a continuous and homogenous film of ~ 480 nm of YBCO thickness. However, in the low magnification cross-section STEM-HAADF images is observed the presence of a large pores of ~ 200 nm at the interface with the STO substrate (Figure 4.15A). This interface pores, depending on their size, could be a source of reducing the superconducting cross-section [33, 34, 216–218]. Therefore, the interface porosity observed was also investigated and will be discussed in the following sections. In addition, agglomeration of BHO NCs with ~ 25-35 nm of size and some even larger are identified by EDX on the top of the film. Despite the layer of BHO NCs on top of the film, some epitaxial BHO NCs of < 20 nm and random BHO NCs of ≥ 20 nm are detected inside the film by HRTEM characterisation of a near-surface area (grey region below agglomerated BHO NCs layer). The HRTEM image (Figure 4.15B) shows an epitaxially embedded BHO NC of ~ 10 nm in the YBCO matrix.

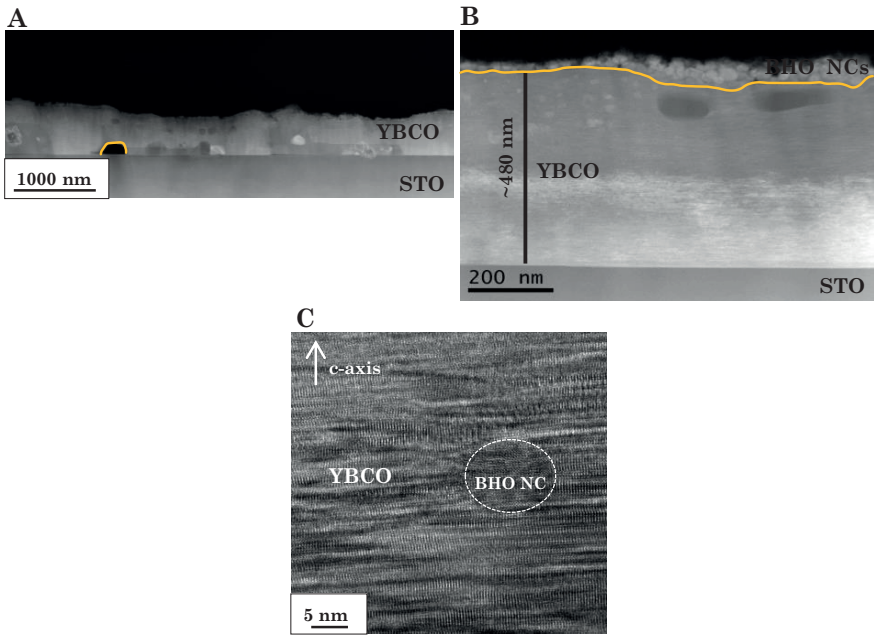

Figure 4.15 (A) Cross-sectional low-magnification STEM-HAADF image showing a interface pore indicated by a yellow line, (B) Cross-sectional high-magnification STEM-HAADF image where agglomeration of NCs at the surface was indicated by a yellow line (C) Bright-field HRTEM image showing epitaxially embedded BHO NC of epitaxial YBCO growth from nanocomposite film of 3-6 composition and 12% mol BHO (5 nm) with Jc of 2.1 MA/cm^2 at 77 K.

In conclusion, despite the high self-field Jc achieved for nanocomposite film of 2.1 MA/cm^2 at 77 K the cross-sectional TEM analysis allows to study NC distribution and identified, in this case, pushing of the BHO NCs towards the YBCO surface. The migration and agglomeration of NCs to the YBCO surface would decrease the NC density inside the film decreasing the amount of pinning sites. For these reasons, the next section is focused on the strategies to overcome the NC pushing effect.

4.3.2.3 NC pushing and trapping processes in TLAG films

4.3.2.3.1 NC size tunning effect on NC pushing and trapping

The formation of nanocomposite films through the preformed-NPs approach, based on the introduction of preformed NCs to the YBCO precursor solution,

provides more control over the final NP characteristics such as size and size distribution in the YBCO film [85, 95, 97]. The homogeneous distribution of NCs in the YBCO matrix is important to maximize the density of pinning centres [81, 86]. However, limitations such as either NC pushing to the YBCO surface or accumulation at the substrate interface have been observed in previous works with TFA and low-fluorine CSD routes using preformed-NCs such as CeO_2, ZrO_2 and $SrTiO_3$ NCs [95, 97, 226]. In addition, the pushing of NCs on the top of the film was also identified in the TLAG process using the spontaneous-segregation approach to grow BZO-nanocomposites films [55].In the previous section (4.3.2.2) we observed the presence of BHO NCs on the top of the film which could be explained with the pushing/trapping theory where the basis principles are described in the following subsection.

Pushing/trapping effect

The pushing/trapping phenomena of an insoluble particle through a liquid by an advancing solid-liquid interface during a solidification process is well described in different types of materials [27, 227, 228]. The ability of the liquid to push or trap solid particles during the crystallisation process depends on the forces acting in the particle due to the interaction with the solid-liquid interface. An attractive viscous force and a repulsive force due to interfacial energy ($\Delta\sigma_0$) are considered. The forces are influenced by various parameters defining a critical radius (r*) at which the particle will be trapped in the solid, following the equation:

$$r^* \propto \frac{\Delta\sigma_0}{\eta R} \tag{4.5}$$

where η is the liquid viscosity and R is the growth rate. According to the theory, larger particles (particle size exceeds the r*) tend to be trapped whereas small particles (particle size below the r*) are pushed out of the growing solid-liquid interface. Therefore, the behaviour of NCs during the YBCO growth and their interaction with the growth interface can be modified by increasing the YBCO film growth rate by adjusting the processing conditions and increasing viscosity by changing liquid composition and processing parameters. Another strategy could be the decrease of interface energy which depends on NC composition, faceting, and liquid properties among others and also by the NC size

through the tune of the initial NP size to reach r*. Due to the high growth rates found in TLAG process [42] small-sized NCs should be able to be trapped.

Following the basic principles of the pushing/trapping theory, the first strategy to avoid pushing was to increase the initial NC size above ~ 5 nm. In the work of Cayado et al. [95] modifying the preformed CeO_2 NC size from ~2 nm to 6 nm they elimitated the pushing effect observed in TFA-nanocomposites films. For these reasons, firstly we carried out an effort to optimise and understand the synthesis of $BaMO_3$ colloidal solutions (Chapter 2) for fine control of the final NC size (section 2.3.1.3.1). This allowed the study of the distribution of NCs in grown nanocomposite films with an initial BZO NC size above 5 ± 1 nm, particularly with BZO NC sizes of 7 ± 2 nm and 10 ± 2 nm, and with 3–7 composition, which proved to be the most effective for producing the highest Jc in pristine films, and due to pushing/trapping effect is dependent on NC size but not on liquid composition.

Thorough cross-sectional low-magnification STEM-HAADF images (Figure 4.16A-C) of the nanocomposite films with different initial NC sizes we measured YBCO film thickness of ~ 400-450 nm. Furthermore, large pores of the maximum size of ~ 500 nm are also observed in different areas of the interface with STO substrate for nanocomposite with ~ 7 nm (Figure 4.16B) and 10 nm-sized NCs (Figure 4.16C), as was previously observed for nanocomposite with ~ 5 nm (Figure 4.16A). The interface porosity could be also a problem to reach high critical current densities as depending on their size superconducting cross-section is reduced [216–219]. In addition, we postulated that interface substrate porosity, in this case, has a different origin than the dewetting observed in nanocomposite films grown with the slow-heating ramp (section 4.3.1.2). The discussion of this topic and the strategies to avoid it will be discussed later in section 4.3.2.4.

The NC arrangement in the film was also analysed by high-magnification STEM-HAADF images. Increasing the NC size from ~ 5 nm to ~ 7 nm we observe a reduction of NC pushing as some BZO NCs are identified at the top of the surface but not forming a continuous NC layer (Figure 4.16B) as in the case of ~ 5 nm-sized BHO NCs (Figure 4.16A). In the nanocomposite film using ~ 10 nm of preformed BZO NCs (Figure 4.16C, we also observe less quantity of NCs accumulated on the surface. Despite that the pushing effect is limited by ~

10 nm sized-NCs and some BZO NCs of ~ 10-12 nm are detected inside the film (Figure4.17B) some larger particles of 50-100 nm are also present (Figure4.17A). In this particular case, we cannot assume that these larger particles are formed due to NC coarsening or agglomeration or are large secondary phases. The high density of defects generated by the presence of NCs inside the YBCO matrix difficulties, in some cases, the identification of NCs by TEM analysis especially, if they are epitaxially oriented.

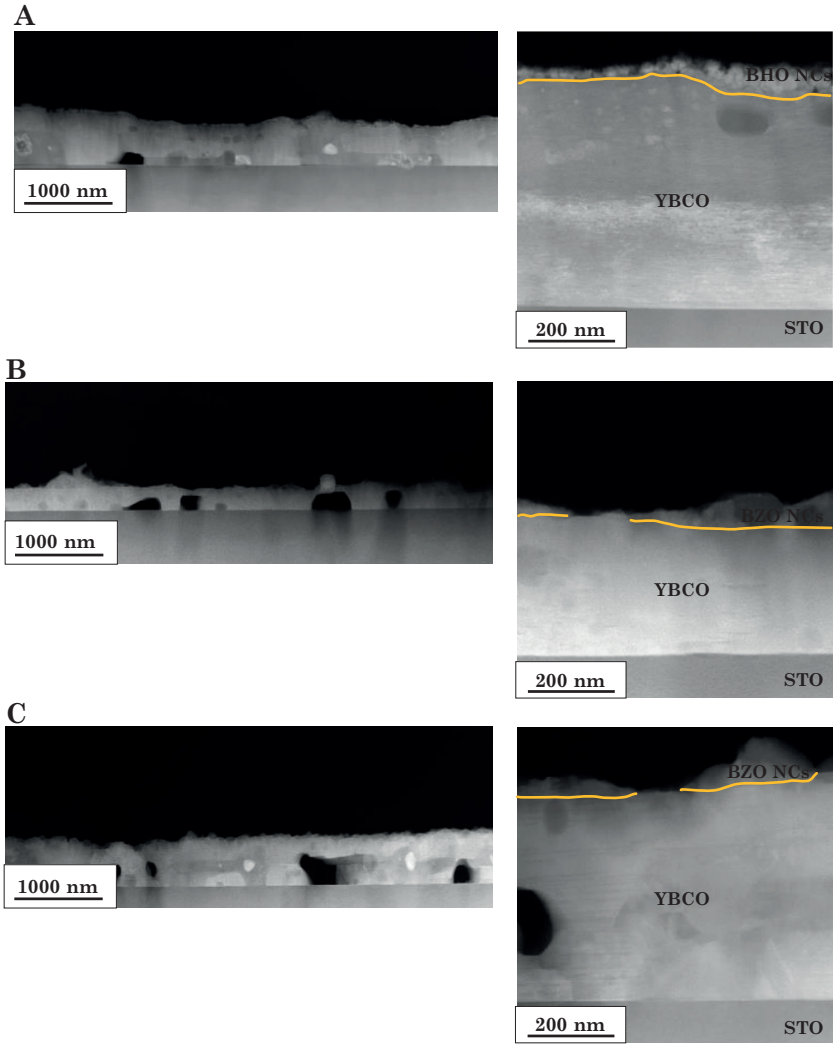

Figure 4.16 Cross-sectional low-magnification (right) and high-magnification (left) STEM-HAADF images of grown nanocomposite films using preformed-NCs with an initial size of (A) 5 ± 1 nm (B) 7 ± 2 nm (C) 10 ± 2 nm.

Despite that the pushing effect is limited by ~ 10 nm sized-NCs and some BZO NCs of ~ 10-12 nm are detected inside the film (Figure4.17B) some larger particles of 50-100 nm are also present (Figure4.17A). In this particular case, we cannot confirmed that these larger particles are larger NCs generated by NC coarsening, or secondary phases but could decrease superconducting cross-section. The high density of defects generated by the presence of NCs inside the YBCO matrix difficulties, in some cases, the identification of NCs by TEM analysis especially, if they are epitaxially oriented.

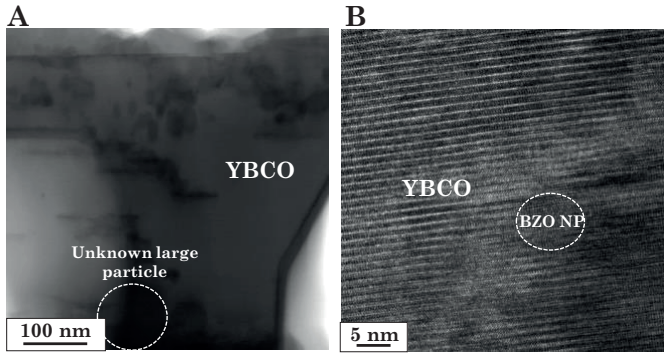

Figure 4.17 (A) Bright-field Scanning Transmission Electron Microscopy (BF-STEM) image with a large particle of ~ 100 nm identified and (B) BF-HRTEM image with an epitaxial BZO NP of ~ 10 nm from nanocomposite film using preformed-BZO NCs with 10 ± 2 nm.

These results show that by increasing the initial NC size from 5 ± 1 nm to 7 ± 2 nm and/or 10 ± 2 nm the NC pushing effect can be reduced during YBCO crystallisation through the TLAG process. Larger NCs of 7 ± 2 nm and/or 10 ± 2 nm display a higher tendency to be trapped within the YBCO matrix than 5 ± 1 nm-sized NCs. These results suggest that the critical radius (r*) has been reached or nearly achieved with this larger NC size, as the NC pushing, although not completely avoided, was effectively limited.

Going in the direction of improving pinning properties, we focused on the conditions that favoured the higher number of small-sized NCs homogeneously distributed inside the YBCO matrix. For this reason, the next section is based on the optimisation of the growth parameters to enhance pinning properties using 7 ± 2 nm sized-BZO NCs for nanocomposite film formation. This initial NC size is closer to the vortex diameter (few nanometers) at the temperature range of interest than 10 ± 2 nm sized-NCs expecting a higher pinning effect.

In addition, ~7nm-sized NCs should also show a higher tendency to be trapped inside the film (higher number of pinning sites) than the ~5 nm-sized NCs, according to the pushing/trapping theory. Furthermore, despite the rapid TLAG YBCO growth kinetics, the NC coarsening due to the heating treatment should be slightly smaller for 7 ± 2 nm than 10 ± 2 nm NCs.

4.3.2.3.2 Optimising nanocomposite growth conditions using 7 nm size NCs: PO_2 base effect

In this section, we will focus on understanding and optimising the growth conditions of PO_2-route for strong epitaxial YBCO nanocomposite films using ~ 7 nm sized-NCs where NC pushing is limited. In the case of previous nanocomposite films with ~ 5 nm sized-NCs, the highest self-field Jc obtained was 2.1 MA/cm^2 at 77 K using 3-6 composition and decreasing the final PO_2 from $1.8{\cdot}10^{-3}$ to 10^{-3} bar. In the case of pristine samples, the highest Jc self-field value (2.5 MA/cm^2 at 77 K) was obtained with 3-7 composition heating at 835 °C with a PO_2 jump from 10^{-5} bar to 10^{-3} bar. The increase of the final PO_2 also did not result in an improvement of texture quality or properties. For these reasons, we optimised another growth parameter, the PO_2 used during the heating treatment (PO_2 base) for 3-7 composition. We expected to know its effect in the kinetics of the first stage of the PO_2-route for nanocomposite growth. At this stage, $BaCO_3$ elimination and coarsening of intermediate phases are crucial processes to be controlled.

To investigate the PO_2 base parameter in the formation of nanocomposite films with 12% mol BZO NCs of 7 nm size and 3-7 composition, we performed two experiments. One film was grown at 835 °C with a PO_2 jump from 10^{-5} bar to 10^{-3} bar and another from 10^{-6} bar to 10^{-3} bar. The corresponding results of YBCO texture and surface morphology are shown in Figure 4.18A-B. We observe that at both PO_2 base samples are full c-axis textured. In addition, both nanocomposite films show homogeneous surfaces with some small spherical particles of CuO phase on the top which come from the copper excess of 3-7 composition [33, 46].

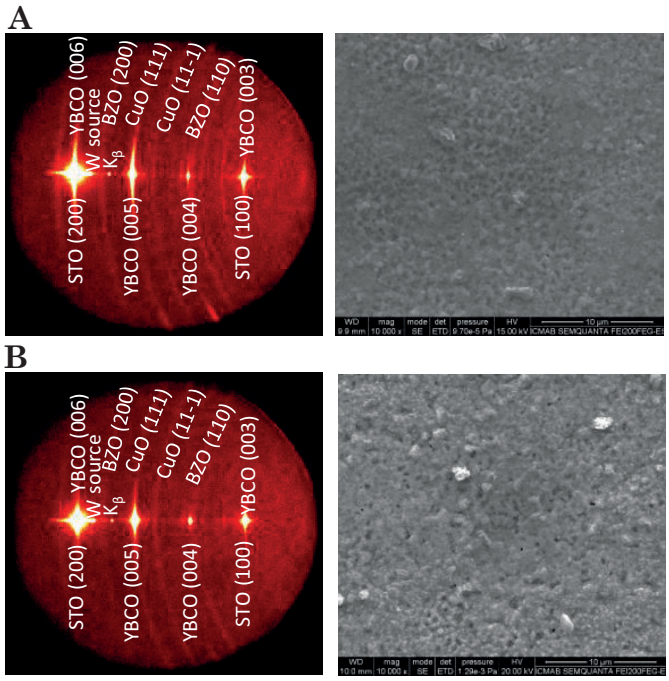

Figure 4.18 2D GADDS XRD and SEM images of nanocomposite films with 3-7 composition grown with fast heating ramp at (A) at 835 °C with a PO_2 jump from 10^{-5} bar to 10^{-3} bar and (B) at 835 °C with a PO_2 jump from 10^{-6} bar to 10^{-3} bar.

Rocking curve, ϕ scan and c-axis lattice parameter were evaluated in order to test the crystalline quality of the nanocomposite films grown at different PO_2 base and the values are plotted in Figure 4.19A. The values obtained $\Delta\omega$ = 0.33-0.44°,$\Delta\phi$ = 0.72-0.87° and c ~ 11.69 Å are in the range of the previous strong epitaxial thin nanocomposite TLAG films (100 nm) of $\Delta\omega$ = 0.1-0.5°, $\Delta\phi$ = 0.6-1° and c = 11.67-11.69 Å [10, 55]. We can observe that sightly lower values are obtained for nanocomposite grown from 10^{-6} bar which are closer to the values of the best performance of pristine films ($\Delta\omega$ = 0.18°, $\Delta\phi$ = 0.6° and c ~ 11.68 Å). Despite the slight differences observed, it seems that decreasing the PO_2 base from 10^{-5} to 10^{-6} produces nanocomposite films with high crystalline and texture quality.

To investigate more about the PO_2 base parameter, which is involved in the first step of the PO_2-route, we carried out two quench processes at both PO_2 base. GI XRD measurements were done to better check the polycrystalline phases such as $BaCO_3$ and secondary phases. As we discussed in section 4.3.2.1 at 10^{-5} bar complete $BaCO_3$ elimination was observed, and $BaCu_2O_2$ phase was

the main intermediated specie found. The comparison of GI XRD patterns of both nanocomposite quench experiments (Figure 4.19B) shows that we achieved the same main intermediate phases but the PO_2 base decreased to 10^{-6} bar promotes the reduction of the intensities of some secondary phases peaks such as $BaCu_3O_4$, $Ba_2Cu_3O_6$ and Y_2BaCuO_5 (grey squares).

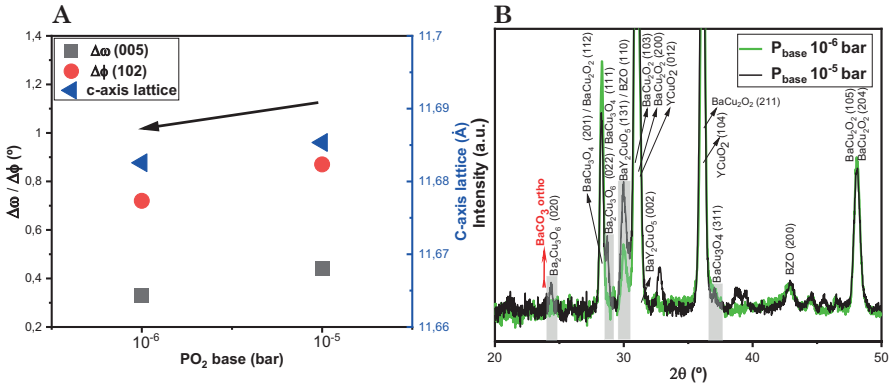

Figure 4.19 (A) Summary of $\Delta\omega$, $\Delta\phi$ and c-axis parameter of nanocomposite films grown at 835 °C with a PO_2 jump from 10^{-5} to 10^{-3} bar and from 10^{-6} to 10^{-3} and (B) GI XRD pattern comparison of nanocomposites quenched at 10^{-5} bar (black) and 10^{-6} (green) films. Identified reflections that reduced their intensity at 10^{-6} bar are indicated with grey square. Planes were assigned with the reference patterns: 00-005-0378 (BZO), 04-016-5583 ($Ba_2Cu_3O_6$), 00-038-1434 (Y_2BaCuO_5), 04-009-6869 ($BaCu_3O_4$), 00-039-0245 ($BaCu_2O_2$) and 00-039-0244 ($YCuO_2$).

Finally, the Jc self-field of both nanocomposites grown from different PO_2 bases were measured. The Jc self-field at 77 K obtained of nanocomposite grown at 835 °C with a PO_2 jump from 10^{-5} to 10^{-3} was 1.1 MA/cm^2, confirming an improvement of Jc with 3-7 composition using ~ 7 nm-sized NCs compared to the previous Jc values obtained with ~ 5 nm-sized NCs of 0.7 MA/cm^2 at 77 K (section 4.3.2.2). This is possibly related to the limiting NC pushing using ~ 7 nm-sized NCs, previously confirmed with TEM analysis (Figure 4.16B), which improved superconducting properties. Moreover, the Jc self-field at 77 K increases from 1.1 MA/cm^2 to 2.5 MA/cm^2 by the decreasing the PO_2 base from 10^{-5} to 10^{-6} bar with 3-7 composition. This last value reaches the best critical current density of pristine films (2.5 MA/cm^2 at 77 K). SQUID measurements comparison between pristine and nanocomposite films are shown in Figure 4.20A. The Jc enhancement is possibly associated with the slightly better epitaxial growth and sight reduction of secondary phases growing at 835 °C and using the PO_2 jump from 10^{-6} to 10^{-3} bar for nanocomposite films. These slight improvements

suggest less coarsening during heating at 10^{-6} bar but further studies should be done to elucidate this relevant aspect.

As discussed in the previous section, the NC pushing is limited using 7 nm-sized BZO-nanocomposite films. Thus, to evaluate the vortex pinning efficiency, derived from the density of SFs and the associated localized strain regions generated inside the nanocomposite and pristine films, Jc(H) dependence was measured from SQUID to determine the crossover magnetic field (μ_oH*) values.μ_oH* is defined as the magnetic field where Jc reaches the 80% of Jc self-field value [10]. In addition, μ_oH* characterises when the single-vortex regime changes to vortex-vortex interaction regime, indicating that Jc starts to decrease with the magnetic field. Therefore, μ_oH* increases with the density of defects in the film and can be used as a measure of the vortex pinning density [47, 80, 83, 229]. We observe in the Jc(H) dependence and normalised field dependence (Figure 4.20B and inset) that nanocomposite film shows a smoother Jc(H) dependence than pristine film. This, suggests that the single vortex pinning regime determined by μ_oH* is shifted towards higher magnetic fields. The μ_oH* values at 5 K (0.16 T) and 77 K (0.02 T) of nanocomposite film doubles the pristine μ_oH* values of 0.07 T at 5 K and 0.01 T at 77 K. Moreover, μ_oH* obtained are in the range of the highest values of TFA-CSD YBCO nanocomposite films measured by SQUID [47, 85]. The μ_oH* elongation by a factor of ~ 2 of the nanocomposite TLAG films as compared to pristine implies an improvement of vortex pinning by introducing NCs. A detailed discussion of the pinning properties of TLAG nanocomposite is given in section 4.3.2.5.

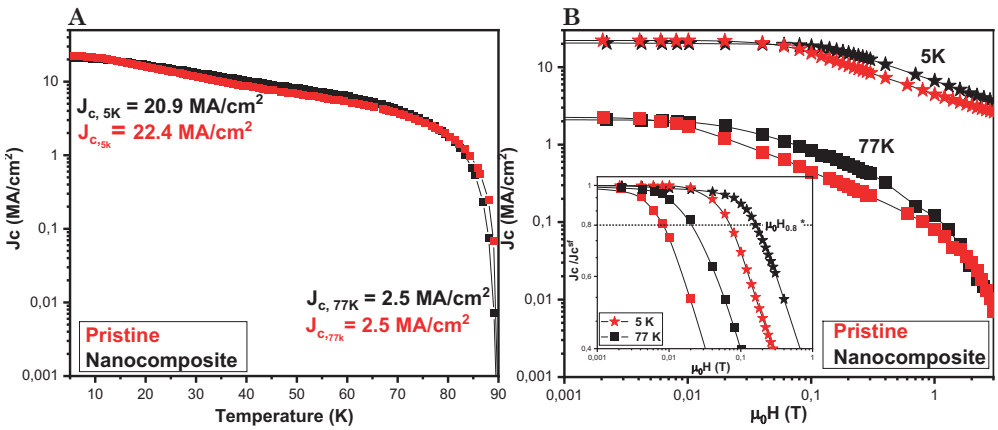

Figure 4.20 (A) Jc (T) dependence at self field and (B) Jc (H) dependence and normalised field dependence to its maximum Jc self-field value (inset) at self-field obtained from SQUID measurements at 5 and 77 K of nanocomposite film with 12%mol 7 nm sized BZO NCs (orange) and pristine (black) film.

Finally, the reproducibility of the nanocomposite TLAG film that reached Jc self-field of 2.5 MA/cm^2 using 12%mol of BZO NCs (7 nm) grown at the optimal growth conditions investigated, has been demonstrated. The characterisation of YBCO texture, surface morphology, and Jc self-field measured by SQUID and Tc measured from resistivity (ρ) of three replicates, is shown in Figure D.1 A-D. The comparison of the results obtained confirms that the TLAG-CSD approach is highly reproducible for nanocomposite film formation using the developed nanocomposite precursor solution.

In conclusion, these results confirmed an improvement of critical current densities with 3-7 composition for nanocomposite films by the increase of NC size from ~ 5 nm (0.7 MA/cm^2) to ~ 7 nm (1.1 MA/cm^2) together with the decrease of PO_2 base from 10^{-5} to 10^{-6} bar (2.5 MA/cm^2). Furthermore, the limitation of the pushing effect using 7 nm-sized BZO NCs produced the increase of single-vortex pinning plateau (μ_0H*) compared to pristine, suggesting that we have limited the NC pushing effect. The next two sections are focused on the improvement of vortex pinning efficiency by the increase of the NC amount (% mol) and film thickness, evaluating their influence on YBCO texture quality and physical properties.

4.3.2.3.3 Influence of NC amount on YBCO texture quality and physical characterisation

Previously reported results of varying NC amount from 6-32 %mol in thin TLAG nanocomposite films with 100 nm of total thickness [10, 55] did not result in a strong effect on texture quality ($\Delta\omega < 0.6°$). Moreover, self-field Jc at 77 K in the range of 1.7-2.2 MA/cm^2 were achieved for nanocomposite films with 6 and 12 %mol. Then, the increase of NP amount to 24 and 32%mol results in the drop of the Jc to 0.2 MA/cm^2 that was attributed to the presence of ab-YBCO nucleation and NC agglomeration.

To investigate the influence of the NC amount also in thicker nanocomposite films (400-500 nm), nanocomposites with 6,12,18 and 24 % mol of 7 nm-sized BZO NCs and 3-7 composition were grown using the optimal conditions found in the previous section 4.3.2.3.2. The effect of the different NC densities on YBCO texture was analysed by 2D GADDS XRD. The GADDS XRD images (Figure 4.21A) show the fully YBCO epitaxial nucleation obtained from 6 to 24% mol of NC amount using the same defined growth conditions. The integration of GADDS XRD images allows us to detect how the most intense peak of the cubic phase of BZO, the (110) peak, increases with the NC amount (Figure 4.21B). Furthermore, the ω-scan measurements (Figure 4.21C) confirm that the presence of NCs inside the film up to 24 %mol does not show a strong influence on the epitaxial grain alignment, obtaining $\Delta\omega$ values below 0.5°. In addition, the surface microstructure of the nanocomposite films was analysed by SEM. The SEM images show smooth surfaces for all the %mol tested (Figure 4.21D).

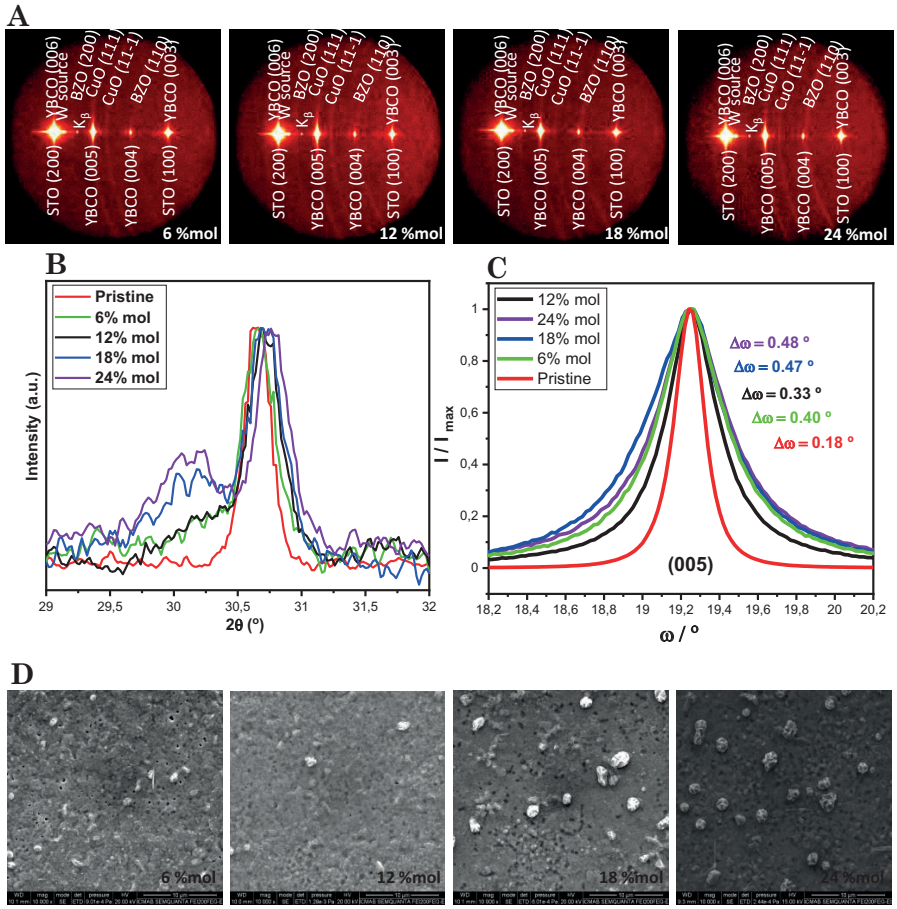

Figure 4.21 (A) 2D GADDS XRD images of nanocomposites films grown with 6,12,18 and 24 %mol (from left to right) of BZO NCs (7 nm), (B) Comparision of integrated XRD patterns (normalising each XRD pattern with their corresponding intensity reached of (004) YBCO reflection) varying the % mol and including a pristine film with a zoom in the θ-2θ region (29-32 °) of the most intense peak of BZO, the (110) plane. (C) Rocking curves (ω-scans) of YBCO (005) reflection of pristine and nanocomposite films and (D) SEM images of nanocomposite films grown with 6,12,18 and 24 %mol (left to right) of BZO NCs (7 nm).

Regarding physical properties, Figure 4.22A summarised the critical temperatures (Tc) obtained from resistivity measurements using Van der Pauw method (section A.8.2.1) for nanocomposite films modifying the NC amount (6-24 % mol) including pristine film. The fluctuation of the Tc values from replicates of pristine, 12 %mol and 18 %mol-nanocomposite films is given by the error bars (standard deviations). A Tc of ~ 90 K is obtained for the whole range

of NC content, confirming that neither zirconium nor carbon ions are intercalated in the YBCO structure, as expected. Thus, confirming the purity of YBCO phase. As the cation substitution in the YBCO matrix due to the presence of preformed-NCs is assumed to be less probable, the sightly drop of Tc in the case of nanocomposite films (6-18 %mol) compared to pristine might be related to the strain generated on the YBCO structure from the contribution of epitaxial embedded NCs. This strain results from a lattice mismatch of approximately 8% between BZO and YBCO [10, 55, 230, 231]. Additionally, the reduction in Tc could also be influenced by the oxygen content (Hall carrier densities) in these films, measured by transport measurements, which suggest slightly overdoped conditions [10]. The 24 %mol-nanocomposite film does not follow the same tendency of Tc diminishment, possibly related to the NC agglomeration tendency at increased NC amounts. If agglomerated NCs remain inside the film a reduction of Jc self-field would have been observed, which will be discussed later.[10, 55]. However, if NCs aggregate and remain within the film, and if non-agglomerated NCs push to the surface as well, the epitaxial NC density inside the film will decrease. The lower expected epitaxial NC density, which provides strain in the YBCO matrix, could affect the expected expansion of the c-axis with 24 %mol, probably explaining the Tc value being similar to pristine film.

Moreover, the effect of tuning the NC amount with nanocomposite films on critical current density was also evaluated. Figure 4.22B shows an overview of self-field Jc values at 5 K and 77 K as a function of the NC amount, including the fluctuation of the Jc from the replicates of pristine, 12 %mol and 18 %mol-nanocomposite films by error bars. Jc self-fields at 5 K and 77K are kept varying the NC amount in the range of 19.3-23.9 and 2.4-2.6 MA/cm^2. Therefore, there are only slight variations in critical current densities with NC amount, and all nanocomposite films from 6-24 % mol exhibit high Jc values at 5K and 77K. The increased variability in Jc self-fields, as indicated by the error bars, for the 18%mol-nanocomposite may be attributed to sightly reproducibility problems concerning non-controlled NC pushing or NC agglomeration at this increased NC content. However, their effect is not sufficient to hinder current percolation or reduce the Jc but contributes to larger differences in Jc values among replicates. Consequently, the effort performed for optimising nanocomposite films with propionate-based colloidal precursor solution with controlled initial NC characteristics (Chapter 2), such as 7 nm-sized NCs with high stability, has

proven to be very effective for TLAG nanocomposite films. It was demonstrated in Chapter 3 that these developed precursor solutions provide nanocomposite precursor films that retain the initial small sizes of NC and have a homogenous NC distribution, which allows them to reach high performances up to 24% mol, as demonstrated in this section, optimising also the growth conditions. This becomes a significant improvement compared to the previous thin (100 nm) TLAG nanocomposite films from acetate-based precursor solutions, where a Jc reduction to < 0.2 MA/cm^2 at increased NC amounts of 24% and 32%mol was observed related to NC agglomeration.

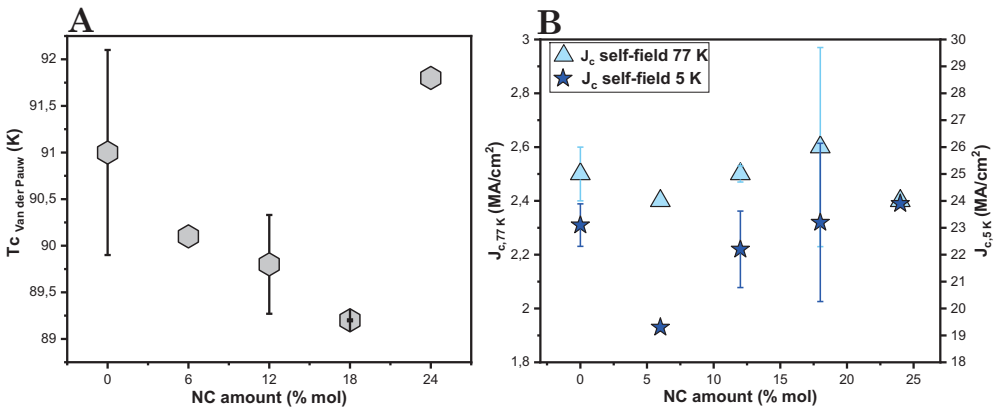

Figure 4.22 (A) Tc measurements by Van der Pauw method and (B) Jc self-field values (5 K and 77 K) from SQUID of nanocomposite films of different %mol and pristine films. Errors bars correspond to the standard deviation of the different obtained values at the same %mol.

Finally, we characterised by TEM the microstructure of the nanocomposite films with 6 to 24 % mol. The STEM-HAADF images show that using 7 nm-sized NCs the pushing effect is limited in 6 and 12 % mol (Figure 4.23A and B). However, as the NC content is increased to 18 and 24 % mol (Figure 4.23C and D), we observe NC agglomeration forming a layer on top of the film surface, which could explain the higher Tc value obtained in the range of pristine film for 24 %mol. Furthermore, NC agglomeration within the film is also detected in the case of 24 %mol (Figure 4.23D) confirming that this could be a source of the drop in Jc self-field observed. The uncontrolled pushing effect becomes more pronounced at higher NC amounts of 18 % mol and 24 % mol. This explains the slight variations in reproducibility of Jc self-field observed in the case of 18 % mol compared to 12 % mol.

In addition, concerning the previously identified interface porosity of 12 % mol, it is not observed in the cases of nanocomposite films using 6 % mol, 18 % mol and 24 % mol. This observation will be discussed in detail in section 4.3.2.4.

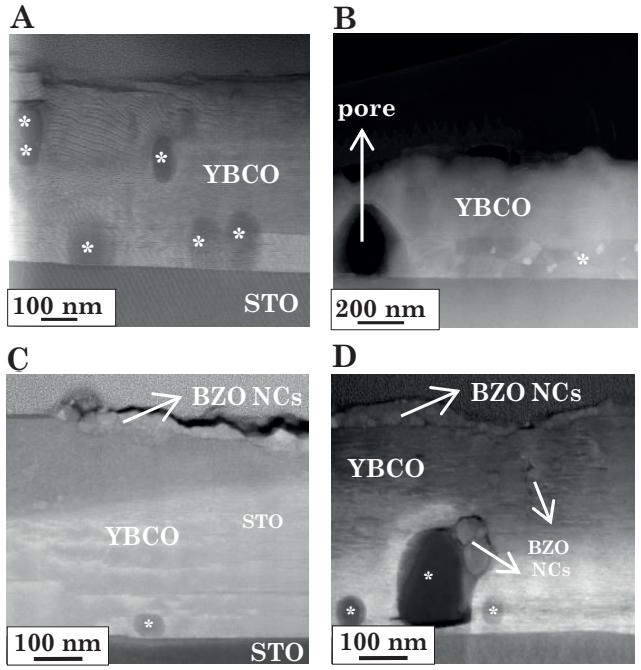

Figure 4.23 STEM-HAADF images of nanocomposite films using 7 nm sized BZO NCs with (A) 6%mol, (B) 12%mol, (C) 18%mol and (D) 24%mol. Secondary phases are identified by star marks.

The influence of varying %mol of preformed-BZO NCs on the YBCO microstructure in terms of nanostrain and defect landscape and the vortex pinning efficiency will be analysed in section 4.3.2.5. Furthermore, the influence of increased film thickness on nanocomposite films will also be evaluated, but firstly, its effect on texture quality and physical properties will be discussed in the following section.

4.3.2.3.4 Influence of increased film thickness on YBCO texture quality and electromagnetic characteristics

Going in the direction of implementing TLAG methodology for coated conductors (CCs), many requirements need to be ensured first for YBCO nanocomposite films on STO. Increase the YBCO film thickness (in the range of 1 micrometre or higher) maintaining a good Jc that consequently increases the total critical current Ic (A), or critical current per centimetre-width, I_{c-w} (A/cm-w) is one of the requirements.

To prove the compatibility of the TLAG process with the growth of thick nanocomposite films, we increased the thickness through the multi-deposition method by spin-coating from 425 ± 25 nm to 650 ± 25 nm for 6%mol BZO and up to 875 ± 25 nm for 18%mol BZO in nanocomposite films (3-7 composition). The thick nanocomposite films (650 ± 25 nm and 875 ± 25 nm) were grown under the PO_2 route processing conditions optimised for 425 nm of thickness (section 4.3.2.3.2) heating at 835 °C with a PO_2 jump from 10^{-6} bar to 10^{-3} bar.

First, the surfaces of the thick nanocomposite films with 6 %mol and 18 %mol were characterised through SEM technique (Figure 4.24A-B). SEM images indicate dense and flat surfaces without considerable differences in surface morphologies by thickness increase.

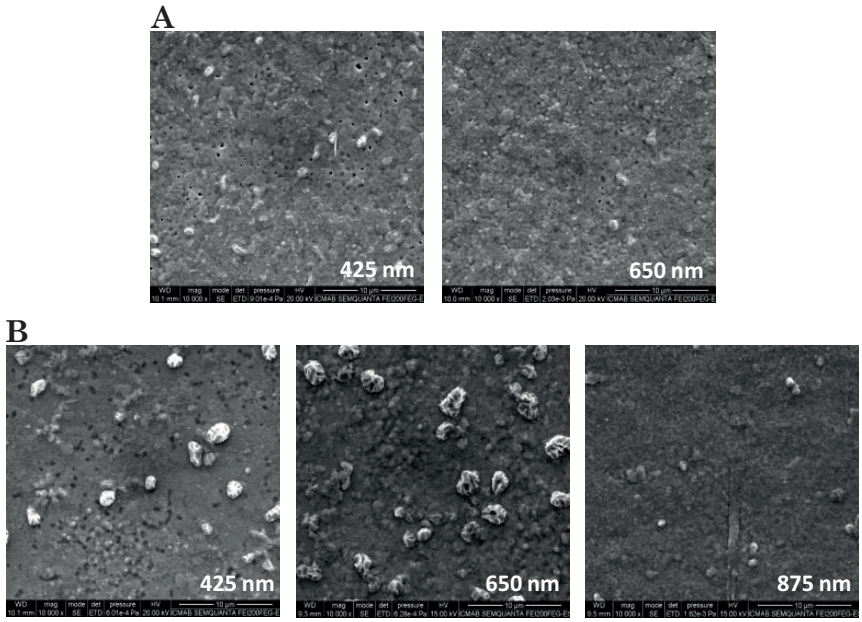

Figure 4.24 SEM images of (A) multideposited nanocomposite films (425 ± 25 nm and 650 ± 25 nm) with 6%mol BZO and (B) multideposited nanocomposite films (425 ± 25 nm, 650 ± 25 nm and 875 ± 25 nm) with 18%mol BZO grown at 835 °C with a PO_2 jump from 10^{-6} to 10^{-3} bar.

The YBCO texture of 6 %mol and 18 %mol nanocomposite films increasing thickness was further studied by 2D GADDS XRD images (Figure 4.25A and B, respectively). The 2D GADDS XRD images show that at 650 ± 25 nm some random YBCO nucleation denoted as YBCO (103) remained and the intensity of the ring becomes more pronounced at 875 ± 25 nm (18 %mol-nanocomposite film case).

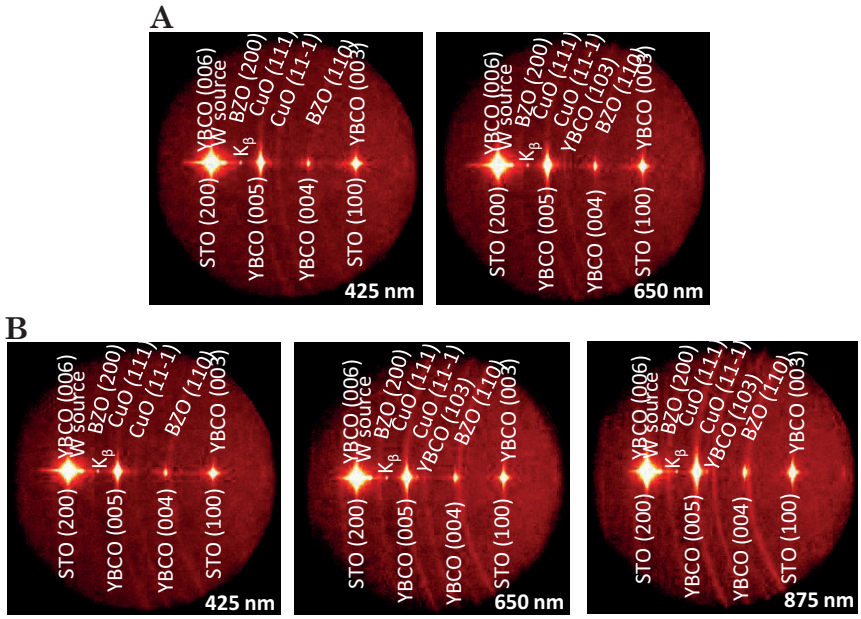

Figure 4.25 2D GADDS XRD images of (A) multideposited nanocomposite films (425 ± 25 nm and 650 ± 25 nm) with 6%mol BZO and (B) multideposited nanocomposite films (425 ± 25 nm, 650 ± 25 nm and 875 ± 25 nm) with 18%mol BZO grown at 835 °C with a PO_2 jump from 10^{-6} to 10^{-3} bar.

In addition, HR XRD measurements (Figure 4.26A-B) show a high intensity of the YBCO (00l) peaks for all nanocomposite films indicating a high degree of epitaxial nucleation while a minor fraction of YBCO ab-grains, indicated as YBCO (200) reflection, is also detected. The peak signal of ab-grains increases by increasing film thickness, especially for 18%mol-nanocomposite films with 650 ± 25 nm to 875 ± 25 nm of film thickness (Figure 4.26B). The higher amount of a/b grains in 18%mol-nanocomposite film with 875 ± 25 nm of film thickness can also be detected through SEM in backscattered electrons (BSE) imaging mode, as shown in Figure 4.26C. Nonetheless, the contribution of misoriented grains is very small compared with the high intensity of the YBCO (00l) peaks (epitaxial YBCO reflections), and consequently, we can consider that the biaxial texture is well preserved up to ~ 900 nm of film thickness.

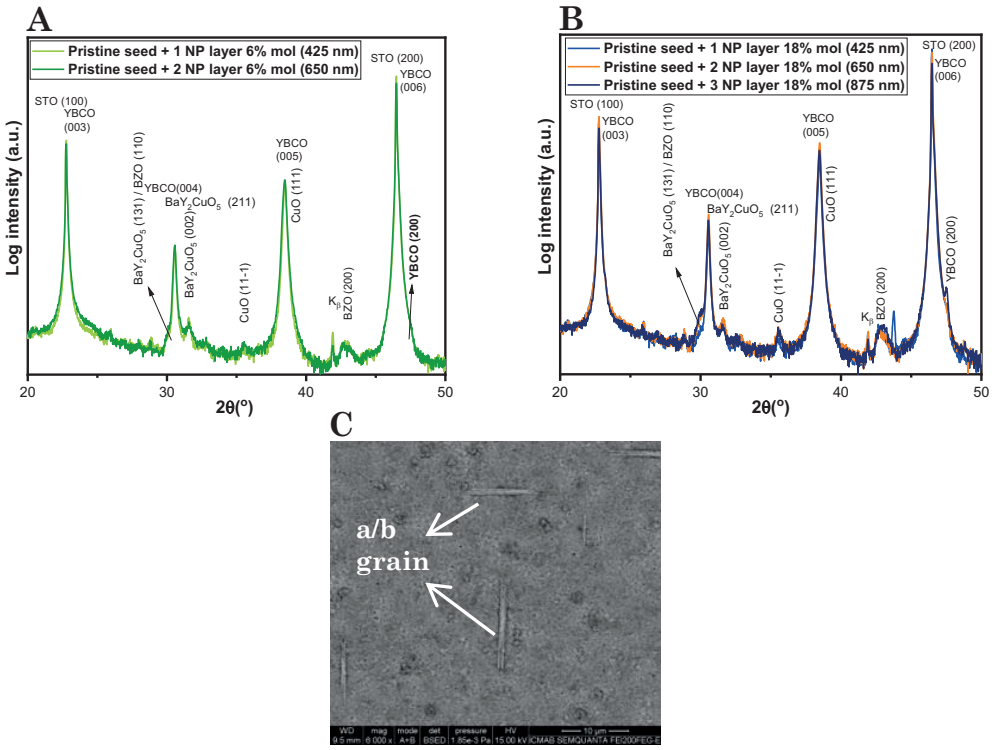

Figure 4.26 HR XRD patterns of (A) multideposited nanocomposite films (425 ± 25 nm and 650 ± 25 nm) with 6%mol BZO and (B) multideposited nanocomposite films (425 ± 25 nm, 650 ± 25 nm and 875 ± 25 nm) with 18%mol BZO grown at 835 °C with a PO_2 jump from 10^{-6} to 10^{-3} bar. (C) SEM image in backscattered electrons (BSE) imaging mode from nanocomposite film of 875 nm and 18%mol BZO where a/b grains are identified.

Complementary, the texture degree of c-axis grains for films of different multidesposited thicknesses (425 ± 25 nm to 650 ± 25 nm and 875 ± 25 nm) using 6 %mol and 18 %mol was evaluated. The rocking curves are shown in Figure 4.27A. The values of $\Delta\omega(005)$ of thick films tested for 6 %mol and 18 %mol slightly increased from those of 425 nm thick films. The texture quality of the nanocomposite films seems not to be influenced by thickness increase, obtaining $\Delta\omega(005)$ in the range of 0.4-0.55 ° for 650 ± 25 nm and 875 ± 25 nm of total thickness, confirming the good texture also for up to ~ 900 nm.

Additionally, the critical current densities of the thicker films were determined through inductive measurements. The results show that the self-field Jc values at 77 K and 5 K are kept increasing thickness from ~425 to ~650 nm in the range of 2.3-2.6 MA/cm^2 and 19.3-27.4 MA/cm^2 respectively. In the case

of increasing thickness up to ~900 nm for 18% mol, the drop of Jc is observed from 2.6 to 1.5 MA/cm^2 at 77 K and 27.4 to 16.2 MA/cm^2) at 5 K. We believe that the texture quality observed where small random and ab-grains were present in the thick sample could not solely explain the decrease of Jc by a factor of approximately 2. However, the a/b grains observed in the SEM image (Figure 4.26C) could contribute to hindering current percolation. In addition, the slightly higher values of the rocking curves seem to follow the same direction.

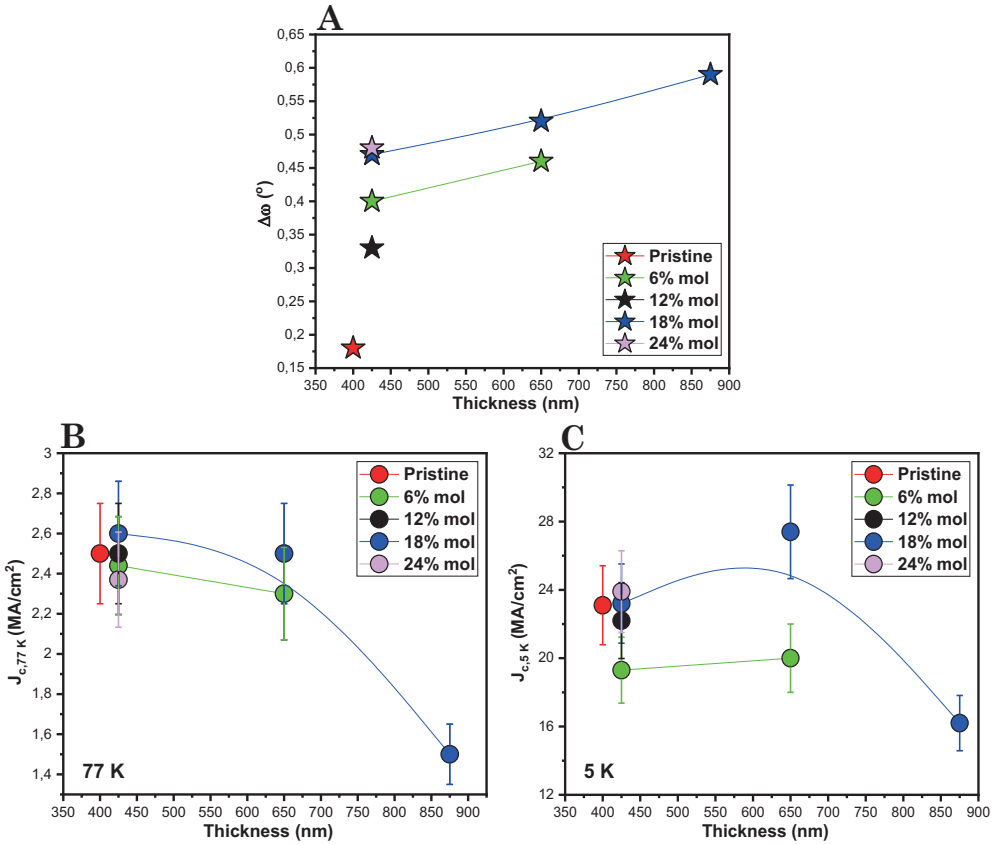

Figure 4.27 (A) $\Delta\omega$ dependence with film thickness, (B) self-field Jc at 77K and (C) self-field Jc at 5K versus thickness of pristine film and nanocomposite films with 6, 12, 18, and 24% mol NCs of different film thickness (425 ± 25 nm to 650 ± 25 nm and 875 ± 25 nm).

Then, we evaluated if the PO_2-route system and the growth conditions used were enough to completely eliminate the $BaCO_3$ phase for 875 nm of film thickness, which is another possible source of superconducting cross-section reduction [10, 65, 66]. The GI XRD pattern (Figure 4.28) shows complete $BaCO_3$

elimination, although some minor secondary phases, such as $Ba_2Cu_3O_6$ and BaY_2CuO_5 are detected. These results suggest that the diminished critical current density (Jc) in thick nanocomposite film may be associated with a decrease in the superconducting cross-section. This reduction could be related to the presence of larger secondary phases or a/b-grains within the film. Despite the potential limitations to critical current density (Jc), further fine-tuning of growth conditions, such as a slight increase in temperature or a decrease in Po_2 is expected to increase the Jc of ~900 nm thick nanocomposite film, currently limited to 1.5 MA/cm^2 at 77K.

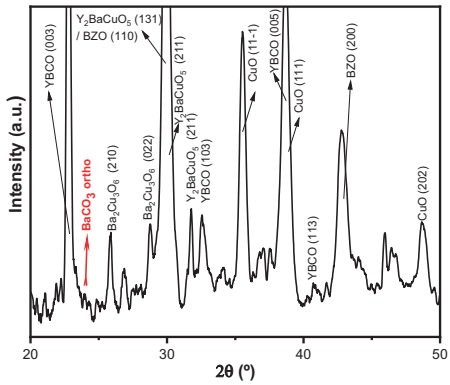

Figure 4.28 GI XRD pattern of nanocomposite film (seed pristine and 3 NP layers with 18% mol BZO) after growth at 835°C with a PO_2 jump from 10^{-6} to 10^{-3} bar. Planes were assigned with the reference patterns: 04-006-6962 (YBCO), 00-005-0378 (BZO), 04-016-5583 ($Ba_2Cu_3O_6$), 00-038-1434 (Y_2BaCuO_5) and 00-048-1548 (CuO).

Regarding the YBCO growth of thick nanocomposites films, we have demonstrated the robustness of the TLAG process through the PO_2-route when we found the optimal processing conditions achieving high epitaxial films ($\Delta\omega(005) \leq 0.6$ °) with good critical current densities (1.5-2.6 MA/cm^2 at 77K) from 425 to 875 nm of film nanocomposite thickness. The vortex pinning improvement by the increased thickness in nanocomposite films will be investigated in section 4.3.2.5.

4.3.2.3.5 Influence of NC composition on YBCO texture quality and electromagnetic characteristics

After the optimisation with BZO NCs where we achieved good texture, performance, and reproducibility of nanocomposite films, we decided to investigate the effect of NC composition. Previous studies showed no differences in YBCO nucleation and superconducting self-field properties using both NC compositions [10, 55]. Both of them are effective in improving the pinning landscape, but nanostrain and crossover magnetic field are slightly higher for BHO than BZO observed in the cases of trifluoroacetate (TFA) [47, 85], low-fluorine TFA-route [48, 86, 93, 94, 232] and TLAG process [10, 55]. This was explained by the slightly higher lattice mismatch of ϵ^{BHO} (8.9%) than ϵ^{BZO} (8.4%), which induces a higher density of defects, but also by the higher melting point of BHO (~ 2600 °C) than BZO (~ 2500 °C). The NC coarsening and aggregation in REBCO films are related to the melting point of NCs, showing a higher tendency to coarsening and aggregation when the growth temperature is close to the NC composition melting point as the atomic mobility increases [55, 214]. Consequently, the tendency towards coarsening and agglomeration should be higher for BZO than for BHO. Therefore, a film with higher densities of smaller, non-aggregated and homogenously distributed NCs is more favourable in the case of BHO composition [55] and was also demonstrated for YBCO nanocomposite grown from low-fluorine colloidal solutions with different AMO_3-type NCs (A= Ba and Sr and M= Zr, Hf and Ti) [86].

Concerning this, we checked the compatibility with BHO NCs of 6 ± 2 nm with the TLAG-CSD process using propionate-based YBCO precursor solutions and growing under the optimised conditions for BZO NCs.The YBCO texture from 2D GADDS XRD image of BHO-nanocomposite film is shown in Figure 4.29A. The BHO-nanocomposite film shows strong epitaxial nucleation grown under the same conditions as the BZO-nanocomposite films with 7 ± 2 nm-sized BZO NCs (Figure 4.18B). The YBCO texture quality was also evaluated and slight differences were observed. The $\Delta\omega$ obtained for BHO-nanocomposite film is 0.45° compared to 0.33° obtained from BZO-nanocomposite film.

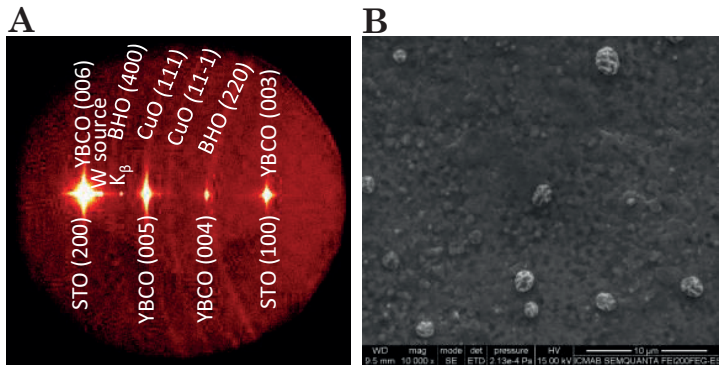

Figure 4.29 (A)2D GADDS XRD and (B) SEM image of nanocomposite films with 3-7 composition of one SEED pristine layer (200 nm) and one NP layer with 12% mol BHO NCs (~ 425 nm) grown at 835 °C with a PO_2 jump from 10^{-6} bar to 10^{-3} bar.

Regarding the superconducting properties, a high Jc value is also achieved for BHO-nanocomposite film of 2.7 MA/cm^2 at 77K and 27 MA/cm^2 at 5K. The Jc(T) (Figure 4.30A) and Jc(H) (Figure 4.30B) dependence of BHO-nanocomposite film were evaluated through SQUID measurements. The Jc(T) and Jc(H) curves of both NC compositions are compared. BHO composition shows a slightly higher Jc(T) and Jc(H) dependence than BZO. The crossover magnetic field (μ_oH*) values determined show similar pinning behaviour of both nanocomposite films. A μ_oH* of 0.16 T at 5 K and 0.02 T at 77 K for BZO-nanocomposite film and 0.15 T at 5 K and 0.02 T at 77 K for BHO-nanocomposite film are obtained. A Tc of 93K was also determined by resistivity measurement for BHO-nanocomposite film, and together with the 89.8 K of Tc obtained for BZO-nanocomposite film, the Hf and Zr cation substitutions in the YBCO structure were discarded.

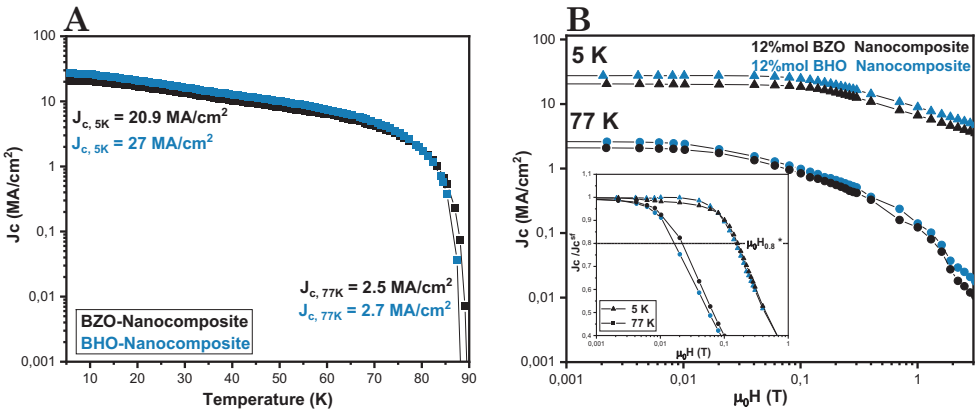

Figure 4.30 (A) Jc(T) dependence at self-field and (B) Jc(H) dependence at 5 K and 77 K from SQUID measurements of nanocomposite films with 12% mol BHO NCs (blue) and 12% mol BZO NCs (black).

These preliminary results with BHO-nanocomposite films demonstrated the compatibility of the developed nanocomposite precursor solution with BHO NCs with TLAG process. High epitaxial growth, high critical current densities, and similar pinning properties as for BZO NCs were reached. Further characterisation and optimisation of the BHO-nanocomposite films should be performed to investigate in detail the existence of differences in the pinning behaviour between both NC compositions.

4.3.2.3.6 Pristine CAP layer effect for hindering NC pushing

The optimisation of nanocomposite films with ~ 7 nm sized BZO NCs performed in the previous sections, confirmed that we can reach strong epitaxial nucleation and high critical current densities of 2.4-2.6 MA/cm^2 at 77K using 6-24 %mol for 425 nm of total film thickness. In addition, the compatibility with multideposited films up to 875 nm with high Jc of 1.5-2.6 MA/cm^2 at 77K for 6 and 18 %mol was demonstrated. The improvement of superconducting properties was possibly related to the restricted of NC pushing using ~ 7 nm sized-NCs instead of ~ 5 nm according to pushing/trapping theory and as cross-section TEM images confirmed in Figure 4.16A and B.

Here, we focused on another strategy to overcome the NC pushing effect based on the use of a different multilayered architecture in nanocomposite films. The strategy was based on the use of a pristine layer on top of the NP layer

(pristine CAP layer). We performed an experiment growing a multideposited nanocomposite film with 3-7 composition of a pristine seed layer (200 nm) followed by an NP layer of 12% mol 5 nm sized BHO NC (225 nm) and pristine CAP layer (200 nm). We tested using ~ 5 nm sized-BHO NCs, as 5 nm of NC size shows the highest tendency of over-surface pushing (section 4.3.2.3.1) being the best NC size for the proposed strategy. In addition, ~ 5 nm sized-BHO NCs were also used as the pinning efficiency depends on the size of pinning centres where an improvement is observed when the initial mean NC size is closer to the vortex diameter and due to less NC coarsening is obtained after the growth process [47]. This particular nanocomposite film was grown at 835 °C with a PO_2 jump from 10^{-5} to 10^{-3} bar given the high pristine volume in the multilayered architecture of the film.

The YBCO texture was analysed by 2D GADDS XRD (Figure 4.31A) showing highly epitaxial growth with some minor contribution of random nucleation denoted as YBCO (103). The overall texture quality analysis of the nanocomposite film shows good out-of-plane ($\Delta\omega$ ~ 0.4°) texture. In addition, the Jc self-field of the nanocomposite film was measured by SQUID reaching 1.1 MA/cm^2 and 10 MA/cm^2 at 77 K and 5 K, respectively. Further complete elimination of random nucleation and improvement of Jc self-field could be achieved through a fine-tuning of the growth conditions for thick nanocomposite films (~ 625 nm) in lower supersaturation conditions, where epitaxial nucleation is more favoured. The SEM image of the resulting film is shown in Figure 4.31B. The surface morphology closely resembles that of films without a pristine CAP layer (Figure 4.18B), although it exhibits a slightly smoother appearance.

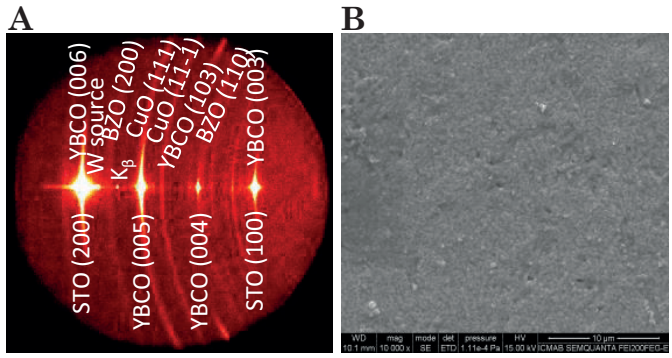

Figure 4.31 (A) 2D GADDS XRD image and (B) SEM image of nanocomposite film with seed pristine layer and 1 NP layer with 12% mol 5 nm BHO and pristine CAP layer (~ 625 nm) grown at 835 °C with a PO_2 jump from 10^{-5} to 10^{-3} bar.

Initially, to identify NC accumulation on the surface of nanocomposite film using the pristine CAP layer, cross-sectional SEM was performed. The cross-section SEM view obtained from a FIB cut (Figure 4.32A) indicates that NCs appear to be trapped within the film as no NC agglomeration is observed on top of the surface. This contrasts with the previously observed case of nanocomposites utilizing 5 nm-sized NCs without a pristine CAP layer (Figure 4.16A). Moreover, we identify pores that produce discontinuities in the YBCO films in the interface STO/YBCO that were previously detected in nanocomposite films (Figure 4.16A-C).

The NC distribution within the YBCO matrix was studied by BF-STEM and HRTEM. The BF-STEM image (Figure 4.32B) shows that BHO NCs are trapped under the pristine CAP layer and no NCs are detected on the surface. In addition, CuO particles are detected inside the film, suggesting that some CuO phases were not expelled to the surface during YBCO growth. This, together with the contribution of some random nucleation, could explain the lower self-field Jc reached. Although the BF-STEM image suggests that NCs are accumulated in one region of the film (dark-contrasted particles in the region identified as YBCO + BHO NCs), the HRTEM images performed in this region (Figure 4.32C and D) show that NCs remain homogeneously distributed in this region and no NC accumulation at the CAP pristine layer interface was detected. The most NC detection in the region denoted as YBCO+BHO, below the pristine layer, could be explained by the expected distribution from the multilayered architecture used for this nanocomposite film, which is based on a SEED pristine layer, NP layer and CAP pristine layer.

Furthermore, BHO NCs with a size of ~ 7-11 nm are epitaxially embedded in the c-axis YBCO matrix (Figure 4.32C-E) while some ~ 20 nm-sized BHO NCs identified show randomly oriented distribution (Figure 4.32D). This suggests that there is a coarsening effect, with a maximum factor of 2-4 to the initial NC size, as the mean final NC size measured ranges from approximately 7-20 nm. This effect is likely attributed to coalescence occurring during the high-temperature treatments employed in the film formation process [25].

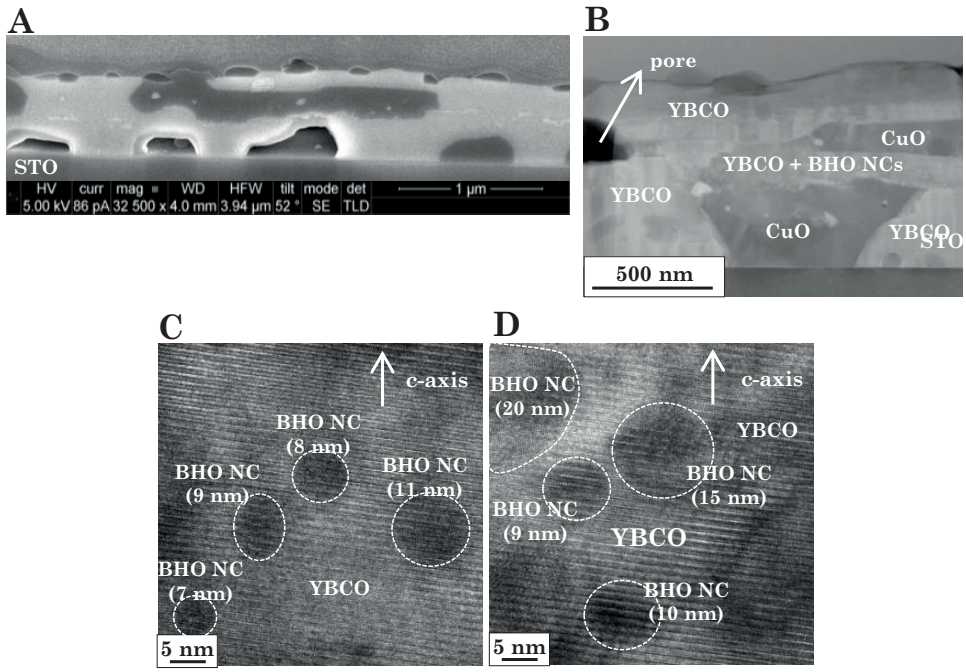

Figure 4.32 (A) Cross-sectional SEM image (B) BF-STEM image (C) BF-HRTEM image showing epitaxially embedded BHO NCs from the region denoted as YBCO+BHO NCs in BF-STEM image and (D) BF-HRTEM image showing epitaxially embedded BHO NCs and randomly oriented BHO NC of ~ 20 nm from the region denoted as YBCO+BHO NCs in BF-STEM image.

As a final remark, despite the interface porosity issue, the presence of minor misoriented grains or secondary phases within the film in thick nanocomposite film (above ~ 425 nm), under the processing conditions used, a further fine-tuning of temperature and pressure is expected to improve the texture quality and performance. This is particularly crucial for nanocomposite films based on multilayered architectures comprising pristine and nanocomposite layers with expected different growth conditions. Nevertheless, we have shown that NC pushing is effectively completely avoided through the use of a pristine CAP layer. We propose that this effective strategy may be attributed to the different viscosities of the liquid phase generated in the pristine and nanocomposite layers in the multilayered architecture film, which difficulties the NC diffusion within the pristine CAP layer. A detailed discussion of this effect will be provided in the subsequent section. In addition, the thickness of the pristine CAP layer also needs to be optimised to find the minimum thickness to avoid NC

pushing while diminishing the derived effects from the different growth conditions of the pristine and nanocomposite layers.

4.3.2.4 Strategies towards avoiding interface substrate porosity in TLAG nanocomposite films

In previous sections, it was observed by cross-sectional low-magnification STEM-HAADF images of nanocomposites films with the layer architecture of pristine seed (200 nm) and 1 NP layer (225 nm) of 12% mol BZO NCs (5, 7 and 10 nm) (Figure 4.16A-C) the presence of pores, mainly in the substrate-SEED pristine interface. Furthermore, it was also identified in the previous section for the thick nanocomposite film with the architecture: pristine seed (200 nm), 1 NP layer (225 nm) of 12% mol BHO NCs (5 nm) and pristine CAP layer (200 nm) (Figure 4.32A).

These holes are uncovered areas of STO, are at the substrate interface, and are surrounded by YBCO grains. It is important to note that these voids are different from the voids observed during the slow-heating ramp (dewetting), where the substrate interface was completely covered and holes were discontinuities in film thickness that did not reach the substrate (Figure 4.5B). Poor grain connectivity due to bad wetting generating pores is one of the many factors that produce a reduction in superconducting cross-section [216–218]. Hence, we performed an investigation on the interface porosity identified in nanocomposite films, considering it as one of the potential factors restricting the critical current density to 2.6 MA/cm^2.

There are several sources of porosity in YBCO films described in references, as we mentioned in section 4.3.1.2. Poor wetting might arise from the low viscosity that promotes high liquid diffusivity, which favours bad wetting to minimise the high interfacial energy between the liquid phase and substrate (bad wetting). Moreover, low nucleation density can be promoted by the high lattice mismatch between YBCO and the substrate, favouring dewetting. In all two scenarios, the formation of faceted, separated grains is necessary to minimise the interface energy. In the case of fast heating, the pores have no defined shape and are predominantly situated at the substrate interface without extending to the film surface. This suggests that the origin of the observed porosity may be

distinct from the factors analysed in section 4.3.1.2.

Other sources reported are residual porosity in pyrolyzed films and voids derived from a/b-grains or secondary phases [25, 233–235]. In Chapter 3, it was demonstrated by TEM that the microstructure of pyrolyzed nanocomposite films was very compact with no observable pores. Additionally, very few a/b-grains or secondary phases are detected by XRD and TEM characterization, discarding their significant influence on the observed high density of pores in the films.

Furthermore, these holes could resemble bubbles generated through the release of by-products in gaseous phases. In the TLAG process, the possible gaseous diffusion problems could come from the release of CO_2 from the $BaCO_3$ elimination ($BaCO_{3(s)} + Cu_zO_{(s)} \rightarrow BaCu_zO_{2(s)} + CO_{2(g)}$). This explanation, appears less probable, as we would expect to detect the formation of porosity in the initial stage of the PO_2-route when the elimination of $BaCO_3$ occurs. However, the STEM-HAADF image of a quenched sample (heating to 835 °C at 10^{-6} bar below YBCO instability line) does not show the presence of holes (Figure 4.33).

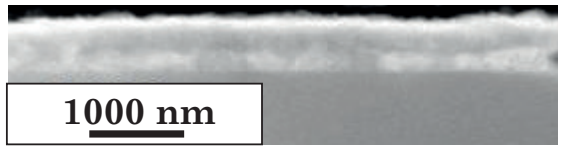

Figure 4.33 Cross-sectional STEM-HAADF of a nanocomposite film with a pristine SEED (200 nm) and a NP layer of 12%mol BZO (225 nm) quenched at 835 °C and PO_2 of 10^{-6}.

The STEM-HAADF characterisation of a multideposited pristine film (Figure 4.34A), composed of one pristine layer (200 nm) and another pristine layer (200 nm), exhibits a completely pore-free continuous layer. This observation suggests that the porosity arises during the formation of the transient liquid phase in the second step of the PO_2-route and is more prominent in multilayered films with varied compositions, such as nanocomposite films based on one pristine seed layer (200 nm) and one NP layer with 12 %mol nanocomposites (225 nm) (Figure 4.34B).

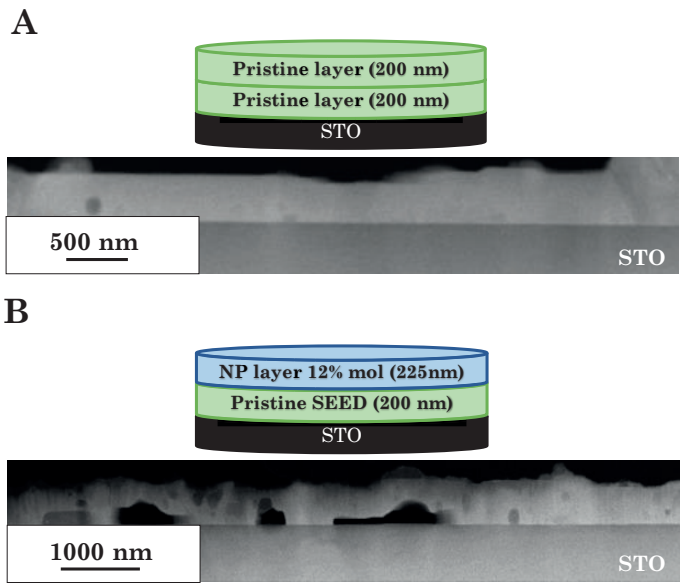

Figure 4.34 Scheme of multilayered architecture and cross-sectional STEM-HAADF images of (A) the best performance pristine film and (B) the best performance nanocomposite film.

To investigate whether the proposed origin contributes to this porosity, we followed two different strategies, expecting to decrease composition differences of the transient liquid formed during YBCO growth in the case of multideposited nanocomposite layers:

1. Decrease the NC amount in the nanocomposite layer from 12 %mol to 6 %mol.

2. Modify multilayered architectures of nanocomposite films decreasing the thickness of the pristine seed layer from 400 nm to 25 nm or even eliminating the seed pristine layer. In TFA-CSD route [47, 85, 95], the use of a thin pristine YBCO layer prior to the nanocomposite layer is found a good approach to avoid the accumulation of preformed NCs at the YBCO/substrate interface than then perturb the heteroepitaxial nucleation of YBCO. In the case of a thin TLAG process, the seed layer is reported to ensure better reproducibility of the biaxial texture of nanocomposite films [55].

The schemes and the corresponding cross-sectional SEM images of the different multilayered architectures grown are shown in Figure 4.35A-C. Cross-sectional SEM images obtained from FIB-cuts show that pores at the YBCO/STO

interface are totally eliminated by either decreasing the NC amount from 12 %mol to 6 % mol in the NP layer (Figure 4.35A), using a thinner pristine seed layer of 25 nm (Figure 4.35B) or removing the pristine seed layer prior to NP layer (Figure 4.35C). These results can be attributed to possible variations in the rheological behaviour of the transient liquid phase formed from the pristine layer compared to nanocomposite layer. Analogous to Ba-Cu-O liquid composition, we expected differences in viscosity if NCs are present in the Ba-Cu-O liquid phase. The presence of NCs will increase the solid phase fraction, which consequently increases the viscosity and decreases the diffusion coefficient following Equations 4.4 and 4.2, respectively. As a consequence, the different viscosities of the liquids could lead to different scenarios during the liquid formation, such as the generation of pores. It is reported that the mixture/blending of liquids with high viscosity differences produces different effects such as stratification in the mixture that need to be overcome to obtain a uniform mixture that requires different approaches and a certain time [236–238]. Moreover, the differences in viscosities of the liquid phase generated in nanocomposite and pristine layer difficulting the mixing of liquids, could explain the no observation of NC pushing using a pristine CAP layer in the previous section.

Further, as we previously mentioned in section 4.3.2.3.3, interface porosity was identified only in STEM-HAADF images of nanocomposites film (SEED pristine ~ 200 nm + 1 NP layer ~ 225 nm) with 12% mol but not for nanocomposite films with increased NC amounts of 18% mol and 24% mol. Interestingly, in the cases of 18% mol (Figure 4.23C) and 24% mol (Figure 4.23D) we also observe a lack of pores at the substrate interfaces. In both cases, the absence of pores could be attributed to the same effect observed at 6%mol. The uncontrolled NC pushing, more pronounced at 18% mol and 24% mol, leads to a lower NC density inside the film compared to the initially defined NC amount. Consequently, by reducing the NC amount inside the film, the differences in viscosities between the liquids formed in the pristine seed layer and the NP layer become more similar. This results in a more uniform transient liquid phase, preventing the formation of defects such as pores, as in the 6% mol case.

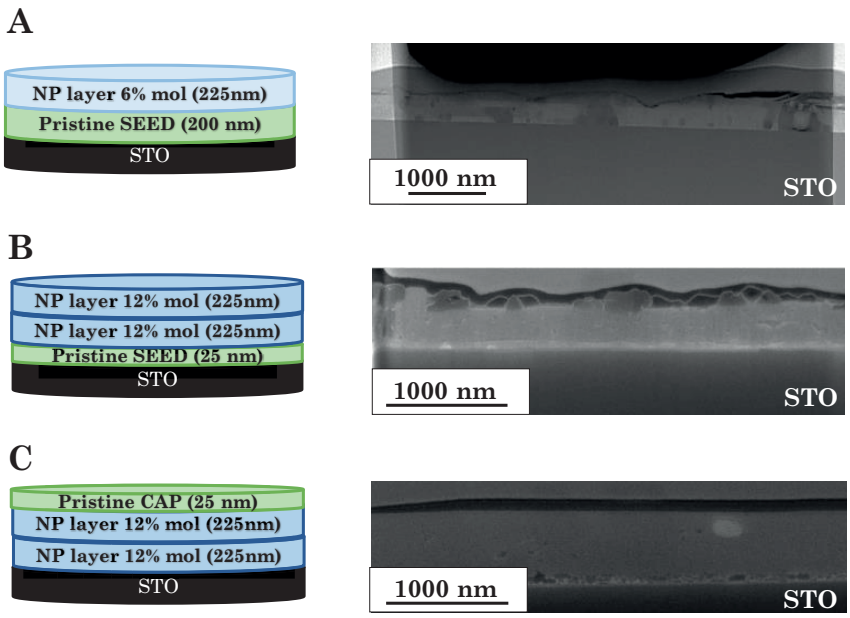

Figure 4.35 Scheme of multilayered architecture and cross-sectional SEM images of nanocomposite films with (A) pristine SEED (200 nm) and 1 NP layer 6% mol NC (225 nm), (B) pristine SEED (25 nm) and 2 NP layer 12% mol NC (450 nm) and (C) 2 NP layer 12% mol NC (450 nm) and pristine CAP layer (25 nm).

Following the proposed strategies, it is possible to decrease the differences in the viscosities of the liquids formed within the layers of the multilayer architecture. Consequently, this could lead to more similar properties and behaviours of the liquids, resulting in a more homogeneous liquid phase. This, in turn, could contribute to the formation of a uniform film covering the STO substrate without the presence of pores.

To conclude, these preliminary experiments have demonstrated that achieving completely pore-free continuous nanocomposite films is feasible by reducing the NC amount (% mol) of the NP layer, diminishing the thickness of the pristine seed layer, or eliminating the pristine seed layer. Moreover, diminishing the thickness of the pristine seed layer to 25 nm of multilayered architecture in nanocomposite films could be a potential candidate to enhance the performance of TLAG nanocomposite films, as the tendency of NCs to accumulate at the substrate interface is expected to be lower than without a pristine SEED layer, based on the previous investigations [47, 85, 95]. Considering these results, we

proposed the use of a thin pristine SEED layer and a thin pristine CAP layer in the multilayered architecture of nanocomposite samples to avoid NC pushing and interface subtrate porosity.

4.3.2.5 Vortex pinning and defect landscape of TLAG nanocomposite films

In previous sections, we focused on optimising the processing conditions of YBCO crystallisation and solving the encountered issues that could potentially diminish the total current carrying capacity. We have successfully identified the optimal growth conditions to achieve high-quality epitaxial nanocomposite films, along with strategies to avoid NC pushing and interface porosity.

The objective of fabricating YBCO nanocomposite film throught the incorporation of preformed NCs as artificial pinning centres (APC) is to enhance their performance by effectively pinning vortices. Vortex pinning avoids energy dissipation resulting from the movement of vortices, particularly at elevated temperatures and high magnetic fields. In this section, we evaluated the nanoscale defects generated in the TLAG nanocomposite films of section 4.3.2.3.3 and 4.3.2.3.4. This involves the analysis of the microstructure by TEM and the vortex pinning characteristics by SQUID measurements along with transport measurements. The aim is to establish a correlation between the pinning landscape and the superconducting properties of the films. The TEM analysis was performed by Dr.K.Gupta from SUMAN group while transport measurements were carried out by A.Kethamkuzki performing her phD thesis in the SUMAN group.

4.3.2.5.1 TEM analysis

The presence of defects inside the film, either if are naturally generated during growth such as stacking faults (SFs) or by the introduction of secondary phases such as NCs, is essential to enhance superconducting properties [83, 84]. We analysed the defect landscape of a nanocomposite film with 6%mol by high-resolution STEM-HAADF images and compared that with a pristine film. In both samples, we can observe a high density of SFs (extra Cu-O chain) which are planar defects (green arrows) but it seems that nanocomposite film

exhibits (Figure 4.36B) higher density of SFs than pristine film (Figure 4.36A). These defects are not uniformly distributed across pristine and nanocomposite samples. Moreover, in the STEM-HAADF of the nanocomposite film Figure 4.36B), we can distinguish between two regions (green and orange) with different microstructures that are associated with the multilayered nanocomposite architecture used of the pristine SEED layer (green region) and NP layer (orange region). The pristine layer exhibits a medium density of SFs in comparison with the NP layer, which shows a higher density of SFs. In a zoomed-in from the green region of the pristine layer, a medium density of SFs can be better seen, while a zoomed-in image from the yellow region of the nanocomposite layer shows the higher density of SFs generated due to embedded NCs in the matrix. In this case, we also observed, as we previously mentioned in other sections, that NCs with sizes above 20 nm show random orientation, whereas NC sizes of $\leq$ 20 nm are epitaxial-oriented. This NC behaviour will be discussed in detail later, analysing high-resolution STEM-HAADF of nanocomposite films with higher NC amounts (12-24%mol).

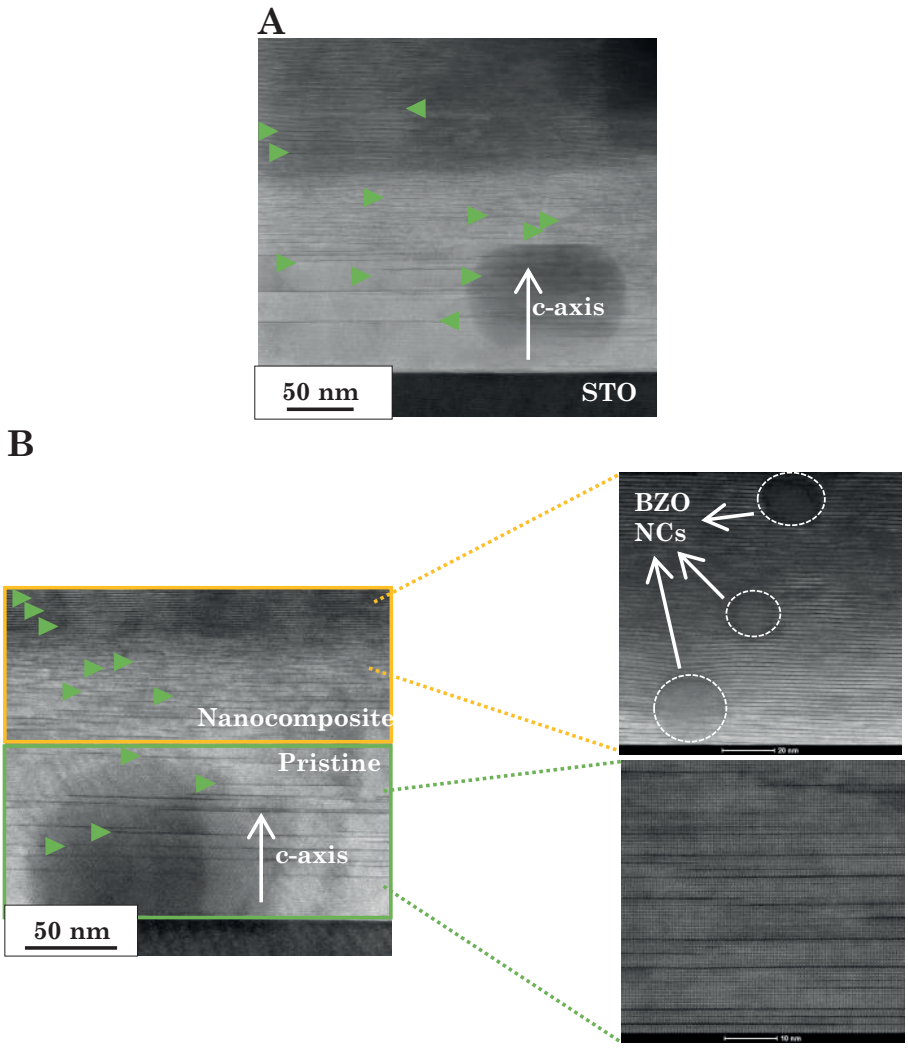

Figure 4.36 High-resolution STEM-HAADF images of (A) pristine film (B) nanocomposite film using 7 nm sized BZO NCs with 6%mol. SFs are indicated by green triangles. Green square identified the pristine layer region with medium density of SFs and yellow square identified the nanocomposite layer region with high density of SFs. STEM-HAADF images at high magnification of green square and yellow square regions show the lower density of SFs in the pristine layer compared to the NP layer with embedded BZO NCs.

In the case of the TFA-CSD route, a high density of SFs ($YBa_2Cu_4O_8$ intergrowths) can be reached through nanocomposite films. The presence of random NCs produces a high density of SFs as a mechanism to relax the incoherent interfaces due to the high lattice mismatch of NCs with YBCO [83, 85, 239–241].

Subsequently, improvements in pinning efficiency were demonstrated by incorporating flash heating ramps during the growth process, which induces less NC coarsening and a higher density of SFs [47]. In contrast, pristine films grown through the TLAG-CSD process already exhibit a high density of SFs. In the case of nanocomposite films, it was observed that using NC size close to the vortex diameter and considering the fast kinetics of YBCO crystallisation from a liquid phase using the TLAG process, NCs have the ability to rotate being epitaxially aligned in the c-axis YBCO matrix. It was postulated that the embedded NCs with small-sized and epitaxial orientations could potentially act as core pinning centres [10, 42, 55]. In our case, we previously observed in the optimal scenario where NC pushing is prevented, through the use of a pristine CAP layer (section 4.3.2.3.6), that the initial ~5 nm sized NCs ended in sizes within the range of 7-20 nm. In addition, small-sized NCs in the range of 7-11 nm showed an epitaxial orientation in the c-axis YBCO matrix, while some large-sized NCs (~ 20 nm) were randomly oriented (Figure 4.32C-E).

Then, we performed a similar analysis on nanocomposite films with higher NC amounts (%mol) and an initial NC size of ~7 nm. An overview of high-resolution STEM-HAADF images of films with varying NC amounts (6-24% mol) is shown in Figure 4.37A-D. These films exhibit a high density of SFs extending throughout the entire YBCO cross-section, where, in some cases, distinguishing between short and long SFs becomes challenging due to the abundance of defects. We observed that NCs are homogeneously distributed inside the film except for the 24%mol where NC agglomeration was previously identified (Figure 4.23D). In addition, we observe that some of the initially 7 nm-sized NCs are also able to rotate, ending with epitaxial orientation inside the film with a final size of 10-20 nm. The coarsening of NCs relative to their initial size could be associated with the grain coalescence during high-thermal treatments [25, 86]. Moreover, certain NCs, particularly those exceeding 20 nm in size, show a random orientation in the c-axis YBCO matrix.

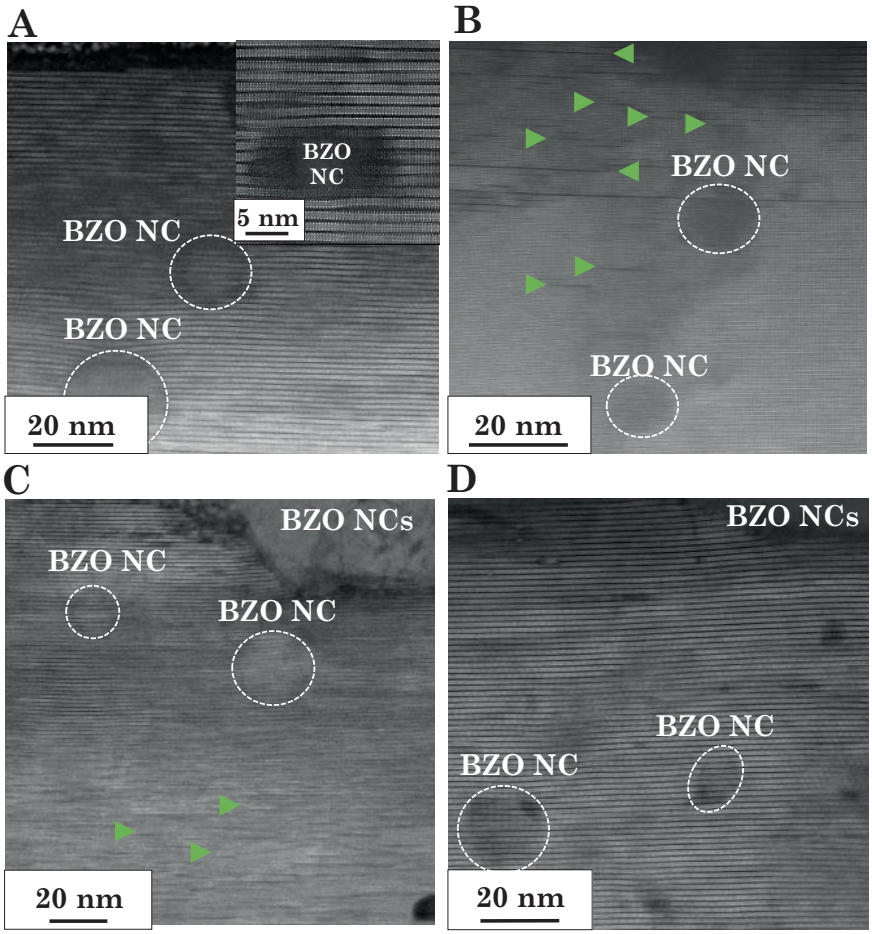

Figure 4.37 High-resolution STEM-HAADF images of nanocomposite films using 7 nm sized BZO NCs with (A) 6%mol, (B) 12%mol, (C) 18%mol and (D) 24%mol. SFs are indicated by green triangles.

Considering the results from the TEM analysis, the higher density of SFs defects observed in nanocomposite film, generated due to embedded randomly oriented NCs in the matrix, could act as pinning centres. Moreover, small-sized and epitaxial-oriented NCs could also contribute to the vortex pinning improvement by acting themselves as pinning centres.

Complementary, we investigated and evaluated the contribution of NC orientations present in these films by performing 2D GADDS XRD measurement centred on the most intense reflection of the NC phase (ll0) at χ = 45°, where epitaxial diffraction of NCs appears. In the 2D GADDS XRD image, randomly oriented NC diffraction appears as a ring in the (ll0) reflection of the NC phase,

while an epitaxial-oriented NC diffraction signal manifests as a pole. Subsequently, a previously used methodology was employed to calculate the volume percentage of the randomly oriented NC fraction using the integrated areas from the ring and pole regions of the (ll0) reflection of BZO NCs and the Equation [10, 55, 239]. Details about the calculation procedure for the NC random fraction (%) are described in Appendix A.1.3.

The 2D GADDS XRD measurement at χ = 45° was performed, and NC random fraction (%) was determined for the nanocomposite film with 6% mol of BZO NCs. This nanocomposite film was expected to exhibit a higher density of NCs inside the film, as previous TEM analyses indicated less NC pushing compared to increased NC amounts. The resulting 2D GADDS XRD image at χ= 45° is shown in Figure 4.38. Notably, within the (ll0) reflection of the BZO phase, we observe the presence of a spot and a ring, which confirms the presence of epitaxial and randomly oriented NCs in the film, consistent with the previous TEM analysis. Moreover, the volume fraction of randomly oriented particles obtained ranged between 45-65%. Based on the TEM analysis, it is probably closer to the lower range considering that random-oriented NCs tend to be larger and are expected to give more XRD intensity. Therefore, both TEM analysis and the determined value of the NC random fraction corroborate the presence of a mixture of both NC orientations in nanocomposite films, potentially influencing the vortex pinning landscape.

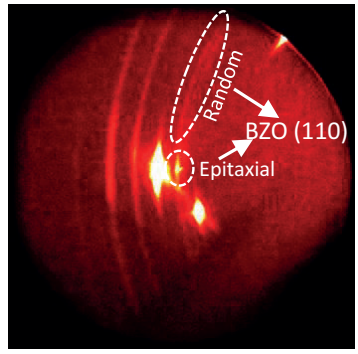

Figure 4.38 2D GADDS XRD image at χ = 45° of the BZO (110) reflection of nanocomposite film with 6% mol BZO NCs.

Furthermore, despite porosity, NC pushing, and NC agglomeration, which could be detrimental to the improvement of superconducting properties, the

nanocomposite films show enough total current percolation to reach high self-field Jc values in the range of 2.4-2.6 MA/cm^2. In the following section, the vortex pinning efficiency of these nanocomposite films will be evaluated to determine their superconducting properties by increasing the magnetic field.

4.3.2.5.2 Vortex pinning analysis and correlation with defect landscape

The evaluation of the vortex pinning properties of the nanocomposite films from the sections 4.3.2.3.3 and 4.3.2.3.4 was performed by the following physical measures:

1. Field dependence of Jc. Nanoscale defects inside the film act as pinning centres, shifting the Jc (H) plateau to high magnetic fields. As a result, the crossover magnetic field between the single vortex pinning regime and collective vortex regime, defined by μ_0H* and determined at 80% of Jc sel-field [10], increases with the density of defects. In the single vortex pinning regime, the vortices are pinned individually, and in the collective regime, the vortex-vortex interactions become relevant, producing the decay of Jc with the applied magnetic field [47, 83, 229]. Therefore, the μ_0H* is an indication of the density of pinning centres capable of pinning individual vortices. We evaluated the Jc dependence with magnetic field by SQUID measurements of magnetization versus applied field using the Bean critical state model [242] (Appendix A.8.1).

2. Nanostrain (ϵ). The vortex pinning mechanism of CSD films has been demonstrated to be mainly dependent on the presence of highly strained areas in the YBCO matrix which are localised at the surroundings of the stacking faults (SFs) [80, 83, 239–241]. The introduction of random NCs in YBCO leads to the formation of defects in the microstructure, such as $YBa_2Cu_4O_8$ intergrowths (SFs), due to the high lattice mismatch between NC and YBCO (incoherent interface). Consequently, these SFs generate highly strained localised areas, nanostrain, in the YBCO matrix where Cooper pair formation is suppressed [83, 240, 241]. The nanostrain can be determined by θ-2θ HR-XRD measurements following the William-Hall method [87, 239, 243] described in Appendix A.1.2, which involved the analysis of the broadening of the (00l) Bragg reflections. The evaluation of nanostrain allows the correlation of local strain deviations in the YBCO matrix of the films, derived from the accommodation of

structural defects, with the pinning properties.

3. Angular dependence of Jc. We mainly identified $YBa_2Cu_4O_8$ intergrowths in pristine and nanocomposite films that are planar (2D) anisotropic defects for H//ab, but these defects can produce additional distortions, the 3D isotropic nanostrain defect [80]. Twin boundaries, especially if they have certain lengths, will also contribute to the vortex pinning as 1D anisotropic defect for H//c. Furthermore, oxygen vacancies could also contribute as 0D isotropic defects (section 1.1.4). The isotropic and anisotropic behaviour of defects inside the film depending on the orientation of the applied magnetic field can be investigated through Jc(θ) measurements at different temperatures and magnetic fields by transport measurements (Appendix A.8.2.2).

Firstly, the Jc(H) behaviour from SQUID measurements of the best pristine film is compared with different nanocomposite films varying NP amount (6-24% mol) in Figure 4.39A. The film thickness of all films is in the range of 400-425 nm. The initial Jc values at self-field for the different nanocomposite indicate that we reached high critical currents like with the pristine film, varying the NP amount from 6 to 24% mol. Moreover, nanocomposite films outperform pristine films at both temperatures (5 and 77 K) under high magnetic fields. This can be better analysed through the normalised Jc(H) dependence in Figure 4.39B. In addition, slight differences are observed with varying NP amounts, which will be discussed in detail later by crossover field (μ_oH*) determination.

Then, the same analysis (Figure 4.39C) was performed for a pristine film (400 nm of thickness) and nanocomposite films with 6% mol and 18% mol modifying the film thickness from 425 to 650 and from 425 to 650 and to 875 nm respectively. The initial Jc self-field values for nanocomposites show that we can maintain high critical current densities by increasing the film thickness from 425 to 875 nm. Furthermore, nanocomposite films exhibit a slower decay of Jc with the magnetic field, and the self-field Jc plateau extends to higher magnetic fields as the film thickness increases. This is more clearly observed in normalised Jc(H) curves (Figure 4.39D).

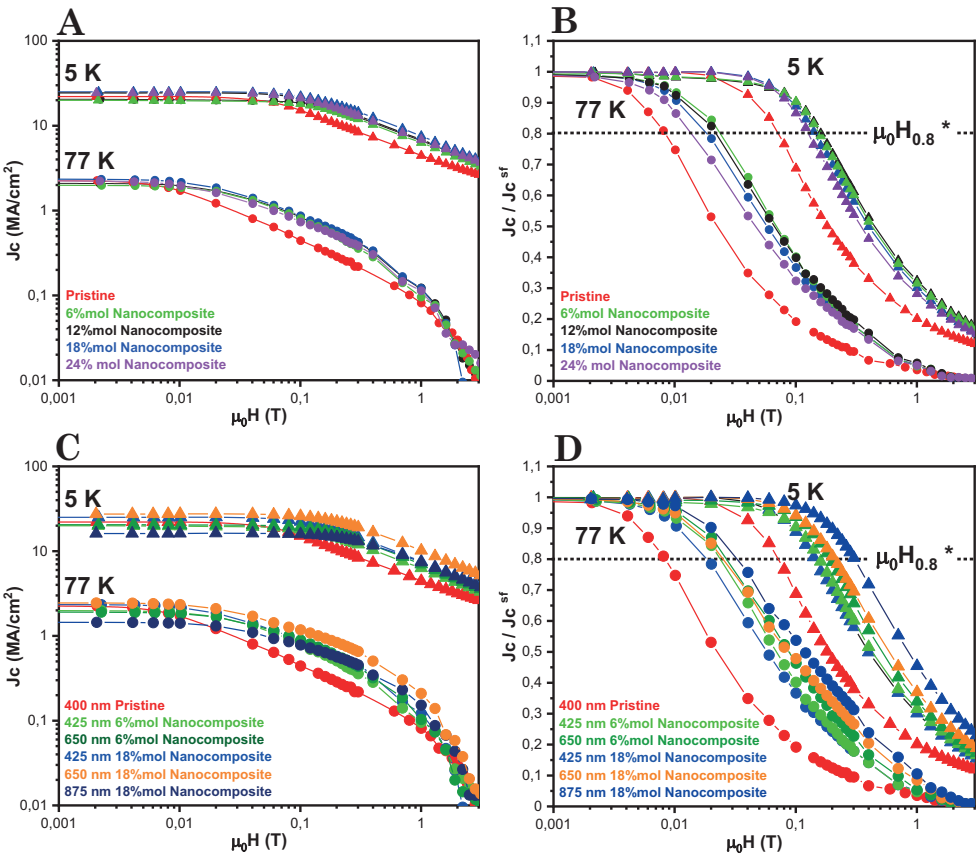

Figure 4.39 Jc(H) SQUID measurements at 5 K and 77 K of a (A) Pristine film (400 nm of thickness) and nanocomposite films varying NP amount 6-24% mol (425 nm of thickness), (B) corresponding normalized values to each maximum self-field Jc of Jc(H) curves from (A), (C) Pristine film (400 nm of thickness) and nanocomposite films varying thickness 425-875 nm and (D) corresponding normalised values to each maximum self-field Jc of Jc(H) curves from (C).

Therefore, the nanocomposite films show a smoother dependence of Jc with magnetic field compared to pristine, as emphasised by the dashed line at 80% of Jc sel-field of normalised Jc (H) curves (Figure 4.39B and D). The extension of the Jc self-field plateau is associated with the enlargement of the single vortex pinning regime defined by the crossover field (μ_0H*). The μ_0H* values at 77K and 5K of pristine and nanocomposite films are shown in Figures 4.40A-D. First, when considering varying NC amounts (6-24% mol) at both temperatures (Figures 4.40A and B) all nanocomposites demonstrate the capability of enlarging the single vortex pinning regime to higher magnetic fields. This extension starts from the initial values of 0.012 T at 77K and 0.08 T at 5 K for the pristine film

and reaches 0.014-0.024 T at 77K and 0.127-0.157 T at 5K for nanocomposite films, respectively. However, the linear correlation expected between μ_0H* and the NC amount [10, 55], through the formation of higher density of defects, is not observed in our case. The absence of a clear influence of the NC amount on the single vortex pinning regime may be attributed to the limited NC pushing effect in the case of 7 nm-sized NCs. However, this effect becomes more pronounced for 18% mol and 24% mol, as observed in TEM, together with the NC agglomeration present in 24% mol.

Therefore, due to the uncontrolled NC pushing, which is not completely avoided in these films, the initial NC amount used for nanocomposite film formation is not equal to the final NC density inside the film after growth. This might explain why the μ_0H* does not increase with NC amount and the observed sightly irreproducibility of Jc and μ_0H* observed for 18% mol. Despite this, further enhancement of single-vortex pinning by NC amount should be observed by using the pristine CAP layer in multilayer nanocomposite films, where NC pushing has been demonstrated to be completely avoided. This approach will enable the investigation of the real effect of the NC amount, considering that the initial NC amount used will be kept inside the film after YBCO growth. Therefore, texture studies should proceed in this direction.

We also investigated the effect of increased nanocomposite film thickness, as the TFA-CSD nanocomposite case, where the elongation of single-vortex pinning by the nanocomposite layer thickness was demonstrated [47]. The SQUID measurements at 77 K (Figure 4.40C) and 5 K (Figure 4.40D) were performed using low (6% mol) and high (18% mol) NC amounts. The μ_0H* at 5 K in 6% mol and 18% mol nanocomposites continuously increases with the film thickness, from 0.157 T (425 nm) to 0.194 T (650 nm) for 6% mol and from 0.157 T (425 nm) to 0.208 T (650 nm) and to 0.307 T (875 nm) for 18% mol. These results suggest that the enlargement of the single vortex pinning regime towards higher fields with increasing film thickness is probably due to an overall increase in the total density of defects [47, 244]. Further, TEM characterization of the microstructure and additional physical measurements will be necessary to confirm the increased density of defects in thicker films.

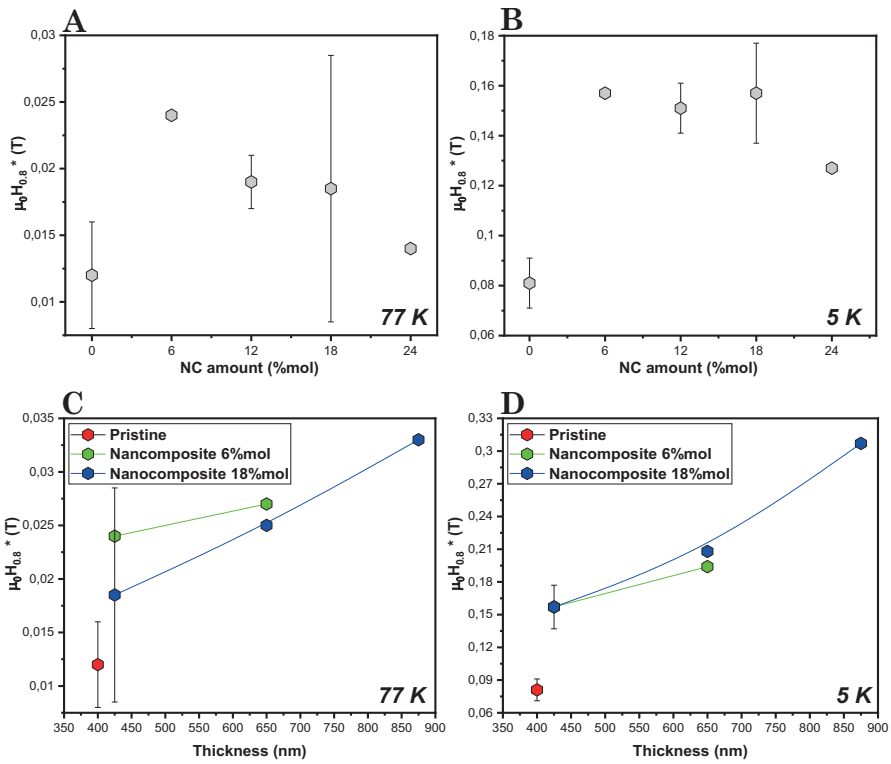

Figure 4.40 Correlation between (A) NC amount at 77K, (B) NC amount at 5K (C) Film thickness at 77K (D) Film thickness at 5K and crossover magnetic filed μ_0H*.Errors bars correspond to the standard deviation of the different obtained values (μ_0H*) at the same %mol.

In summary, we enhanced vortex pinning by adding NCs and increasing the thickness of the NC layer. This implies an increase in the density of defects capable of pinning vortices compared to pristine films. Then, we analysed the correlation of the defect landscape comparing the nanostrain (resulting from strain deviations of the c-axis of the YBCO matrix [80]) with the pinning properties (μ_0H*). Figure 4.41A-B shows the dependence of the μ_0H* at 77K and 5K with nanostrain. The introduction of NCs into YBCO leads to a significant increase in nanostrain (ϵ) and elongation of the single vortex pinning regime (μ_0H*) at 77 K and 5 K. The higher values for nanocomposite films compared to pristine films indicate that nanocomposite films incorporate a higher amount of SFs.

However, we detected in TEM random-oriented and larger-sized NCs and epitaxial-oriented and smaller-sized NCs embedded in the YBCO matrix. It is

known that random NCs create SFs and distortions in the TFA-CSD route [80, 83, 85, 240, 241]. Moreover, in thin TLAG films, an independent increase in μ_0H* from the related nanostrain was observed when small-sized and epitaxial-oriented NCs were detected [10, 55]. Considering this observation, it was postulated that nanocomposite films with small-sized NCs (similar range as the vortex core diameter) epitaxially oriented and grown by the TLAG process have the capability of acting as core pinning centres [10, 55]. For these reasons, although distinguishing between both pinning contributions in our case is challenging, we proposed the presence of both, considering the existence of some random NCs, inducing SFs, and some small-sized NCs epitaxially oriented, along with the high density of stacking faults (SFs) already generated by the fast TLAG process as found in pristine films. Further optimisation and additional microstructural and physical measurements would be necessary to elucidate the relevance of each contribution in the improvement of pinning properties.

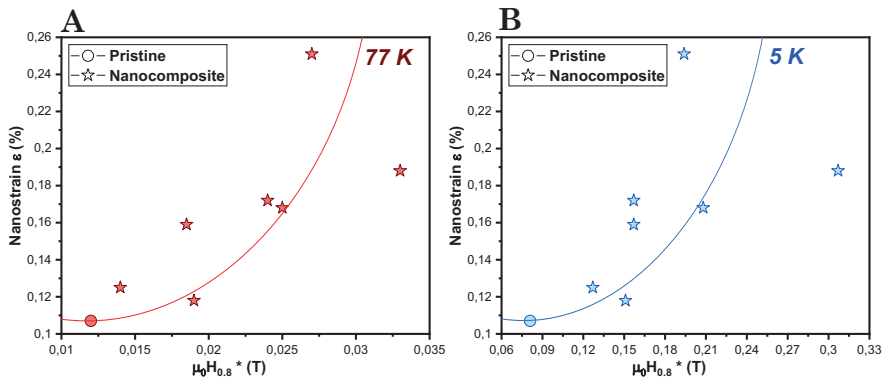

Figure 4.41 Evolution of μ_0H* with ϵ of nanocomposite films compared to pristine film at (A) 77K and (B) 5K.

Complementary, angular dependence of Jc measurements of a nanocomposite film were performed to investigate the pinning ability based on the orientation of the applied magnetic field, influenced by the defects introduced by the incorporation of NCs. Angular measurements were carried out at 0.1 T, 1 T and 5 T to evaluate the behaviour in the smoother Jc(H) plateau region (the nanocomposite sample surpassed pristine film beyond 0.01 T at 77k) and also at higher magnetic fields. Figure 4.42 shows the Jc(θ) curves at 77K of pristine film and the 12% mol nanocomposite film.

The overall in-field Jc values in nanocomposite film exceed the values observed in pristine film and seem to be angular independent. This can be attributed to the increase in isotropic pinning contribution compared to pristine films due to the presence of small-sized NCs homogeneously distributed and the higher nanostrain from the higher density of SFs generated. These NCs act as pinning centres in all directions of the applied magnetic field. The higher density of SFs ($YBa_2Cu_4O_8$ intergrowths), which are defects in the a/b plane direction, results also in the broadening of the a/b peak (θ = 90°). In addition, the high density of these defects also leads to a reduction in the vertical coherence of the twin boundaries, identified by the c-axis peak at θ = 180°, which is not visible for the nanocomposite film across all applied magnetic fields. This observation suggests a strong enhancement in pinning due to the introduction of NCs. This behaviour remains consistent for the different measured magnetic fields, although the difference in Jc becomes more pronounced at higher applied magnetic fields. Therefore, the variations in the Jc(θ) curves indicate that nanocomposite and pristine films exhibit different pinning efficiencies depending on the direction of the magnetic field, reflecting the different defect landscapes in their microstructures. Furthermore, these results demonstrate the interest in introducing NCs into YBCO films as an approach for increasing the superconducting properties at high magnetic fields.

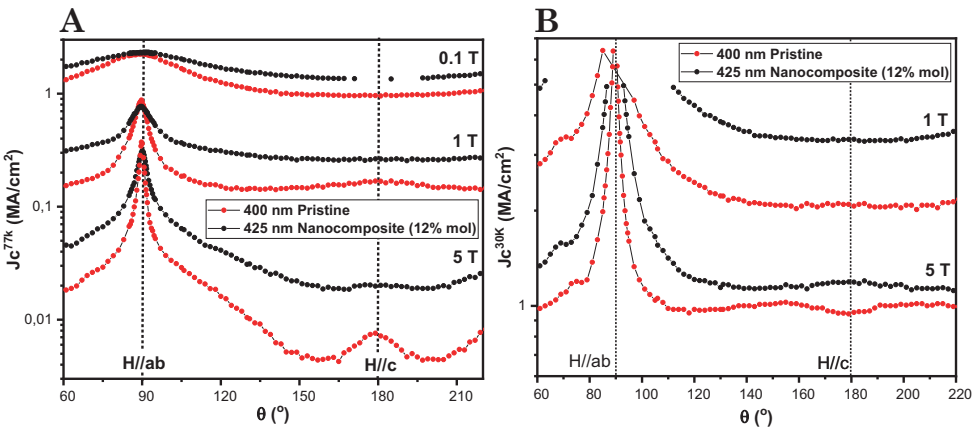

Figure 4.42 (A) Angular dependence at 77 K. The comparison is made at 0.1 T, 1 T and 5 T between nanocomposite (black) and pristine films (red). The black-dashed lines indicated the angles of the magnetic field applied at 90° and 180° directions, H//ab and H//c, respectively.(B) Angular dependence at 30 K. The comparison is made at 1 T and 5 T between nanocomposite (black) and pristine films (red).

In addition, as the pinning efficiency also depends on temperature, we also evaluated the angular dependence of Jc from nanocomposite and pristine films at 30 K for 1T and 5T values of the applied magnetic field. The Jc(θ) curves are shown in Figure 4.42B. At 30K, it is also observed the in-field isotropic Jc increased for nanocomposite films, which indicates that small-sized NCs and nanostrain from SFs are also pinning efficient at low temperatures and high magnetic fields. Moreover, it can also observe the broadening of the a/b peak (θ = 90°) resulting from the higher density of SFs in nanocomposite film compared to pristine film (sharper a/b peak). In this case, the pristine sample at 5T shows a decrease of Jc at θ = 180° while in nanocomposite film, this dip is not detected. This dip is attributed to twin boundaries that extend coherently across the full YBCO layer, allowing vortex channelling, which is suppressed in the case of nanocomposite films and was associated with the higher density of SFs compared to pristine films [10].

In conclusion, while further analysis and optimization of nanocomposite films is necessary to properly evaluate pinning properties when issues such as NC pushing and interface porosity are resolved, we have successfully enhanced the superconducting properties. The introduction of small-sized NCs increases the nanostrain compared to pristine films, possibly attributed to the defects generated in the YBCO matrix by the presence of randomly oriented NCs. Simultaneously, epitaxially oriented NCs also observed may act as pinning centres. Consequently, it causes a much smoother decay of Jc with the magnetic field (higher μ_oH* values) and a reduction of the Jc anisotropy.

4.3.2.6 *In-situ* synchrotron XRD experiments

The utilisation of in-situ XRD analysis for analysing precursor films based on acetate was crucial in the past [10, 33, 43, 44, 55]. This analysis enabled the development of the kinetic phase diagram of YBCO films formed via the TLAG process and the determination of its kinetic mechanism. Fast growth rates of 100 nm/s were determined for 100 nm film thickness. During the doctoral thesis, the derived knowledge proved to be an essential tool for determining the optimal processing conditions to achieve high-performance films at rapid growth rates. However, the analysis was conducted using YBCO precursor films derived from acetate precursor solutions, which had distinct microstructure properties and

thicknesses compared to precursor solutions based on propionate. These differences are significant in the context of the ultra-fast non-equilibrium TLAG process. Consequently, complementary evidence of the compatibility of nanocomposite precursor films based on propionate precursor solutions for TLAG was accomplished via *in-situ* XRD growth experiments with synchrotron light.

Unless otherwise specified, the precursor films for -in-situ experiments were composed of nanocomposites with 3-7 composition, which reached the best performance in ICMAB experiments, and with a thickness of 400-500 nm (one layer of SEED pristine precursors and one layer of NPs with 12 %mol BHO or BZO NCs). A detailed experimental description of the sep-up, *in-situ* conditions, data treatment, and analysis is described in Appendix D.1.

The phase evolution during *in-situ* growth conditions enables an understanding of the TLAG mechanism and the kinetic parameters that govern the process and promote c-axis nucleation at high growth rates. For *in-situ* conditions, the effect of processing parameters including temperature, PO_2, heating gradient, gas flow, PO_2-jump speed, and P_{total} on the achievement of strong epitaxial nucleation was studied but is not discussed here. Despite this, this work investigates the phase evolution of $BaCO_3$-Y_2O_3-CuO system from pyrolyzed nanocomposite films using one of the different growth conditions found as a result of a set of experiments with strong epitaxial nucleation. At P_{total} = 0.025 mbar, PO_2 = 0.005 mbar the nanocomposite precursor film was heated at a rate of 4.5°C/s (300°C/min) until it reached a temperature of 850°C. At this point, the P_{total}, PO_2 increased from P_{total} = 0.025 mbar, PO_2 = 0.005 mbar to P_{total} = 100 mbar, PO_2 = 7 mbar. Based on the kinetic phase diagram of the acetate-based precursor solution as depicted in Figure 1.11, the following reactions are the ones expected at each stage of the PO_2-route:

1st step: low PO_2

$$BaCO_{3(s)} + CuO_{(s)} + Y_2O_{3(s)} \rightarrow BaCO_{3(s)} + Cu_2O_{(s)} + Y_2O_{3(s)} \quad (4.1)$$

$$BaCO_{3(s)} + Cu_2O_{(s)} + Y_2O_{3(s)} \rightarrow BaCu_2O_{2(s)} + Cu_2O_{(s)} + Y_2O_{3(s)} \quad (4.2)$$

2nd step: low PO_2

$$BaCu_2O_{2(s)} + Cu_2O_{(s)} + Y_2O_{3(s)} \rightarrow (Ba\text{-}Cu^{I/II}\text{-}O)_{(l)} + Y_2O_{3(s)} \quad (4.3)$$

$$(Ba\text{-}Cu^{I/II}\text{-}O)_{(l)} + Y_2O_{3(s)} \rightarrow YBa_2Cu_3O_{7-\delta} \quad (4.4)$$

Considering this, we investigated the in-situ phase evolution of precursor

nanocomposite films using propionate-based precursor colloidal solutions resulting from the analysis of the area under the curve (AUC) normalised to its maximum value from the fitting of the integrated intensity of the corresponding XRD peaks. The resulting phase evolution from the initial heating step at low PO_2, during PO_2 jump, and dwell step at high PO_2 versus time and temperature is shown in Figure 4.43A.

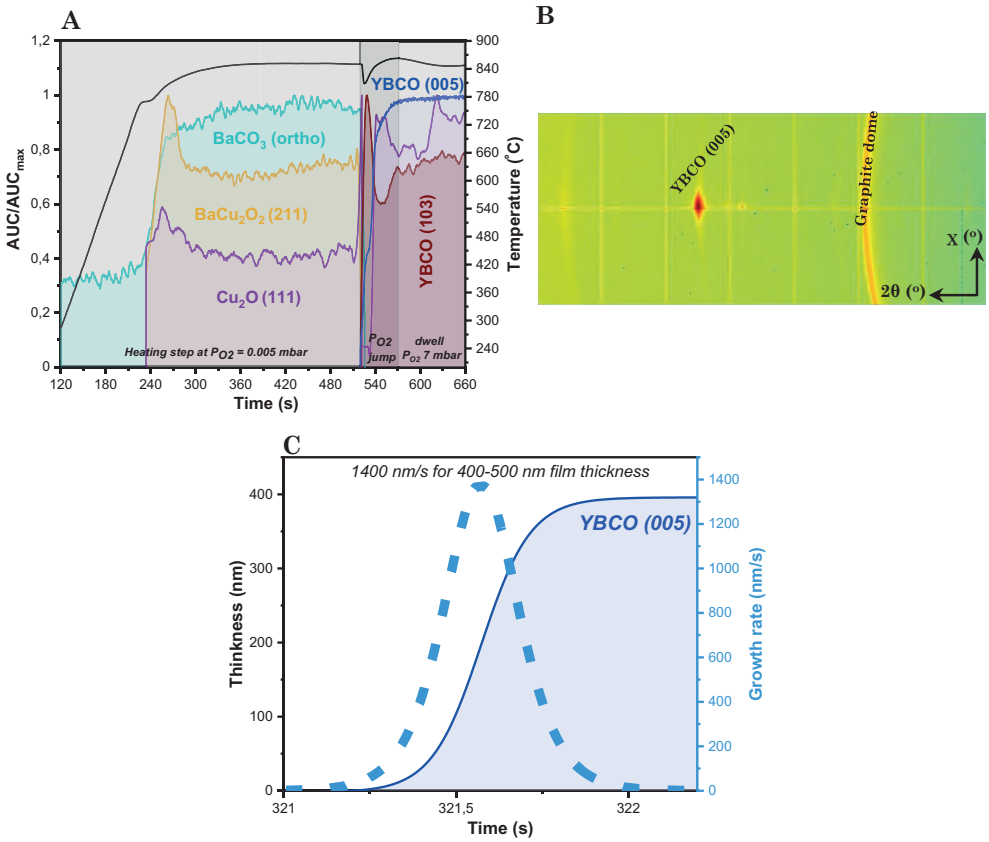

Figure 4.43 (A) XRD phase evolution (integrated signal of the respective XRD peak) as a function of time, including temperature evolution of nanocomposite precursor film heated at 4.5°C/s (300 °C/min) to T = 850°C at P_{total} = 0.025 mbar, PO_2 = 0.005 mbar performing a PO_2 jump to P_{total} = 100 mbar, PO_2 = 7 mbar. Each signal is normalised to its maximum value for better visibility. (B) 2D-XRD image of nanocomposite film grown in full-liquid region of the kinetic phase diagram and (C) Derivative of the fitting curve from the evolution of integrated AUC normalised with the thickness of the in-situ YBCO (005) reflection signal over time with the calculated growth rate.

In the first step at low PO_2, we observe only a peak from $BaCO_3$ that crystallises at ~780 °C, suggesting that there is a high degree of $BaCO_{3(s)}$, $CuO_{(s)}$

and $Y_2O_{3(s)}$ phases in amorphous state, in agreement with the previous observation of amorphous matrix in HRTEM of nanocomposite pyrolyzed precursor film in section 3.3.2.2. Therefore, the lack of detection of crystalline CuO and $Y_2O_{3(s)}$ could be attributed to a high degree of amorphous contribution. Although the presence of $CuO_{(s)}$ is expected at low temperatures, as at ~780-800 °C it is observed the formation of $Cu_2O_{(s)}$ and $BaCu_2O_2$ phases, coming from the reduction of amorphous $CuO_{(s)}$ (according to reaction 4.1) and from the reaction of amorphous $BaCO_3$ with $CuO_{(s)}$, respectively.

We observed the reduction of amorphous $CuO_{(s)}$ to crystalline $Cu_2O_{(s)}$ at higher temperatures than the reported ones [75], at ~650 °C. In addition, amorphous $BaCO_{3(s)}$ could react with amorphous $Cu_xO_{(s)}$, resulting in $BaCu_2O_{2(s)}$ phase (reaction 4.2). The suggested reactions in the heating step at low PO_2 resulted in $BaCu_2O_{2(s)}$, $BaCO_{3(s)}$,$Cu_2O_{(s)}$ $Y_2O_{3(s)}$ as crystalline intermediate phases before jumping. We expected from the kinetic phase diagram and the experiments at ICMAB (4.3.2.1, the complete elimination of $BaCO_{3(s)}$ before jump at ~850 °C. However, this could be attributed to the poor and no-linear gas exchange and the reduced volume of the furnace used in the in-situ conditions, hindering the complete $BaCO_{3(s)}$ elimination. [44, 59]. This could become worse for thicker and less porous precursor films compared to precursor films from an acetate-precursor solution.

Then, at the initial of PO_2-jump with a fast speed of ~50s, we observe the complete elimination of $BaCO_{3(s)}$, $BaCu_2O_{2(s)}$ and $Cu_2O_{(s)}$ followed by the formation of epitaxial YBCO (005) and random YBCO (103). This confirmed that as soon as it reached PO_2-T region, where the (Ba-Cu-O) liquid phase and YBCO are stable, the liquid is formed from the reaction of $BaCu_2O_{2(s)}$ with $Cu_xO_{(s)}$ and YBCO crystallises (reactions 4.3 and 4.4). Therefore, despite some $BaCO_{3(s)}$ remained before jump, it disappeared at the initial of the jump through $BaCO_{3(s)}$ + $Cu_2O_{(s)}$ →$BaCu_2O_{2(s)}$ + $Cu_2O_{(s)}$. Additionally, the formation of $Cu_2O_{(s)}$ during the jump, reveals the excess copper due to the 3-7 composition.

Furthermore, performing several experiments for proper control of thermodynamic and kinetic parameters in in-situ conditions to promote full c-axis nucleation, we found a wide range of PO_2-T windows of highly epitaxial nucleation (not shown here). Notably, we reached full c-axis nucleation (Figure 4.43B) in full-liquid ($BaCu^{I/II}O$) regions of the kinetic phase diagram with ultra-fast

growth rates of 1400 nm/s for 400-500 nm of nanocomposite film thickness. The experiment was performed using an ultrafast acquisition time of 15 ms/frame compared to the standard experiments for phase evolution analysis of precursor, intermediate, and final phases using 200 ms/frame. The growth rates were calculated by the derivative of the fitting curve from the evolution of integrated AUC normalised with the thickness of the in-situ YBCO (005) reflection signal over time, as Figure 4.43C shown.

Hence, this, together with the experiments of pristine films conducted in L. Saltarelli's thesis, demonstrates the potential of precursor solutions based on propionate to enhance the growth rates of the TLAG process. Specifically, the in-situ XRD analysis revealed that precursor solutions based on propionates increased growth rates from 100 nm/s in 100 nm films utilising acetate precursor solutions to an estimated 1000-2000 nm/s in 400-500 nm nanocomposite and pristine films utilising the propionate precursor solutions.

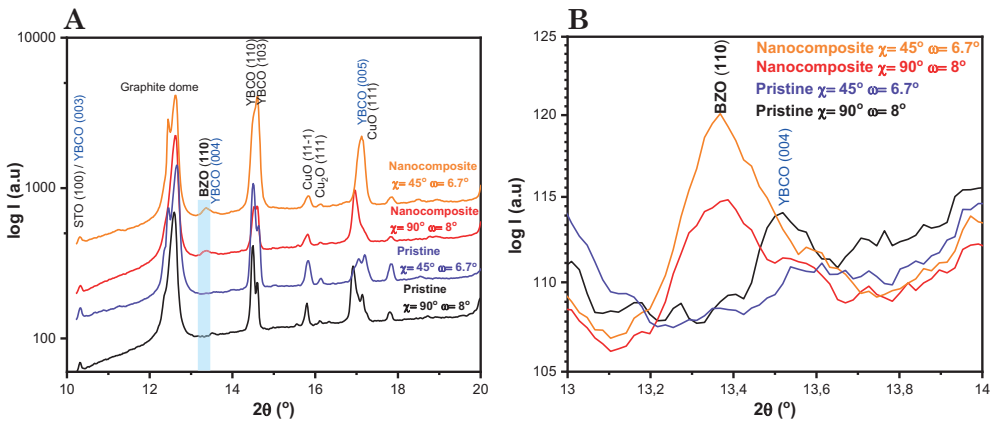

Figure 4.44 (A) Integrated 2D XRD scan after in-situ experiment of nanocomposite film and pristine film in 45° and ω to 6.7° and χ=90° and ω=8° diffraction configurations. The 2D XRD scan is obtained through integration in χ of the 2D-XRD image and (B) Zoom in on the 2θ range corresponding to the BZO (110) peak positions from the 2D XRD (A).

Finally, as we discussed in the previous section about the nanocomposite film microstructure analysis of samples grown at ICMAB, some of the NCs are randomly oriented, while others were able to rotate being epitaxially oriented. These results are further complemented here through in-situ studies. The reorientation of NCs during YBCO crystallisation was confirmed from previously

in-situ XRD studies with acetate-precursor solutions [10, 55] performing experiments aligned with Bragg condition of BZO or BZO (ll0) plane, which is the strongest reflection of the cubic phase and moving the χ angle of sample stage to 45° and ω to 6.7° to observe the diffraction coming from epitaxially embedded NCs. Therefore, to observe the behaviour of NCs in nanocomposite films prepared using propionate-based colloidal precursor solutions, we performed experiments using this diffraction configuration of χ=45° and ω=6.7° at one of the optimal processing conditions found with the highest epitaxial nucleation (heating at P_{total} = 0.025 mbar, PO_2 = 0.005 mbar up to 850 °C with a PO_2-jump to P_{total} = 100 mbar, PO_2 = 7 mbar). To maximise the intensity of NC peak, the nanocomposite precursor film used was composed of one SEED pristine layer + 3 NP layers with 18 %mol BZO NCs of 7 nm-size (~ 900 nm).

The integration of the 2D-XRD scan resulting from the growth under in-situ conditions is shown in Figure 4.44A. In addition, the 2D-XRD scan at χ=45° and ω=6.7° is compared with the standard diffraction configuration of χ=90° and ω=8°, where the BZO (110) peak comes from the diffraction of random-oriented NCs. Moreover, we compared it with a pristine film of 6 layers to confirm the correct assignment of the NC peak. The results show that the peak at ~ 13.3° of 2θ is present in nanocomposite film but not in pristine film, confirming that it comes from the diffraction of BZO (110). In addition, the intensity of this peak increases at χ=45°, in agreement with the fact that NCs are able to rotate in the Ba-Cu-O liquid phase and epitaxially align at the growth front when YBCO crystallises. This can be better observed in zoom on the region of the BZO (110) reflection (Figure 4.44B). Consequently, the reorientation of NCs is also demonstrated in nanocomposite films based on precursor solutions of propionate via in-situ XRD and TEM analyses of samples grown at ICMAB, which identified both random and epitaxial-oriented NCs.

In summary, in-situ XRD analysis was a very useful technique used during the PhD thesis for understanding the mechanism involved in the non-equilibrium TLAG process. This also entailed investigating the kinetic and thermodynamic parameters that promote c-axis nucleation in Y-Ba-Cu-O precursor films formed from propionate-based nanocomposites at high growth rates. The outcomes demonstrated that the utilisation of precursor films based on propionate improved the growth rates from 100 nm/s to 1000-2000 nm/s, which is 1.5-3 orders

of magnitude faster than alternative growth techniques. In addition, it was confirmed that NCs are capable of rotating during YBCO growth in these samples as well. Some extensive analysis of the in-situ XRD experiments is still ongoing and will be part of a future publication.

4.4 Conclusions

In this Chapter, we investigated deeply the insights of the epitaxial growth and superconducting properties of nanocomposite film growth by TLAG method through PO_2-route. We demonstrated the compatibility of the developed YBCO colloidal precursor solution containing BZO and BHO NCs with TLAG process.

Starting with the optimisation of growth conditions using a slow heating ramp (~0.2 °C/s) we encountered challenges such as bad wetting and the formation of large secondary phases inside the film, limiting the critical current to 1.0 MA/cm^2. The observed bad wetting in nanocomposite films was attributed to the high diffusivity of the transient Ba-Cu-O liquid phase formed during the YBCO growth. The increase of nucleation density by the use of a high supersaturated liquid composition as 2-3 instead of 3-7 was an effective tool to eliminate poor wetting. The notable improvement of texture quality and properties was achieved by using a high heating ramp (~1 °C/s) possibly related to the reduction of the formation of large secondary phases and less coarsening of YBCO precursor phases. These results indicated that the heating ramp is a relevant parameter in the kinetically controlled and non-equilibrium growth process through TLAG PO_2-route.

In the second part of the chapter, while optimising nanocomposite films with 5 nm-sized NCs, new challenges appeared, hindering high critical current densities, such as NC pushing and interface porosity, as observed by STEM-HAADF images. Considering the NC pushing effect, using 7 nm-sized NCs and tunning growth conditions, such as PO_2 based, mitigated this issue in agreement with the pushing/trapping theory. This optimisation led to strong epitaxial nucleation and high Jc self-fields. Highly epitaxial YBCO textured nanocomposite films ($\Delta\omega < 0.5°$) with high Jc values (2.4-2.6 MA/cm^2) were successfully obtained with NC amount ranging from of 6-24% mol. However, slight variations of Jc self-fields between replicates were observed in the 18% mol case.

This was attributed to non-controlled NC pushing at increased NC contents, an effect confirmed by TEM.

Furthermore, we have demonstrated that TLAG can effectively eliminate $BaCO_3$ in 875 nm thick nanocomposite film. This efficient removal of the precursor phase is crucial for achieving good YBCO texture and high current percolation. Epitaxial nanocomposite films (≤ 0.6 °) with good critical current densities (1.5-2.6 MA/cm^2 at 77K) were also obtained increasing film thickness from 425 to 875 nm with 6 and 18% mol. The reduction of Jc to 1.5 MA/cm^2 at 77K in thick nanocomposite film of 875 nm may be associated with a decrease in the superconducting cross-section, possibly due to the presence of some minor non-oriented grains or secondary phases inside the film. This could be solved by further optimisation of process conditions

Preliminary results demonstrated that BZO and BHO NC compositions are compatible with the developed nanocomposite precursor solution and with the TLAG process. Both compositions exhibit similar behaviour concerning YBCO nucleation, superconducting properties, and pinning characteristics at this stage.

Apart from the achievements reached with 7 nm-sized NCs where NC pushing is restricted, it was demonstrated by TEM characterisation that NC pushing with 5 nm-sized NCs is effectively eliminated through the utilisation of a pristine CAP layer.

Additionally, the identified interface porosity in nanocomposite films was also considered one of the potential factors limiting the critical current density. Modifying the multilayered architecture of nanocomposite films by decreasing the NC amount of the NP layer to 6%mol, diminishing the thickness of the pristine seed layer or eliminating the pristine seed layer resulted in completely pore-free continuous nanocomposite films. The proposed strategies aimed to reduce differences in the properties and behaviour, such as viscosity, of the liquid phase formed within the multilayers of nanocomposite films. This, in turn, was postulated to lead to the formation of a more homogeneous final mixture of the liquid phase, thereby avoiding defects like pores where a thin SEED pristine layer is a potential strategy to improve superconducting properties of nanocomposite films.

Nanocomposite films were extensively analysed by TEM to establish a correlation between their defect microstructure and pinning properties. STEM-HAADF images confirmed that, despite the limitation of NC pushing with 7nm-sized NCs, the pushing effect becomes again significant at higher NC amounts, specifically at 18%mol and 24%mol. However, it was avoided with the use of a CAP layer. In addition, both pristine and nanocomposite samples exhibited a high density of SFs across the whole films, a characteristic commonly observed in TLAG films. The microstructure of nanocomposites was shown to be significantly affected by the introduction of small NCs, as evidenced by STEM images and nanostrain values when compared to pristine films. Additionally, STEM analysis showed that small-sized NCs (7-20 nm) in our case had the ability to rotate during YBCO growth, ultimately ending up epitaxially oriented with the c-axis of YBCO, while larger-sized NCs (>20 nm) exhibited a random distribution.

The measurement of Jc versus applied field provided evidence of the enhancement of vortex pinning performance in nanocomposite films, surpassing pristine films above ~ 0.1 T at 5K and ~ 0.02 T at 77K. This confirms the enlargement of the single vortex pinning regime by the introduction of NCs, effectively increasing the number of pinning sites in the film. Despite the uncontrolled NC pushing and agglomeration, resulting in the observation of no linear correlation between μ_0H* with NC amount observation, a linear correlation was observed with increasing NP layer thickness, indicating an overall increase in the total density of defects in thicker nanocomposite films. In summary, nanocomposite films exhibit significantly higher pinning efficiency compared to pristine films, attributed to the larger nanostrain and μ_0H* values obtained. This improvement may be attributed to the pinning contribution of random NCs, creating a high density of stacking faults, and small-sized and epitaxial NCs, potentially acting as core pinning sites.

Angular-dependent electrical transport measurements of Jc(θ) revealed a more isotropic pinning contribution for 12% mol nanocomposite films across all directions of the applied magnetic field, surpassing the in-field Jc of the pristine films. Although further optimization of nanocomposite films is required to properly evaluate the pinning properties of samples with complete resolution of NC pushing and interface porosity issues, the already demonstrated improvement in pinning properties is closer to the requirements of coated conductors used in

applications under high magnetic fields.

Finally, in-situ XRD analysis was crucial for understanding the mechanisms in the non-equilibrium TLAG process and investigating kinetic and thermodynamic parameters influencing epitaxial nucleation at high growth rates. It was essential for enhancing c-axis nucleation in the Y-Ba-Cu-O system using propionate-based nanocomposite precursor films. The evolution of precursor phases, intermediate phases, and final phases was in agreement with the kinetic phase diagram for acetate-based precursor solutions. Furthermore, it was demonstrated that ultrafast growth rates of 1000-2000nm/s were reached with propionate-based precursor solutions, and the ability of NCs to rotate in the liquid during YBCO growth related to the liquid-assisted and fast kinetics of the TLAG process.

5

General conclusions and perspectives

5.1 General conclusions

This thesis presents a novel methodology for preparing superconducting nanocomposite films via TLAG-CSD using YBCO colloidal solutions. The synthesis, optimisation, and characterisation of nanoparticle solutions have been studied and characterised. The application of nanoparticle solutions in nanocomposite films has been designed, investigated, and characterised in detail, and the improvement of superconducting properties has been demonstrated.

The main conclusions drawn from the results obtained in this thesis are:

- **Nanoparticle synthesis**: We investigated and optimised the synthesis of $BaMO_3$ (M=Zr and Hf) and BaM_2O_6 (M=Ta and Nb) NP solutions using the H2S2 process from N. Chamorro et al. For $BaMO_3$ (M=Zr and Hf) NCs, it has been shown that the presence of ammonia in the precursor solution is a crucial factor influencing hydrolysis reactions, leading to precise control of NC size (~5,7 and 10 nm), size homogeneity, and reproducibility. We also unravelled the effect of polyol-type stabilisers on the control of NC size and shape, demonstrating the ability to tailor the surface with different stabilisers based on desired dispersion characteristics. Solvothermal temperature and the type of solvent significantly impact the crystallinity and stability of the NCs, respectively. In addition, $BaMO_3$ (M=Zr and Hf) NC solution stability for over 2 years was demonstrated. Finally, the compatibility of the H2S2 method with microwave thermal activation was demonstrated, offering a faster alternative to autoclave synthesis and enabling potential scale-up.

  The synthesis of BaM_2O_6 (where M=Ta and Nb) NPs in solution with a small-size and non-aggregated represents a groundbreaking achievement. In this case, higher temperatures and longer reaction times are required in the H2S2 process, and a post-synthetic surface modification based on ligand stripping proved successful for NP disaggregation, obtaining a homogenous NC solution of small-sized NCs of ~ 3-4 nm. Surface chemistry analysis using IR and EGA-MS techniques was relevant to postulate the surface stabilisers in the aggregated-NP system, focusing on the optimal ligand exchange strategies. Preliminary results suggest the compatibility

of stripped BaM2O6 NPs with YBCO growth, indicating their further potential application in nanocomposite film formation. Overall, the studies provide comprehensive insights into controlling nanoparticle synthesis for desired features for further application.

- **Nanocomposite film fabrication**: A novel methodology for preparing nanocomposite films for TLAG-CSD using YBCO colloidal solutions was developed. The combination of metal precursor salts based on propionates, an additive, and including preformed-NC solution as a solvent mixture for the dissolution of salts. This resulted in increased solution concentration, NC concentration in the colloidal YBCO precursor solution, and in the viscosity, thus reaching thicker nanocomposite films. The study demonstrated the production of high-quality precursor films with a proper nanocrystalline precursor microstructure to enhance the TLAG growth process. The solvent system for YBCO colloidal precursor solutions was optimised to ensure the stability of the NC solution and the solubility and stability of propionate salts. The stabilisation of NC solutions in YBCO precursor solutions involved various studies, including XRD, TEM, TGA, and rheology measurements, and several months of stabilisation were demonstrated. The optimisation process highlights the importance of achieving stable YBCO colloidal precursor solutions for the CSD-TLAG process.

- **Transient Liquid Assisted Growth (TLAG) process compatibility**: Finally, the developed formulation of YBCO precursor colloidal solution was demonstrated to be compatible with TLAG process through PO_2-route, enabling the formation of nanocomposite films with strong epitaxial YBCO growth with 3–7 composition in thicker films (400–500 nm of total thickness) at high growth rates (1000–2000 nm/s) and high-performance (Jc = 2.4–2.6 MA/cm^2 at 77K) up to very high NC amounts (6-24% mol).

  The growth optimisation, involving slow and fast heating ramps, revealed different limitations to obtaining high critical current density films, where microstructure analysis by TEM was essential to understand and address the different obstacles. Critical issues such as dewetting, NC pushing, and interface porosity (bad wetting) were addressed through different approaches.

We demonstrated that the dewetting effect could be mitigated by increasing nucleation density using high supersaturated liquid compositions (2–3) and tunning processing conditions with the slow heating ramp. Despite this, slow heating showed a limited critical current, possibly due to the formation of large secondary phases inside the film. The texture quality and properties were notably improved through the use of a fast-heating ramp, confirming the significant role of these kinetic parameters in the non-equilibrium TLAG process. Additionally, dewetting was avoided in the case of the 3-7 composition, which favoured better epitaxial growth.

The optimisation with 5 nm-sized NCs and a 3–7 composition using a fast-heating ramp introduced new challenges to reaching high current densities, including NC pushing and interface porosity. The NC pushing was mitigated by using 7 nm-sized NCs, probably because they are closer to the critical radius following the pushing-trapping theory. Nevertheless, this pushing effect was completely eliminated using a pristine CAP layer on top of the nanocomposite layers. We proposed that this was due to a difference in viscosity between the transient liquids of the pristine and nanocomposite layers. Despite this, the CAP layer strategy requires further study to identify the optimal thickness and achieve better epitaxial YBCO growth. In the case of 7 nm-sized NCs, nanocomposites reached high critical current densities (1.5–2.6 MA/cm^2) in thick films (~400–900 nm) from 6 to 18% mol $BaMO_3$ NCs. Also, preliminary results show that the BHO NC composition was compatible with the novel nanocomposite precursor solution and the TLAG process.

Interface porosity was also identified as a limitation factor that can yield reduced current carrying performance, and therefore it was also investigated. Modifications in the multilayered architecture resulted in pore-free nanocomposite films. Strategies aimed at reducing differences in properties and behaviour of the liquid phase formed at the different layers, such as viscosity, were proposed. The use of a thin SEED pristine layer emerged as a potential strategy to improve superconducting properties while preventing possible NC interface accumulation.

- **Vortex pinning analysis**: vortex pinning characteristics using a set of standard YBCO films of high critical current density (Jc = 1.5–2.6 MA/cm^2

at 77K) and a total film thickness of ~400–900 nm. Through structural measurements from XRD, microstructure studies from TEM analysis, and inductive and electrical transport measurements, we correlated the defect landscape with pinning properties, showing higher pinning efficiency in nanocomposite films compared to pristine films. TLAG nanocomposite films exhibit a high density of SFs and benefit from the combination of a mixture of epitaxial-oriented NCs (7-20 nm) in the YBCO matrix, able to act themselves as pinning centres, as well as larger (above 20 nm) and randomly oriented NCs, that generate additional pinning defects resulting from nanostrain. These factors collectively contribute to the enhanced efficiency of pinning. Thus demonstrating the complex but efficient vortex-pinning microstructure generated through the introduction of NCs in non-equilibrium and the fast kinetics of the TLAG process. In addition, we demonstrated that in the TLAG nanocomposite films, the decay of Jc as a function of magnetic field is smoother, the in-field performance improved, and angular isotropy enhanced as compared to pristine films.

- ***In-situ* synchrotron XRD experiments**: *In-situ* XRD analysis plays a crucial role in understanding non-equilibrium TLAG processes and kinetic parameters influencing epitaxial nucleation and growth. Growth rates of up to 1000–2000 nm/s in both nanocomposite and pristine films were demonstrated through *in-situ* XRD. Finally, the behaviour of nanoparticles in TLAG nanocomposite films was investigated, and it was shown that they are able to rotate in the liquid during YBCO growth to minimise the interface energy, despite the ultrafast kinetics of the TLAG process.

Overall, this work provides insights into the challenges and successes of nanocomposite film growth through the TLAG-CSD method, highlighting strategies for overcoming the issues encountered and demonstrating improved pinning properties with the developed YBCO colloidal precursor solution. These advancements bring the TLAG nanocomposite films closer to aligning with the requirements for applications at high magnetic fields. Moreover, the work demonstrates the capability of surpassing present cost and throughput constraints in the industrial fabrication process through growth rates that exceed by a factor of 10 the current growth methods and with competitive film thickness and performance.

5.2 Perspectives

During this PhD thesis, we realised that there is further insight to be uncovered and optimised. Concerning nanoparticle synthesis, a comprehensive understanding of the surface chemistry of NPs and ongoing investigation of the formation mechanism, particularly for BaM2O6 (M=Ta and Nb) NP solutions, which are synthesised for the first time in this work, will enable precise control over the final NP characteristics, ensuring stabilisation within the desired system. In addition, more efforts should be made towards the microwave approach, which provides short heating times and scalability.

In the context of superconducting nanocomposites, future research should primarily concentrate on optimising the thickness of SEED and CAP-pristine layers of the multilayered architecture proposed for nanocomposite films. This emphasis is intended to mitigate interface porosity and prevent the pushing of NCs with 5 nm-sized, which are expected to yield high pinning efficiency and high critical currents. Simultaneously, this approach aims to minimise differences in growth conditions and properties between pristine and nanocomposite layers. Furthermore, there is a need to carry out fine-tuning of processing conditions for thick films ($\geq$ 900 nm) and optimise growth on commercial metallic substrates. Overall, the results acquired in this PhD thesis are ready to be transferred to the fabrication of high-throughput and low-cost TLAG nanocomposite-coated conductors.

A

Appendix Characterisation techniques

A.1 X-Ray diffraction

X-ray diffraction (XRD) is a powerful and widely used technique in the structural analysis of crystalline materials. This non-destructive technique relies on the fact that the wavelength of X-rays is comparable to the spacing between planes in crystalline materials. When a monochromatic X-ray beam interacts with a crystalline matrix, it scatters in various directions based on the crystallographic planes with the same wavelength as the incident beam. For certain incident angles, the diffracted beam will interfere constructively according to Bragg's law [245, 246]:

$$2d_{hkl} \cdot \sin\theta = n\,\boldsymbol{\lambda} \tag{A.1}$$

where d_{hkl} is the distance between crystalline planes with Miller indices (hkl), θ is the incident angle, n is an integer, and λ is the wavelength. Each family of crystalline planes, characterised by a specific spacing, diffracts only at a particular incident angle θ, enabling their identification. The diffraction pattern, intensity vs 2θ, is recorded for each incident angle.

In the case of polycrystalline materials with randomly distributed grains, the scattered intensity forms a ring due to each plane family diffracting in its specific diffraction direction for each oriented grain. For epitaxial samples, constructive interference only occurs at specific configurations, as planes oriented in one direction fulfil Bragg's law under specific conditions. The diffraction configuration becomes crucial for extracting information, which depends on angles involving the incoming beam, sample stage, and detector. The incoming and diffracted beam angles (ω and θ) are modified through motorised arm movements, while sample rotational angles (χ and ϕ) are adjusted through tilt and rotation of the sample stage. The typical Bragg-Brentano configuration used in X-ray diffraction systems is shown in Figure [245–247].

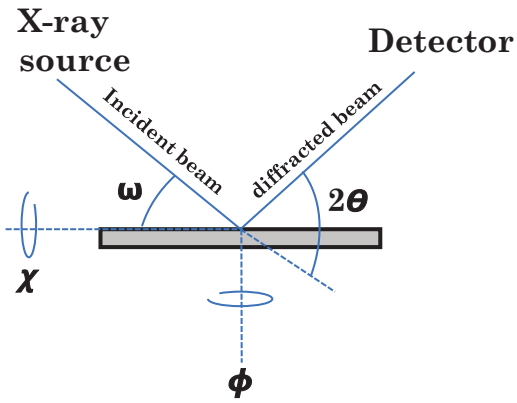

Figure A.1 Scheme of typical Bragg-Brentano configuration for XRD.

In this study, two diffractometers operated at ICMAB were employed: the Bruker D8 Discover with a Lynxeye XE energy-dispersive with a 1D detector and the Bruker-AXS D8 Advance equipped with a two-dimensional detector, a General Area Detector Diffraction System (GADDS).

Different measurements were conducted on each diffractometer [10, 33, 55]:

- **2D XRD measurements with GADDS**: Due to the wide angular range detectable in GAADS (up to 30° in 2θ and 60° in χ), it is a widely used technique to quickly assess the texture quality of films in one single image. The texture quality of the films was evaluated through standard 2-2θ measurements between 15-55° at a fixed 2θ of 35°, χ of 90° (to cover epitaxial and random diffraction of reflections) with a ω of 10° and ϕ= 0 with acquisition times of 30 minutes. For precursor films, a measurement with a tilted substrate was used to eliminate substrate peaks and avoid their overlapping with the polycrystalline peaks from the film. In addition, epitaxial-aligned nanocrystals can be detected in a different diffraction configuration due to the epitaxial diffraction of (ll0) of the NC phase appearing at χ= 45. In this case, we performed a 2-2θ measurement during 1h at χ= 45, 2θ= 30 and ϕ= 0.
- **HR XRD measurements with Bruker D8 Discover**: 2-2θ scans were performed to identify phases and grain orientation in films. Each peak position can be identified to its corresponding phase through comparison

with data sheets. 2-2θ measurements were performed between 5-120° with a step of 0.02° for films. In this configuration, rocking curves were recorded to probe the out-of-plane orientation of epitaxially aligned grains (c-axis tilt). This is done by keeping the angle between the incident beam and detector fixed while scanning in ω. The constant angle ensures that the Bragg condition remains unchanged providing exclusive information on the misalignment angle of c-axis grains.

However, in this geometry, random phases are strongly reduced in intensity as the diffraction configuration is in Bragg with (00l) reflections of YBCO. Grazing incidence (GI) geometry was used to enhance polycrystalline phase intensities, such as precursor phases, intermediated phases from quench processes, secondary phases or nanocrystals which are in general random-oriented phases. Through GI measurements we can eliminate the high-intensity epitaxial (00l) peaks of YBCO (00l) and (h00) reflections of STO substrate by performing a 2-2θ scan with a very low ω angle of ≈1°. Specifically, to only detect NCs in precursor films with HR XRD, we performed GI measurements during 1h in 2-2θ of 29-32° which is in the range of the most intense reflection of NC phase, the (ll0).

Concerning the determination of the crystalline structure of initial NCs, powder HR XRD measurements can be performed with a 2-2θ scan of 10-80°.

A.1.1 Nanoparticle crystallite (Sherrer) size determination

Regarding crystallinity analysis of nanoparticles, powder 2-2θ (10-80 °) HR XRD measurements in the Bruker D8 Discover X-ray diffractometer have been employed. By comparing the experimental XRD pattern with the database of the expected phase, we can determine the specific crystalline structure present in our system. Furthermore, we can calculate the crystalline size (β_s) of the nanoparticles through the obtained XRD patterns and using the Sherrer equation:

$$\beta_S = \frac{K\lambda}{D \cdot \cos\theta} \tag{A.2}$$

where K is a shape parameter (0.9 for spherical particles), λ the wavelength of X-ray diffraction, D the full width at half maximum of the most intense peaks and θ the angle between the incident and the dispersed rays [153, 154]. The final NP crystallite (Sherrer) size was obtained from the mean of the sizes determined from the full widths at half maximum of the two most intense peaks of the cubic phase, the (ll0) and (l00). Once the two full widths at half maximum were determined through peak fitting, the instrumental error was subtracted. For the instrumental error, the XRD pattern from the powder LaB_6 compound was considered.

A.1.2 Nanostrain analysis

The local strain distortions in a crystalline structure (nanostrain) can be determined using the Williamson-Hall method [239, 243, 248]. We analysed the broadening of (00l) YBCO peaks obtained from the full θ-2θ HR XRD pattern by fitting each (00l) YBCO reflection with Lorentzian peak shape to obtain the value of full width at half maximum (FWHM). The total broadening (Equation A.3) of Bragg's reflections (β_{total}) is produced by crystallite sizes (β_s) defined by the Sherrer equation (Equation A.2) [153, 154] and local strain deviations (β_ϵ) related by the Stoke-Wilson equation (Equation A.4) [249]:

$$\beta_{total} = \beta_s + \beta_\epsilon \tag{A.3}$$

$$\beta_\epsilon = \epsilon \cdot \frac{\sin\theta}{\cos\theta} \tag{A.4}$$

where K is a shape-parameter (0.9-1), λ is the wavelength of X-ray diffraction, D the crystallite size, θ the angle between the incident and the dispersed rays and ϵ nanostrain. The Williamson-Hall analysis separates both broadening contributions by the relation:

$$\beta_{total} \cdot \cos\theta = 4\epsilon \cdot \sin\theta + \frac{\lambda}{D} \tag{A.5}$$

where ϵ can be calculated from the slope of the linear fit from plotting $\beta_{total}\cdot\cos(\theta)$ vs $4\cdot\sin(\theta)$ considering β_{total} related to the FWHM for Lorentzian fitting of each YBCO (00l) peak [10, 239].

A.1.3 NC random fraction determination

The methodology employed for determining the random fraction (%) of nanocrystals (NCs) was originally introduced by A. Llordes et al. through the application of GADDS 2D-XRD integration on any given NP reflection [239]. Detecting diffraction from epitaxial NCs necessitates performing 2D GADDS XRD measurements for one hour in the Bragg conditions of the most intense reflection of the cubic phase of NCs, specifically the (ll0) plane, with the diffraction configuration set at χ = 45° and ω = 15°. This configuration enables the recording of the epitaxial (ll0) spot intensity (I_{spot}) from epitaxially-oriented NCs and the randomly distributed ring intensity (I_{ring}) of the same reflection resulting from the diffraction of randomly oriented NCs. Exemplaries of 2D-XRD images are presented in Figure A.2A-B. Subsequently, upon obtaining the XRD pattern, it is necessary to integrate the areas corresponding to the epitaxial and random contributions of the (ll0) reflection, along with their respective backgrounds.

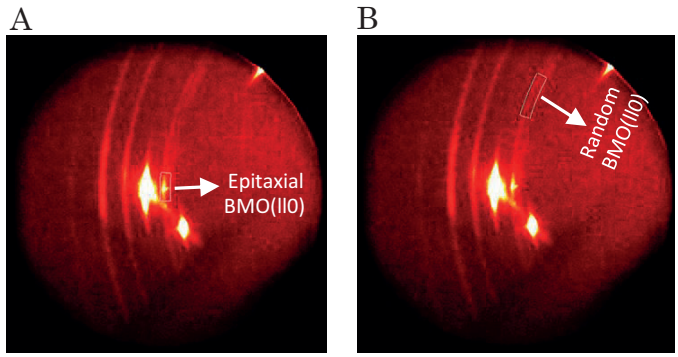

Figure A.2 2D GADD XRD images showing the chosen regions for the integration of (A) epitaxial part (spot intensity) and (B) random part (ring intensity).

To integrate the epitaxial part, a narrow range of 2θ is selected, centred on the spot ($\Delta 2\theta$ = 1.5°), with $\Delta\chi$ of 12°. The same range of 2θ and χ is employed to integrate the ring from randomly oriented NCs by moving up or down to a χ value in the ring region. Once $\Delta\chi$ values are fixed for both the spot and ring,

these values are employed to integrate the background, varying the 2θ in the background region with a width of ($\Delta 2\theta$ = 1.5°). The corresponding areas of the integrated background are subtracted from the obtained I_{spot} and I_{ring}.

Finally, the random contribution is subtracted from the epitaxial one to ensure that only the epitaxial part is considered. The random fraction ($I_{random}/I_{epitaxial}$) can be calculated by applying the following Equation:

$$\frac{I_{random}}{I_{epitaxial}} = \frac{I_{ring} \cdot \frac{360}{\Delta\chi} \cdot 4\pi}{8 \cdot I_{pole}} \tag{A.6}$$

A.1.4 Lattice parameter determination

For the c-axis determination, the Nelson-Riley method was employed [250]. First, (00l) reflections with l= 4,5,7,8,10,11 and 13 of YBCO from 2-2θ HR XRD measurements are fitted to extract the 2θ value for each peak. Then, the interplanar spacing for each plane (d) was determined following Equation A.1. Moreover, 2θ values are used to calculate the Nelson-Riley (NR) parameter from the corresponding equation:

$$NR = \frac{cos^2(\theta)}{sin\,(\theta)} + \frac{cos^2(\theta)}{\theta} \tag{A.7}$$

Finally, NR values are plotted versus d values, and the c-axis was obtained from the intercept value of the y-axis from the linear fit.

A.2 Microscopic techniques

A.2.1 Optical Microscopy

The homogeneity characterisation of precursor nanocomposite films was performed by optical microscopy (OM) which uses a magnifying lens and visible light resolution. The optical microscope images were acquired using a Leica DM1750 M at ICMAB.

A.2.2 Transmission Electron Microscopy

Transmission Electron Microscopy (TEM), along with other electronic microscope techniques, is a powerful technique able to obtain information down to the nanoworld. By employing an electron beam instead of conventional visible light, TEM enhances resolution, providing images with atomic resolution, given that electrons have wavelengths 100,000 times shorter than those of photons. This enables the measurement of the size and shape of nanoscaled systems within a range spanning from a few nanometers to microns [251–254].

The fundamental principle underlying TEM involves the interaction between an accelerated electron beam and the sample. Electrons, emitted by an electron gun, form a beam accelerated by an anode-cathode device. The electron beam is controlled and focused by electromagnetic lenses before being transmitted through the sample affixed to the specimen stage. The resolution limit of the image is determined by the objective lens, while the magnification system consists of the projector and intermediate lenses. The final image is obtained by projecting transmitted electrons onto a fluorescent screen or recording them in an electron detector with the aid of computer monitor software [251–254].

When electrons impact the sample, some pass through without interacting (non-scattered or transmitted electrons), while others scatter upon impact with the sample. Consequently, TEM microscopy employs two contrast modes: transmitted and scattered electrons, each providing distinct information about the sample. Scattered electrons offer insights into the crystallinity via electron diffraction patterns, while transmitted electrons scatter elastically, enabling the imagining observation of particle distribution, shape, and size in the sample. Within transmission mode, electrons can also scatter inelastically, allowing chemical composition determination through Energy Dispersive X-ray Spectroscopy (EDS) or Electron Energy Loss Spectroscopy (EELS) [251–254].

In this thesis, depending on the type of sample and resolution needed, different TEM equipment was used:

- **Nanoparticle solutions**: TEM characterisation was performed using a 20 kV JEOL 1210 TEM, which has a resolution point of 3.2 Å from ICMAB by technical support and Jeol JEM 1400 TEM of 120kV from from Servei

de Microscòpia of UAB as self-user. For higher resolution images, especially when analysing the structural lattice of the NCs, High-Resolution Transmission Electron Microscopy (H-RTEM) images were performed and obtained on a 200 kV JEOL 2011 TEM, with a resolution point of 1.8 Å at 200 kV from Servei de Microscòpia of UAB as self-user.The samples were prepared for TEM analysis by depositing a drop of as-prepared NC-diluted dispersion on amorphous carbon-coated grids and then drying them in air.

- **TLAG nanocomposite films** [10, 255]: TEM analysis of grown YBCO nanocomposite films was used to analyse the microstructure, atomic-defect structure, and phase composition. Dr. K. Gupta, a post-doctoral researcher in our group (SUMAN), conducted TEM studies. Two distinct TEM microscopes were employed based on the desired resolution. A FEI Tecnai G2 F20 operating at 200kV was utilised at the "Institut Català de Nanociència i Nanotecnologia" (ICN2) for low-magnification images. Moreover, HR-TEM images of TLAG nanocomposite films were also performed in TEM from ICN2. Additionally, for high-resolution images, Scanning transmission electron microscopy (STEM) was carried out with a FEI Titan 60-300 microscope, equipped with a Gatan TRIDIEM 866 ERS energy filter, an X-FEG gun, and a CETCOR probe corrector, operated in STEM mode at 300 kV at the Advanced Microscopy Laboratory (AML) in Zaragoza. This microscope was equipped with multiple annular and circular detectors, allowing different contrast imaging modes and the extraction of different types of information. In this work, the High-Angle Annular Dark-Field (HAADF) imagining mode was used, which allows a direct correlation between contrast and atomic density. In addition, this microscope is also equipped with an Electron Energy Loss Spectrometer (EELS) capable of detecting scattered electrons and determining the chemical composition of the samples. Cross-sectional specimens were prepared by conventional methods based on mechanical polishing or by focused ion beam etching (FIB). Electron-transparent lamellas can be obtained through both techniques, but FIB etching allows precise region selection and reduced thicknesses.

A.2.3 Scanning Electron Microscopy

The surface morphology and composition of TLAG nanocomposite films was also characterised using Scanning Electron Microscopy (SEM) and energy-dispersive X-ray (EDX) spectroscopy, respectively, with a QUANTA FEI 200 FEG- ESEM at ICMAB as a self-user. This SEM operated under a high vacuum of 15 keV. The SEM technique relies on utilising a focused electron beam to obtain surface morphology and composition information about the sample.

Specimen preparation is unnecessary for the final YBCO films, as they become electrically conductive after oxygenation. The samples are introduced into a high-vacuum chamber and exposed to a focused beam of high-energy electrons. In this method, the beam is directed towards the surface of the sample, interacting with atoms in the initial tens of nanometers of the film. Two distinct types of electrons are scattered and subsequently detected by SEM detectors. Secondary electrons, generated through inelastic interaction with ionised surface atoms, create contrast based on the depth at which these atoms are situated. Consequently, the secondary electron (SE) detector produces a high-resolution topography image, enabling an examination of the surface morphology of the films. Additionally, the SEM is equipped with a detector for backscattered electrons, which are electrons with higher energy resulting from interactions with atomic nuclei. This electron detection allows the identification of the chemical composition of specific areas within the sample, such as individual grains. This technique is referred to as Energy Dispersive X-ray Spectroscopy (EDX).

A.3 Dynamic light scattering technique

Dynamic Light Scattering (DLS) and Z-potential analyses have been carried out in the Characterization of Soft-Materials Services at ICMAB using a Zetasizer Nano ZS in back-scattering mode (173°) with a measurement range of 0.6 nm–6.0 μm and a sensitivity of 0.1 mg/mL. The DLS measurements were used to analyse the particle size distribution and the hydrodynamic diameter of NPs in solution [256].

The technique is based on the light scattering from particles irradiated

with an incident laser that are subjected to Brownian motion. Brownian motion is a random movement resulting from the interaction between dispersed particles and the solvent where they are dispersed. The velocity of particles subjected to a Brownian motion depends on the hydrodynamic size and viscosity of the solvent. The hydrodynamic size of nanoparticles is the size of the NP core and the shell surrounding the NP surface, which includes the capping ligands and the solvation ions, as a difference from TEM, where only the NP core is observable (Figure A.3A). From the particle Brownian motion, we can calculate the diffusion coefficient (D) related to the hydrodynamic diameter (d) through the Stokes-Einstein equation [256–258]:

$$D = \frac{kT}{3\pi\eta d} \tag{A.8}$$

The DLS recorded the intensity fluctuations with the time of the scattering light from particles and generated a correlation function, which is transformed into an intensity vs. hydrodinamic size by applying an algorithm. To have a better approximation of the size distribution, intensity versus hydrodinamic size is transformed to volume vs. hydrodynamic size using particle optics.

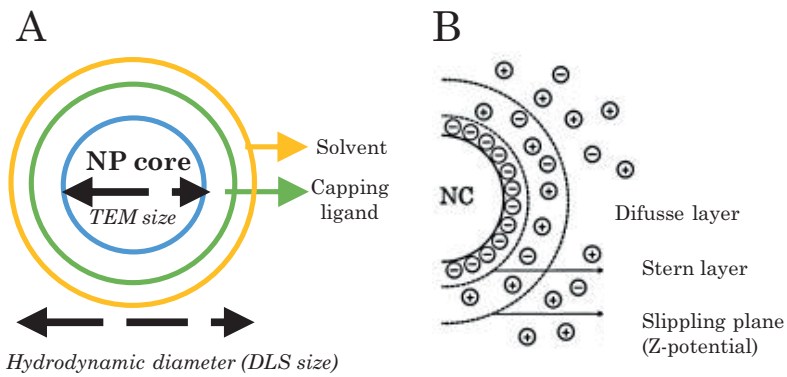

Figure A.3 (A) Schematic representation of the different diameters of an NP and (B) Schematic representation of which part measures the Z-Potential in an NC solution. Adapted from [115]

In addition, using the same DLS equipment, the stability of nanoparticle solutions can be determined through the surface charge of nanoparticles (Figure

A.3B) in the Slippling plane (Z-Potential) by the measure of electrophoretic mobility. The Z-potential (Z) is related to the electrophoretic mobility (U_E) through Henry Equation:

$$Z = \frac{U_E \cdot 3\eta}{2 \cdot \mathcal{E} \cdot A} \tag{A.9}$$

where A is the Henry function, ϵ dielectric constant and ε the viscosity. The instrument automatically performs the conversion from electrophoretic mobility to the Z-potential value. For colloidal solutions electrostatically stabilised, a higher value of Z-potential indicates higher stability of NC dispersion, with a limit value of ≥ ± 30 mV [176, 177, 256, 258, 259].

A.4 Fourier Transform Infrared Spectroscopy

Fourier transform infrared spectroscopy (FT-IR) equipment (Spectrophotometer Jasco 4700 with energy range: 300-7800 cm^{-1}) with an Attenuated Total Reflectance accessory (ATR) for powder samples was used to analyse the surface chemistry of powder nanoparticle samples. The analyses have been carried out at the ICMAB Spectroscopy Service. Before any measurement, a background spectrum is acquired to eliminate the influence of water and CO_2 emissions from the surrounding atmosphere.

A.5 Thermal analysis techniques

The thermal studies were performed in collaboration with J.Farjas from the University of Girona.

A.5.1 Thermogravimetry analysis (TGA) technique

The organic decomposition process of YBCO precursor colloidal solutions and organic decomposition from NP surfaces from powder NP samples has been studied through thermogravimetry analysis (TGA) using a Mettler Toledo thermobalance. First, for the YBCO precursor colloidal solution measurements, the

solutions were deposited on a substrate and dried for 5 min at 75 °C. Then, these samples were heated at a constant rate of 5 K/min under a humid oxygen flow of 80 ml/min. The humid oxygen flow utilised in a pyrolysis process was replicated by flowing the carrier oxygen gas at standard temperature and pressure (25°C, 1 atm) in a distilled water flask. In the case of powder nanoparticles, the samples were heated at a constant rate of 10 K/min under a dry oxygen flow of 60 ml/min.

A.5.2 EGA-MS technique

Evolved Gas Analysis (EGA) through mass spectrometry (MS) is an essential method for identifying volatile products during the thermal degradation of substances. Operating under vacuum conditions, EGA-MS provides high sensitivity and minimises the possible secondary reactions between volatiles. This makes it particularly suitable for decomposition processes involving the release of various radicals from the surface of nanoparticles.EGA-MS provides information on the mass of organic molecules lost at different temperatures and the mass spectrum of each detected volatile in the system [59, 200].

The EGA-MS setup comprises a quartz tube maintained at a pressure of 10^{-6} bar. EGA-MS experiments were run by placing the powder nanoparticles at one closed end of the quartz tube, on a platinum sheet equipped with a K thermocouple to measure the sample temperature. The quartz tube is situated inside a low-resistance tubular furnace to conduct the experiments at 5K/min. The other end of the quartz tube was connected to a quadrupole mass spectrometer, specifically a Microvision Plus model from MKS, to analyse the evolving gases from the sample. This configuration enables the continuous monitoring of volatile evolution and its fragments with respect to the sample temperature [59, 200].

A.6 Inductively Coupled Plasma Mass Spectrometry (ICP-MS) analysis

The Inductively Coupled Plasma Mass Spectrometry (ICP-MS) analysis was used to determine the total content of metals (Ba,Ta and Nb) in powder samples of BaM_2O_6 nanoparticles and confirm the stoichiometry of these compounds. The ICP-MS analysis was performed at Servei d'Anàlisi Química at the UAB.

The samples were prepared following the protocol Servei d'Anàlisi Química based on a microwave digestion (microwave digestor Milestone, model Ultrawave) of powder NPs using a concentrated solution of HCl, HNO_3 and HF acids. Then, liquid samples are initially nebulised to generate an aerosol, which is then transferred to the argon plasma that is inductively coupled by radiofrequencies. The high-temperature plasma atomised and ionised the sample. The ions generated are guided and focused by electrostatic lenses into the quadrupole mass analyser. Ions are separated by the mass analyser based on their m/z ratio (defined as the mass of an ion divided by its charge), and the detector measures these ions [260, 261].

A.7 YBCO nanocomposite precursor solution characterisation: rheological properties and contact angle

A.7.1 Viscosity

The viscosity was measured with a HAAKE RheoStress RS600 from Thermo at room temperature by the "controlled stress method". In response to applied forces, the resistance of liquids is measured by a rheometer. Particularly is based on the correlation of the shear rate generated by a liquid contained within a rotating and stationary cylinder with viscosity.

A.7.2 Contact angle

The contact angle enables the quantification of the degree of wettability exhibited by a liquid on a specific surface. The evaluation of our solutions is conducted on STO substrates using imaging analysis of photographs of sessile droplets using a Drop Shape Analyzer DSA 100 from Kruss [262].

A.7.3 Water content

The water content of the solution was measured through the KarlFischer titration method [206, 207] with a Nittoseiko Analytech, Model CA-310 equipped with a VA-200 vaporizer.

A.8 Physical characterisation techniques

A.8.1 SQUID dc-magnetometry: Jc(T,H) measurements

Inductive critical densities (Jc at self-field) through Jc(T,H) measurements were obtained with a commercial superconducting quantum interference device (SQUID) magnetometer from Quantum Design equipped with a superconducting magnet of 7T. The measurements were conducted by Dr.B.Bozzo and Dr.F.Vallés. Inductive SQUID measurements are fast and non-destructive, besides allowing a broad range of temperature and magnetic field variations. Therefore, they have been extensively used in this thesis for evaluating the superconducting properties of the samples.

Jc(T) measurements were performed in Zero Field Cooled conditions (ZFC) by cooling down the films to 5K in self-field. Then the magnetic moment is saturated with a 3T magnetic field which is suddenly removed. Subsequently, the Jc(T) magnetisation is measured during the temperature increase and no external field is applied.

On the contrary, Jc(H) measurements were performed by cooling the sample until the desired temperature, typically 5K or 77K, followed by the increasing of the magnetic field to a maximum of 7 T while the magnetization values are

being measured at a constant temperature and then, decreased to close the hysteresis loop. Therefore, a magnetic field parallel to the c-axis is applied from 0T to 7T and then reversed until -7T, measuring hysteretic magnetisation curves.

Inductive critical current densities were calculated by the Bean critical state model [242, 263] following the equation:

$$J_c = \frac{3m}{a^3 t} \tag{A.10}$$

Where m is the magnetisation value, a is the effective radius of a circular area that would cover the full surface of the measured sample and t is the thickness.

A.8.2 Electrical transport characterisation

Electric transport measurements were carried out at ICMAB by a member of our group, A.Kethamkuzhi, using a PPMS Quantum Design system equipped with a 9T superconducting magnet. Electrical transport assessments were conducted employing two primary configurations, each employing a 4-point contact method. Van der Pauw geometry was employed for resistivity measurements while four-terminal sensing on patterned bridges was used to investigate the pinning performance of TLAG nanocomposite films.

A.8.2.1 Determination of Tc by Van der Pauw method

The Tc values of TLAG nanocomposite films were obtained using the van der Pauw method which is a non-destructive technique. This method consists of the use of 4 silver resistance contacts placed on top of the sample to directly measure the voltage drop produced by an applied electrical current while increasing the temperature. Thus, determining the resistivity as a function of temperature using the voltage and the film thickness. The Tc values were determined by applying the maximum derivative to the resistivity versus temperature plot as Figure A.4 shown [10, 264].

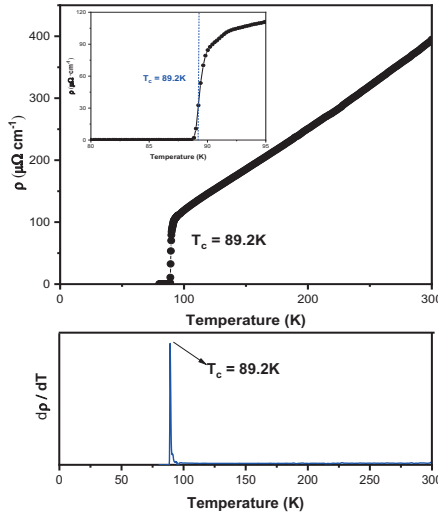

Figure A.4 Measurements performed in Van der Pauw geometry to obtain the dependence of temperature with resistivity. Tc values are determined through the maximum derivative criteria (blue curve).

A.8.2.2 Transport measurement: Jc (θ)

The evaluation of critical current involves that the electrical current needs to be confined in bridges with relatively low cross-sections. The pattered bridges were fabricated through a photolithography process, with subsequent deposition of four silver contacts through sputtering. After patterning, the samples are placed and connected to a commercially available electrical probe to perform transport measurements in PPMS unit. An electrical current is applied to the contacted patterned samples, and the resulting voltage drop is measured. The critical current is determined as the minimum current required to generate a 10μV/cm electric field in the superconductor. This experimental setup was utilised to assess the critical current at varying temperatures, under different applied magnetic fields (up to 9T), and with different orientations of the magnetic field [10, 265].

B

Appendix Chapter 2

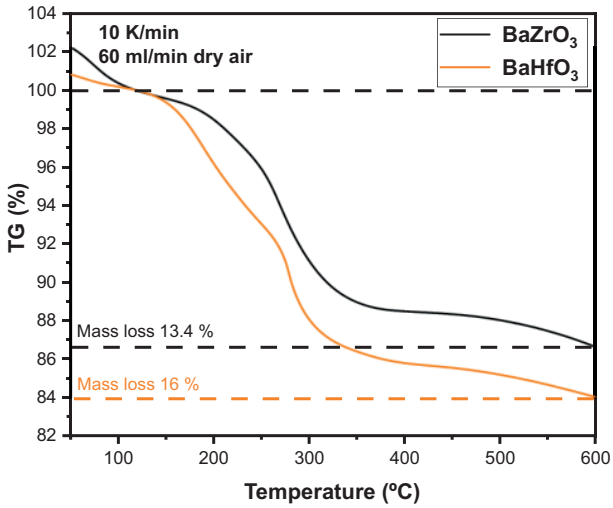

Figure B.1 TGA analysis of $BaZrO_3$ (black) and $BaHfO_3$ (orange) NCs powders.

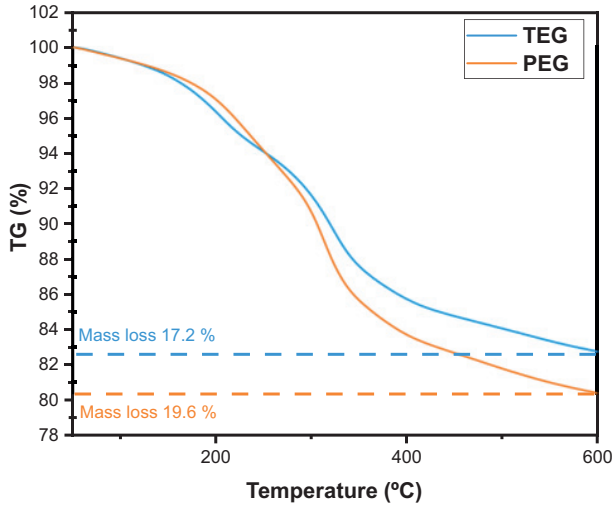

Figure B.2 TGA analysis of $BaZrO_3$ NCs stabilised with TREG (blue) and PEG (orange)

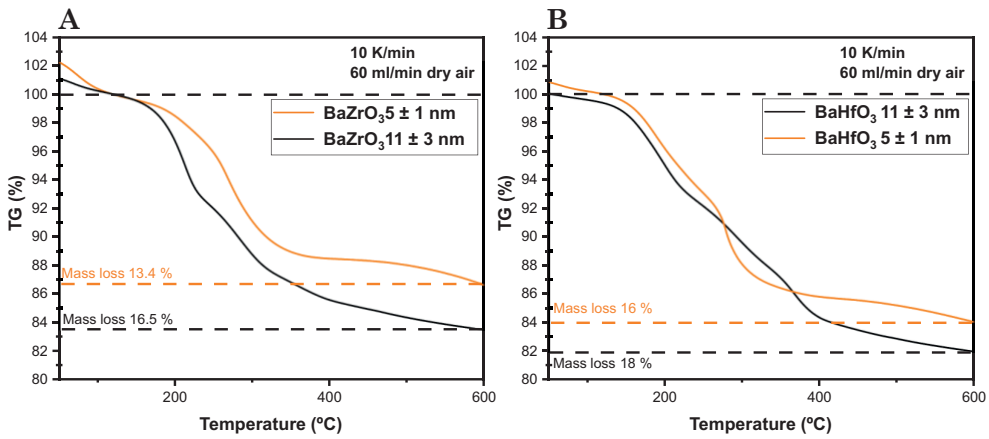

Figure B.3 TGA analysis of (A) $BaZrO_3$ NCs and (B) $BaHfO_3$ NCs of 5 ± 1 nm (orange) and 11 ±3 nm (black) of size

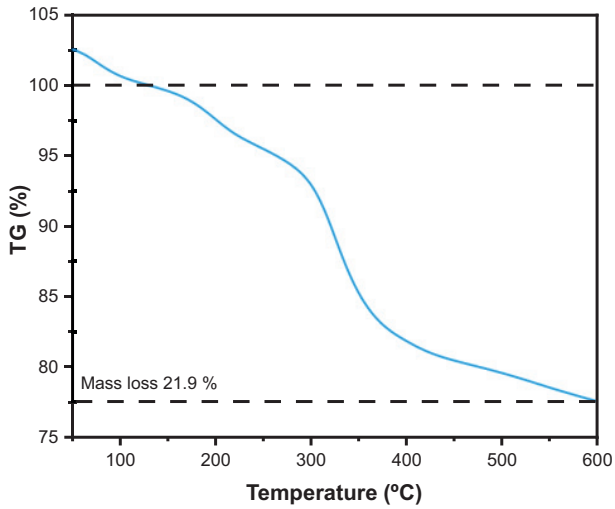

Figure B.4 TGA analysis of $BaZrO_3$ NCs synthesised via MW method

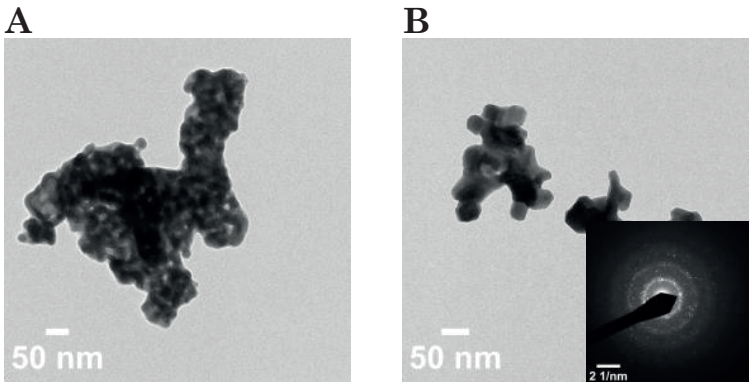

Figure B.5 TEM images of (A) $BaNb_2O_6$ powder NPs after annealing at 700 °C and (B) $BaTa_2O_6$ powder NPs after annealing at 900 °C with SAED pattern inset.

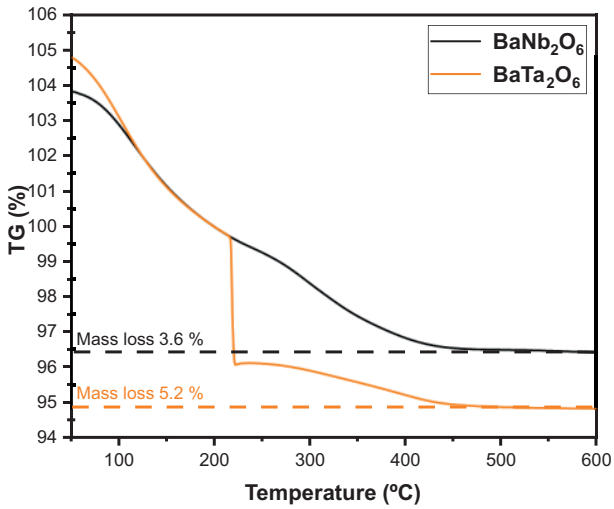

Figure B.6 TGA analysis of $BaNb_2O_6$ (black) and $BaTa_2O_6$ (orange) NCs powders.

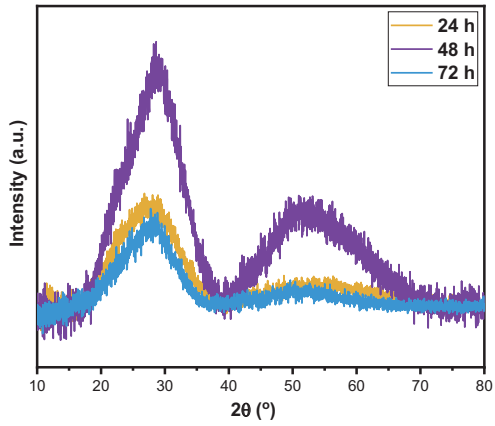

Figure B.7 Powder XRD patterns of $BaNb_2O_6$ NPs synthesised at 220 °C during 24 h (orange), 48 h (purple) and 72 h (blue).

B.1 Application of stripped-$BaNb_2O_6$ NPs in YBCO nanocomposite films

The hydrophilic surface resulting from ligand stripping exchange provides electrostatic stabilization of $BaNb_2O_6$ NPs in polar media. In addition, the small-sized (< 10 nm), homogenous distribution and crystallisation temperatures of 700-900 °C previously demonstrated make them suitable to be compatible with YBCO precursor solutions and nanocomposite film growth. Although the stripping treatment is still under optimisation, in terms of cleaning from reagent excess to obtain a final stable colloidal solution allowing better NP characterisation, we tested for the first the compatibility and the behaviour of the application of preformed $BaNb_2O_6$ NPs in nanocomposite YBCO films.

YBCO-$BaNb_2O_6$ precursor solution with 4.8 %mol was prepared by mixing 50/50 v/v of stripped solution and fluorine-free YBCO precursor solution. The procedure followed for the preparation of pristine-YBCO precursor solution is described in [46] and in chapter 3. The nanocomposite precursor film was prepared by depositing the nanocomposite precursor solution on 5x5 mm $SrTiO_3$ (STO) single crystal substrate via spin coating (6000 rpm for 2 min) followed by a low thermal treatment (500 °C) called pyrolysis. Details of preparation, conditions and thermal profiles for deposition and pyrolysis steps for multilayer depositions were explained in the section (chapter 3 experimental). Then, the crystallisation of nanocomposite precursor films into the final YBCO nanocomposite films was performed at 820 °C for 180 min in a humid N_2 atmosphere with an O_2 partial pressure of 200 ppm. Finally, the superconducting YBCO phase was obtained by another thermal treatment at 450 °C for 210 min with dry O_2 flow of 0.3 L/min.

Firstly, the resulting nanocomposite precursor film was characterised by optical microscopy (OM) to check the homogeneity, reflectometry to measure the film thickness and 2D X-ray diffraction measurement (GADDS) to check the crystalline precursor phases. The OM image (Figure B.8A) shows homogeneous deposition but the quality of the precursor layer was far from optimal [46], exhibiting a rough surface with some defects. The observed inhomogeneities could be attributed to that the nanocomposite precursor solution was not optimal for the desired quality. In this initial optimisation, we mixed

50/50 v/v of stripped solution in ACN/DMF and pristine-YBCO precursor solution in Methanol (MeOH)/ Propionic acid (Hprop) and maybe the solvent ratio and reagent excess from the stripping solution employed was not the most favourable and compatible with YBCO precursor salts to ensure enough stability which ends up in homogeneous deposition.

The final nanocomposite precursor film consists of a YBCO seed layer at the interface with STO, avoiding possible interface problems and improving texture quality [47, 55, 97] (details discussed in chapter 3) and two nanocomposite layers. A total thickness of 660 ± 50 nm was determined by reflectometry shown in Figure B.8B).

Concerning the novel fluorine-free YBCO precursor solution developed, which is a propionate-based solution, the expected and desired precursor phases for the transient liquid assisted growth process (TLAG) are CuO, Y_2O_3, and mainly orthorhombic $BaCO_3$ phases [42, 46]. In our case, XRD analysis of YBCO-$BaNb_2O_6$ nanocomposite precursor film (Figure B.8C) shows mainly BaF_2 and CuO phases. The formation of BaF_2 phase, in spite of we used a fluorine-free YBCO precursor solution, is associated with the presence of BF_4^- anions stabilising stripped-$BaNb_2O_6$ NP solution. The fluorine content present in stripped-$BaNb_2O_6$ solution (4% less fluorine content than low-fluorine trifluoroacetate solution [266]) seems enough to react with barium precursor salt after the first thermal treatment. Therefore, the growth mechanism associated with this nanocomposite layer is assigned to the low-fluorine TFA process, extensively investigated within the group before the development of the TLAG process, which will be discussed in the subsequent chapters concerning the $BaMO_3$-nanocomposite films. Nevertheless, we think that these recently synthesised BaM_2O_6 NPs would also be very interesting for the TLAG process as well for which further effort should be made in future work to identify an alternative post-surface functionalisation that does not involve flour.

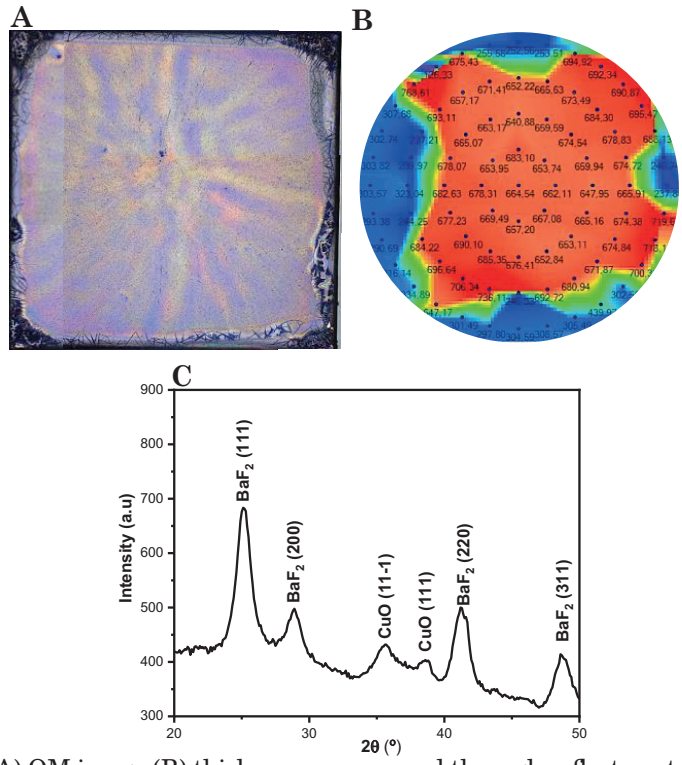

Figure B.8 (A) OM image (B) thicknesses measured through reflectometry and (C) 2D-scan GADDS XRD of nanocomposite precursor film with 4.8% mol of $BaNb_2O_6$ NPs (BaF_2 and CuO phases assigned with reference patterns 00-004-0452 and 00-048-1548 respectively form the International Centre of Diffraction Data).

The phases obtained after the pyrolysis confirm that the subsequent growth process has to be a low-flour TFA method (also known as BaF_2-based route). As the YBCO precursor phases obtained from the deposition of YBCO-$BaNb_2O_6$ precursor solution with 4.8 %mol were not the desired and expected for TLAG process, we used the BaF_2 growth route [34, 85, 266] for YBCO crystallisation. The structure and phase composition of the final grown nanocomposite YBCO film was characterised by 2D-XRD analysis. The texture of the film is shown in 2D-scan GADDS XRD (Figure B.8A) observing that non-fully epitaxial YBCO (YBCO (004) and (005)) was achieved displaying some polycrystalline character (low intensity of YBCO (102) and (103) peaks were identified). In addition, complete phase assignation was performed by the integration of 2D-scan GADDS XRD (Figure B.8C). The typical secondary phases from the growth of YBCO films (Y_2BaCuO_5 and $BaCuO_2$) were identified [34, 85]. Finally, we appreciated the peak at 29.3 ° which can be attributed to $BaNb_2O_6$ (400) with some

contribution of $BaCuO_2$ (600) peak suggesting that the NPs crystallise during the growth thermal treatment at 820 °C being stable as the initial NP composition is retained. This result matches well with annealing studies performed (section 2.3.2.1) where we observed that $BaNb_2O_6$ crystallise at 700 °C in an orthorhombic phase of $CaTa_2O_6$-type structure which is the same phase observed after growth treatment conditions at 820 °C of YBCO-$BaNb_2O_6$ nanocomposite film.

Finally, surface morphology was evaluated through Scanning Electron Microscopy (SEM). The SEM image (Figure B.8B) displays homogeneous and rather compact layers with low porosity and some solid phases homogeneously distributed at the top of the surface. These precipitates could come from the secondary phases and the excess of CuO (coming from the copper excess in the composition of YBCO precursor salts used in solution preparation).

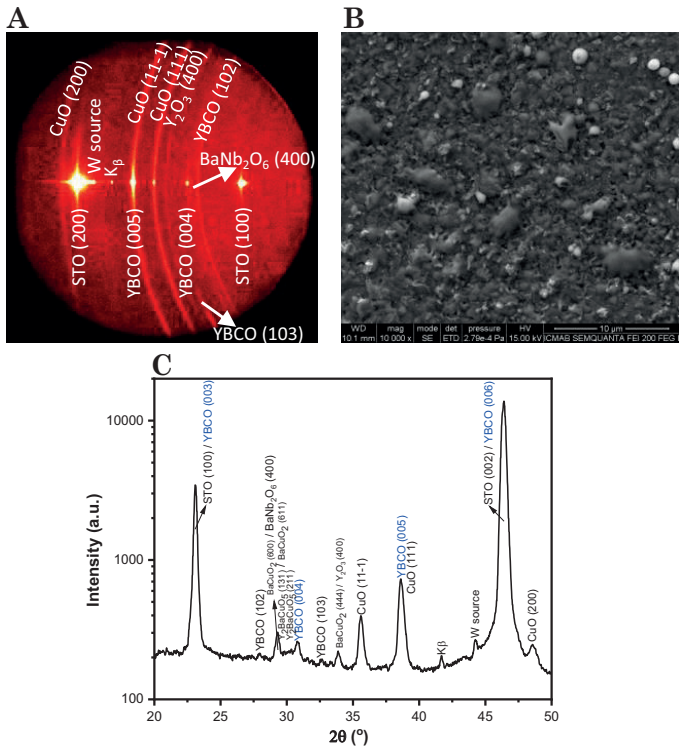

Figure B.9 (A) 2D-scan GADDS XRD which the main phases identified (B) SEM image and (C) Integrated X-Ray pattern from 2D-scan GADDS XRD of nanocomposite grown film with 4.8% mol of $BaNb_2O_6$ NPs. PDF cards used for XRD peak identification were Y_2O_3 (00-041-1105), CuO (00-048-1548), $BaNb_2O_6$ (00-014-0027), $BaCuO_2$ (00-038-1402), $Y2_BaCuO_5$ (00-038-1434), STO (00-035-0734) and YBCO orthorhombic (04-006-6962).

The results of this first trial of the application of preformed-$BaNb_2O_6$ NPs onto YBCO films demonstrated the compatibility of these NPs in terms of NP composition stability and the YBCO epitaxial growth achieved. The (400) $BaNb_2O_6$ NP peak and the YBCO (00l) peaks (YBCO (003), YBCO (004), YBCO (005) and YBCO (006)) were clearly identified (Figure B.8C). The low-intense polycrystalline phases associated with YBCO (102) and YBCO (103) peaks could be completely eliminated by tunning the growth conditions of BaF_2-route to achieve full epitaxial film. Furthermore, YBCO-$BaNb_2O_6$ precursor solution could be also fully optimised in order to obtain more homogeneous precursor films with the desired and expected phases of fluorine-free YBCO precursor films suitable for TLAG process. We could try to perform a ligand exchange based on two steps, the stripping reaction followed by the attachment of a new fluorine-free capping ligand which stabilises the NPs in the desired and more compatible solvents for fluorine-free YBCO solutions.

C

Appendix Chapter 3

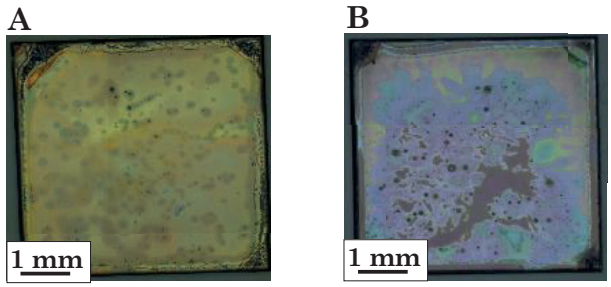

Figure C.1 OM images of nanocomposite precursor films of 3-7 composition using 1.5M + 12% mol BZO with %v/v ratio MeOH:Hprop of 50:50 using (A) 3.4%v/v MEA and (B) 4%v/v MEA

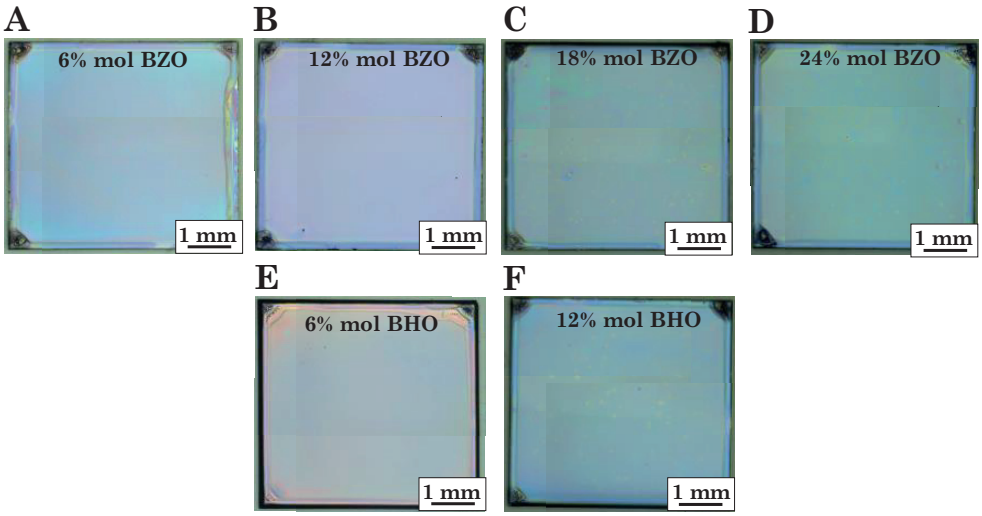

Figure C.2 OM images of nanocomposite precursor films (seed layer + 1 NP layer) of 3-7 composition using 1.5M + 3.4%v/v MEA + 5 nm-sized BZO NCs varying NC content (A) 6% mol, (B) 12% mol, (C) 18% mol, (D) 24% mol and nanocomposite precursor films (seed layer + 1 NP layer) of 3-7 composition using 1.5M + 3.4%v/v MEA + 5 nm-sized BHO NCs varying NC content (E) 6% mol and (F) 12% mol.

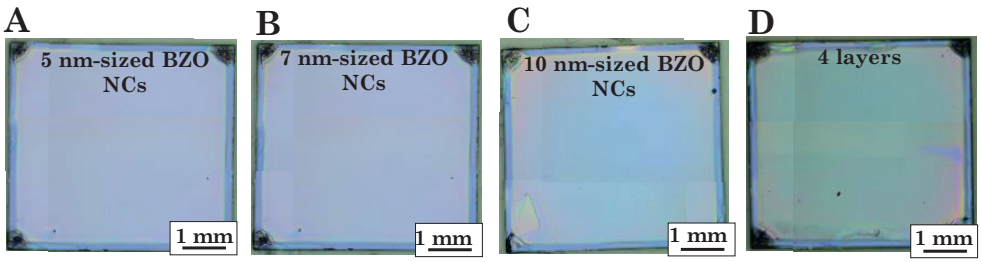

Figure C.3 OM images of nanocomposite precursor films (seed layer + 1 NP layer) of 3-7 composition using 1.5M + 3.4%v/v MEA + 12% mol BZO NCs varying NC size (A) 5 nm (B) 7 nm, (C) 10 nm and (D) 24% mol. OM image of nanocomposite precursor film composed of seed layer + 3 NP layer of 3-7 composition using 1.5M + 3.4%v/v MEA + 12% mol 5 nm-sized BZO NCs.

D

Appendix Chapter 4

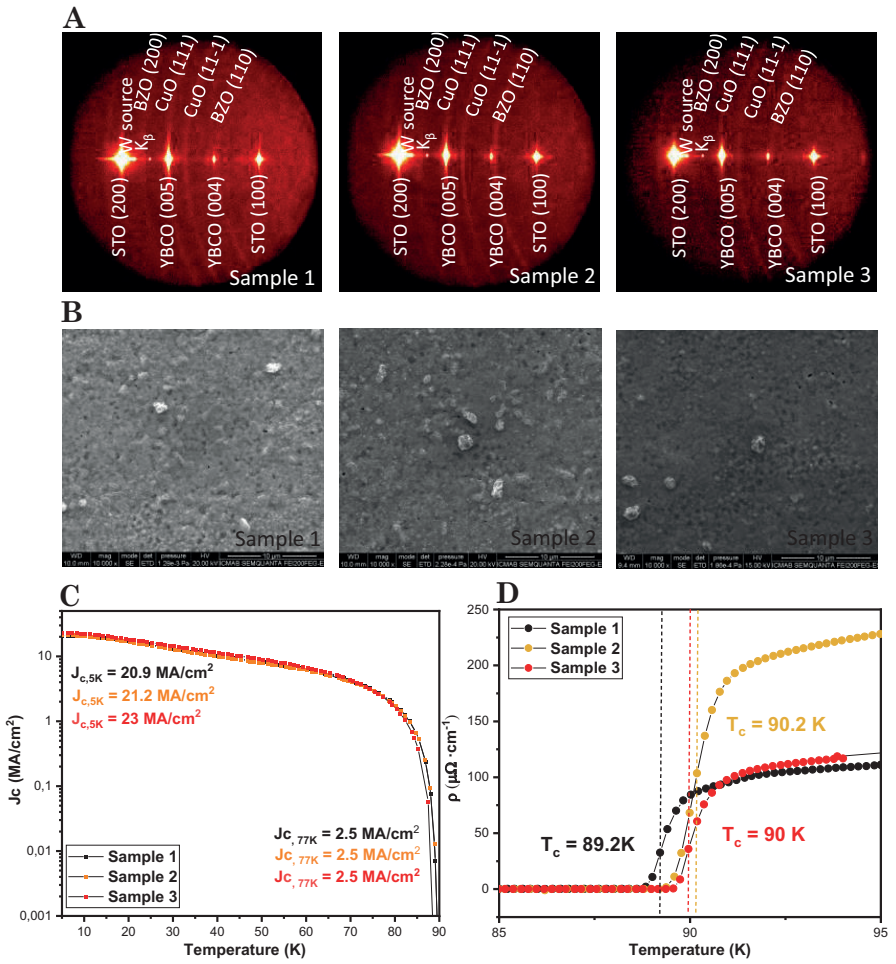

Figure D.1 (A) 2D GADDS XRD images (B) SEM images (C) Jc(T) dependence obtained from SQUID measurements and (D) ρ(T) dependence with the corresponding Tc determined values from three replicates of nanocomposites films with 12%mol BZO (7 nm) grown at 835 °C, heating with fast ramp, with a PO_2 jump from 10^{-6} to 10^{-3} bar.

D.1 *In-situ* XRD characterisation with synchrotron light

Five stays of in-situ growth experiments were conducted at the Soleil Synchrotron in the DiffAbs (Diffraction and Absorption) beamline and at the ALBA Synchrotron in the Non-Crystalline Diffraction-SAXS WAXS Experimental Techniques (NCD-SWEET) beamline. Beamline scientists Dr. C. Mocuta in France

and Dr. E. Solano in Spain supported the running of the experiments and collaborated on the optimisation of the setup and diffraction conditions to ensure the highest quality diffraction signal in-situ during the synchrotron experiments, respectively. The objective of DiffAbs is to investigate rapid phase transitions by employing hard X-ray photons with energies ranging from 3 to 23 keV. The beamline is equipped with a six-axis diffractometer, multiple sample environments to analyse thermal profiles in controlled atmospheres, and two detectors (XPAD 2D area detector and 0D point detector) that enable the acquisition of data in the range of 100 ms. For substrate alignment and texture measurements, a 0D point detector was employed, while a two-dimensional hybrid pixel area detector (XPAD) was utilised to monitor the evolving phases in situ throughout the growth process. The NCD-SWEET beamline, which possesses four distinct detectors and a beam energy ranging from 6.5 to 20 keV, enables a variety of measurement configurations. However, for our purposes, we opted for the Rayonix-supplied detector LX255-HS, which is used for WAXS measurements.

Employing a reference STO single crystal with established lattice parameters allowed for an energy adjustment of 18 keV at both beamlines. Initially, the detector position and beam energy were adjusted to cover an angular range of 2θ = 10°- 20° and χ = -9 - 9°. These adjustments ensured a sufficient separation of overlapping peaks and covered a wider range of recorded angles.

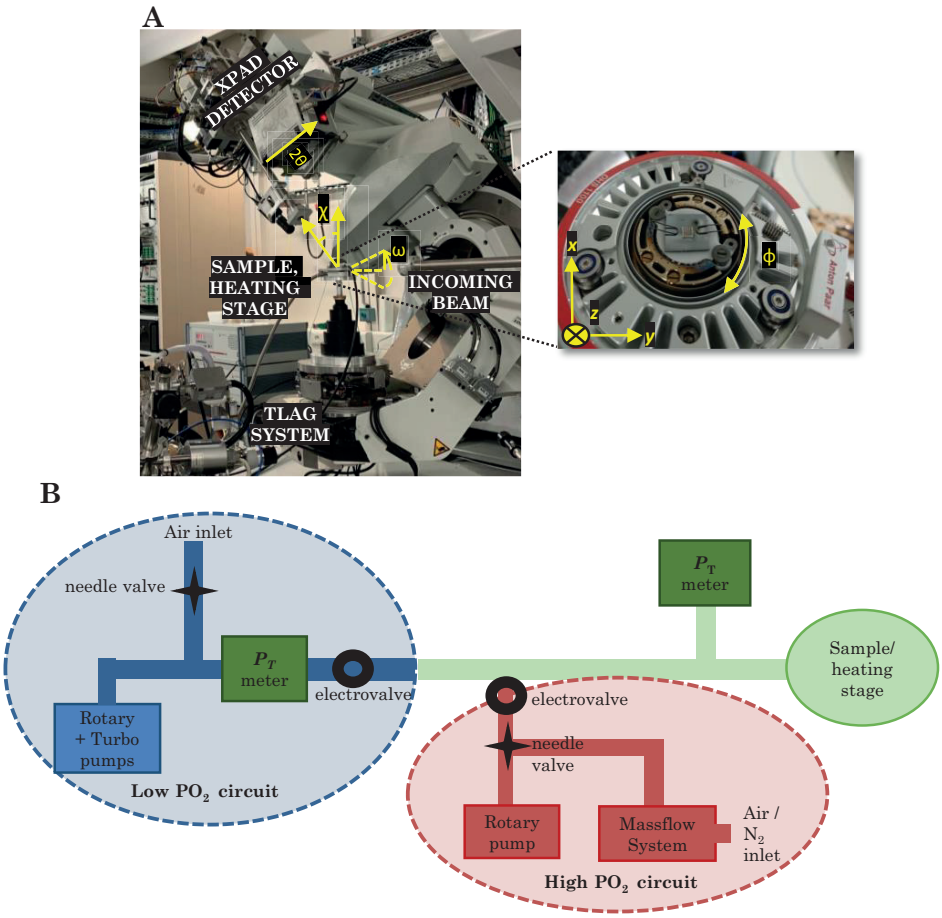

Figure D.2 (A) Experimental set-up showing sample stage, detectors, incoming beam and TLAG system with main motorised movements highlighted in yellow. The inset shows a top view of the heating stage and sample translational movements. (B) Schematical representation of the two vacuum circuits of the TLAG system.

It is possible to modify the Eulerian coordinates (see Figure D.2A) by employing multiple motors. Sample stage motors include the capability to modify translational motions in the x, y, and z directions, as well as the angles ϕ, χ and ω. Furthermore, it is possible to adjust 2θ using the XPAD 2D area detector motor.

Concerning the sample set-up, a commercially accessible dome heating stage (AntonPaar, DHS1100) is employed. This stage enables rapid heating ramps up to 4.5 °C/s, temperatures up to 1100 °C, and is suitable for use in both vacuum and controlled gas atmospheres. Elastic clamps hold the sample on top of a silicon wafer positioned on top of the heating stage, which is covered by a

graphite X-ray transparent dome capable of functioning under vacuum conditions.

The sample heating stage is linked to a system that was developed and optimised during the doctoral thesis to enhance in-situ conditions to carry out experiments employing the two TLAG routes and thereby simulate ICMAB growth conditions. The TLAG PO_2-route required the implementation of two separate vacuum circuits. A schematic representation is illustrated in Figure D.2B). To achieve the lower PO_2 during the heating stage (0.01-0.005 mbar), it is needed to use a turbo pump connected in series with a rotary pump during the heating step. The PO_2 is controlled through the adjustment of needle value at the end of pumps connected to an air gas entrance following $P_{total}=PO_2/5$. While in the high PO_2 circuit the P_{total}/PO_2 is regulated using a rotary pump linked to massflows, which permits the use of various air/nitrogen mixtures to achieve the desired P_{total}/PO_2. As a result, the desired values of P_{total} and PO_2 are modified by combining the values of the air/nitrogen mixture in massflows connected to a needle. The P_{total} can be determined and recorded using pressure metres.Both vacuum circuits are connected and controlled through two electrovalves, allowing both circuits to be switched on and off in remote control to perform PO_2 jumps.As a result, the low-pressure circuit is prepared before beginning the experiment. Subsequently, the sample is heated outside the hutch, a process that is also remotely controlled together with the in-situ XRD acquisition. After the desired temperature has been achieved, the low-pressure is closed and the high-pressure circuit is opened. The regulation of mass flows, temperature profiles, and electrovalves' switching are all remotely controlled via a variety of programs that Jordi Aguilar Larry developed.

For the data acquisition, different configurations were used to follow the phase evolution, adjusted through the motorised movements mentioned above. The main diffraction configurations are:

- χ=90° and ω=8.1°: closed to Bragg conditions of YBCO (005) reflection. The ω is a sight shift from Bragg conditions to avoid oversaturation of the detector.
- χ=45° and ω=6.7°: to be in Bragg conditions of (ll0) plane of BZO or BHO NC phases to study the NC reorientation behaviour during YBCO growth.

For standard acquisition, the in-situ 2D-XRD images have been acquired

at a rate of 100–200 ms/frame. During the crystallisation of YBCO, certain relevant data regarding phase transformation was lost due to the rapid kinetics of the TLAG process. Dr. C. Mocuta contributed to the implementation of an ultrafast acquisition from 15 to 2 milliseconds per frame during the most latest times on the DiffAbs beamline. The implementation of this extremely fast data acquisition was limited to the pressure jump step as a result of the tremendous volume of data produced and the maximal acquisition frames per experiment. This achievement enables the calculation and demonstration of the incredibly fast growth rates that can be obtained via the TLAG process.

Following in-situ experiments, the enormous unprocessed data was processed to integrate the enormous 2D-XRD images from each experiment and correlate them to time, temperature, and pressure conditions that were recorded for each integration. Jordi Aguilar designed the data treatment procedure along with a graphical user interface that visualised the evolution of in-situ 2D XRD images and the corresponding integrated XRDs with time, temperature, and pressure for each experiment. Moreover, after peak identification in the graphical user interface, the phase evolution analysis can be performed through the peak fitting of each in-situ integrated XRD by another programme developed by Jordi Aguilar.

Bibliography

(1) Mangin, P.; Kahn, R., *Superconductivity: an introduction*; Springer: 2016.

(2) Kaur, H.; Kaur, H.; Sharma, A. *Materials today: Proceedings* **2021**, *37*, 3612–3614, DOI: /10.1016/j.matpr.2020.09.771.

(3) Alade, I. O.; Rahaman, M. S.; F. Qahtan, T. *Journal of Superconductivity and Novel Magnetism* **2022**, *35*, 2621–2637, DOI: /10.1007/s10948-022-06326-1.

(4) Sharma, R. G., *Superconductivity: Basics and applications to magnets*; Springer Nature: 2021; Vol. 214.

(5) Waldram, J. R., *Superconductivity of metals and cuprates*; CRC Press: 2017, DOI: 10.1201/9780203737934.

(6) Larbalestier, D.; Gurevich, A.; Feldmann, D. M.; Polyanskii, A. *Nature* **2001**, *414*, 368–377, DOI: /10.1038/35104654.

(7) Obradors, X.; Puig, T. *Superconductor Science and Technology* **2014**, *27*, 044003, DOI: 10.1088/0953-2048/27/4/044003.

(8) Gurevich, A. *Annu. Rev. Condens. Matter Phys.* **2014**, *5*, 35–56, DOI: 10.1146/annurev-conmatphys-031113-133822.

(9) Matsushita, T. et al., *Flux pinning in superconductors*; Springer: 2007; Vol. 164.

(10) Banchewski, J. Transient Liquid Assisted Growth of YBCO Superconducting Films: Growth Kinetics, Physical Properties and Vortex Pinning, Ph.D. Thesis, Univeristat Autònoma de Barcelona, 2020, https://ddd.uab.cat/record/241156.

(11) Crabtree, G. W.; Nelson, D. R. *Physics Today* **1997**, *50*, 38–45, DOI: /10.1063/1.881715.

(12) Kwok, W.-K.; Welp, U.; Glatz, A.; Koshelev, A. E.; Kihlstrom, K. J.; Crabtree, G. W. *Reports on Progress in Physics* **2016**, *79*, 116501, DOI: 10.1088/0034-4885/79/11/116501.

(13) Puig, T.; Gutierrez, J.; Obradors, X. *Nature Reviews Physics* **2023**, 1–17, DOI: /10.1038/s42254-023-00663-3.

(14) Malozemoff, A. *Annual review of materials research* **2012**, *42*, 373–397, DOI: /10.1146/annurev-matsci-100511-100240.

(15) Hilgenkamp, H.; Mannhart, J. *Reviews of Modern Physics* **2002**, *74*, 485, DOI: /10.1103/RevModPhys.74.485.

(16) Rogalla, H.; Kes, P. H., *100 years of superconductivity*; Taylor & Francis: 2011.

(17) MacManus-Driscoll, J. L.; Wimbush, S. C. *Nature Reviews Materials* **2021**, *6*, 587–604, DOI: /10.1038/nature0109.

(18) Magnuson, M.; Schmitt, T.; Strocov, V. N.; Schlappa, J.; Kalabukhov, A. S.; Duda, L.-C. *Scientific reports* **2014**, *4*, 7017, DOI: /10.1038/srep07017.

(19) Tallon, J. L. *IEEE Transactions on Applied Superconductivity* **2014**, *25*, 1–6, DOI: 10.1109/TASC.2014.2379660.

(20) Chow, C. C.; Ainslie, M. D.; Chau, K. *Energy Reports* **2023**, *9*, 1124–1156, DOI: 10.1016/j.egyr.2022.11.173.

(21) Haran, K. S.; Kalsi, S.; Arndt, T.; Karmaker, H.; Badcock, R.; Buckley, B.; Haugan, T.; Izumi, M.; Loder, D.; Bray, J. W., et al. *Superconductor Science and Technology* **2017**, *30*, 123002, DOI: 10.1088/1361-6668/aa833e.

(22) Matias, V.; Hammond, R. H. *Physics Procedia* **2012**, *36*, 1440–1444, DOI: 10.1109/TASC.2014.2379660.

(23) Matsumoto, K.; Mele, P. *Superconductor Science and Technology* **2009**, *23*, 014001, DOI: 10.1088/0953-2048/23/1/014001.

(24) MacManus-Driscoll, J.; Foltyn, S.; Jia, Q.; Wang, H; Serquis, A; Civale, L; Maiorov, B; Hawley, M.; Maley, M.; Peterson, D. *Nature materials* **2004**, *3*, 439–443, DOI: https://doi.org/10.1038/nmat1156.

(25) Obradors, X; Puig, T; Gibert, M; Queralto, A; Zabaleta, J; Mestres, N *Chemical Society Reviews* **2014**, *43*, 2200–2225, DOI: 10.1039/C3CS60365B.

(26) Schneller, T.; Waser, R.; Kosec, M.; Payne, D., *Chemical solution deposition of functional oxide thin films*; Springer: 2013, DOI: 10.1007/978-3-211-99311-8.

(27) Shiohara, Y.; Endo, A. *Materials Science and Engineering: R: Reports* **1997**, *19*, 1–86, DOI: /10.1016/S0927-796X(96)00198-2.

(28) Benz, K.-W.; Neumann, W., *Introduction to crystal growth and characterization*; John Wiley & Sons: 2014.

(29) Kelton, K.; Greer, A. L., *Nucleation in condensed matter: applications in materials and biology*; Elsevier: 2010.

(30) Granozio, F. M.; Salluzzo, M; di Uccio, U. S.; Maggio-Aprile, I; Fischer, Ø *Physical Review B* **2000**, *61*, 756, DOI: /10.1103/PhysRevB.61.756.

(31) Ichino, Y.; Sudoh, K.; Miyachi, K.; Yoshida, Y.; Takai, Y. *IEEE transactions on applied superconductivity* **2003**, *13*, 2735–2738, DOI: 10.1109/TASC.2003.811972.

(32) Obradors, X; Martínez-Julián, F; Zalamova, K; Vlad, V.; Pomar, A; Palau, A; Llordés, A; Chen, H; Coll, M; Ricart, S, et al. *Physica C: Superconductivity and its applications* **2012**, *482*, 58–67, DOI: /10.1016/j.physc.2012.04.020.

(33) Soler Bru, L. Liquid-assisted ultrafast growth of superconducting films derived from chemical solutions, Ph.D. Thesis, Univeristat Autònoma de Barcelona, 2019, https://ddd.uab.cat/record/241156.

(34) Obradors, X.; Puig, T; Ricart, S; Coll, M; Gazquez, J; Palau, A; Granados, X *Superconductor Science and Technology* **2012**, *25*, 123001, DOI: 10.1088/0953-2048/25/12/123001.

(35) Wu, J.; Shi, J. *Superconductor Science and Technology* **2017**, *30*, 103002, DOI: 10.1088/1361-6668/aa8288.

(36) Wee, S. H.; Gao, Y.; Zuev, Y. L.; More, K. L.; Meng, J.; Zhong, J.; Stocks, G. M.; Goyal, A. *Advanced Functional Materials* **2013**, *23*, 1912–1918, DOI: /10.1002/adfm.201202101.

(37) Thomas, O; Hudner, J; Östling, M; Mossang, E; Chenevier, B; Weiss, F; Boursier, D; Senateur, J. *Journal of alloys and compounds* **1993**, *195*, 287–290, DOI: /10.1016/0925-8388(93)90741-5.

(38) Majkic, G.; Galstyan, E.; Selvamanickam, V. *IEEE Transactions on Applied Superconductivity* **2014**, *25*, 1–4, DOI: 10.1109/TASC.2014.2372902.

(39) Kursumovic, A; Tomov, R.; Hühne, R; MacManus-Driscoll, J.; Glowacki, B.; Evetts, J. *Superconductor Science and Technology* **2004**, *17*, 1215, DOI: 10.1088/0953-2048/17/10/024.

(40) Lee, J.-H.; Lee, H.; Lee, J.-W.; Choi, S.-M.; Yoo, S.-I.; Moon, S.-H. *Superconductor Science and Technology* **2014**, *27*, 044018, DOI: 10.1088/0953-2048/27/4/044018.

(41) MacManus-Driscoll, J.; Bianchetti, M; Kursumovic, A; Kim, G; Jo, W; Wang, H; Lee, J.; Hong, G.; Moon, S. *APL Materials* **2014**, *2*, DOI: /10.1063/1.4893339.

(42) Soler, L.; Jareño, J.; Banchewski, J.; Rasi, S.; Chamorro, N.; Guzman, R.; Yáñez, R.; Mocuta, C.; Ricart, S.; Farjas, J., et al. *Nature communications* **2020**, *11*, 344, DOI: 10.1038/s41467-019-13791-1.

(43) Rasi, S.; Queraltó, A.; Banchewski, J.; Saltarelli, L.; Garcia, D.; Pacheco, A.; Gupta, K.; Kethamkuzhi, A.; Soler, L.; Jareño, J., et al. *Advanced Science* **2022**, *9*, 2203834, DOI: 10.1002/advs.202203834.

(44) Rasi, S.; Soler, L.; Jareno, J.; Banchewski, J.; Guzman, R.; Mocuta, C.; Kreuzer, M.; Ricart, S.; Roura-Grabulosa, P.; Farjas, J., et al. *The Journal of Physical Chemistry C* **2020**, *124*, 15574–15584, DOI: 10.1021/acs.jpcc.0c03859.

(45) Queraltó, A.; Banchewski, J.; Pacheco, A.; Gupta, K.; Saltarelli, L.; Garcia, D.; Alcalde, N.; Mocuta, C.; Ricart, S.; Pino, F., et al. *ACS Applied Materials & Interfaces* **2021**, *13*, 9101–9112, DOI: /10.1021/acsami.0c18014.

(46) Saltarelli, L.; Gupta, K.; Rasi, S.; Kethamkuzhi, A.; Queraltó, A.; Garcia, D.; Gutierrez, J.; Farjas, J.; Roura-Grabulosa, P.; Ricart, S., et al. *ACS applied materials & interfaces* **2022**, *14*, 48582–48597, DOI: 10.1021/acsami.2c11414.

(47) Li, Z.; Coll, M.; Mundet, B.; Chamorro, N.; Vallès, F.; Palau, A.; Gazquez, J.; Ricart, S.; Puig, T.; Obradors, X. *Scientific reports* **2019**, *9*, 5828, DOI: 10.1038/s41598-019-42291-x.

(48) Miura, M.; Maiorov, B.; Sato, M.; Kanai, M.; Kato, T.; Kato, T.; Izumi, T.; Awaji, S.; Mele, P.; Kiuchi, M., et al. *NPG Asia Materials* **2017**, *9*, e447–e447, DOI: /10.1038/am.2017.197.

(49) Suenaga, M. *Physica C: Superconductivity* **2002**, *378*, 1045–1051, DOI: /10.1016/S0921-4534(02)01582-4.

(50) Chen, H; Zalamova, K; Pomar, A; Granados, X; Puig, T; Obradors, X *Superconductor Science and Technology* **2010**, *23*, 034005, DOI: 10.1088/0953-2048/23/3/034005.

(51) Sánchez-Valdés, C.; Puig, T; Obradors, X *Superconductor Science and Technology* **2015**, *28*, 024006, DOI: 10.1088/0953-2048/28/2/024006.

(52) Qu, T.; Zhu, Y.; Feng, F.; Lin, G.; Deng, S.; Lu, H.; Zhang, X.; Fu, Q.; Xiao, S.; Zeng, P., et al. *IEEE Transactions on Applied Superconductivity* **2016**, *26*, 1–5, DOI: 10.1109/TASC.2016.2549041.

(53) Queraltó, A.; Sieger, M.; Gupta, K.; Meledin, A.; Barusco, P.; Saltarelli, L.; de Palau, M.; Granados, X.; Obradors, X.; Puig, T. *Superconductor Science and Technology* **2022**, *36*, 025003, DOI: 10.1088/1361-6668/acaad3.

(54) Obradors, X; Puig, T; Pomar, A; Sandiumenge, F; Pinol, S; Mestres, N; Castano, O; Coll, M; Cavallaro, A; Palau, A, et al. *Superconductor Science and Technology* **2004**, *17*, 1055, DOI: 10.1088/0953-2048/17/8/020.

(55) Jareño Cerulla, J. Transient liquid assisted growth of superconducting nanocomposite films, Ph.D. Thesis, Univeristat Autònoma de Barcelona, 2020, https://ddd.uab.cat/record/243303.

(56) Vermeir, P.; Feys, J.; Schaubroeck, J.; Verbeken, K.; Lommens, P.; Van Driessche, I. *Materials Research Bulletin* **2012**, *47*, 4376–4382, DOI: /10.1016/j.materresbull.2012.09.033.

(57) Zhao, Y.; Chu, J.; Qureishy, T.; Wu, W.; Zhang, Z.; Mikheenko, P.; Johansen, T. H.; Grivel, J.-C. *Acta Materialia* **2018**, *144*, 844–852, DOI: /10.1016/j.actamat.2017.11.050.

(58) Chu, J.; Zhao, Y.; Khan, M. Z.; Tang, X.; Wu, W.; Shi, J.; Wu, Y.; Huhtinen, H.; Suo, H.; Jin, Z. *Crystal Growth & Design* **2019**, *19*, 6752–6762, DOI: /10.1021/acs.cgd.9b01120.

(59) Rasi, S. Advanced thermal analysis of rebco superconductors precursor films and functional oxides, Ph.D. Thesis, Universitat de Girona, 2019.

(60) Ramesh, R; Hwang, D; Ravi, T.; Inam, A; Barner, J.; Nazar, L; Chan, S.; Chen, C.; Dutta, B; Venkatesan, T, et al. *Applied physics letters* **1990**, *56*, 2243–2245, DOI: /10.1063/1.102932.

(61) Huhtinen, H; Palonen, H; Paturi, P *IEEE transactions on applied superconductivity* **2012**, *23*, 7200104–7200104, DOI: 10.1109/TASC.2012.2228891.

(62) Sahu, N.; Parija, B; Panigrahi, S *Indian Journal of Physics* **2009**, *83*, 493–502, DOI: /10.1007/s12648-009-0009-z.

(63) Arvanitidis, I; Siche, D.; Seetharaman, S *Metallurgical and materials transactions B* **1996**, *27*, 409–416, DOI: /10.1007/BF02914905.

(64) Vermeir, P.; Cardinael, I.; Schaubroeck, J.; Verbeken, K.; Backer, M.; Lommens, P.; Knaepen, W.; D'haen, J.; De Buysser, K.; Van Driessche, I. *Inorganic chemistry* **2010**, *49*, 4471–4477, DOI: 10.1021/ic9021799.

(65) Parmigiani, F.; Chiarello, G.; Ripamonti, N; Goretzki, H; Roll, U *Physical Review B* **1987**, *36*, 7148, DOI: /10.1103/PhysRevB.36.7148.

(66) Parinov, I. A., *Microstructure and properties of high-temperature superconductors*; Springer Science & Business Media: 2013, DOI: /10.1007/978-3-642-34441-1.

(67) Villarejo, B.; Pop, C.; Ricart, S.; Mundet, B.; Palau, A.; Roura-Grabulosa, P.; Farjas, J.; Puig, T.; Obradors, X. *Journal of Materials Chemistry C* **2020**, *8*, 10266–10282, DOI: 10.1039/D0TC01846E.

(68) MacManus-Driscoll, J.; Bravman, J.; Beyers, R. *Physica C: Superconductivity* **1995**, *241*, 401–413, DOI: 10.1016/0921-4534(94)02369-7.

(69) Nevriva, M; Pollert, E; Matejkova, L; Triska, A *J. Cryst. Growth;(Netherlands)* **1988**, *91*, DOI: /10.1016/0022-0248(88)90265-5.

(70) Chu, P.-Y.; Buchanan, R. C. *Journal of materials research* **1994**, *9*, 844–851, DOI: /10.1557/JMR.1994.0844.

(71) Taïr, F.; Carreras, L.; Camps, J.; Farjas, J.; Roura, P.; Calleja, A.; Puig, T.; Obradors, X. *Journal of Alloys and Compounds* **2017**, *692*, 787–792, DOI: /10.1016/j.jallcom.2016.08.072.

(72) Chen, N.; Rothman, S.; Routbort, J.; Goretta, K. *Journal of materials research* **1992**, *7*, 2308–2316, DOI: 10.1557/JMR.1992.2308.

(73) Kuršumović, A; Cheng, Y.; Glowacki, B.; Madsen, J; Evetts, J. *Journal of crystal growth* **2000**, *218*, 45–56, DOI: /10.1016/S0022-0248(00)00519-4.

(74) Lee, B.-J.; Lee, D. N. *Journal of the American Ceramic Society* **1991**, *74*, 78–84, DOI: /10.1111/j.1151-2916.1991.tb07300.x.

(75) Ellingham, H. J. *J. Soc. Chem. Ind* **1944**, *63*, 125–160, DOI: /10.1002/jctb.5000630501.

(76) Lindemer, T.; Specht, E. *Physica C: Superconductivity* **1995**, *255*, 81–94, DOI: /10.1016/0921-4534(95)00460-2.

(77) Stangl, A. Oxygen kinetics and charge doping for high critical current YBCO films, Ph.D. Thesis, Univeristat Autònoma de Barcelona, 2019, {UniveristatAutÃšnomadeBarcelona}.

(78) Jorgensen, J.; Veal, B.; Paulikas, A. P.; Nowicki, L.; Crabtree, G.; Claus, H; Kwok, W. *Physical Review B* **1990**, *41*, 1863, DOI: /10.1103/PhysRevB.41.1863.

(79) Liang, R.; Bonn, D.; Hardy, W. *Physical Review B* **2006**, *73*, 180505, DOI: /10.1103/PhysRevB.73.180505.

(80) Llordes, A.; Palau, A; Gázquez, J; Coll, M; Vlad, R; Pomar, A; Arbiol, J.; Guzman, R.; Ye, S; Rouco, V, et al. *Nature materials* **2012**, *11*, 329–336, DOI: /10.1038/nmat3247.

(81) Puig, T; Gutiérrez, J; Pomar, A; Llordés, A; Gazquez, J; Ricart, S; Sandiumenge, F; Obradors, X *Superconductor Science and Technology* **2008**, *21*, 034008, DOI: /10.1088/0953-2048/21/3/034008.

(82) Kihlstrom, K. J.; Civale, L.; Eley, S; Miller, D. J.; Welp, U.; Kwok, W. K.; Niraula, P.; Kayani, A.; Ghigo, G.; Laviano, F., et al. *Superconductor Science and Technology* **2020**, *34*, 015011, DOI: 10.1088/1361-6668/ab9f64.

(83) Palau, A; Vallès, F; Rouco, V; Coll, M; Li, Z; Pop, C; Mundet, B; Gàzquez, J; Guzman, R; Gutierrez, J, et al. *Superconductor Science and Technology* **2018**, *31*, 034004, DOI: /10.1088/1361-6668/aaa65e..

(84) Foltyn, S.; Civale, L; MacManus-Driscoll, J.; Jia, Q.; Maiorov, B; Wang, H; Maley, M *Nature materials* **2007**, *6*, 631–642, DOI: 10.1038/nmat1989.

(85) Obradors, X.; Puig, T; Li, Z.; Pop, C.; Mundet, B.; Chamorro, N.; Vallés, F.; Coll, M.; Ricart, S.; Vallejo, B, et al. *Superconductor Science and Technology* **2018**, *31*, 044001, DOI: 10.1088/1361-6668/aaaad7.

(86) Díez-Sierra, J.; López-Domínguez, P.; Rijckaert, H.; Rikel, M.; Hanisch, J.; Khan, M. Z.; Falter, M.; Bennewitz, J.; Huhtinen, H.; Schafer, S., et al. *ACS Applied Nano Materials* **2020**, *3*, 5542–5553, DOI: 10.1021/acsanm.0c00814.

(87) Gutierrez, J; Llordes, A; Gazquez, J; Gibert, M; Roma, N; Ricart, S; Pomar, A; Sandiumenge, F; Mestres, N; Puig, T, et al. *Nature materials* **2007**, *6*, 367–373, DOI: 10.1038/nmat1893.

(88) Coll, M; Ye, S; Rouco, V; Palau, A; Guzman, R; Gazquez, J; Arbiol, J; Suo, H; Puig, T; Obradors, X *Superconductor Science and Technology* **2012**, *26*, 015001, DOI: 10.1088/0953-2048/26/1/015001.

(89) Coll, M; Guzman, R; Garcés, P; Gazquez, J; Rouco, V; Palau, A; Ye, S; Magen, C; Suo, H; Castro, H, et al. *Superconductor Science and Technology* **2014**, *27*, 044008, DOI: 10.1088/0953-2048/27/4/044008.

(90) Ercolano, G; Harrington, S.; Wang, H; Tsai, C.; MacManus-Driscoll, J. *Superconductor Science and Technology* **2010**, *23*, 022003, DOI: 10.1088/0953-2048/23/2/022003.

(91) Ercolano, G; Bianchetti, M; Sahonta, S.-L.; Kursumovic, A; Lee, J.; Wang, H; MacManus-Driscoll, J. *Journal of Applied Physics* **2014**, *116*, DOI: /10.1063/1.4890459.

(92) Celentano, G; Rizzo, F; Augieri, A; Mancini, A; Pinto, V; Rufoloni, A; Vannozzi, A; MacManus-Driscoll, J.; Feighan, J; Kursumovic, A, et al. *Superconductor Science and Technology* **2020**, *33*, 044010, DOI: 10.1088/1361-6668/ab6ee5.

(93) Miura, M.; Tsuchiya, G.; Harada, T.; Sakuma, K.; Kurokawa, H.; Sekiya, N.; Kato, Y.; Yoshida, R.; Kato, T.; Nakaoka, K., et al. *NPG Asia Materials* **2022**, *14*, 85, DOI: /10.1038/s41427-022-00432-1.

(94) Izumi, T; Nakaoka, K *Superconductor Science and Technology* **2018**, *31*, 034008, DOI: 10.1088/1361-6668/aa9dd2.

(95) Cayado, P.; De Keukeleere, K.; Garzón, A; Perez-Mirabet, L; Meledin, A; De Roo, J.; Vallés, F; Mundet, B; Rijckaert, H.; Pollefeyt, G., et al. *Superconductor Science and Technology* **2015**, *28*, 124007, DOI: 10.1088/0953-2048/28/12/124007.

(96) Cayado, P.; Mundet, B.; Eloussifi, H.; Vallés, F.; Coll, M.; Ricart, S.; Gázquez, J.; Palau, A.; Roura, P.; Farjas, J., et al. *Superconductor Science and Technology* **2017**, *30*, 125010, DOI: 10.1088/1361-6668/aa8ffe.

(97) De Keukeleere, K.; Cayado, P.; Meledin, A.; Vallès, F.; De Roo, J.; Rijckaert, H.; Pollefeyt, G.; Bruneel, E.; Palau, A.; Coll, M., et al. *Advanced Electronic Materials* **2016**, *2*, 1600161, DOI: 10.1002/aelm.201600161.

(98) Rijckaert, H.; Cayado, P.; Nast, R.; Diez Sierra, J.; Erbe, M.; López Dominguez, P.; Hänisch, J.; De Buysser, K.; Holzapfel, B.; Van Driessche, I. *Coatings* **2019**, *10*, 17, DOI: 10.1088/1361-6668/ac7ae3.

(99) Rijckaert, H.; Malmivirta, M.; Banerjee, S.; Billinge, S. J.; Huhtinen, H.; Paturi, P.; De Buysser, K.; Van Driessche, I. *Superconductor Science and Technology* **2022**, *35*, 084008, DOI: 10.1088/1361-6668/ac7ae3.

(100) Takagahara, T.; Takeda, K. *Physical Review B* **1992**, *46*, 15578, DOI: /10.1103/PhysRevB.46.15578.

(101) Guisbiers, G. *Nanoscale Research Letters* **2010**, *5*, 1132–1136, DOI: /10.1007/s11671-010-9614-1.

(102) Shapira, P.; Youtie, J.; Porter, A. *Scientometrics* **2010**, *85*, 595–611, DOI: 10.1007/s11192-010-0204-x.

(103) Niederberger, M.; Pinna, N., *Metal oxide nanoparticles in organic solvents: synthesis, formation, assembly and application*; Springer Science & Business Media: 2009.

(104) Kazim, S.; Nazeeruddin, M. K.; Grätzel, M.; Ahmad, S. *Angewandte Chemie International Edition* **2014**, *53*, 2812–2824, DOI: /10.1002/anie.201308719.

(105) Chavali, M. S.; Nikolova, M. P. *SN applied sciences* **2019**, *1*, 607, DOI: /10.1007/s42452-019-0592-3.

(106) Oskam, G. *Journal of sol-gel science and technology* **2006**, *37*, 161–164, DOI: /10.1007/s10971-005-6621-2.

(107) Murthy, S.; Effiong, P.; Fei, C. C., *Metal oxide nanoparticles in biomedical applications*; Elsevier: 2020, pp 233–251.

(108) Opherden, L.; Sieger, M.; Pahlke, P.; Hühne, R.; Schultz, L.; Meledin, A.; Van Tendeloo, G.; Nast, R.; Holzapfel, B.; Bianchetti, M., et al. *Scientific reports* **2016**, *6*, 1–10, DOI: 10.1038/srep21188.

(109) Suzuki, T.; Oomura, S.; Imamura, K.; Inoue, M.; Higashikawa, K.; Awaji, S.; Nakaoka, K.; Izumi, T.; Kiss, T. *IEEE Transactions on Applied Superconductivity* **2017**, *28*, 1–4, DOI: 0.1109/TASC.2013.2238975.

(110) Vassen, R.; Cao, X.; Tietz, F.; Basu, D.; Stöver, D. *Journal of the American Ceramic Society* **2000**, *83*, 2023–2028, DOI: /10.1111/j.1151-2916.2000.tb01506.x.

(111) Maekawa, T.; Kurosaki, K.; Yamanaka, S. *Journal of alloys and compounds* **2006**, *407*, 44–48, DOI: /10.1016/j.jallcom.2005.06.030.

(112) Rizzo, F; Augieri, A; Angrisani Armenio, A; Galluzzi, V; Mancini, A; Pinto, V; Rufoloni, A; Vannozzi, A; Bianchetti, M; Kursumovic, A, et al. *APL Materials* **2016**, *4*, DOI: 10.1063/1.4953436.

(113) Thanh, N. T.; Maclean, N; Mahiddine, S *Chemical reviews* **2014**, *114*, 7610–7630, DOI: 10.1021/cr400544s.

(114) Wang, X.; Zhuang, J.; Peng, Q.; Li, Y. *Nature* **2005**, *437*, 121–124, DOI: 10.1038/nature03968.

(115) Martínez Esaín, J. The surface chemistry of metal fluoride nanocrystals, Ph.D. Thesis, Univeristat Autònoma de Barcelona, 2019, https://ddd.uab.cat/record/204086.

(116) Wang, F.; Richards, V. N.; Shields, S. P.; Buhro, W. E. *Chemistry of Materials* **2014**, *26*, 5–21, DOI: 10.1021/cm402139r.

(117) Cheah, P.; Qu, J.; Li, Y.; Cao, D.; Zhu, X.; Zhao, Y. *Journal of Magnetism and Magnetic Materials* **2021**, *540*, 168481, DOI: 10.1016/j.jmmm.2021.1684813.

(118) Heuer-Jungemann, A.; Feliu, N.; Bakaimi, I.; Hamaly, M.; Alkilany, A.; Chakraborty, I.; Masood, A.; Casula, M. F.; Kostopoulou, A.; Oh, E., et al. *Chemical reviews* **2019**, *119*, 4819–4880, DOI: 10.1021/acs.chemrev.8b00733.

(119) Niederberger, M.; Pinna, N. *Metal oxide nanoparticles in organic solvents: Synthesis, formation, assembly and application* **2009**, 7–18, DOI: 10.1007/978-1-84882-671-7_2.

(120) Feng, S.-H.; Li, G.-H. In *Modern inorganic synthetic chemistry*; Elsevier: 2017, pp 73–104, DOI: /10.1016/B978-0-444-63591-4.00004-5.

(121) Walton, R. I. *Chemistry–A European Journal* **2020**, *26*, 9041–9069, DOI: /10.1002/chem.202000707.

(122) Niederberger, M; Antonietti, M *Nanomaterials Chemistry: Recent Developments and New Directions* **2007**, 119–137, DOI: 10.1002/9783527611362.ch3.

(123) Feldmann, C.; Jungk, H.-O. *Angewandte Chemie International Edition* **2001**, *40*, 359–362, DOI: 10.1002/1521-3773(20010119)40:2<359::AID-ANIE359>3.0.CO;2-B.

(124) Feldmann, C. *Solid State Sciences* **2005**, *7*, 868–873, DOI: 10.1016/j.solidstatesciences.2005.01.018.

(125) Hachani, R.; Lowdell, M.; Birchall, M.; Hervault, A.; Mertz, D.; Begin-Colin, S.; Thanh, N. T. K. *Nanoscale* **2016**, *8*, 3278–3287, DOI: 10.1039/C5NR03867G.

(126) Dong, H; Chen, Y.-C.; Feldmann, C *Green chemistry* **2015**, *17*, 4107–4132, DOI: 10.1039/C5NR07681A.

(127) De Keukeleere, K.; De Roo, J.; Lommens, P.; Martins, J. C.; Van Der Voort, P.; Van Driessche, I. *Inorganic chemistry* **2015**, *54*, 3469–3476, DOI: 10.1021/acs.inorgchem.5b00046.

(128) Niederberger, M.; Garnweitner, G. *Chemistry–A European Journal* **2006**, *12*, 7282–7302, DOI: /10.1002/chem.200600313.

(129) Pinna, N.; Garnweitner, G.; Antonietti, M.; Niederberger, M. *Advanced Materials* **2004**, *16*, 2196–2200, DOI: 10.1002/adma.200400460.

(130) Pinna, N.; Niederberger, M. *Angewandte Chemie International Edition* **2008**, *47*, 5292–5304, DOI: 10.1002/anie.200704541.

(131) Pinna, N. *Journal of Materials Chemistry* **2007**, *17*, 2769–2774, DOI: 10.1039/B702854G.

(132) Chamorro, N.; Martínez-Esaín, J.; Puig, T.; Obradors, X.; Ros, J.; Yáñez, R.; Ricart, S. *RSC advances* **2020**, *10*, 28872–28878, DOI: 10.1039/D0RA03861J.

(133) Chamorro Garcia, N. Hybrid approach to obtain high-quality $BaMO_3$ nanocrystals for $YBa_2Cu_3O_{7-\delta}$ superconducting nanocomposite, Ph.D. Thesis, Univeristat Autònoma de Barcelona, 2021, https://ddd.uab.cat/record/241162.

(134) Pinna, N.; Antonietti, M.; Niederberger, M. *Colloids and Surfaces A: Physicochemical and Engineering Aspects* **2004**, *250*, 211–213, DOI: 10.1016/j.colsurfa.2004.04.078.

(135) Buha, J.; Arčon, D.; Niederberger, M.; Djerdj, I. *Physical Chemistry Chemical Physics* **2010**, *12*, 15537–15543, DOI: 10.1039/C0CP01298J.

(136) Baruwati, B.; Varma, R. S. *Crystal growth & design* **2010**, *10*, 3424–3428, DOI: 10.1021/cg100123q.

(137) Gömpel, D.; Tahir, M. N.; Panthöfer, M.; Mugnaioli, E.; Brandscheid, R.; Kolb, U.; Tremel, W. *Journal of Materials Chemistry A* **2014**, *2*, 8033–8040, DOI: 10.1039/C4TA00183D.

(138) Li, J.; Dai, W.; Yan, J.; Wu, G.; Li, L.; Guan, N. *Chinese Journal of Catalysis* **2015**, *36*, 432–438, DOI: 10.1016/S1872âĂŘ2067(14)60215âĂŘ1.

(139) Gaikwad, S.; Samuel, V.; Pasricha, R.; Ravi, V *Bulletin of Materials Science* **2005**, *28*, 121–123, DOI: 10.1007/BF02704230.

(140) Natarajan, N; Samuel, V.; Pasricha, R.; Ravi, V *Materials Science and Engineering: B* **2005**, *117*, 169–171, DOI: 10.1016/j.mseb.2004.11.009.

(141) Xu, T.; Zhao, X.; Zhu, Y. *The Journal of Physical Chemistry B* **2006**, *110*, 25825–25832, DOI: 10.1021/jp065307k.

(142) De Roo, J.; De Keukeleere, K.; Hens, Z.; Van Driessche, I. *Dalton Transactions* **2016**, *45*, 13277–13283, DOI: 10.1039/C6DT02410F.

(143) De Roo, J.; Baquero, E. A.; Coppel, Y.; De Keukeleere, K.; Van Driessche, I.; Nayral, C.; Hens, Z.; Delpech, F. *ChemPlusChem* **2016**, *81*, 1216–1223, DOI: 10.1002/cplu.201600372.

(144) De Roo, J.; Van Driessche, I.; Martins, J. C.; Hens, Z. *Nature materials* **2016**, *15*, 517–521, DOI: 10.1038/nmat4554.

(145) De Roo, J.; Justo, Y.; De Keukeleere, K.; Van den Broeck, F.; Martins, J. C.; Van Driessche, I.; Hens, Z. *Angewandte Chemie International Edition* **2015**, *54*, 6488–6491, DOI: anie.201500965.

(146) Green, M. L.; Parkin, G. *Journal of Chemical Education* **2014**, *91*, 807–816, DOI: 10.1021/ed400504f.

(147) Owen, J. *Science* **2015**, *347*, 615–616, DOI: 10.1126/science.1259924.

(148) Rosen, E. L.; Buonsanti, R.; Llordes, A.; Sawvel, A. M.; Milliron, D. J.; Helms, B. A. *Angewandte Chemie International Edition* **2012**, *51*, 684–689, DOI: 10.1002/anie.201105996.

(149) De Roo, J.; Van den Broeck, F.; De Keukeleere, K.; Martins, J. C.; Van Driessche, I.; Hens, Z. *Journal of the American Chemical Society* **2014**, *136*, 9650–9657, DOI: 10.1021/ja5032979.

(150) Boles, M. A.; Ling, D.; Hyeon, T.; Talapin, D. V. *Nature materials* **2016**, *15*, 141–153, DOI: /10.1038/nmat4526.

(151) Dong, A.; Ye, X.; Chen, J.; Kang, Y.; Gordon, T.; Kikkawa, J. M.; Murray, C. B. *Journal of the American Chemical Society* **2011**, *133*, 998–1006, DOI: 10.1021/ja108948z.

(152) U. Holzwarth, N. G. *Nature nanotechnology* **2011**, *6*, 534–534, DOI: 10.1038/nnano.2011.145.

(153) Patterso, A. *J. Phys. Rev* **1939**, *56*, 978–982, DOI: 10.1103/PhysRev.56.978.

(154) Langform, J. I.; Wilson, A. J. C. *Journal of applied crystallography* **1978**, *11*, 102–113, DOI: 10.1107/S0021889878012844.

(155) Butler, J. Theory of the stability of lyophobic colloids, 1948, DOI: /10.1038/162315b0.

(156) Derjaguin, B.; Landau, L. *Progress in Surface Science* **1993**, *43*, 30–59, DOI: /10.1016/0079-6816(93)90013-L.

(157) Greenwood, N. N.; Earnshaw, A., *Chemistry of the Elements*; Elsevier: 2012.

(158) Lim, H. M.; Lee, Y.; Lee, S.-H.; Lim, C.; Kim, D. S. *Research on Chemical Intermediates* **2012**, *38*, 1203–1213, DOI: 10.1007/s11164-011-0459-8.

(159) Martínez-Esaín, J.; Puig, T.; Obradors, X.; Ros, J.; Yáñez, R.; Faraudo, J.; Ricart, S. *Angewandte Chemie* **2018**, *130*, 14963–14967, DOI: 10.1002/ange.201806273.

(160) Martínez-Esaín, J.; Faraudo, J.; Puig, T.; Obradors, X.; Ros, J.; Ricart, S.; Yáñez, R. *Journal of the American Chemical Society* **2018**, *140*, 2127–2134, DOI: 10.1021/jacs.7b09821.

(161) Brinker, C. J.; Scherer, G. W., *Sol-gel science: the physics and chemistry of sol-gel processing*; Academic press: 2013.

(162) Levy, D.; Zayat, M., *The Sol-Gel Handbook, 3 Volume Set: Synthesis, Characterization, and Applications*; John Wiley & Sons: 2015; Vol. 1.

(163) Livage, J.; Henry, M.; Sanchez, C. *Progress in solid state chemistry* **1988**, *18*, 259–341, DOI: 10.1016/0079-6786(88)90005-2.

(164) Simonsen, M. E.; Søgaard, E. G. *Journal of sol-gel science and technology* **2010**, *53*, 485–497, DOI: 10.1007/s10971-009-2121-0.

(165) Borlaf, M.; Moreno, R. *Open Ceramics* **2021**, *8*, 100200, DOI: 10.1016/j.oceram.2021.100200.

(166) Danks, A. E.; Hall, S. R.; Schnepp, Z. *Materials Horizons* **2016**, *3*, 91–112, DOI: 10.1039/C5MH00260E.

(167) Turova, N. Y.; Turevskaya, E. P.; Kessler, V. G.; Yanovskaya, M. I., *The chemistry of metal alkoxides*; Springer Science & Business Media: 2007.

(168) Van den Eynden, D.; Pokratath, R.; De Roo, J. *Chemical Reviews* **2022**, *122*, 10538–10572, DOI: 10.1021/acs.chemrev.1c01008.

(169) Fleeting, K.; Jones, A.; Otway, D.; White, A. P.; Williams, D., et al. *Journal of the Chemical Society, Dalton Transactions* **1999**, 2853–2859, DOI: 10.1039/A901666J.

(170) Spijksma, G. I.; Seisenbaeva, G. A.; Fischer, A.; Bouwmeester, H. J.; Blank, D. H.; Kessler, V. G. *Journal of sol-gel science and technology* **2009**, *51*, 10–22, DOI: 10.1007/s10971-009-1988-0.

(171) Spijksma, G. I.; Seisenbaeva, G. A.; Bouwmeester, H. J.; Blank, D. H.; Kessler, V. G. *Polyhedron* **2013**, *53*, 150–156, DOI: 10.1016/j.poly.2013.01.046.

(172) Spijksma, G. I.; Blank, D. H.; Bouwmeester, H. J.; Kessler, V. G. *International journal of molecular sciences* **2009**, *10*, 4977–4989, DOI: 10.3390/ijms10114977.

(173) Fiévet, F; Ammar-Merah, S; Brayner, R; Chau, F; Giraud, M; Mammeri, F; Peron, J; Piquemal, J.-Y.; Sicard, L; Viau, G *Chemical Society Reviews* **2018**, *47*, 5187–5233, DOI: 10.1039/C7CS00777A.

(174) Xiong, L.; Shen, B.; Behera, D.; Gambhir, S. S.; Chin, F. T.; Rao, J. *Nanoscale* **2013**, *5*, 3253–3256, DOI: 10.1039/c3nr00335c.

(175) Długosz, O.; Banach, M. *Colloids and Surfaces A: Physicochemical and Engineering Aspects* **2020**, *606*, 125453, DOI: 10.1016/j.colsurfa.2020.125453.

(176) Kaszuba, M.; Corbett, J.; Watson, F. M.; Jones, A. *Philosophical transactions of the royal society a: mathematical, physical and engineering sciences* **2010**, *368*, 4439–4451, DOI: 10.1098/rsta.2010.0175.

(177) Rodriguez-Loya, J.; Lerma, M.; Gardea-Torresdey, J. L. *Micromachines* **2023**, *15*, 24, DOI: /10.3390/mi15010024.

(178) Delgado, A.; González-Caballero, F; Hunter, R.; Koopal, L.; Lyklema, J **2005**, DOI: 10.1351/pac200577101753.

(179) Ohshima, H *Encyclopedia of Colloid and interface science* **2013**, 148–207, DOI: 10.1007/978-3-642-20665-8_162.

(180) Ohshima, H. In *Electrical Phenomena at Interfaces*; Routledge: 2018, pp 2–18, DOI: 10.1007/978-3-642-20665-8_15.

(181) Herzberger, J.; Niederer, K.; Pohlit, H.; Seiwert, J.; Worm, M.; Wurm, F. R.; Frey, H. *Chemical reviews* **2016**, *116*, 2170–2243, DOI: 10.1021/acs.chemrev.5b00441.

(182) De Lucas, A.; Rodríguez, L.; Pérez-Collado, M.; Sanchez, P.; Rodríguez, J. F. *Polymer international* **2002**, *51*, 1066–1071, DOI: 10.1002/pi.909.

(183) Sakharov, A.; Skibida, I. In *Studies in Surface Science and Catalysis*; Elsevier: 1994; Vol. 82, pp 629–637, DOI: 10.1016/S0167-2991(08)63457-6.

(184) Back, D. M.; Schmitt, R. L. *Kirk-Othmer Encyclopedia of Chemical Technology* **2000**, DOI: 10.1002/0471238961.0520082502010311.a01.pub2.

(185) De Roo, J.; De Keukeleere, K.; Feys, J.; Lommens, P.; Hens, Z.; Van Driessche, I. *Journal of nanoparticle research* **2013**, *15*, 1–11, DOI: 10.1007/s11051-013-1778-z.

(186) Bilecka, I.; Niederberger, M. *Nanoscale* **2010**, *2*, 1358–1374, DOI: 10.1039/B9NR00377K.

(187) Abubakarov, A.; Pavlenko, A.; Shilkina, L.; Turik, A.; Verbenko, I.; Reznichenko, L.; Andryushin, K.; Andryushina, I.; Sadykov, H.; Parinov, I., et al. *Applied Sciences* **2018**, *8*, 1932, DOI: 10.3390/app8101932.

(188) Mumme, W. G.; Grey, I. E.; Roth, R. S.; Vanderah, T. A. *Journal of Solid State Chemistry* **2007**, *180*, 2429–2436, DOI: 10.1016/j.jssc.2007.06.014.

(189) Layden, G. *Materials Research Bulletin* **1967**, *2*, 533–539, DOI: 10.1016/0025-5408(67)90029-3.

(190) Kutahyali Aslani, C.; Klepov, V. V.; zur Loye, H.-C. *Journal of Solid State Chemistry* **2021**, *294*, DOI: 10.1016/j.jssc.2020.121833.

(191) Babalola, B. J.; Ayodele, O. O.; Olubambi, P. A. *Heliyon* **2023**, DOI: 10.1016/j.heliyon.2023.e14070.

(192) Goovaerts, K.; Lambrechts, P.; De Munck, J.; Bergmans, L.; Van Meerbeek, B., *Encyclopedia of materials: science and technology*; Elsevier Science: 2002, DOI: 10.1016/B0-08-043152-6/01622-3.

(193) Sukhorukov, G. B.; Antipov, A. A.; Voigt, A.; Donath, E.; Möhwald, H. *Macromolecular Rapid Communications* **2001**, *22*, 44–46, DOI: 10.1002/1521-3927(20010101)22:1<44::AID-MARC44>3.0.CO;2-U.

(194) Gankanda, A.; Cwiertny, D. M.; Grassian, V. H. *The Journal of Physical Chemistry C* **2016**, *120*, 19195–19203, DOI: 10.1021/acs.jpcc.6b05931.

(195) Noei, H.; Qiu, H.; Wang, Y.; Löffler, E.; Wöll, C.; Muhler, M. *Physical Chemistry Chemical Physics* **2008**, *10*, 7092–7097, DOI: 10.1039/B811029H.

(196) Chandran, K; Nithya, R; Sankaran, K; Gopalan, A; Ganesan, V *Bulletin of Materials Science* **2006**, *29*, 173–179, DOI: 10.1007/BF02704612.

(197) Pretsch, E.; Bühlmann, P.; Affolter, C.; Pretsch, E.; Bhuhlmann, P; Affolter, C, *Structure determination of organic compounds*; Springer: 2000, DOI: 10.1007/978-3-540-93810-1.

(198) Baltrusaitis, J.; Schuttlefield, J.; Zeitler, E.; Grassian, V. H. *Chemical Engineering Journal* **2011**, *170*, 471–481, DOI: 10.1016/j.cej.2010.12.041.

(199) Chandran, K; Kamruddin, M; Ajikumar, P.; Gopalan, A; Ganesan, V *Journal of nuclear materials* **2006**, *358*, 111–128, DOI: 10.1016/j.jnucmat.2006.07.003.

(200) Martínez-Esaín, J.; Puig, T.; Obradors, X.; Ros, J.; Farjas, J.; Roura-Grabulosa, P.; Faraudo, J.; Yáñez, R.; Ricart, S. *Nanoscale advances* **2019**, *1*, 2740–2747, DOI: 10.1039/C9NA00098D.

(201) Farjas, J; Camps, J; Roura, P; Ricart, S; Puig, T; Obradors, X *Thermochimica acta* **2011**, *521*, 84–89, DOI: 10.1016/j.tca.2011.04.009.

(202) Clarà Saracho, A.; Haigh, S. K.; Hata, T.; Soga, K.; Farsang, S.; Redfern, S. A.; Marek, E. *Scientific Reports* **2020**, *10*, 10168, DOI: 10.1038/s41598-020-66831-y.

(203) De Roo, J.; Yazdani, N.; Drijvers, E.; Lauria, A.; Maes, J.; Owen, J. S.; Van Driessche, I.; Niederberger, M.; Wood, V.; Martins, J. C., et al. *Chemistry of Materials* **2018**, *30*, 5485–5492, DOI: 10.1021/acs.chemmater.8b02523.

(204) Erdem, D.; Shi, Y.; Heiligtag, F. J.; Kandemir, A.; Tervoort, E; Rupp, J. L.; Niederberger, M. *Journal of Materials Chemistry C* **2015**, *3*, 9833–9841, DOI: 10.1039/C5TC02214B.

(205) Deblock, L.; Goossens, E.; Pokratath, R.; De Buysser, K.; De Roo, J. *JACS Au* **2022**, *2*, 711–722, DOI: 10.1021/jacsau.1c00565.

(206) Scholz, E., *Karl Fischer titration: determination of water*; Springer Science & Business Media: 2012.

(207) Calleja, A; Ricart, S; Palmer, X; Luccas, R.; Puig, T; Obradors, X *Journal of sol-gel science and technology* **2010**, *53*, 347–352, DOI: 10.1007/s10971-009-2100-5.

(208) Wu, L.; Ek, M.; Song, M.; Sichen, D. *steel research international* **2011**, *82*, 388–397, DOI: 10.1002/srin.201000207.

(209) Konijn, B.; Sanderink, O.; Kruyt, N. P. *Powder technology* **2014**, *266*, 61–69, DOI: /10.1016/j.powtec.2014.05.044.

(210) An, Z.; Zhang, Y.; Li, Q.; Wang, H.; Guo, Z.; Zhu, J. *Powder technology* **2018**, *328*, 199–206, DOI: /10.1016/j.powtec.2017.12.019.

(211) Rekhi, S.; Bhalla, G.; Trigunayat, G. *Physica C: Superconductivity* **1998**, *307*, 51–60, DOI: 10.1016/S0921-4534(98)00404-3.

(212) Rasband, W. ImageJ. US national institutes of health, Bethesda, MD, 1997.

(213) Avramov, I *Journal of Non-Crystalline Solids* **2009**, *355*, 745–747, DOI: /10.1016/j.jnoncrysol.2009.02.009.

(214) Feighan, J.; Kursumovic, A; MacManus-Driscoll, J. *Superconductor Science and Technology* **2017**, *30*, 123001, DOI: /10.1088/1361-6668/aa90d1.

(215) Krauns, C.; Tagami, M; Yamada, Y; Nakamura, M; Shiohara, Y *Journal of materials research* **1994**, *9*, 1513–1518, DOI: /10.1557/JMR.1994.1513.

(216) Solovyov, V. F.; Li, Q.; Wiesmann, H.; Oleynikov, P.; Zhu, Y. *Superconductor Science and Technology* **2008**, *21*, 125013, DOI: 10.1088/0953-2048/21/12/125013.

(217) Castaño Linares, Ó.; Cavallaro, A.; Palau Masoliver, A.; González, J.; Rossell, M. D.; Puig, T.; Piñol, S; Mestres Andreu, N.; Sandiumenge Ortiz, F.; Pomar Barbeito, A., et al. *IEEE Transactions on Applied Superconductivity, 2003, vol. 13, num. 2, p. 2504-2507* **2003**, DOI: /10.1109/TASC.2003.811832.

(218) Pomar, A; Gutiérrez, J; Palau, A; Puig, T; Obradors, X *Physical Review B* **2006**, *73*, 214522, DOI: /10.1103/PhysRevB.73.214522.

(219) Coll, M; Gazquez, J; Pomar, A; Puig, T; Sandiumenge, F; Obradors, X *Physical Review B* **2006**, *73*, 075420, DOI: /10.1103/PhysRevB.73.075420.

(220) Ward, A. *Transactions of the Faraday Society* **1937**, *33*, 88–97, DOI: /10.1039/TF9373300088.

(221) Doremus, R. H. *Journal of Applied Physics* **2002**, *92*, 7619–7629, DOI: /10.1063/1.1515132.

(222) Ojovan, M. I.; Travis, K. P.; Hand, R. J. *Journal of Physics: Condensed Matter* **2007**, *19*, 415107, DOI: 10.1088/0953-8984/19/41/415107.

(223) Jothi Prakash, C.; Prasanth, R *Journal of Materials Science* **2021**, *56*, 108–135, DOI: /10.1007/s10853-020-05116-1.

(224) MacManus-Driscoll, J.; Kursumovic, A; Maiorov, B; Civale, L; Jia, Q.; Foltyn, S.; Wang, H *IEEE transactions on applied superconductivity* **2007**, *17*, 2537–2541, DOI: 10.1109/TASC.2007.898171.

(225) Tafto, J; Suenaga, M.; Wang, T; Sabatini, R.; Moodenbaugh, A.; Levine, S *MRS Online Proceedings Library (OPL)* **1987**, *99*, 511, DOI: 10.1557/proc-99-511.

(226) Bruneel, E.; Rijckaert, H.; Diez Sierra, J.; De Buysser, K.; Van Driessche, I. *Crystals* **2022**, *12*, 410, DOI: /10.3390/cryst12030410.

(227) Uhlmann, D. R.; Chalmers, B; Jackson, K. *Journal of Applied Physics* **1964**, *35*, 2986–2993, DOI: /10.1063/1.1713142.

(228) Pötschke, J.; Rogge, V. *Journal of Crystal Growth* **1989**, *94*, 726–738, DOI: /10.1016/0022-0248(89)90097-3.

(229) Vallès, F.; Palau, A.; Abraimov, D.; Jaroszynski, J.; Constantinescu, A.-M.; Mundet, B.; Obradors, X.; Larbalestier, D.; Puig, T. *Communications Materials* **2022**, *3*, 45, DOI: /10.1038/s43246-022-00266-y.

(230) Sieger, M.; Hänisch, J.; Pahlke, P.; Sparing, M.; Gaitzsch, U.; Iida, K.; Nast, R.; Reich, E.; Schultz, L.; Holzapfel, B., et al. *IEEE Transactions on Applied Superconductivity* **2014**, *25*, 1–4, DOI: /10.1109/TASC.2014.2372903.

(231) Sieger, M.; Pahlke, P.; Lao, M.; Eisterer, M.; Meledin, A.; Van Tendeloo, G.; Ottolinger, R.; Hänisch, J.; Holzapfel, B.; Usoskin, A., et al. *IEEE Transactions on Applied Superconductivity* **2016**, *27*, 1–7, DOI: 10.1109/TASC.2016.2644858.

(232) Miura, S; Yoshida, Y; Ichino, Y; Matsumoto, K; Ichinose, A; Awaji, S *Superconductor Science and Technology* **2015**, *28*, 065013, DOI: 10.1088/0953-2048/28/6/065013.

(233) Teranishi, R; Yoshida, J; Mori, N; Yamada, K; Mukaida, M; Kiss, T; Inoue, M; Matsuda, J; Nakaoka, K; Izumi, T, et al. *Physica C: Superconductivity* **2009**, *469*, 1332–1335, DOI: 10.1016/j.physc.2009.05.024.

(234) Gazquez, J; Coll, M; Roma, N; Sandiumenge, F; Puig, T; Obradors, X *Superconductor Science and Technology* **2012**, *25*, 065009, DOI: 10.1088/0953-2048/25/6/065009.

(235) Bretos, I.; Schneller, T.; Falter, M.; Bäcker, M.; Hollmann, E.; Wördenweber, R.; Molina-Luna, L.; Van Tendeloo, G.; Eibl, O. *Journal of Materials Chemistry C* **2015**, *3*, 3971–3979, DOI: 10.1039/C4TC02543A.

(236) Jones, P. N.; Ozcan-Taskin, G. *Chemical Engineering & Technology: Industrial Chemistry-Plant Equipment-Process Engineering-Biotechnology* **2005**, *28*, 908–914, DOI: 10.1002/ceat.200500012.

(237) Regner, M.; Östergren, K.; Trägårdh, C. *Industrial & engineering chemistry research* **2008**, *47*, 3030–3036, DOI: 10.1021/ie0708071.

(238) Bouwmans, I; Bakker, A; Van den Akker, H. *Chemical Engineering Research and Design* **1997**, *75*, 777–783, DOI: 10.1205/026387697524443.

(239) Llordés, A. Superconducting Nanocomposite Films Grown by Chemical Solution Deposition: Synthesis, Microstructure and Properties, Ph.D. Thesis, Univeristat Autònoma de Barcelona, 2010.

(240) Guzman, R.; Gazquez, J.; Mundet, B.; Coll, M.; Obradors, X.; Puig, T. *Physical Review Materials* **2017**, *1*, 024801, DOI: /10.1103/PhysRevMaterials.1.024801.

(241) Rouco, V; Bartolomé, E; Palau, A; Coll, M; Obradors, X; Puig, T *Superconductor Science and Technology* **2012**, *25*, 122001, DOI: 10.1088/0953-2048/25/12/122001.

(242) Bean, C. P. *Physical review letters* **1962**, *8*, 250, DOI: /10.1103/PhysRevLett.8.250.

(243) Jiang, H.; Rühle, M; Lavernia, E. *Journal of materials research* **1999**, *14*, 549–559, DOI: /10.1557/JMR.1999.0079.

(244) Li, Z.; Coll, M.; Mundet, B.; Palau, A.; Puig, T.; Obradors, X. *Nanoscale Advances* **2020**, *2*, 3384–3393, DOI: 10.1039/D0NA00456A.

(245) Bragg, W. H.; Bragg, W. L. *Proceedings of the Royal Society of London. Series A, Containing Papers of a Mathematical and Physical Character* **1913**, *88*, 428–438, DOI: /10.1098/rspa.1913.0040.

(246) Birkholz, M., *Thin film analysis by X-ray scattering*; John Wiley & Sons: 2006.

(247) Lifshin, E., *X-ray Characterization of Materials*; John Wiley & Sons: 2008.

(248) Williamson, G.; Hall, W. *Acta metallurgica* **1953**, *1*, 22–31, DOI: /10.1016/0001-6160(53)90006-6.

(249) Stokes, A.; Wilson, A. *Proceedings of the physical society* **1944**, *56*, 174, DOI: 10.1088/0959-5309/56/3/303.

(250) Nelson, J. B.; Riley, D. *Proceedings of the Physical Society* **1945**, *57*, 160, DOI: 10.1088/0959-5309/57/3/302.

(251) Pérez Mirabet, L. Synthesis, characterization and functionalization of metal and metal oxide nanoparticles: TEM microscopy study, Ph.D. Thesis, Univeristat Autònoma de Barcelona, 2014, https://ddd.uab.cat/record/117867?ln=en.

(252) Wang, Z. Transmission electron microscopy of shape-controlled nanocrystals and their assemblies, 2000, DOI: /10.1021/jp993593c.

(253) Wang, Z. L. *Advanced Materials* **2003**, *15*, 1497–1514, DOI: /10.1002/adma.200300384.

(254) Inkson, B. J. In *Materials characterization using nondestructive evaluation (NDE) methods*; Elsevier: 2016, pp 17–43, DOI: /10.1016/B978-0-08-100040-3.00002-X.

(255) Guzmán Aluja, R. In-depth investigation of the origin, evolution and interaction of structural defects in YBCO nanocomposite thin films, Ph.D. Thesis, Univeristat Autònoma de Barcelona, 2014, https://ddd.uab.cat/record/116398.

(256) Instruments, M. Dynamic light scattering: an introduction in 30 minutes. Technical note, 2012.

(257) Lim, J.; Yeap, S. P.; Che, H. X.; Low, S. C. *Nanoscale research letters* **2013**, *8*, 1–14, DOI: /10.1186/1556-276X-8-381.

(258) Bhattacharjee, S. *Journal of controlled release* **2016**, *235*, 337–351, DOI: 10.1016/j.jconrel.2016.06.017.

(259) Hassan, P. A.; Rana, S.; Verma, G. *Langmuir* **2015**, *31*, 3–12, DOI: /10.1021/la501789z.

(260) Wilschefski, S. C.; Baxter, M. R. *The Clinical Biochemist Reviews* **2019**, *40*, 115, DOI: 10.33176/AACB-19-00024.

(261) Ammann, A. A. *Journal of mass spectrometry* **2007**, *42*, 419–427, DOI: /10.1002/jms.1206.

(262) Ström, G.; Fredriksson, M.; Stenius, P. *Journal of colloid and interface science* **1987**, *119*, 352–361, DOI: /10.1016/0021-9797(87)90280-3.

(263) Bean, C. P. *Reviews of modern physics* **1964**, *36*, 31, DOI: /10.1103/RevModPhys.36.31.

(264) Der Pauw, V. *Philips Tech. Rev.* **1958**, *20*, 220.

(265) Rouco Gómez, V. Controlling vortex pinning and dynamics of nanostructured YBCO thin films grown by chemical solution deposition, Ph.D. Thesis, Univeristat Autònoma de Barcelona, 2014, https://ddd.uab.cat/record/127057.

(266) Palmer, X; Pop, C.; Eloussifi, H.; Villarejo, B; Roura, P; Farjas, J; Calleja, A; Palau, A; Obradors, X; Puig, T, et al. *Superconductor Science and Technology* **2015**, *29*, 024002, DOI: 10.1088/0953-2048/29/2/024002.